Understanding Key Biomechanical Factors that Influence Rotator Cuff Tear Propagation

by

Gerald Dave A. Ferrer

Bachelor of Science in Bioengineering, University of Pittsburgh, 2015

Submitted to the Graduate Faculty of the

Swanson School of Engineering in partial fulfillment

of the requirements for the degree of

Doctor of Philosophy

University of Pittsburgh

2020

UNIVERSITY OF PITTSBURGH

SWANSON SCHOOL OF ENGINEERING

This dissertation was presented

by

Gerald Dave A. Ferrer

It was defended on

March 6, 2020

and approved by

Steven D. Abramowitch, PhD, Associate Professor,
Departments of Bioengineering and Clinical and Translational Science Institute

Kang Kim, PhD, Associate Professor,
Departments of Medicine, Bioengineering, Mechanical Engineering and Materials Science

Spandan Maiti, PhD, Associate Professor,
Departments of Bioengineering, Mechanical Engineering and Materials Science

Volker Musahl, MD, Professor,
Departments of Orthopaedic Surgery and Bioengineering

Dissertation Director: Richard E. Debski, PhD, Professor,
Departments of Bioengineering and Orthopaedic Surgery

Understanding Key Biomechanical Factors that Influence Rotator Cuff Tear Propagation

Gerald Dave A. Ferrer, PhD

University of Pittsburgh, 2020

The high frequency of rotator cuff tears in an aging population, combined with their capacity to cause pain and limit normal activity, underscores the importance of treating these injuries in a judicious manner. However, high failure rates have been reported for non-operative and surgical treatment. Tear propagation may explain high failure rates of treatment as larger tears are more difficult to treat and are associated with worse clinical outcomes. Abnormal glenohumeral arthrokinematics and localized changes in mechanical properties are factors that explain why some tears propagate more easily than others. Furthermore, clinicians lack a tool to non-invasively quantify tendon mechanical properties. Therefore, the objective of this dissertation is to better understand the role of glenohumeral arthrokinematics and location specific mechanical properties on tear propagation as well as the utility of ultrasound techniques to quantify mechanical properties of tendons through in-vivo, cadaveric, and computational experiments.

Following exercise therapy for 5 subjects with a rotator cuff tear, glenohumeral arthrokinematics for internal/external rotation with the arm at the side did not improve. Abnormal glenohumeral arthrokinematics may be a result of unbalanced force couples, exposing the torn supraspinatus tendon to loads that may promote tendon remodeling that increases the likelihood of tear propagation. Using a subject-specific finite element model of a supraspinatus tendon, tendon remodeling in terms of increased stiffness at the tear tips lead to more tear propagation. Cadaveric experiments showed that quantitative ultrasound measures, which analyze the grayscale echotexture of an ultrasound image, correlates to measures of tendon quality as quantified through

histology. Acoustic Radiation Force Impulse (ARFI) imaging a technique where localized radiation forces push onto the tissue, the resulting displacement is measured. The mechanical properties of the tissue can then be inferred. However, our findings suggest that ARFI imaging is limited for high stiffness tissues such as tendons. Despite large differences in tissue modulus, differences in ARFI displacement are minimal. Ultimately, understanding how changes in localized tendon mechanical properties influence tear propagation and the capabilities of currently available ultrasound techniques to measure tendon mechanical properties will enable clinicians to make better treatment decisions for patients with a rotator cuff tear.

Table of Contents

List of Tables

List of Figures

Preface

Reflecting on my time as a graduate student, I can honestly say “Life was good”. Those positive experiences would not have been possible without the support of so many people. First and foremost, I want to thank my Ph.D. advisor, Dr. Richard E. Debski. I wouldn’t be here today without your mentorship and guidance. Thank you for taking the chance with me as an undergraduate student sticking with me for graduate school. I have learned a great deal from you and I will be eternally grateful for every time you pushed me to challenge myself and asked the tough questions that always kept me thinking. I would also like to thank Dr. Debski’s wife, Mandy, and daughter, Riley, for their hospitality and support along the way.

A big thanks to the rest of my committee for their guidance and expertise as well: Dr. Volker Musahl, Dr. Kang Kim, Dr. Spandan Maiti and Dr. Steven Abramowitch. Dr. Musahl, thank you helping me understand the clinical importance of our research and for always being timely in your feedback despite your incredibly busy schedule. Dr. Kim, thank you for being there to answer all of my ultrasound related questions, and opening my eyes to the vast capabilities of ultrasound. Dr. Maiti, thank you for helping me understand the complex world of computational modeling. Dr. Abramowitch, thank you for being the jack-of-all trades, guiding me through a variety of issues from experimental design for mechanical testing to computational modeling.

To all of my friends, whom there are too many to name, thank you for all the good times. I have been lucky enough to grow up in Pittsburgh, and have many of my childhood, high school, college and graduate school friends along the way help me maintain a stable work-life balance. While I still stink at trivia, KanJam and any character not named Olimar in SSB Brawl, I am a self-proclaimed, semi-professional darts, pickleball and fantasy football player/manager.

I also want to thank my family for all their support. Mom and Dad, thank you for all your love and support by pushing me to be better in all that I do. Also, thanks for all the homecooked meals and a functional washer and dryer for me to do my laundry. To my siblings Danielle and Derek, I appreciate our subtle competitive spirit, where no one wants to be outdone by the other. Congratulations Danielle on graduating from Pitt with honors in Mechanical Engineering and best of luck with your new job with CaptiveAire. Derek, keep up the good work in high school and I'm excited to see where you decide to go to college to. Also, thanks for the constant reminders that your GPA is higher than mine, but don't forget you still can't beat me in tennis/pickleball.

To my extended family at the ORL, I appreciate all of your support both in and out of the lab. To my first mentors Matt Miller and Jonathan Gustafson. You two were great role models of how to be a successful Ph.D. student. To the current Ph.D. students in the lab, Sene Polamalu and Luke Mattar, the lab is in good hands with you two. I want to thank you guys for picking me up when the going gets tough and keeping me grounded. To all the orthopedic residents during my time (Jason, Conor, Neel, Rob and Chris), thanks for always being there to answer my clinical questions and helping me with dissections and suturing. In addition, and for the same reasons, thanks to all my international orthopaedic friends and colleagues (Masa, Jan, Elmar, Thomas, Tetsu, Tomo, Satoshi[2] and Joao), hopefully someday I get the opportunity to visit all of you in your home countries.

Finally, Dr. Erika Pliner, my wonderful girlfriend. I couldn't imagine getting through grad school without you. Thank you for your endless encouragement, support and advice throughout this journey. Most importantly, thank you for bringing me happiness and a smile to my face every day…just like I am right now as I type this.

1.0 Introduction and Background

The glenohumeral joint is considered a ball and socket joint due to the articulation between the humeral head and the glenoid cavity of the scapula. It is one of the most mobile joints in the body, but also one of the most unstable (1, 2). The rotator cuff is a group of four muscles and tendons that play a critical role in providing stability to the glenohumeral joint by compressing the humeral head into the glenoid cavity (3). Injuries to the rotator cuff such as a rotator cuff tear, can cause severe pain and a loss of shoulder function. Furthermore, rotator cuff tears are extremely prevalent in an aging population (4-6).

Ultrasound has been shown to be a capable diagnostic tool for detecting rotator cuff tears, providing clinicians a cost efficient, non-invasive way to diagnose patients. However, clinicians usually evaluate the state of the tissue in ultrasound images subjectively, and there is a clear need for the development of technology to quantitatively assess mechanical properties of the tendon to better understand their in-vivo function (7).

Treating rotator cuff tears by non-operative (eg. exercise therapy) and operative means remains difficult, with high failure rates being reported (8, 9). While the reasons for high failure rates are unclear, increased tear propagation may be a reason since larger tear sizes are associated with poor clinical outcomes (10-12). Factors such as abnormal arthrokinematics and location specific changes in mechanical properties of the tendon may result in increased tear propagation (13-15). Therefore, the focus of this dissertation is understanding these key factors that may lead to tear propagation in order to improve treatment decisions for patients with a rotator cuff tear.

1.1 Glenohumeral Joint Anatomy and Function

The glenohumeral joint (glenoid and humerus) is one of the four joints that make up the shoulder complex. The other joints forming the shoulder complex are the sternoclavicular (sternum and clavicle), acromioclavicular (acromion and clavicle) and scapulothoracic (scapula and thorax) joints. These four joints work together to allow for the motion of the shoulder through a complex relationship between bony articulations as well as constraints of static (eg. labrum and capsule), and dynamic structures (1). Of the four shoulder joints, the glenohumeral joint is at the greatest risk of instability because of the bony articulation between the large humeral head and small glenoid surface, much like a golf ball on a tee. During normal motion, less than a third of the humeral head is in contact with the glenoid cavity (16-18). Even with such little articulation between the humeral head and glenoid cavity, joint translations is constrained to less than 2 mm of motion (19-21). The precise stabilization of the joint requires a delicate balance between different static and dynamic stabilizers to maintain the compression of the humeral head and glenoid cavity.

In addition to the bony anatomy and articulation, other important static stabilizers of the glenohumeral joint include the glenoid labrum and joint capsule. The glenoid labrum is a fibrous structure that surrounds the rim of the glenoid and functions to increase congruity by deepening the glenoid and creating a suction effect as well as serve as an attachment site for the glenohumeral capsule (17, 22, 23). The glenohumeral capsule is a continuous sheet of ligamentous tissue that functions to stabilize the joint by becoming “tight” in extreme ranges of motion (24-26). The most important dynamic stabilizer of the glenohumeral joint is the rotator cuff (27).

1.1.1 Rotator Cuff Muscles and Tendons

The rotator cuff consists of a group of four muscles and tendons that surround the glenohumeral joint whose main function is to stabilize the shoulder: supraspinatus, subscapularis, infraspinatus and teres minor (Figure 1.1, Figure 1.2, and Figure 1.3) (17, 28). While each individual rotator cuff muscle and tendon have their own unique function, when working together, the rotator cuff serves as an active stabilizer of the glenohumeral joint by compressing the humeral head into the glenoid cavity. Specifically, there is a coronal and transverse force couple that stabilizes the humeral head in both the superior-inferior and anterior-posterior direction. In the coronal plane, the force couple consists of the deltoid and supraspinatus muscle elevating the humeral head, while the inferior portions of the subscapularis, infraspinatus and teres minor counteracting that force by depressing the humeral head (29). In the transverse plane, the subscapularis pulls the humeral head anteriorly, while the infraspinatus and teres minor pull the head posteriorly (30). Because the rotator cuff tendons attach much closer to the joint center of rotation, their moment arm is smaller and thus their main function is stability rather than motion. Injuries to the rotator cuff such as a rotator cuff tear can disrupt the normal force balance and contribute to long-term dysfunction (31, 32).

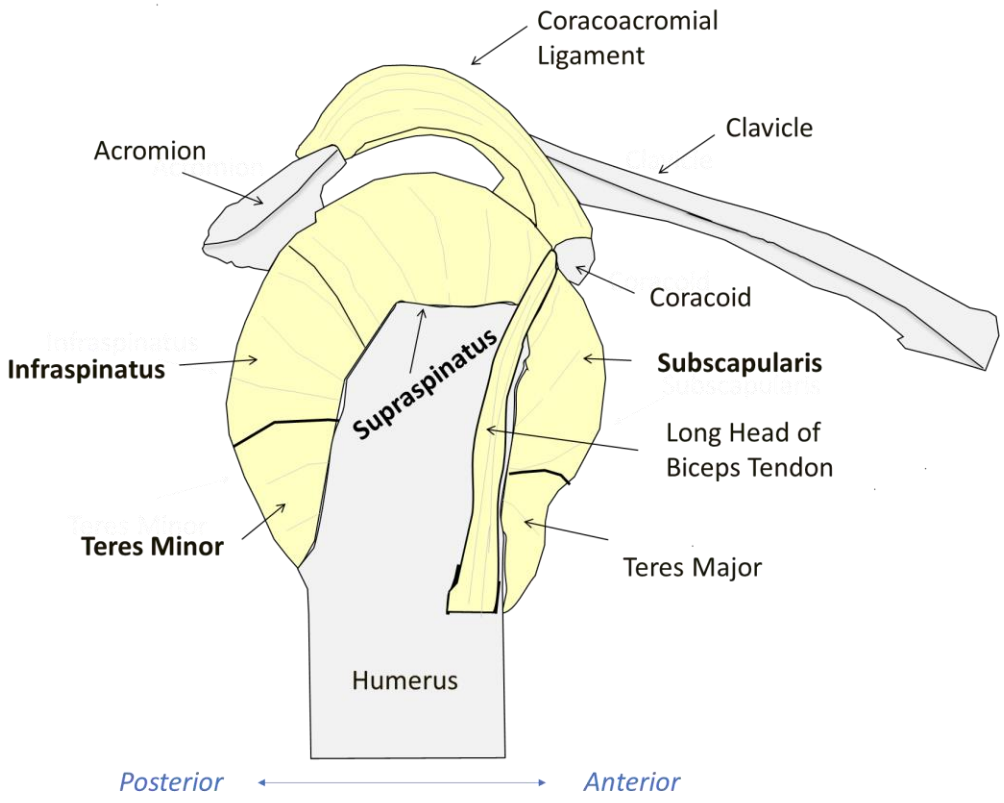

Figure 1.1: Lateral view of right shoulder.Yellow represents tendons and gray represents bone. Bold indicates rotator cuff tendons.

The supraspinatus functions to initialize abduction of the humerus. At larger angles of abduction (> 30°), the supraspinatus works with the deltoid to abduct the arm, but at this point, the deltoid is the principal muscle at work abducting the arm (33). The supraspinatus is located on the superior aspect of the shoulder, with the supraspinatus muscle originates in the supraspinatus fossa (posterior aspect of the scapula), passing under the acromion and inserting onto the superior aspect of the greater tuberosity (Figure 1.1). Because of its superior location, the supraspinatus also functions as a passive restraint to superior migration of the humeral head. Near the insertion site, the supraspinatus tendon shares fibers with the anterior aspect of the infraspinatus tendon, which often results in load sharing between these tendons (34).

The infraspinatus functions to externally rotate the humerus (35). Located in the posterior side of the shoulder, the infraspinatus originates from the lateral aspect of the scapula and inserts onto the middle facet of the greater tuberosity (Figure 1.1 and Figure 1.2). Inferior to the infraspinatus is the teres minor. The teres minor shares the same muscle origin as the infraspinatus, but inserts onto the inferior facet of the greater tuberosity (Figure 1.1 and Figure 1.2). Similar to the infraspinatus, the teres minor functions to externally rotate the humerus, though to a lesser degree (40% of the external rotation force compared to 60% from the infraspinatus) (36). The infraspinatus and teres minor also resist posterior and superior translations (37).

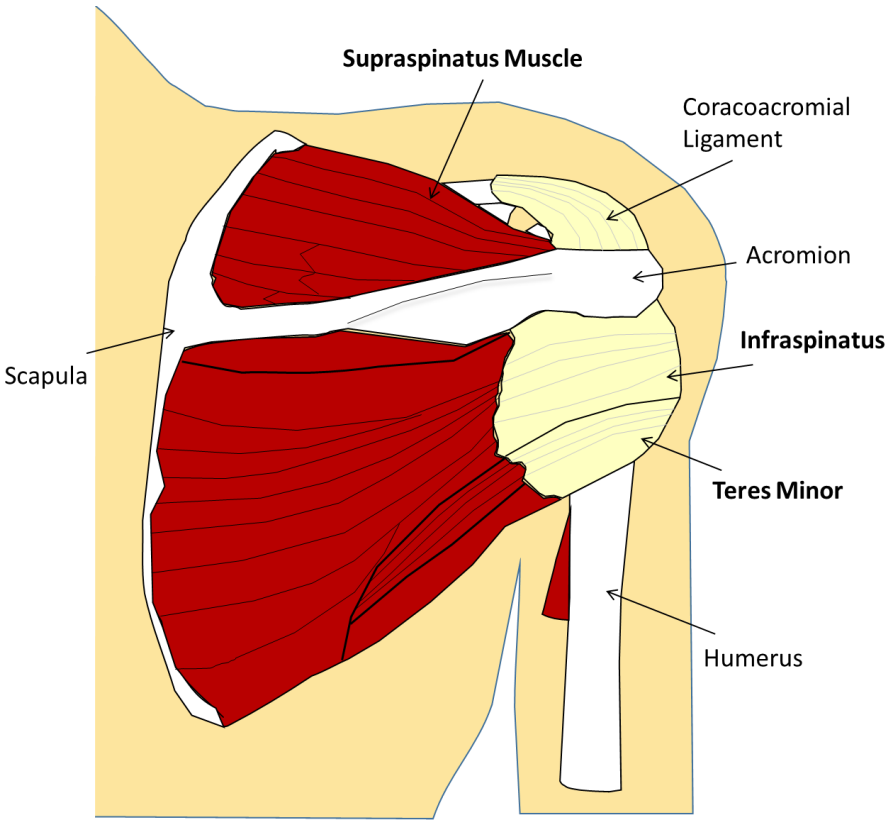

Figure 1.2: Posterior view of right shoulder. Yellow indicates tendon, red indicates muscle, and white indicates bone. Bold represents rotator cuff tendons/muscles.

On the anterior aspect of the shoulder is the subscapularis. It is the only component of the rotator cuff that is on the anterior side of the shoulder. The main function of the subscapularis is to internally rotate the humerus (27). The subscapularis muscle originates in the subscapularis fossa (anterior surface of scapula) and inserts onto the lesser tuberosity of the humeral head (Figure 1.1 and Figure 1.3). The tendinous insertion of the subscapularis does not interact with the supraspinatus tendon as it is separated by the long head of the biceps tendon. The subscapularis also resists anterior and inferior translation of the humeral head.

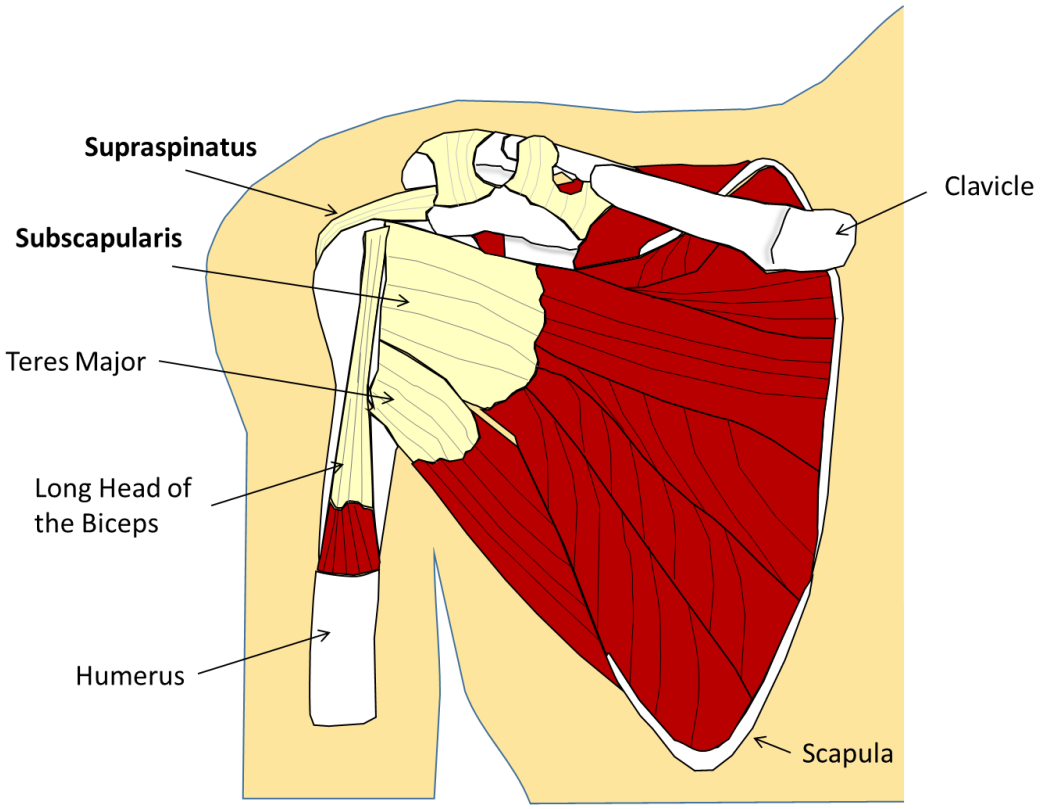

Figure 1.3: Anterior view of right shoulder. Yellow indicates tendon, red indicates muscle, and white indicates bone. Bold represents rotator cuff tendons/muscles.

1.2 Rotator Cuff Tears: Impact and Treatment

In the United States alone, roughly 4.5 million people each year visit the clinic due to shoulder pain, resulting in treatment costs of over $6 billion annually (38, 39). Injuries to the rotator cuff, specifically rotator cuff tears, are a primary cause of shoulder pain and loss of shoulder strength and motion, often preventing patients from living an active lifestyle (40). Typically, rotator cuff tears occur in the supraspinatus tendon (Figure 1.4), making motions such as raising your arm above your head difficult. The incidence rate of rotator cuff tears in the general population is about 20-30% (4, 5). In an aging population, rotator cuff tears pose a significant clinical problem. The incidence rate increases with age, with studies reporting an incidence rate as high as 50% for those over the age of 60 (6, 41, 42). The high frequency of rotator cuff tears, combined with their capacity to cause severe pain and limit normal activity, underscores the importance of timely and effective treatment.

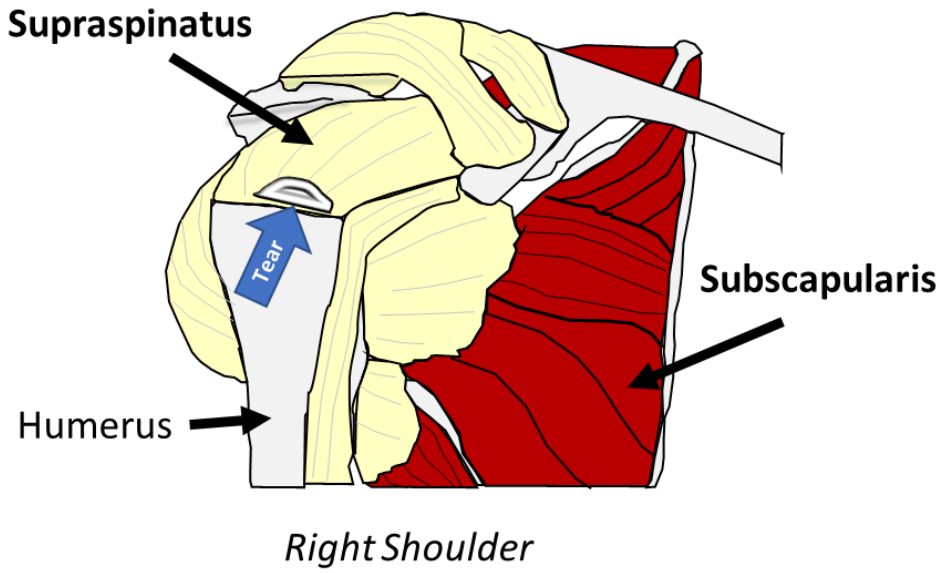

Figure 1.4: Isolated supraspinatus tendon tear

1.2.1 Treatment of Rotator Cuff Tears

Currently, rotator cuff tears are treated either non-operatively or by surgery, though there is no consensus as to the most appropriate treatment on a patient-by-patient basis (43, 44). Non-operative treatment through corticosteroid injections and exercise therapy are often the first course of action to treat rotator cuff tears (45-48). Other non-operative management techniques such as transcutaneous nerve stimulation, iontophoresis and ultrasound therapy exist, but there is a paucity of data supporting the efficacy of these treatments (49). The ultimate goal of non-operative management is to reduce/eliminate pain and restore shoulder function (49, 50). Since rotator cuff tears create an imbalance of the force couples that stabilize the glenohumeral joint, a key focus of exercise therapy is to strengthen the surrounding muscles to compensate for the loss of function. However, exercise therapy fails in 25-50% of individuals (51, 52). Individuals with larger tears have been associated with poor clinical outcomes (eg. more pain) as well as significant increases (>2mm) in rotator cuff tear size in half of the patients within two years following exercise therapy (53, 54). In the cases where non-operative treatment is ineffective, patients pursue surgical repair.

The success of surgical repair for rotator cuff tears is quite variable with failure rates being reported from 10-90% (55, 56). A lot of different factors play a role in the success or failure of surgical repair such as tissue quality, age, fatty infiltration, repair method (eg. double vs single row), and tear size. Similar to non-operative management, tear size have been associated with poor clinical outcomes, with larger tears being associated with higher re-tear rates after surgery (57-60). For a rotator cuff repair construct, the tissue-suture interface is a primary location for surgical failure. Poor tissue quality due to tendon degeneration from the presence of a tear may explain why re-tears at the tendon-suture interface of surgically repaired rotator cuff tears occur (56, 61-69).

1.3 Factors of Rotator Cuff Tear Propagation

There is a multitude of extrinsic and intrinsic factors behind the development and propagation of rotator cuff tears (41, 70). Extrinsic mechanisms originate external to the tendon and occur when compressive, shear or tensile forces are applied to the rotator cuff tendons causing them to tear. Impingement is a specific type of extrinsic mechanism where the rotator cuff tendon and surrounding bone impinge with one another is known to cause rotator cuff tears. Subacromial impingement occurs due to the narrowing subacromial space for the tendon between the acromion and humeral head, causing excessive compressive and shear forces onto the tendon (71). Internal impingement is another extrinsic mechanism where the articular side of a rotator cuff tendon is impinged between the posterior superior glenoid rim and the humeral head. Extrinsic mechanisms of rotator cuff tears are generally due to anatomic, biomechanical or a combination of both. Specifically, the anatomic and biomechanical factors that have been shown to influence the risk of developing a rotator cuff tear include acromion shape, bone spurs, muscle strength and abnormal glenohumeral kinematics. Intrinsic mechanisms originate within the tendon and are associated with degenerative changes of the tendon due to aging. Specific factors that contribute to the intrinsic mechanisms of rotator cuff tears include poor tendon vascularity, altered tendon morphology and poor mechanical properties.

1.3.1 Abnormal Glenohumeral Arthrokinematics

Pathologic changes in glenohumeral joint kinematics and arthrokinematics have been shown to occur due to rotator cuff tears in cadaveric, rat and in vivo studies (15, 72-74). Glenohumeral arthrokinematics parameters such as joint translations and contact path length (ie. translation of the humeral head on the glenoid) are important to consider when treating rotator cuff tears because it is related to joint stability. Increased joint translations and contact path length compared to healthy individuals would be indicative of joint instability that would need to be addressed. For a healthy individual or individuals with a surgically repaired rotator cuff tear doing a coronal or scapular plane abduction motion, the overall range of glenohumeral joint translation in the superior-inferior direction has been reported to be <3 mm (75-77). Similarly, the normal anterior-posterior glenohumeral joint translation range for healthy individuals performing an external rotation motion has been reported to be between 1-2 mm (75, 78).

The force couples in the shoulder, composed of the deltoid, supraspinatus, infraspinatus and subscapularis (79), work together to stabilize the glenohumeral joint. As a result of a rotator cuff tear involving the supraspinatus, joint instability may occur because not all muscles used to stabilize the glenohumeral joint would be functioning normally and the force couples may be unbalanced. As a result of the unbalanced force couples, the torn supraspinatus tendon may experience loads that lead to tendon remodeling scenarios that may predispose the tendon to an increased likelihood of tear propagation. Furthermore, persistent abnormal arthrokinematics may injure the structures within the glenohumeral joint and ultimately result in a larger tear over time.

Most in vivo studies that address non-operative management such as exercise therapy have focused on investigating changes in glenohumeral kinematics and arthrokinematics for scapular-plane and coronal-plane abduction (74, 80-87). However, changes in glenohumeral

arthrokinematics for other motions such as internal and external rotation with the arm at the side following a rotator cuff tear is not well understood. Other motions such as internal/external rotation with the arm at the side are important to consider as it is commonly used during activities of daily living.

1.3.2 Changes in Location Specific Mechanical Properties

Mechanical properties are important to understand because they are directly related to function. The tensile modulus of supraspinatus tendons are >100 MPa and ultimate stress is >10 MPa (88, 89). It is known that the mechanical properties differ within the supraspinatus tendon. For an intact supraspinatus tendon, the anterior third is the strongest and stiffest followed by the middle then posterior third (88). Since torn tendons cannot bear any loads, the remaining intact fibers have to compensate and bear extra load. Thus, tear propagation may occur more easily especially if the remaining tendon has poor tissue quality and inferior mechanical properties (58). For example, anteriorly located tears propagate more easily than middle or posteriorly located tears because the strongest part of the supraspinatus tendon was compromised (90-92).

Mechanical properties of tendon are directly related to the composition and microstructure of the tendon (93). Water is the main constituent of tendons, accounting for 70% of the total weight. The remaining 30% is primarily composed of collagen proteins which are highly aligned with the long axis of the tendon, providing high tensile strength and stiffness. The remaining part of the tendon is the extracellular matrix, primarily composed of elastin fibers and proteoglycans (94). Elastin is highly elastic and is the main constituent bearing load during low levels of loading before the collagen fibers are recruited (ie. toe region of stress-strain curve). Proteoglycans are important in regulating collagen fibrillogenesis (ie. assembly of collagen) (95, 96). Furthermore proteoglycan composition can changed locally throughout the tendon based on mechanical stimuli, resulting in changes in the assembly of collagen (94, 97, 98). Therefore, the presence of a tear may alter the tendon composition and microstructure, thus altering the mechanical properties throughout the tendon. Previous studies that investigated healing of degenerative ligaments, which have similar properties as tendons, showed moduli less than half of the intact ligament (99, 100).

For a supraspinatus tendon tear, regional differences in tendon degeneration as well as inhomogeneous stress and strain patterns throughout the tendon have been observed (91, 92, 101-106). These changes in overall tendon degeneration and increased strain have been shown to be a significant factor that contributes to rotator cuff tear propagation (91, 92, 102-104, 107-109). However, the effect of localized changes in mechanical properties due to tendon remodeling on tear propagation is not well understood.

1.4 Evaluation of Tissue Quality

While the current gold standard for detecting rotator cuff tears is through arthroscopy, this is an invasive procedure for the patient. Non-invasive diagnostic modalities such as ultrasonography and magnetic resonance imaging (MRI) are becoming more widely used by clinicians to diagnose whether a patient has a rotator cuff tear (110-114). In the hands of an expert, ultrasound has been shown to have similar efficacy in detecting the presence and size of a rotator cuff tear as MRI in terms of both specificity and sensitivity when compared to the gold standard of arthroscopy (112, 114, 115). Evaluation of tissue quality based on ultrasound images is mostly qualitative and depends on the user. Quantifying mechanical properties of tendons with ultrasound remains difficult (116). Recently, ultrasound images have been analyzed quantitatively using different ultrasound techniques such as quantitative ultrasound (QUS) measures (117-119), acoustic radiation force impulse (ARFI) imaging (120-125), and shear wave elastography (116, 126-128).

1.4.1 Quantitative Ultrasound Measures

When traditional B-mode ultrasound images are obtained, clinicians will qualitatively evaluate the quality of the tissue based on their observations. For example, injured tendons would be expected to have disorganized fibers and a hypoechoic appearance. Essentially, tendon health is being evaluated by examining the grayscale image echotexture. Quantitative ultrasound (QUS) measures quantitatively analyzes the grayscale image echotexture by performing first-order statistical analyses (skewness, variance, mean echogenicity, and kurtosis) on the grayscale distribution (Figure 1.5) (117-119, 129). Interpretation of the statistical features that describe the ultrasound image echotexture have been associated with overall tendon quality. Increased tendinopathy was associated with increased measures of skewness and kurtosis as well as decreased measures of variance and echogenicity, with a healthy tendon expected to exhibit highly aligned collagen fibers creating a striped pattern of alternating dark and light bands (117, 118). However, it is still unknown what specific factors of degeneration affect these measures and if QUS measures can be used to measure location specific mechanical properties of tendons.

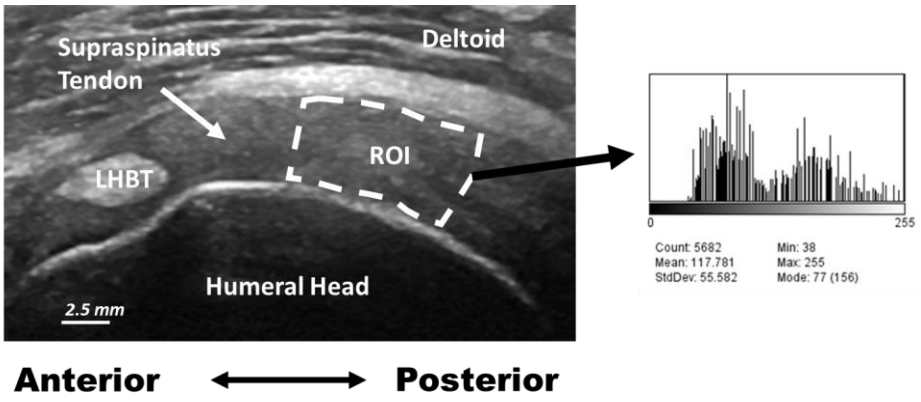

Figure 1.5: Quantitative Ultrasound Measures: Each pixel within a region of interest (ROI) is assigned a value between 0 (black) and 255 (white), and then the grayscale distribution is analyzed.

1.4.2 Acoustic Radiation Force Impulse (ARFI) Imaging

Acoustic Radiation Force Impulse (ARFI) imaging is an ultrasound technique that generates a localized force onto the tissue of interest at a precise location and the resulting tissue displacement is measured (Figure 1.6) (130). Information about the resulting tissue displacement could lead to insights about tissue quality as the amount of displacement may correspond with the mechanical properties of the tissue (eg. modulus). Currently, ARFI imaging is primarily utilized for compliant, isotropic biological tissues such as breast, liver, and arteries where tissue displacements are less than 10µm (120-125, 130). Clinically, ARFI imaging has been used to detect the presence of tumors based on the stiffness of the tissue. However, the utility of ARFI imaging is not fully understood for stiff, anisotropic biological tissues such as tendons. Tendons are transversely isotropic with moduli on the order of hundreds of megapascals, while the commonly investigated breast tissue is isotropic with moduli on the order of kilopascals.

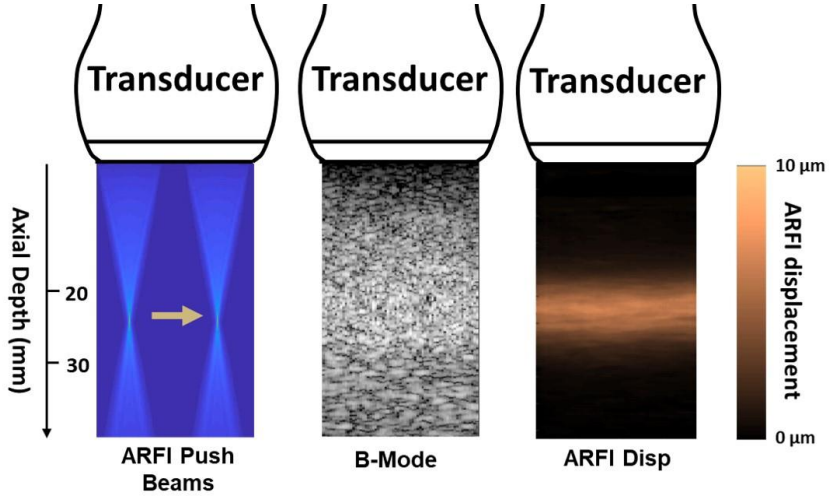

Figure 1.6: ARFI imaging: An ARFI pushing beam focused to a particular depth (25mm) is fired across the transducer aperture width. The B-mode image depicts a homogenous gelatin phantom, and the ARFI displacement image illustrates the resulting displacement from the focused ARFI push.

1.4.3 Shear Wave Elastography

Shear wave elastography is another ultrasound technique used to characterize tendon quality in research settings. Shear wave elastography and ARFI imaging are often used interchangeably in literature despite key differences of the acquired data (131, 132). Similar to ARFI imaging, shear wave elastography utilizes a focused acoustic radiation force to provide a local stress in the tissue which result in shear waves propagating perpendicular to the direction of the acoustic radiation force (128, 133, 134). Unlike ARFI imaging, shear wave elastography measures the speed of the propagating shear waves rather than the tissue displacement at the site of the acoustic radiation force. Shear wave velocity is calculated from the tissue displacement maps in the surrounding tissues which can be used to calculate Young's modulus for isotropic, homogeneous, elastic tissues that undergo small deformations (G = shear modulus, ρ = density, c_s = shear wave velocity, E = Young's modulus, v = Poisson's ratio):

$$\boldsymbol{G = \rho c_s} \qquad \textbf{(1-1)}$$

$$\boldsymbol{E = 2G(1 + v)} \qquad \textbf{(1-2)}$$

However, the estimation of the modulus using the above equations does not hold well for anisotropic and stiff musculoskeletal tissues such as tendons. For commercial ultrasound machines, the stiffness of musculoskeletal tissues often exceeds its measurable range (135, 136). Thus, for musculoskeletal applications, shear wave elastography is good at estimating the relative stiffness based on the magnitude of the shear wave velocities (ie. stiffer tissue = faster shear wave velocity) (116, 135-140). Furthermore, shear wave elastography is useful for understanding the overall stiffness of the entire tissue, but cannot quantify location specific mechanical properties (eg. modulus) within the tissue.

1.5 Finite Element Modeling

Finite element modeling is a useful tool to solve complex engineering and mathematical problems (eg. structural mechanics, heat transfer, electromagnetics, fluid mechanics etc.). The solutions to these complex problems are achieved by breaking down the problem into simpler components (ie. finite elements). While experimental tests can be performed to obtain mechanical properties and understand the behavior of biological tissues, researchers are often limited by the number of specimens and testing conditions that can be performed. Finite element models can be used to address this limitation by re-creating experimental boundary and loading conditions to simulate more testing conditions that could be performed experimentally. Furthermore, material coefficients which describe the mechanical properties of biological tissues can be determined using the inverse finite element method (141, 142). The inverse finite element method optimizes material coefficients by iteratively changing the material coefficients until the finite element analysis result matches the experimental results (Figure 1.7).

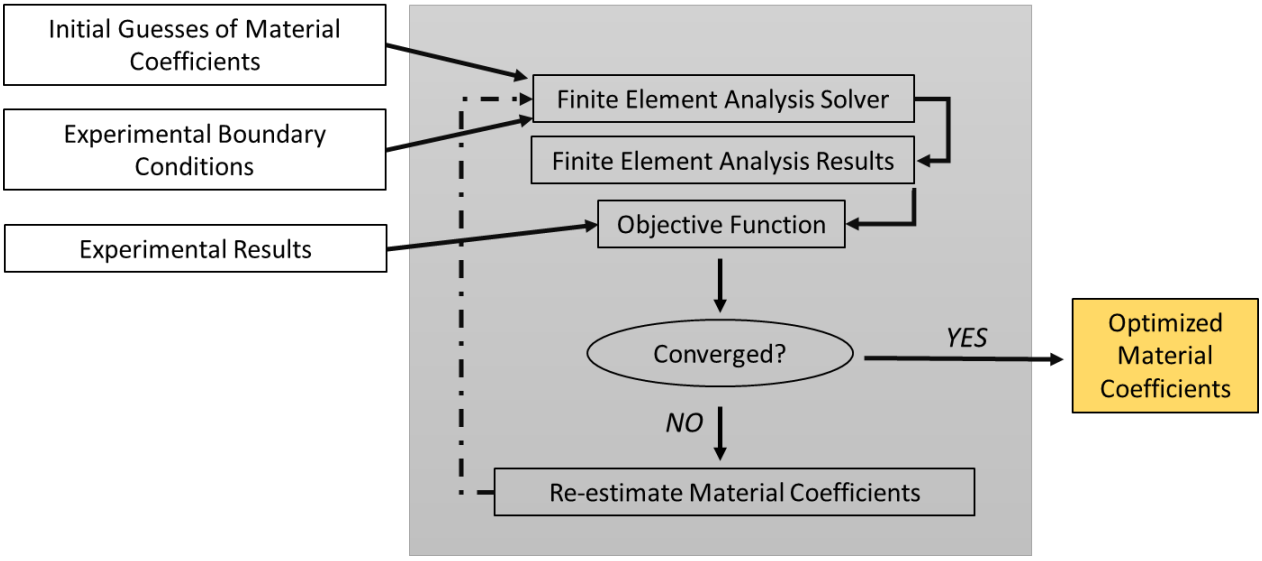

Figure 1.7: Inverse finite element method optimization flowchart

Finite element modeling of rotator cuff tears has primarily been used to investigate the effect of initial tear characteristics (eg. size, location, shape and chronicity) on the likelihood of tear propagation (92, 101, 104, 143-150). Several research groups have shown that as tears get larger, the strength of the tendon decreases, resulting in a partial-thickness tear progressing into a full-thickness tear, or a full-thickness tear propagating into a larger tear (143, 149, 150). In addition, anteriorly located tears were shown to be at a greater risk for tear propagation compared to centrally and posteriorly located tears (145). The stress and strain distribution of the supraspinatus tendon due to factors such as arm position and tear shape have also been investigated, with higher stresses being observed on the articular surface of the tendon and along the edges of a tear (101, 144, 146, 147, 151). However, a drawback of some of the models include simplified geometry, homogeneous isotropic material properties are assumed for the tendon, and the models do not actually simulate tear propagation occurring. As can be seen in all finite element models of a rotator cuff tear, inhomogeneous stresses and strains experienced throughout the

tendon (eg. high stress at tear tips and stress-shielded region along medial edge of tear). As a result, different tendon remodeling scenarios could occur, altering the localized mechanical properties within the tendon. However, the effect of localized tendon remodeling on tear propagation is not well understood.

Finite element models have also been developed for ultrasound techniques such as ARFI imaging (152-156). However, these models focus on compliant tissues (ie. modulus <1 MPa), not stiff anisotropic tissues such as tendons (ie. modulus >100 MPa). Development of finite element models that accurately simulate ARFI imaging could be used to quantify location specific mechanical properties of tendons by using the inverse finite element method.

2.0 Motivation

Rotator cuff tears are a significant clinical problem not only for the patients but the healthcare system as well (38, 39). Rotator cuff tears are extremely prevalent, negatively impact quality of life, with billions of dollars being spent annually in the United States alone to treat this injury. The desire to improve the quality of life and productivity for those with rotator cuff tears in an aging population highlights the importance of being judicious in choosing the most effective treatment.

Both non-operative and surgical treatment of rotator cuff tears have fairly high failure rates (51, 52, 55, 56). Due to the high failure rates of treatment, individuals with this injury do not improve their quality of life, as well as valuable time and money of both the patient and healthcare system are wasted. Thus, there is a clear need to better understand the factors behind high failure rates of treatment. Tear propagation is a key factor that may explain high failure rates of treatment as larger tears are more difficult to treat and have been associated with worse clinical outcomes (53). However, it is not well understood why some tears propagate more easily than others. Therefore, there is a need to identify the important factors that increase the likelihood of tears propagating over time.

Abnormal glenohumeral arthrokinematics indicate joint instability. Joint instability may be as a result of unbalanced force couples, which may expose the torn supraspinatus tendon to loads that increase the likelihood of tear propagation. Furthermore, persistent abnormal arthrokinematics may injure the structures within the glenohumeral joint resulting in a larger tear and therefore increased pain and loss of shoulder function (13, 79). Increased tear propagation may also be due

to changes in mechanical properties of the torn supraspinatus tendon (14). The mechanical properties of the supraspinatus tendon may be location dependent since the tendon may remodel based on regional differences in degeneration and stresses being experienced during repeated loading for a tendon with a tear (107).

Although changes in location specific mechanical properties may influence tear propagation, clinicians need a method or tool to quantitatively evaluate the mechanical properties of the tendon. Ultrasound is a non-invasive, reliable, and cost-effective tool used by clinicians to detect the presence and size of rotator cuff tears (110-113). Currently, the evaluation of tissue quality from ultrasound images is subjective, but recent advancements in ultrasound techniques (eg. quantitative ultrasound measures and ARFI imaging) offer the potential for quantification of location specific tendon mechanical properties. Expanding the utility of current ultrasound techniques to quantify the mechanical properties of the tendon from conventional B-mode ultrasound images will help clinicians improve their surgical technique and monitor the healing of the tissue during and after treatment.

By better understanding tear propagation, appropriate treatment decisions can be made to minimize the likelihood of failed treatment. It is expected that both abnormal glenohumeral arthrokinematics and location specific mechanical properties will significantly influence tear propagation. Clinicians can use the results of this dissertation to better assess and understand why rotator cuff tears develop into larger tears, which are more difficult to treat. Ultimately, delineating the effect of these factors influencing tear propagation will enable clinicians to better determine which patients should be treated non-operatively or be referred for immediate surgical repair.

2.1 Specific Aims

The specific objective of this dissertation is to better understand the utility of ultrasound techniques as well as the role of glenohumeral arthrokinematics and location specific mechanical properties on tear propagation through in-vivo, cadaveric, and computational models. Three specific aims were accomplished to meet the specific objective of this dissertation:

2.1.1 Specific Aim 1

Determine changes in glenohumeral arthrokinematics for internal/external rotation with the arm at the side following exercise therapy.

Hypothesis 1: Exercise therapy will result in improved glenohumeral arthrokinematics in terms of decreased translations and contact path length during internal/external rotation with the arm at the side.

2.1.2 Specific Aim 2

Determine the effect of location specific tendon remodeling on tear propagation and stress distribution using a validated subject-specific finite element model of a supraspinatus tendon.

Hypothesis 3: Positive tendon remodeling (ie. increased stiffness) at the tear tips will result in increased tear propagation due to higher stress concentrations.

2.1.3 Specific Aim 3

Evaluate the utility of different ultrasound techniques (QUS measures and ARFI imaging) to assess location specific changes in tendon quality (from histology) and predict location specific mechanical properties (from materials testing) of different musculoskeletal tissues.

Hypothesis 2A: Increased fatty infiltration, collagen disorganization and cellularity will correlate to increased kurtosis and decreased echogenicity from QUS measures.

Hypothesis 2B: Using the inverse finite element method, mechanical properties of tissues can be accurately predicted based on tissue displacement values from ARFI imaging.

3.0 Aim 1: Changes in Glenohumeral Arthrokinematics Following Exercise Therapy

Non-operative treatment such as exercise therapy is often the first course of action to treat rotator cuff tears (45-48). However, exercise therapy fails in 25-50% of individuals (51, 52). Tear propagation is a key factor that may explain high failure rates of treatment as larger tears are more difficult to treat, have been associated with worse clinical outcomes and studies have shown significant increases (>2mm) in rotator cuff tear size in half of the patients within two years following exercise therapy (53, 54). A key focus of exercise therapy is to strengthen the surrounding muscles to compensate for the loss of function from the tear. However, simply improving the strength of surrounding muscles may not suffice if the joint is unstable because the rotator cuff force couples remain unbalanced. Joint instability, as measured by glenohumeral arthokinematic parameters, may be a result of the unbalanced force couples that exposes the torn supraspinatus tendon to loads that increase the likelihood of tear propagation. While glenohumeral arthrokinematics have been measured for scapular-plane and coronal-plane abduction tasks (74, 80-87), glenohumeral arthrokinematics for other motions common to daily living such as internal and external rotation with the arm at the side following a rotator cuff tear is not well understood. Therefore, the first aim was to determine changes in glenohumeral arthrokinematics for internal/external rotation with the arm at the side following exercise therapy.

3.1 Exercise Therapy for Treatment of Supraspinatus Tears Does Not Alter Glenohumeral Arthrokinematics during Internal/External Rotation with the Arm at the Side

3.1.1 Introduction

Rotator cuff disease is a prevalent and serious clinical issue. Studies have shown the incidence rate of rotator cuff tears to be about 20-30% of the general population (4, 157), increasing with age (6). With an aging population, there is a need to improve the treatment modalities for rotator cuff tears. Non-operative management is a more cost-effective alternative for treating a rotator cuff tear, and is often the initial recommendation for most patients with a rotator cuff tear (158-161). However, non-operative management of rotator cuff tears is successful only 50-75% of the time (158, 159, 162). When non-operative management fails, surgery might eventually be needed, incurring more cost while delaying patient return to function.

To maximize the success rate of treating rotator cuff tears, a better understanding of the reasons for failure is needed. Pathologic changes in glenohumeral joint kinematics and arthrokinematics have been shown to occur due to rotator cuff tears in cadaveric, rat and in vivo studies (15, 72-74). These changes are an important factor to consider when treating rotator cuff tears, since they are likely related to the loss of joint stability. Non-operative management such as exercise therapy is focused on strengthening the rotator cuff and scapular muscles that provide stability to the glenohumeral joint.

Most in vivo studies that address non-operative management such as exercise therapy have focused on investigating changes in glenohumeral kinematics and arthrokinematics for scapular-plane and coronal-plane abduction (74, 80-87). However, changes in glenohumeral kinematics and arthrokinematics for internal/external rotation following a rotator cuff tear are not well understood.

Internal/external rotation in full adduction (arm at the side) is commonly used in exercise therapy to strengthen the infraspinatus and subscapularis, so a patient can compensate for the loss of function due to a tear in the supraspinatus in order to improve joint stability (48). The force couples in the shoulder, composed of the deltoid, supraspinatus, infraspinatus and subscapularis (79), work together to stabilize the glenohumeral joint. As a result of a rotator cuff tear involving the supraspinatus, joint instability may occur for internal/external rotation because not all muscles used to stabilize the glenohumeral joint would be functioning normally. Increased joint translations compared to healthy individuals would be indicative of joint instability that would need to be addressed. Furthermore, the effect of exercise therapy to restore glenohumeral kinematics during internal/external rotation with the arm at the side is unknown and is an important motion to consider as it commonly used for activities of daily living.

Therefore, the objective of was to assess changes of in vivo glenohumeral joint kinematics and arthrokinematics for internal/external rotation motions with the arm at the side of subjects with a symptomatic full-thickness supraspinatus tear before and after a 12-week exercise therapy program. It was hypothesized that improvements in shoulder strength and patient reported outcomes after exercise therapy would improve glenohumeral arthrokinematics in terms of decreased joint translations during internal/external rotation motions with the arm at the side.

3.1.2 Materials and Methods

Five subjects (3 women and 2 men, mean age 60.2 ± 7.6 years, mean BMI 32.0 ± 7.8) were recruited for the study and approved by the University of Pittsburgh Institutional Review Board (PRO11050310). Subjects were eligible to enter the study if they were between 45 and 70 years old with a symptomatic small (< 1cm), chronic full-thickness rotator cuff tear isolated to the supraspinatus tendon. Additionally, the supraspinatus muscle had to show predominantly muscle compared to fat on MRI (Goutallier Grade 2 or less). Subjects were excluded if they were smokers, had any previous shoulder surgeries, injections within 3 months of study participation, exercise therapy within 2 years prior to the study, work-related or traumatic injury, diabetes mellitus, or severe capsular tightness (internal/external rotation less than 30°). Each subject underwent 12 weeks of exercise therapy, where before and after exercise therapy, glenohumeral arthokinematic measurements were made (Figure 3.1).

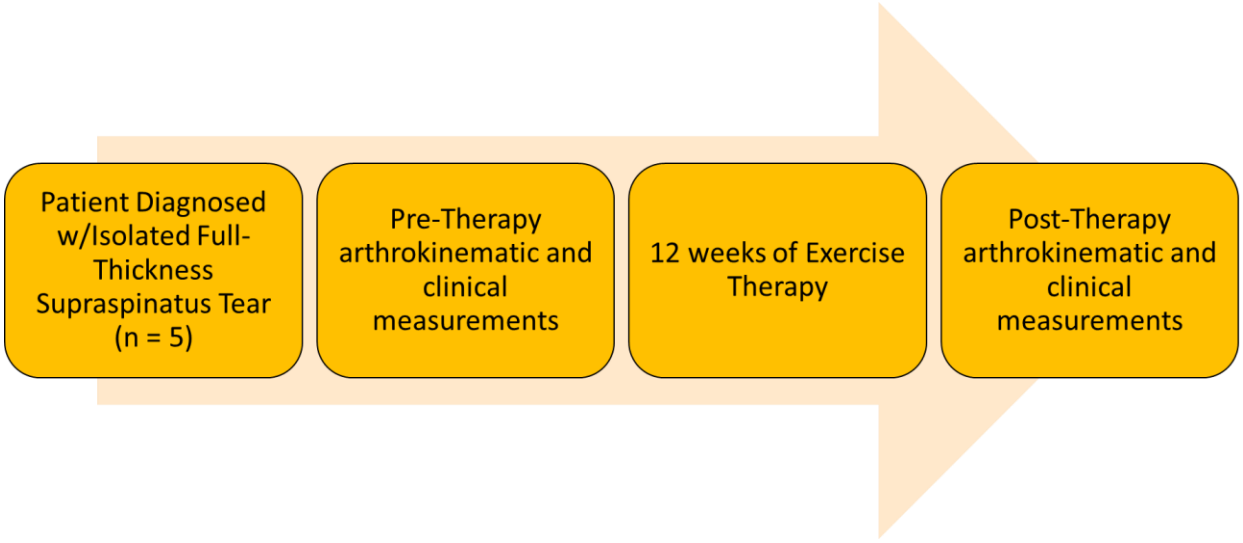

Figure 3.1: Flowchart of testing subjects with supraspinatus tears

3.1.2.1 Exercise Therapy Protocol and Assessments

All five subjects participated in a standard 12-week exercise therapy program for non-operative management of rotator cuff tears, with a focus on strengthening the rotator cuff and scapular muscles, and restoring range of motion (ROM). Subjects were treated with oral nonsteroidal anti-inflammatories as needed. Subjects were not treated with corticosteroid injections to the subacromial space. The first 6 weeks of the program was supervised exercise with a single physical therapist for two 45-60 minute sessions a week. The final 6 weeks consisted of a home exercise program while completing a daily home exercise log to ensure subject compliance. For data collection purposes, an exam at the 12-week time point was included to assess subject status after the completion of the home exercise sessions.

Isometric and active ROM exercises were used to strengthen the rotator cuff and scapular muscles, until the subject could actively move the shoulder through a full ROM continuously and painlessly. Progressive resistance exercises (PREs) were then introduced. Amount of exercise resistance and number of repetitions for each subject was established through the daily adjustable progressive resistance exercise (DAPRE) program (163) (Table 3.1). The specific exercises which focused on each of the rotator cuff muscles (supraspinatus, subscapularis, infraspinatus and teres minor), as well as the serratus anterior and middle and lower trapezius, were selected based upon electromyographic (EMG) evidence of maximal activity for each muscle (164-166). Cold therapy was applied to minimize shoulder pain as needed based on response to exercise, pain level, and subject preference following each exercise session. Subject pain during each session was measured on a scale from 0 to 10, which was used by the physical therapist to adjust the exercise program on an individual basis.

During the exercise therapy sessions at 0 and 12 weeks, isometric shoulder strength and patient-reported symptoms, activity and participation were assessed for each subject. Isometric

strength measurements were taken using a handheld dynamometer (Lafayette Manual Muscle Testing System, Lafayette Instrument Company, Lafayette, IN) for four shoulder positions. The dynamometer was placed distally on the forearm, just proximal to the wrist joint, along the dorsal radius and ulna when taking the measurement. Maximal isometric strength was assessed for external rotation at 0° of coronal plane abduction (infraspinatus bias), external rotation at 90° of abduction (teres minor bias), scapular plane abduction (supraspinatus bias), and internal rotation at 90° of abduction (subscapularis and pectoralis muscles). Subjects performed three trials of each task, and the average value was taken as a measure of isometric strength. At the same time points, subjects filled out three patient-reported outcome measures including the American Shoulder and Elbow Surgeons (ASES) Shoulder Rating Scale (167), Western Ontario Rotator Cuff (WORC) Index (168), and Disabilities of the Arm, Shoulder and Hand (DASH) Outcome Measure (169). The ASES, WORC, and DASH are commonly used to assess patient-reported outcomes for a variety of shoulder conditions including rotator cuff tears. Reliability and validity of ASES (170), WORC (171), and DASH (172) scores for rotator cuff disease have been previously demonstrated. Changes in the ASES, WORC, and DASH scores were compared to minimal clinically important differences (MCID) (173) for each outcome measure to determine if improvements were clinically relevant (174, 175).

Table 3.1: Exercise Therapy Program

Week #1. **Acute Phase**	**Weeks # 2, 3.** **Transitional Phase**	**Weeks # 4, 5, 6.** **Advanced Phase**
PROM cane external rotation	Horizontal adduction stretch	Continued progression of flexibility and strengthening from transitional phase
PROM cane internal rotation	Internal Rotation towel stretch	Proprioceptive neuromuscular facilitation patterns
PROM supine flexion	Sleeper Stretch	Lat pull down
	ER at 0° with elastic resistance	Rhomboids (retractions)
PROM standing extension	IR at 0° with elastic resistance	Pecs (press, flies)
AAROM supine cane external rotation	ER at 90° with elastic resistance	Deltoids (raises)
AAROM standing cane flexion	Subscapularis hug with elastic resistance	Closed kinetic chain protraction with rhythmic stabilization
AAROM standing cane abduction	Scapular Plane Abduction	ADL or sport specific activities
AAROM wall climb / wall walk	Prone Row into external rotation	
AAROM standing cane extension	Prone T's (horizontal abduction at 90°)	
Isometric ER at 0 degrees	Prone Y's (horizontal abduction at 120°)	
Isometric IR at 0 degrees	Serratus protraction with forward flexion	
Side-lying ER in pain-free ROM	Wall push up with plus	
Prone GH extension with ER	Lat pull down	
Scapular Plane Abduction	Rhythmic stabilization with manual resistance	
Scapular Retraction	Biceps curl	
Manually resisted scapular movements	Triceps push down	

PROM: Passive Range of Motion; AAROM: Active Assistive Range of Motion; ADL: Activities of Daily Living; IR: Internal Rotation; ER: External Rotation

3.1.2.2 Glenohumeral Arthrokinematics Protocol and Assessments

A previously established model-based tracking technique using dynamic stereoradiography (DSX) (176) was used to measure glenohumeral arthrokinematics during internal/external rotation with the arm at the side before and after the exercise therapy program. Prior to beginning the exercise therapy protocol, subjects underwent computed tomography (0.625 × 0.625 × 1.25 mm voxels) of the affected shoulder. The DSX system was used to collect x-ray images with the subjects were seated with their affected glenohumeral joint positioned at the center of the system (Figure 3.2). Subjects performed an internal-external rotation trial from a maximum internal rotation position to a maximum external rotation position in the transverse plane over 2 seconds with their arm at the subject's side. A metronome was used to assist in timing of the motion, and subjects were allowed a maximum of two practice trials before collecting data. For each trial, subjects performed 3 internal/external rotation cycles, with data collected on the second cycle.

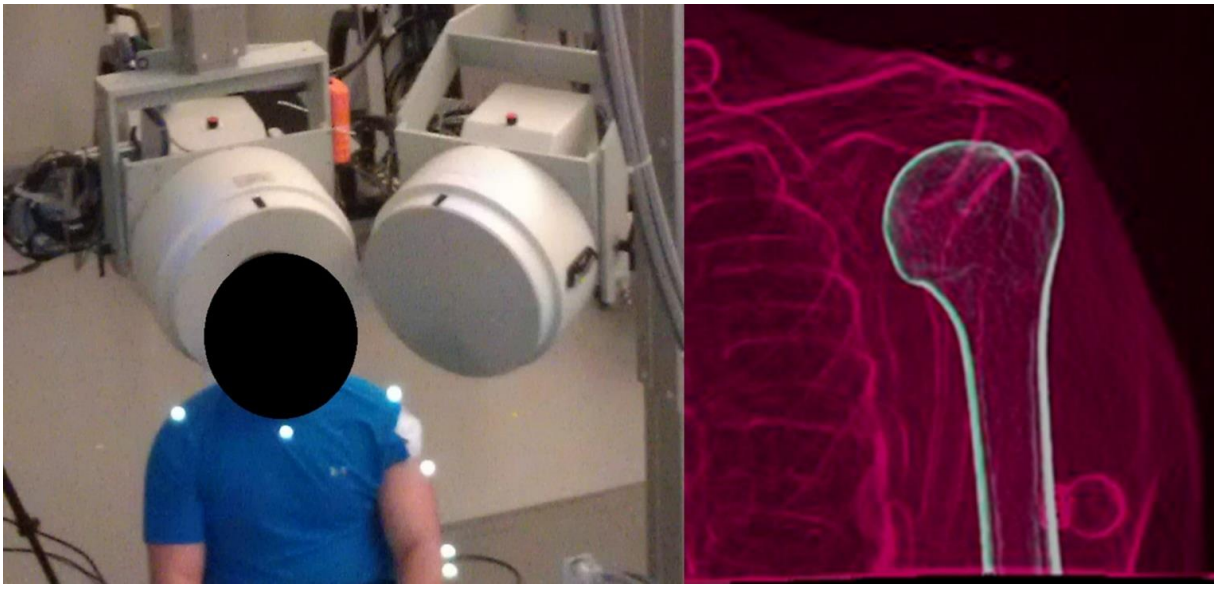

Figure 3.2: Dynamic stereoradiography (DSX) system setup with the subject sitting with the glenohumeral joint centered in the focal point of the two x-ray sources (left) and an example radiographic image used for model based tracking (right).

Details regarding how 3D glenohumeral kinematics and arthrokinematics were calculated using DSX images has been previously described (87, 176). To summarize, first the computed tomography images were segmented using MIMICS 14 software package (Materialise, Leuven, Belgium) to generate subject-specific, three-dimensional (3D) bone models of the humerus and scapula. Digitally reconstructed radiographs (DRR) of the 3D bone models were created using the projected geometry from the biplane imaging system. Then, the DRRs were oriented to match the position of the DSX images for each frame of the dynamic motion. Finally, 3D positions of each bone were determined by calculating local coordinate systems for the humerus and scapula based off International Society of Biomechanics standards to generate glenohumeral kinematics (177). An Euler angle rotation sequence (YXY) was used to determine the translations and rotations of the humerus with respect to the scapula. The accuracy of measuring in vivo shoulder motion for dynamic activities such as internal/external rotation with the arm at the side is ±0.4 mm and ±0.5°, while the dynamic measurement precision was better than ±0.2 mm (87, 176).

Average contact center of the humeral head on the glenoid surface was the main arthrokinematic variable of interest. Contact center location was determined by calculating the centroid of the region of closest contact (200 mm^2) between the glenoid and humeral head (178). From the glenohumeral contact center data, the contact path length (i.e. translation of the humerus on the glenoid through the range of internal/external rotation) was calculated as the change in frame-by-frame position of the joint contact center and was normalized to glenoid height (179). Normalized ranges of anterior-posterior (AP) and superior-inferior (SI) translation of the joint were calculated as the largest difference in anterior-posterior and superior-inferior position of the joint contact center over the entire contact path length. For each subject, contact path length, AP and SI range of translation was used for subsequent statistical analysis.

3.1.2.3 Statistical Analysis

Due to the large variation in ROM between subjects, comparisons between pre- and post-therapy were made on an individual basis using the largest shared ROM between data collection sessions. For example, for a subject with a pre-therapy ROM of 20° of IR and 50° of ER and a post-therapy ROM of 25° of internal rotation and 45° of external rotation, the shared ROM over which kinematic variables were calculated was 20° of internal rotation to 45° of external rotation. Paired t-tests or Wilcoxon Signed Rank tests were performed to compare the contact center path length and AP/SI translation range before and after completion of exercise therapy (0 and 12 week time points). Paired t-tests or Wilcoxon Signed Rank tests were also used to compare the four strength measurements and shoulder questionnaire scores. Pearson's correlation or Spearman's rho correlation coefficients were calculated to determine relationships between changes in the patient-reported outcome scores, shoulder strength, and glenohumeral arthrokinematics from pre- to post-therapy. Significance was set at $p < 0.05$ for all tests.

3.1.3 Results

All five subjects successfully completed the 12 weeks of therapy and none had sought surgical treatment at 24 months follow up. One subject showed poor compliance with the home exercise protocol and did not give maximal effort during supervised exercise therapy sessions as determined by the supervising physical therapist (i.e. did not complete all exercises during scheduled sessions and did not follow the DAPRE program as the other four subjects did). However, this subject was satisfied with their clinical outcome and did not elect to undergo surgical repair after completing the study. The maximum amount of IR/ER achieved during testing varied substantially between subjects, resulting in different ranges of IR/ER for comparison between subjects (Table 3.2). No subject reported any difficulty or pain when performing the IR/ER motion.

Table 3.2: Glenohumeral kinematics/arthrokinematics for each subject pre- and post- exercise therapy

	Subject 1		Subject 2		Subject 3		Subject 4		Subject 5	
	Pre	Post	Pre	Post	Pre	Post	Pre	Post	Pre	Post
IR/ER Range Shared Between Pre- and Post-	26° IR - 25° ER		75° IR - 87° ER		30° IR - 88° ER		59° IR - 1° ER		69° IR - 50° ER	
SI contact center range (% glenoid SI height)	10.4	15.7	32.7	27.6	7.9	8.9	30.9	28.4	15.6	17.1
AP contact center range (% glenoid AP width)	11.9	42.8	34.8	28.5	10.8	12.1	12.8	24.0	15.5	23.8
Contact Path Length (% glenoid height)	28.0	83.9	275.9	155.1	40.2	65.8	106.3	69.4	72.9	88.6

All five subjects showed improvements in isometric shoulder strength and patient-reported outcomes after 12 weeks of exercise therapy (Table 3.3). Strength measures showed significant increases of 54%, 31%, 74%, and 54% for external rotation at 0° abduction ($p < 0.05$), internal rotation at 0° abduction ($p < 0.05$), external rotation at 90° abduction ($p < 0.05$), and scaption at 90° abduction ($p < 0.05$), respectively. Average improvements in the ASES ($p < 0.05$), DASH ($p < 0.05$), and WORC ($p < 0.05$) scores were all greater than the MCID (174, 175).

Table 3.3: Shoulder strength and clinical outcomes before and after exercise therapy

(Average ± Standard Deviation for all 5 subjects)

Clinical Measure	**Pre**	**Post**
Infraspinatus Strength: ER @ 0° abduction (N)	54.2 ± 31.3	83.9 ± 22.3
Subscapularis Strength: IR @ 0° abduction (N)	93 ± 45.2	121.8 ± 36.9
Teres Minor Strength: ER @ 90° abduction (N)	46.7 ± 34.1	81.2 ± 20.3
Supraspinatus Strength: Scaption @ 90° abduction (N)	40.1 ± 27.4	61.9 ± 20.2
ASES Score (MCID = 6.4) [a]	50.7 ± 19.3	88.1 ± 16.3
DASH Score (MCID = 10.2)	35 ± 18.2	5.6 ± 3.4
WORC Score (MCID = 245.26)	1198.8 ± 347.6	344.8 ± 393.2

All differences were statistically significant between time points.

a = Data was non-parametric and used Wilcoxon Signed Rank for comparisons

MCID = Minimal Clinically Important Differences; IR = internal rotation; ER = external rotation

Three of the five subjects showed an increase in glenohumeral contact path length post-therapy (Figure 3.3). Across the five subjects, path length pre-therapy was 104.7 ± 100.5 % glenoid height while post-therapy was 92.6 ± 36.2 %. A similar trend was seen for the absolute AP range of translation. Pre-therapy, the AP range was 17.2 ± 10.0 % glenoid AP width, and post-therapy, the AP range was 26.2 ± 11.1 % glenoid width. The absolute SI range of translation remained relatively the same following therapy for all subjects. Comparing pre- and post-therapy, the SI range of translation was 19.5 ± 11.6 % and 19.5 ± 8.3 % glenoid height, respectively. Exercise therapy did not have a significant impact on glenohumeral contact path length, SI or AP range of translation ($p > 0.05$).

When comparing magnitude of changes in arthrokinematic parameters with the percent strength increase following the full 12 week exercise therapy program, no significant correlations were found. In addition, no correlations were observed between changes in any arthrokinematic variables with the change in ASES, DASH, or WORC scores.

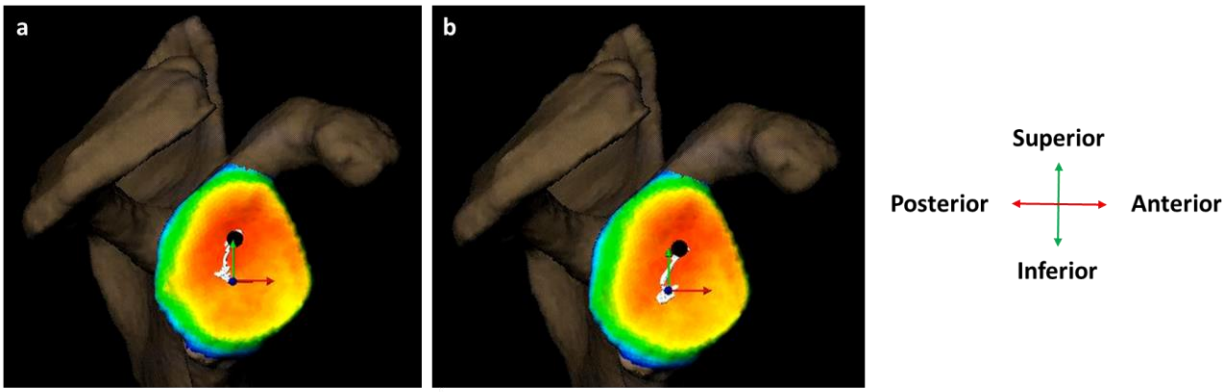

Figure 3.3: Contact path arthrokinematics for a single subject (a: pre-therapy, b: post-therapy). The *black circle* represents the contact center. The *white line* is the path in which the contact center follows throughout the range of motion. Qualitatively, no differences exist in contact path length pre- versus post-therapy.

3.1.4 Discussion

All subjects successfully completed exercise therapy, and showed significant improvements in shoulder strength and patient-reported outcomes (ASES, WORC, DASH). However, these clinical improvements did not lead to any significant changes in glenohumeral arthrokinematics for internal/external rotation with their arm at their side. Our hypothesis that exercise therapy would improve glenohumeral joint arthrokinematics for internal/external rotation motions with the arm at the side in terms of decreased translations was refuted. Exercise therapy had no effect on changing glenohumeral joint arthrokinematics for internal/external rotation with the arm at the side. Rather, exercise therapy was found to only improve shoulder strength and patient satisfaction. While no subjects required surgery and improvements in shoulder strength and patient reported outcomes were found, these should not be the only factors considered when treating patients with rotator cuff tears non-operatively. Non-operative treatment for rotator cuff tears can be further improved by adapting current rehabilitation protocols to address glenohumeral joint arthrokinematics.

While the initial clinical outcomes appear positive in terms of increased shoulder strength and improved test scores (DASH, ASES and WORC), the long-term effects of exercise therapy are still unknown. It is unclear whether these satisfactory outcomes remain or if they will revert back to pre-therapy levels. Cases in which patients return to the clinic seeking more treatment after exercise therapy complaining of pain and joint instability may be due to the failure to improve the arthrokinematics for internal/external rotation motions. This additional treatment would be a financial burden for both the patient and the healthcare system.

The glenohumeral arthrokinematics for internal/external rotation showed increased translations compared to previous studies that investigated glenohumeral internal/external rotation

for healthy subjects, indicating joint instability. In the current study, the average AP range of translation pre-therapy corresponded to 5mm of translation, with previous studies reporting around 2mm of translation (80, 86, 180). Similarly, the average SI range of translation for the present study was 7mm, while previous studies reporting 3-4mm of translation for healthy subjects (180). Investigation of glenohumeral internal/external rotation at higher abduction angles would likely show even larger differences compared to healthy subjects. The current study shows values of translations at least double than healthy subjects, indicating improvements to glenohumeral arthrokinematics are needed to improve joint stability. Joint instability may be as a result of unbalanced force couples, which may expose the torn supraspinatus tendon to loads that increase the likelihood of tear propagation. Thus, current exercise therapy protocols should be altered to also address glenohumeral arthrokinematics with the arm at the side.

Interestingly, the effect of exercise therapy on glenohumeral arthrokinematics may depend on the type of motion. In a previous study that looked at glenohumeral joint arthrokinematics for coronal plane abduction, glenohumeral arthrokinematics were improved in terms of less glenohumeral joint translation following therapy (87). In the current study investigating internal/external rotation with the arm at the side, no differences in glenohumeral arthrokinematics pre- and post-therapy were found. The interaction between the transverse and coronal force couples of the shoulder for stabilization purposes may explain the differences found between different motions. Therefore, it is likely that simply increasing the strength of the surrounding muscles may not be sufficient in restoring glenohumeral arthrokinematics, and that achieving a balanced force couple is more essential. Different exercises may be more effective in changing glenohumeral arthrokinematics for different motions and should be incorporated into future exercise therapy protocols.

A limitation is the small sample size. Although only five subjects were tested, all subjects were representative of the general population of individuals with a degenerative rotator cuff tear that would have been treated with exercise therapy. Post-hoc power analysis indicated that over 100 subjects would be needed to achieve significant differences for contact path length, and SI contact range of translation. An additional 8 subjects would be needed to find differences in AP contact range of translation. Another limitation is that the results only apply to internal/external rotation motions with the arm at the side. Different results may have been obtained if the subjects conducted the same internal/external rotation motions at different abduction angles. Furthermore, the 'normal' glenohumeral arthrokinematics for internal/external rotation motions for each subject are unknown since the contralateral shoulder was not tested. Additionally, how glenohumeral arthrokinematics change over time following exercise therapy is unknown as glenohumeral arthrokinematics at a long term follow up session was not investigated. However, the lack of this information does not take away from the key finding that no significant changes in glenohumeral arthrokinematics were observed between pre- and post-therapy.

Future studies are needed to obtain a better understanding on how exercise therapy affects glenohumeral arthrokinematics and how these changes in glenohumeral arthrokinematics affect the success of therapy. In the future, studies will investigate the changes in glenohumeral arthrokinematics for different arm positions that are representative of tasks common to daily living. In addition, future work will include long-term follow up studies to assess whether the inability to restore glenohumeral arthrokinematics during internal/external rotation with the arm at the side results in subjects eventually needing surgery.

3.1.5 Conclusions

Exercise therapy resulted in clinical improvements with regards to shoulder strength and patient-reported outcomes, but it does not affect glenohumeral arthrokinematics for internal/external rotation with the arm at the side. Current exercise therapy protocols do not influence glenohumeral arthrokinematics for internal/external rotation motions with the arm at the side. While the subjects successfully completed exercise therapy without needing to resort to surgery, there is a lack of understanding as to whether therapy was truly successful since glenohumeral arthrokinematics did not change. Exercise therapy should be adapted to emphasize the importance of improving glenohumeral arthrokinematics for multiple motions, in addition to restoring range of motion, increasing shoulder strength, and reducing pain.

4.0 Aim 2: Effect of Location Specific Tendon Remodeling on Tear Propagation

Finite element modeling is a useful tool to solve complex engineering and mathematical problems by re-creating experimental boundary and loading conditions to simulate more testing conditions than could be performed experimentally. Previous studies using finite element models to investigate rotator cuff tears have focused on the effect of tendon (eg. overall degeneration) and tear characteristics (eg. size, location, and shape) on the stress and strain distribution patterns experienced by the rotator cuff tendons (92, 101, 104, 143-147). Results from these studies suggest that the inhomogeneous stresses and strains experienced throughout the tendon (eg. high stress at tear tips and stress-shielded region along medial edge of tear) may result in different tendon remodeling scenarios which could alter localized mechanical properties within the tendon. Tear propagation is a key factor that may explain high failure rates of treatment as larger tears are more difficult to treat and have been associated with worse clinical outcomes (53). However, the effect of localized tendon remodeling on tear propagation is not well understood. Thus, the purpose of aim 3 of this dissertation is to determine the effect of location specific tendon remodeling on tear propagation and stress distribution using a validated subject-specific finite element model of a supraspinatus tendon.

4.1 Finite Element Analysis of Tendon Remodeling on Tear Propagation

4.1.1 Introduction

Rotator cuff tears, which typically occur in the supraspinatus tendon, are a primary cause of shoulder pain and loss of shoulder function (40). In an aging population, the high frequency of rotator cuff tears, combined with their capacity to cause severe pain and limit normal activity, underscores the importance of timely and effective treatment (6, 41, 42). The success of treatment by non-operative and operative means have been quite variable and the factors behind the success rate of treatment is still debated (43, 44, 51, 52, 55, 56).

A factor that plays a role in the success or failure of treatment is tear propagation. Larger tear sizes have been associated with more pain and higher re-tear rates after surgery (53, 54). Tears may propagate more easily than others because of poor tissue quality due to changes in the mechanical properties of the tendon. Changes in tendon mechanical properties are directly related to the composition and microstructure of the tendon (93).

Histological studies have shown poor tendon quality being associated with changes at the microscopic level (eg. collagen fiber organization, nuclei shape, cellularity and fatty infiltration) (106, 181-185). The composition of constituents found in tendons (eg. proteoglycans) has been shown to be regulated by mechanical stimuli (94, 97, 98, 186, 187). Furthermore, regional differences in degeneration has been shown for tendons with a tear. Within the layers of the tendon, collagen fiber disorganization, myxoid and hyaline degeneration was observed in the deep layers of rotator cuff tendons with a tear (183). At the myotendinous junction, more lipoid degeneration was observed compared to the mid-substance and insertion site for tendons with a tear (188). Since torn tendons cannot bear any loads, the remaining intact fibers have to compensate and bear extra

load. Therefore, the presence of a tear may alter the tendon composition and microstructure, consequently altering the mechanical properties throughout different locations within the tendon (105, 189). For example, degeneration at the insertion site of the supraspinatus tendon due to thinning of tendon fibers and presence of granulation tissue resulted in a decrease in tensile strength, with a majority of the tendons failing at the insertion site (105).

Finite element models to investigate rotator cuff tears have primarily focused on the effect of tear characteristics (eg. size, location, and shape) and overall tissue quality (eg. reduced mechanical properties) on tear propagation (92, 101, 104, 143-147, 190). The results from these studies have showed high stress concentrations at the tear tips and stress-shielding at the medial and lateral tear edges of a tear. Therefore, gross changes in mechanical properties across the entire tendon may not accurately represent the changes in the tendon following a tear (92). Rather, localized changes in mechanical properties may occur due to different tendon remodeling scenarios based on the inhomogeneous stresses and strains observed throughout different locations within the tendon.

The effects of localized tendon remodeling on the changes of tendon mechanical properties as well as their role in tear propagation are not well understood. Mechanical loading has been previously described as a delicate “state switch”, balancing the forces in the tendon which would promote functional tissue remodeling or development of tendon degeneration (191). For example, high stress concentrations may result in positive (ie. increased stiffness) or negative (ie. decreased stiffness) remodeling of the tendon’s structural properties. In addition, negative tendon remodeling may occur in areas of low/no stresses as a result of the tissue no longer being used.

Therefore, the objective was to investigate the effect of localized tendon remodeling on tear propagation for simulated supraspinatus tendon tears. Specifically, evaluate the amount of tear propagation, localized stress distribution around the tear, and the critical load needed for tear propagation based on positive and negative tendon remodeling around the tear where areas of high and low stresses occur.

4.1.2 Methods

4.1.2.1 Model Geometry, Mesh and Material Model

A previously validated, subject-specific finite element model of an intact supraspinatus and infraspinatus tendon was used. The model was validated by using mechanical testing data where the predicted strains from the computational model were within the experimental repeatability of 3% strain (190). Subject-specific model geometry was constructed using CT scans of one cadaveric shoulder specimen (70-year-old male). The mesh used for the supraspinatus and infraspinatus tendon geometry consisted of 33,092 nodes and 150,626 tetrahedral elements and was generated using Hypermesh (Altair Engineering, Troy, MI, USA) (Figure 4.1). The appropriate mesh size was determined after a convergence analysis was performed by increasing the number of elements until the difference in strain predictions was <0.2% strain.

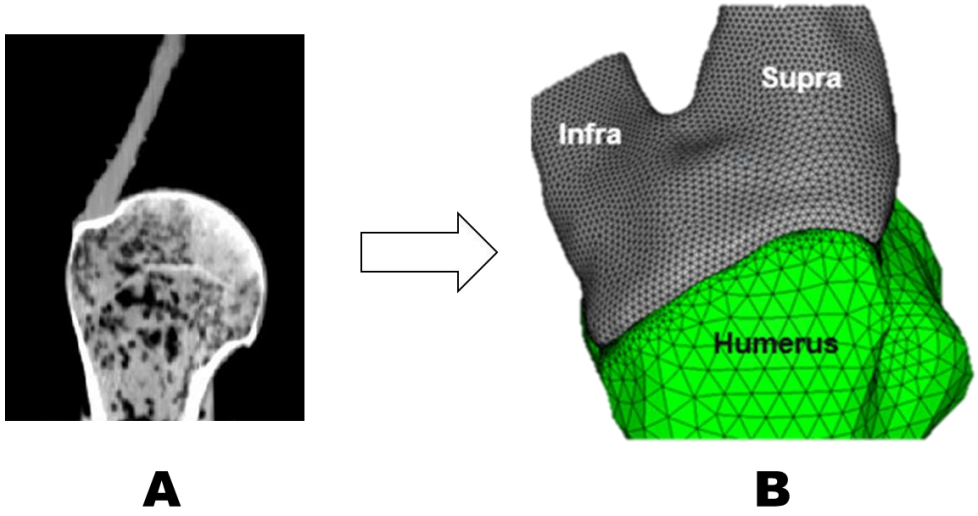

Figure 4.1 Overview of FEM model creation. CT Scans (A) were used to create model geometry (B)

A homogeneous, transversely isotropic, hyperelastic material model was used to define the tendon (104, 192). This material model defined the properties of the extracellular matrix with an isotropic, nearly incompressible Neo-Hookean model, and incorporated collagen fiber modulus and orientation through an exponential function of the pseudo-invariant of right Cauchy-Green deformation tensor. Mechanical properties of the anterior, middle and posterior tendon thirds were determined from load-to-failure mechanical tests of the tendon thirds. The calculated mechanical properties of the tendon thirds were then assigned to the appropriate region of the model, with a linear gradient used to transition the properties between the tendon thirds to minimize stress concentrations (Table 4.1) (92, 143, 190).

A 1-cm wide anteriorly located full-thickness tear approximately 5mm medial to the insertion site was created in the model by "detaching" the relevant adjacent elements (Figure 4.2). An anteriorly located tear was chosen to represent a tear most susceptible to tear propagation (90, 91). The medial location of the tear represents a common location rotator cuff tears, and is also in the same area in where the model was validated for accurate predictions of strain.

Table 4.1: Properties of the supraspinatus tendon thirds used in the model

	Ultimate Stress (MPa)	Collagen Fiber Modulus (MPa)	Fracture Toughness (J)	Max Separation (mm)
Anterior	5.8	10.9	1855	0.64
Middle	5.8	15.4	1546	0.53
Posterior	4.3	8.9	1221	0.57

4.1.2.2 Cohesive Elements

Cohesive elements along the anterior-posterior plane of the tear were incorporated in the model to simulate tear propagation (Figure 4.2). Cohesive elements are special surface elements that have been used to model failure for other biological tissues by allowing the elements on adjacent surfaces to separate at a prescribed critical failure point (193-195). The critical failure point is based on the cohesive traction-separation law (bi-linear relationship between traction and separation) and assumes that the primary mode of failure is tension (196). The fracture toughness represented by the area under the traction-separation curve needed to be defined for the computer simulations and was estimated based on previously collected mechanical testing data of tear propagation (Table 4.1) (90). The traction-separation law is

$$\boldsymbol{\sigma = k_c \delta} \qquad \textbf{(4-1)}$$

where σ represents traction, δ represents jump/separation and k_c is the stiffness of the cohesive elements defined by the failure properties of the material.

$$\boldsymbol{k_c = \left(\frac{S}{1-S}\right)\left(\frac{\sigma_{max}}{S_{initial}}\right)\left(\frac{1}{\delta_{max}}\right)} \qquad \textbf{(4-2)}$$

In this expression, σ_{max} is the intrinsic tensile strength of the tissue. S represents damage to the material, which monotonically decreases from $S_{initial}$ to 0, depending on how close the separation between elements is to the maximum separation. $S_{initial}$ is the initial damage to the material that defines the starting point along the traction-separation curve. $S_{initial}$ for the model was 0.98, commonly used for soft tissue tears (193). Once maximum stress is reached, damage occurs and eventually the cohesive elements separate at the maximum separation δ_{max} (S = 0) to simulate tear propagation.

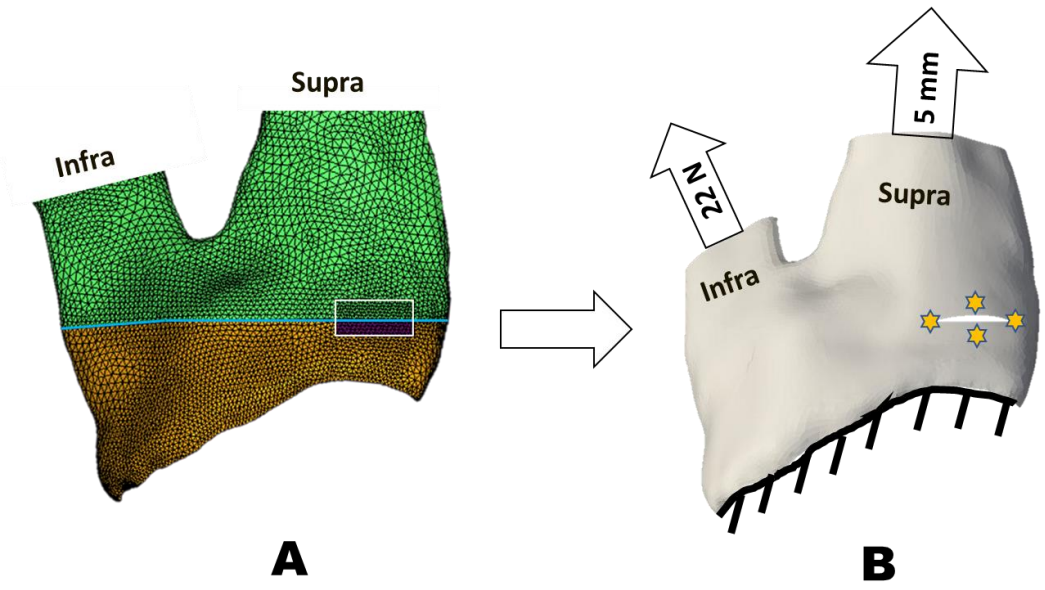

Figure 4.2: A) Example mesh of a tear (white box) and cohesive elements (blue line). B) Boundary and loading conditions as well as the locations where tendon remodeling was incorporated indicated by the yellow stars.

4.1.2.3 Loading and Boundary Conditions

Tear propagation simulations were performed using a custom non-linear, cohesive-volumetric finite element code (104). Based on experimental testing and a rigorous analyses described in a previous study, the reference configuration was determined to be a 40N preload of the supraspinatus tendon at 70° of glenohumeral abduction (190). Therefore, the supraspinatus was positioned to simulate 70° of glenohumeral abduction, and the insertion site attachment of the tendons to the humeral head was assumed to be fixed. A 22 N static load was applied to the infraspinatus tendon to simulate the load-sharing interaction between the infraspinatus and supraspinatus tendons. The medial edge of the supraspinatus tendon was displaced 5 mm and was chosen based on experimental tests of supraspinatus tear propagation (90, 91). The direction of loading for both tendons was along the physiological line of action (Figure 4.2).

4.1.2.4 Localized Tendon Remodeling Scenarios

Localized tendon remodeling was incorporated in the model by modifying collagen fiber modulus. Positive remodeling was represented by a 50% increase in the collagen fiber modulus and negative remodeling a 50% decrease. Tendon remodeling focused on the elements along the medial and lateral edges of the tear and at the tear tips, corresponding to the stress-shielded and high stress concentration regions described in previous studies (Figure 4.2B) (92, 104, 190). Tendon modulus was the main parameter of interest for tendon remodeling based on the inhomogeneous stress distribution found in tendons with a tear because studies have shown the effect of injury, healing and mechanical stimulation to cause similar degrees of changes in tendon stiffness (197-199). In total, 4 remodeling scenarios were simulated: 1) baseline (ie. no remodeling), 2) negative remodeling at the medial and lateral tear edges, 3) positive remodeling at

the anterior and posterior tear tips, and 4) negative remodeling at the anterior and posterior tear tips.

For each tendon remodeling scenario, there were 3 main outcome parameters of interest. First, the amount of the tear propagation in the anterior-posterior direction. Second, the peak maximum principal stress at the tear tips when the medial edge of the supraspinatus tendon was displaced 5 mm. Thirdly, the critical load defined time point in which the maximum load was reached during the 5 mm of supraspinatus displacement.

4.1.3 Results

Qualitatively, similar propagation patterns and stress distributions were observed for all localized tendon remodeling scenarios (Figure 4.3). The tear propagated in the anterior direction, nearly reaching the anterior border of the supraspinatus tendon, as well as in the posterior direction, approaching the posterior third of the supraspinatus tendon. High stress concentrations were observed at the anterior and posterior tear tips, and low stresses were observed at the medial and lateral edges of the tear. The anterior tear tip for all remodeling scenarios had a rounded/blunt shape compared to the posterior tear tip (Figure 4.4).

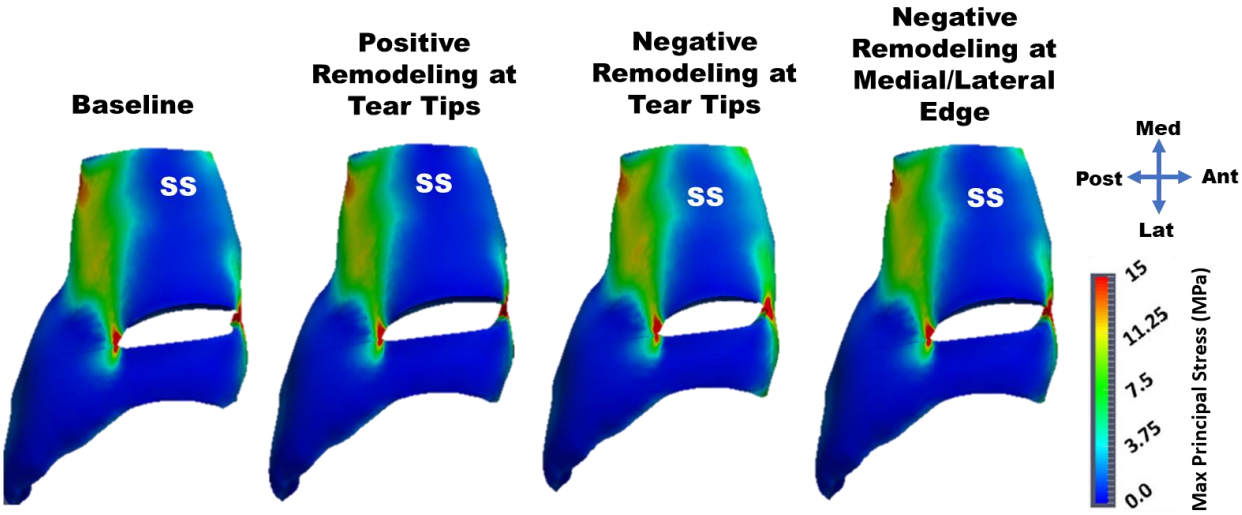

Figure 4.3: Principal stress distribution after 5 mm of supraspinatus tendon (SS) displacement for all tendon remodeling scenarios. Qualitatively, negative remodeling at the tear tips resulted the least amount of tear propagation, though the difference is small.

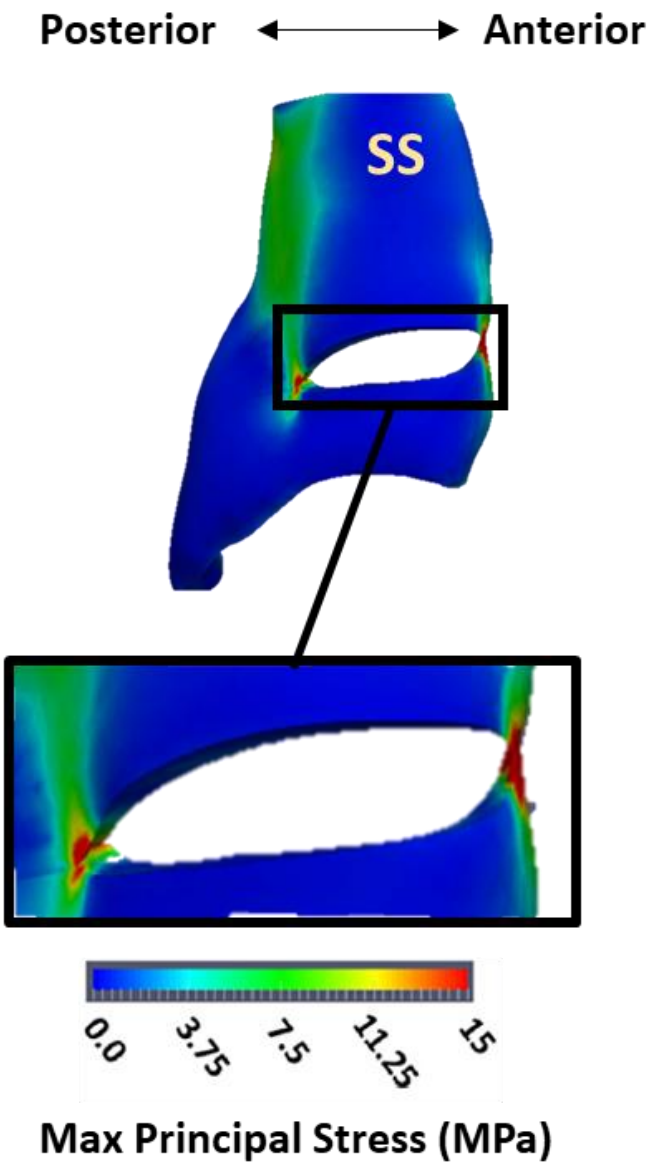

Figure 4.4: Max principal stress distribution of FEM model for positive remodeling at the tear tips with the supraspinatus tendon (SS) is displaced 5 mm at 70° of glenohumeral abduction. Regions of red indicate high stress, regions of blue indicate low stress. More "blunt" tear shape on anterior portion of the tear.

The difference in amount of tear propagation among the four remodeling scenarios was small (range: < 3 mm) (Table 4.2). The baseline scenario resulted in a total of 17.4 mm of tear propagation. Remodeling along the medial and lateral tear edges resulted in a similar amount of tear propagation (< 2% difference) as the baseline scenario (17.7 mm versus 17.4 mm, respectively). Negative remodeling at the tear tips resulted in the least amount of tear propagation, 10% lower than the baseline scenario. Positive remodeling at the tear tips resulted in the most tear propagation, 15% more than negative remodeling at the tear tips scenario.

Similar to the amount of tear propagation, positive remodeling at the tear tips had the highest peak maximum principal stress, and negative remodeling at the tear tips with the lowest among the remodeling scenarios (Table 4.2). The peak maximum principal stress for positive remodeling at the tear tips (25.2 MPa) was 43% larger than negative remodeling at the tear tips, 35% larger than negative remodeling at the medial/lateral tear edge, and 28% larger than baseline.

Table 4.2: Amount of tear propagation and peak maximum prinicpal stress for different localized tendon remodling scenarios

	Amount of Tear Propagation (mm)	Peak Maximum Principal Stress (MPa)
Baseline	17.4	19.7
Positive Remodeling at Tear Tips	18.4	25.2
Negative Remodeling at Tear Tips	16.0	17.6
Negative Remodeling at Medial/Lateral Tear Edge	17.7	18.7

For all tendon remodeling scenarios, critical load occurred between 3.1-3.5 mm of displacement of the medial edge of the supraspinatus tendon, corresponding to approximately 7% bone-to-medial tendon edge strain (Figure 4.5). Negative remodeling at the tear tips had the highest critical load of 278 N. The lowest critical load needed for tear propagation was for the positive remodeling at the tear tips (249 N), 11.5% lower than negative remodeling at the tear tips. Similar critical loads (< 1% difference) were observed for the baseline and negative remodeling of the medial and lateral tear edges scenario.

Overall, positive remodeling at the tear tips resulted in the largest amount of tear propagation, highest peak maximum principal stress, and lowest critical load needed for tear propagation. Conversely, negative remodeling at the tear tips resulted in the least amount of tear propagation, lowest peak maximum principal stress and highest critical load. Negative remodeling along the medial and lateral tear edges showed similar results for all output parameters as the no remodeling condition.

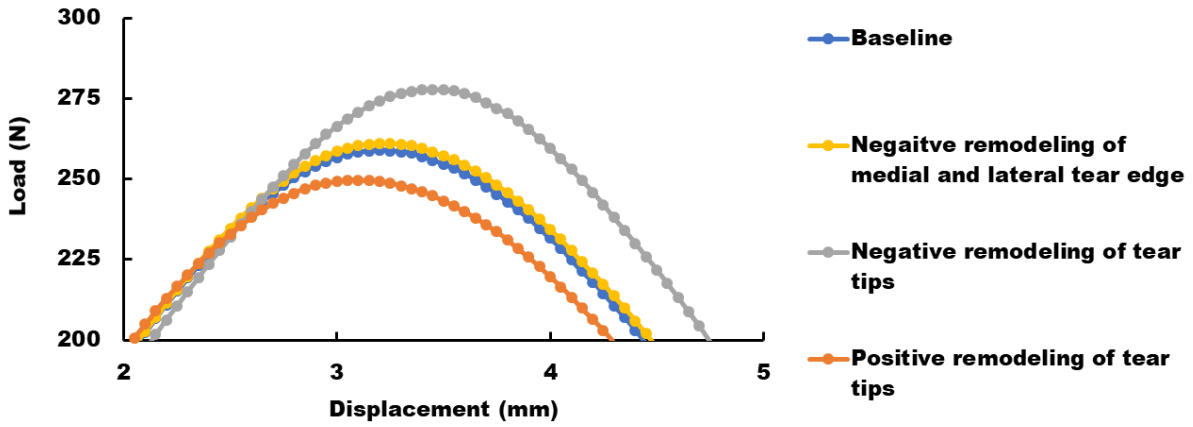

Figure 4.5: Load versus displacement curve for different tendon remodeling scenarios.The peak of each curve represents the critical load needed for tear propagation.

4.1.4 Discussion

The effects of localized tendon remodeling on supraspinatus tendon tear propagation were investigated using a validated, subject-specific finite element model. Tendon remodeling was simulated by localizing changes to the tendon stiffness at the tear tips and medial/lateral tear edges. Overall, only subtle differences were observed for peak maximum principal stress and the amount of tear propagation for all four tendon remodeling scenarios. The critical load values that lead to tear propagation (~250-300 N) are similar to the forces experienced by the supraspinatus tendon during activities of daily living and physical therapy (48, 200).

Remodeling at the tear tips had the greatest effect on influencing the risk of tear propagation whereas remodeling at the medial and lateral tear edges had a minimal impact. The reason for the minimal impact of medial and lateral tear edge remodeling may be because remodeling did not occur in the plane of propagation (ie. anterior-posterior direction) where the cohesive elements were located. Incorporating cohesive elements throughout the model may result in more tendon retraction and different tear shapes. Moreover, critical loads could change if the propensity for the tear to propagate is easier in other directions. However, the modeling of tear propagation only in the anterior-posterior direction reduced the computational complexity while maintaining an accurate representation of the behavior of supraspinatus tendon tear propagation experimentally (90, 143). The clinical implications of this finding would be to monitor the changes in tissue quality directly at the anterior/posterior tips of the tear as the study shows this may be the best predictor.

The FEM model used closely simulates the case of an un-repaired supraspinatus tendon tear for an individual going through physical therapy or normal activities of daily living. Even though the results showed a minimal impact of remodeling at the medial/lateral tear edges, future

analyses of a surgically repaired tendon may provide additional insight of whether localized tendon remodeling in this area is relevant. Re-tears are common following surgical treatment of rotator cuff tears, and they commonly occur at the tissue-suture interface (61, 69). Since the medial tear edge is generally used for suture placement during repair and remodeling of that portion of the tissue may provide information about whether the sutures can hold onto the tissue without re-tearing.

Interestingly, increasing the collagen fiber stiffness at the tear tips led to more tear propagation and the lowest critical load. The finding that increased collagen fiber stiffness at the tear tips leads to a greater risk of tear propagation can be explained by the higher stress concentrations and Hooke's Law. The increased stiffness in the tissue at the tear tips would lead to higher stress concentrations at the tear tips, and thus reaching the critical load to initiate tear propagation at a lower amount of tissue deformation. Conversely, lower tissue stiffness would allow the tissue to deform more before the critical load is reached and tear propagation occurs. The anterior tear tip showed a more "blunt/rounded" shape since the tissue is more compliant and can deform more before reaching the critical load and the tear continues to propagate (Figure 4.4).

The finding that increased collagen fiber stiffness at the tear tips increases tear propagation contradicts previous studies where greater amounts of overall tendon degeneration was associated with a greater risk of tear propagation (92). The previous study defined degeneration as a decrease in both collagen fiber stiffness as well as the ultimate strength of the tendon. However, stiffer does not necessarily mean the tissue will be stronger (eg. scar tissue), therefore only changes in collagen fiber stiffness was assumed. Furthermore, the previous study assumed a global change to the tendon mechanical properties, whereas the current FEM model accounts for the unique stress distribution observed for tendons with a tear and the effect of localized tendon remodeling due to changes in the mechanical environment.

Studies have shown that the mechanical stimuli has a large role in the mechanical properties of musculoskeletal tissues, which can cause both increases and decreases in tissue stiffness (189, 201, 202). It is unknown whether an ideal loading condition exists that promote maintaining tendon strength while minimizing the increase of tendon stiffness at a localized level. Though it may be an interesting approach to mitigating tear propagation, a fine balance is most likely needed because too much loading may induce tear propagation and not enough loading may result in global degeneration of the entire tendon. Clinicians may be more inclined to suggest a more aggressive treatment such as surgery if the tear is believed to be susceptible to tear propagation.

Although, a finite element model with subject-specific geometry, mechanical properties, boundary and loading conditions was used, the results may not be generalizable since these parameters differ for each individual and may not be representative of the typical specimen. For example, the mechanical properties used to model the specimen were strongest and stiffest in the middle third of the tendon, rather than the anterior third (88). Future studies should also investigate the role of localized changes in collagen fiber organization (188). Based on the findings, clinicians should accurately measure tendon stiffness at the tear tips to assess the susceptibility of tear propagation. However, there is still a need to develop such a tool where clinicians can quantitatively and non-invasively assess tendon mechanical properties at precise locations.

4.1.5 Conclusions

The results identify the localized tendon remodeling scenarios that results in the most tear propagation. Specifically, remodeling in terms of increased stiffness at the tear tips resulted in the most propagation, highest stresses and lowest critical load. Future work is needed to better understand the role of localized tendon remodeling for surgically repaired tears as well as the development of a non-invasive tool for clinicians to quantify mechanical properties of tendons. Understanding the role of localized tendon remodeling on tear propagation can provide clinicians insight as to the most appropriate treatment modality for patients with a rotator cuff tear.

5.0 Aim 3: Evaluation of Ultrasound Techniques to Assess Tendon Quality and Quantify Mechanical Properties

Mechanical properties of tendon are important to understand because they are directly related to function. Furthermore, the mechanical properties of tendon are associated with the composition and microstructure of the tendon (93). The presence of a tear may alter the tendon composition and microstructure, thus changing the mechanical properties throughout different locations within the tendon. Consequently, tear propagation may occur more easily especially if the remaining tendon has poor tissue quality and inferior mechanical properties (58).

Although changes in location specific mechanical properties may influence tear propagation, clinicians need a method or tool to quantitatively evaluate the mechanical properties of the tendon. Ultrasound is a non-invasive, reliable, and cost-effective tool used by clinicians to detect the presence and size of rotator cuff tears (110-113). Currently, the evaluation of tissue quality from ultrasound images is subjective, but recent advancements in ultrasound techniques (eg. quantitative ultrasound measures and ARFI imaging) offer the potential for quantification of location specific tendon mechanical properties. Providing clinicians a way to quantitatively assess tendon quality and mechanical properties could help them improve their surgical technique and monitor the healing of tissue during and after treatment. Therefore, the objective of aim 2 of this dissertation was to evaluate the utility of different ultrasound techniques (QUS measures and ARFI imaging) to assess location specific changes in tendon quality (from histology) and predict location specific mechanical properties (from materials testing).

5.1 Correlation of Quantitative Ultrasound Measures and Supraspinatus Tendon Quality

5.1.1 Introduction

Rotator cuff tears are an important clinical issue with a prevalence rate reported to be 20-30% in the general population (4). Tear propagation from physical therapy and re-tears occurring at the tendon-suture interface following surgical repair are common occurrences. A possible reason may be due to poor tissue quality (56, 203). As a result, a need exists for clinicians to assess tendon quality quickly and accurately, which may help in reducing the failure rate of both non-operative and surgical treatment.

Ultrasound is a non-invasive, cost-efficient, accurate and reliable imaging modality that is becoming more widely used by clinicians to diagnose, evaluate, and treat rotator cuff tears (50, 113, 204-207). However, clinicians use ultrasound as a subjective tool to assess whether a rotator cuff tear is present and the overall quality of the tendon. The primary quantitative measurements made with ultrasound are measurements of tissue geometry such as tear size, tendon width, thickness and cross-sectional area (208-210). Recently, quantitative ultrasound (QUS) measures have been shown to be a reliable technique for determining tendon quality by analyzing the grayscale distribution of an ultrasound image (117-119, 211-214). In these studies, an interpretation of features that describe the ultrasound image echotexture (echogenicity, variance, skewness, and kurtosis) were explained. Increased tendinopathy was associated with increased measures of skewness and kurtosis as well as decreased measures of variance and echogenicity, with a healthy tendon expected to exhibit highly aligned collagen fibers creating a striped pattern of alternating dark and light bands (117, 118). While quantitative ultrasound measures have been

established to quantify overall tendon quality (117, 119), specific factors that can affect these measures have yet to be established.

Histology has been used extensively to determine specific factors that influence the quality of the tendon (181-185). These studies have shown poor tendon quality being associated with changes in collagen fiber organization, nuclei shape, cellularity and fatty infiltration. Understanding tendon quality is important since poor tendon quality relates to decreased mechanical properties of the tendon (181). Reduced mechanical properties due to pathologic changes may be one reason for high failure rates of surgical repairs.

By providing a quantitative assessment of specific factors of tendon quality through conventional B-mode ultrasound images, clinicians could adapt their surgical technique accordingly to minimize the failure rate. Therefore, the objective was to determine the feasibility of assessing tendon quality as quantified by histology through changes in quantitative ultrasound measures.

5.1.2 Methods

Eight fresh frozen cadaveric shoulders (2 male, 6 female, 63 ± 12 years) were used, in which the specimens were acquired with approval from the University of Pittsburgh Committee for Oversight of Research and Clinical Training Involving Decedents (CORID). As part of the screening process for all shoulder specimens acquired in our laboratory, ultrasound scans are performed to detect rotator cuff tears. Four of the cadaveric shoulders that were obtained over time had a small tear in the supraspinatus tendon (<1cm in the anterior-posterior direction) confirmed after dissection, and the tear size was measured with digital calipers. All specimens were stored at -20°C and allowed to thaw overnight at room temperature before use.

5.1.2.1 Ultrasound Imaging and Analysis

All ultrasound images were obtained prior to dissection by a single orthopaedic surgeon with over 15 years of expertise in musculoskeletal ultrasound for assessment of rotator cuff tears. Ultrasound images were taken with the specimen in a position of hyperextension and internal rotation of the humerus to expose as much of the supraspinatus tendon as possible under the acromion (ie. simulated Crass position) (112, 215-217). A transverse view of the widest part of the supraspinatus tendon near its insertion to the humerus for the purposes of minimizing the effects of anisotropy on tendon appearance for the quantitative ultrasound measures analysis (118). Furthermore, this approach represents the clinical approach to viewing the supraspinatus tendon in the transverse view. Images were obtained using an ultrasound machine (LOGIQ S8, General Electric Healthcare, Chicago, Illinois, United States) equipped with a 61 mm footprint linear transducer (ML6-15 Transducer, General Electric Healthcare, Chicago, Illinois, United States) (850 x 649 pixels) (Figure 5.1). To minimize variability between the images obtained between

specimens, only one ultrasound examiner obtained the ultrasound images, the long head of the biceps tendon was used as a consistent reference point between specimens, and the relevant parameters of the ultrasound system did not change across all examinations (Frame rate = 18 fps, frequency = 18 MHz, gain = 65 dB, AO% = 100). Furthermore, the ultrasound examiner was blinded to the results of the quantitative ultrasound measures, as described below, to minimize any bias when obtaining the ultrasound image.

Another examiner was responsible for evaluating the quantitative ultrasound measures for the image from each specimen. A single examiner was utilized to evaluate the quantitative ultrasound measures as preliminary tests and prior studies have established low interrater reliability (118). A 1 cm wide region of interest located 1 cm posterior from the posterior margin of the long head of the biceps tendon was manually selected using ImageJ (National Institutes of Health, Bethesda, Maryland, United States) in order to capture the middle third of the supraspinatus tendon. From the selected region of interest, quantitative ultrasound measures (skewness, kurtosis, variance and echogenicity) were calculated using MATLAB (Mathworks, Natick, MA, United States) based on a histogram that describes the grayscale distribution, or echotexture, as a measure of tendon quality (118). The histogram contains information about each pixel in the ultrasound image, where each pixel in the ultrasound images represents a grayscale value ranging from 0 (black) to 255 (white). All histograms were verified to be normally distributed and the full 0-255 range was used for analysis. Skewness, kurtosis and variance were determined through first-order statistics and represent the asymmetry, pointiness and spread of the grayscale histogram. Echogenicity was determined as the mean grayscale value of the region of interest.

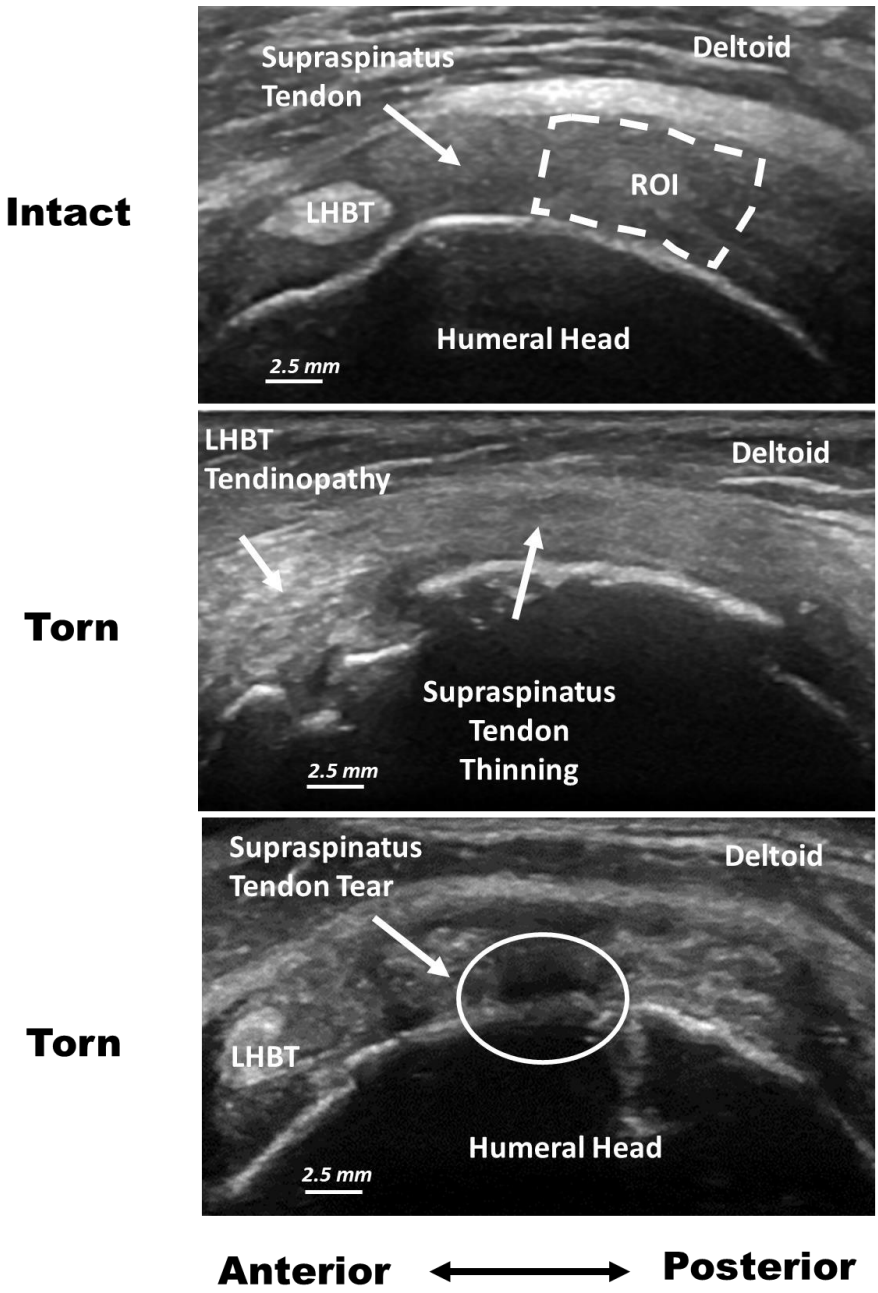

Figure 5.1: Transverse view of an intact and two torn supraspinatus tendons. A 1 cm wide region of interest (ROI) was measured 1 cm away from the posterior margin of the long head of the biceps tendon (LHBT). Quantitative ultrasound measures were made based on the grayscale distribution within the ROI. The middle image demonstrates signs of LHBT tendinopathy and supraspinatus tendon thinning, suggestive of a tear. For the far right image, the dark area within the circle indicates the location of the tear. Damage to the surface of the humeral head can be observed for both the middle and far right image.

5.1.2.2 Histology

Following ultrasound imaging and analysis, all shoulders were dissected, isolating the supraspinatus tendon for the procurement of tissue biopsies for histology. Tissue biopsy samples (~2 x 4 mm) were taken near the insertion site, mid-substance and myotendinous junction for each supraspinatus tendon, ensuring that the longer edge of the rectangle is parallel to the long axis of the tendon. After each piece of tissue was excised, the sample was placed in a histology cassette with the distal edge of the tissue sample at the beveled end of the cassette. Samples were then fixed in 10% buffered formalin for a minimum of 72 hours and were oriented such that the posterior side is the first side to be sectioned. Following fixation and paraffin embedding, each sample was sectioned at a 5 μm thickness and cut along the long axis of the tendon such that 3 slices were obtained throughout the anterior-posterior width of each tissue biopsy. Each slice was stained with hematoxylin and eosin (H&E) to visualize tendon morphology. Light microscopy was used to image each slice with a 20x objective lens across the full tendon thickness, where images were saved for analysis at a later time. Since the tendon consists of layers that are not tendon proper (capsule and bursa), a set percentage of the articular-bursal thickness was removed to ensure the analysis only included the tendon (183).

All histological images were graded for tendon quality using four parameters in a blinded fashion by three independent observers using a semi-quantitative scale. The four parameters chosen to evaluate tendon quality were: collagen fiber organization, nuclei shape, hypercellularity and fatty infiltration (182-185). The semi-quantitative grading scale was adapted from a previous study to create a 4-point scale of tendon quality, with a higher score indicating poor tendon quality and a larger area of the tendon being affected (0 = no change, 1 = slight localized change < 25% of tendon area, 2 = multifocal change 25-50% of tendon area, 3 = diffuse or global change > 50%

of tendon area) (181). Poor collagen fiber organization was evaluated as less aligned collagen fibers (Figure 5.2D = Poor collagen fiber organization; Figure 5.2B = Highly aligned collagen fibers). Nuclei shape indicative of poor tendon quality was evaluated as the increased presence of rounded and less elongated nuclei (Black arrow in Figure 5.2A and Figure 5.2C). Hypercellularity was identified as an increase in the number of cells to form a cluster (Figure 5.2C). Fatty infiltration was determined as the presence of white globules (Arrowhead in Figure 5.2E and Figure 5.2F).

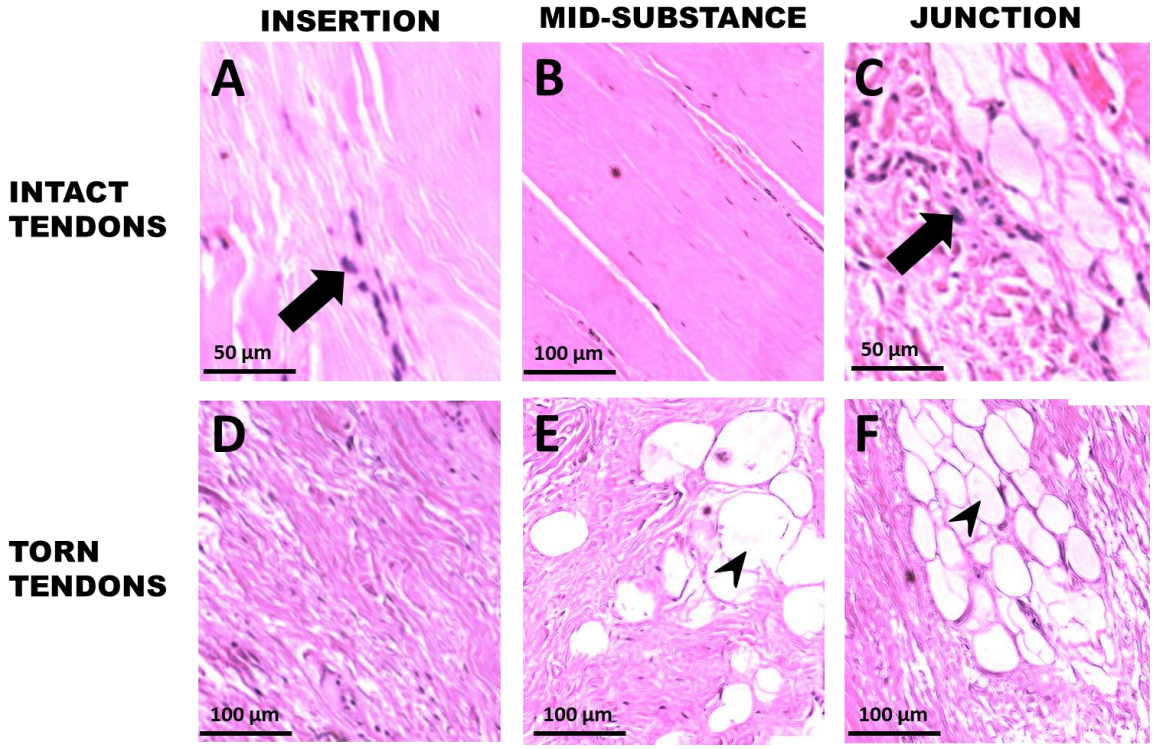

Figure 5.2: H&E stained histological images. The top row shows histological images from an intact tendon (A, B and C), while the bottom row shows histological images from a tendon with a tear (D, E and F). Each column indicates the location where the histological image was obtained from (insertion site = A & D, mid-substance = B & E or myotendinous junction = C & F). Both intact and torn tendons exhibited changes in tendon quality at all location sites in terms of fatty infiltration (black arrowhead), more rounded nuclei shape (black arrow), increased cellularity and disorganized collagen fibers.

The average grade between the three observers for each image was used to represent the tendon quality for each image. For each biopsy sample, the average grade of the three slices were used to represent tendon quality for that location site. The summation of the grades for all four parameters represented the overall tendon quality. Tendon quality of the "entire tendon" was determined as the average grade between all three locations (insertion, mid-substance and myotendinous junction).

5.1.2.3 Statistical Analyses

A Kolmogrov-Smirnov test was performed to determine if the data was normally distributed. When appropriate, non-parametric tests were performed to account for non-normally distributed data. Intraclass correlation coefficient (ICC) determined the inter-rater reliability of grading the histology images. A two-way mixed ANOVA with a post-hoc Bonferonni test evaluated histological grades of tendon quality based on location site (insertion, mid-substance, junction) and tendon state (intact and torn). Independent samples t-tests or Mann Whitney U tests determined the effect of tendon state (intact and torn) on quantitative ultrasound measures and histological grades of tendon quality. The correlation between quantitative ultrasound measures and histological grades of tendon quality were determined through Pearson or Spearman's rho correlation calculations. Significance was set at $p < 0.05$.

5.1.3 Results

The four shoulders with a tear had an anterior-posterior tear width of 14.8 ± 11.8 mm, and a medial-lateral tear width of 11.0 ± 7.0 mm when measured with the shoulder positioned at 0° of abduction. Histological grading between the three examiners showed good inter-rater reliability for overall tendon quality (ICC = 0.89) as well as for each individual parameter of collagen fiber organization, cellularity, nuclei shape and fatty infiltration (ICC = 0.76, 0.77, 0.81 and 0.94, respectively). Qualitatively, most specimens with a tear exhibited damage to the long head of the biceps tendon and the articular surface of the humeral head (Figure 5.1).

Quantitative ultrasound measures showed a wide range of values for all tendons, with no statistically significant difference for any of the quantitative ultrasound measures between the intact and torn tendons (skewness: $p = 0.114$; kurtosis: $p = 0.234$; variance: $p = 0.114$; echogenicity: $p = 0.718$) (Table 5.1). Specifically, the quantitative ultrasound measures of variance and echogenicity tended to be higher for the intact tendons (903 ± 551 and 93 ± 16, respectively) versus the torn tendons (383 ± 83 and 85 ± 19, respectively). The measures of skewness and kurtosis tended to be lower for the intact tendons (0.1 ± 0.1 and -0.1 ± 0.5, respectively) compared to the torn tendons (0.6 ± 0.5 and 1.6 ± 1.5, respectively). In addition, the intact tendons showed more variability than torn tendons for each quantitative ultrasound measure.

Table 5.1: Quantitative ultrasound measures and histological grades for significant correlations

Specimen	Kurtosis	Variance	Skewness	Echogenicity	Cellularity (Insertion)	Fatty Infiltration (Junction)	Fatty Infiltration (Entire Tendon)
1 (Intact)	0.2	376	0.1	92	0.5	1.0	0.3
2 (Intact)	-0.4	1343	0.1	88	1.0	0.4	0.1
3 (Intact)	-0.8	1414	-0.1	114	0.3	0.2	0.1
4 (Intact)	0.4	481	0.2	78	0.5	0.2	0.2
5 (Torn)	0.2	275	0.1	112	0.6	2.1	1.2
6 (Torn)	1.5	404	0.8	75	0.9	1.7	0.7
7 (Torn)	1.0	376	0.2	69	0.5	1.4	0.6
8 (Torn)	3.6	476	1.3	84	1.3	0.4	0.4

From histological analysis, collagen fiber disorganization, rounded nuclei shape, hypercellularity and fatty infiltration were present throughout the tendon (Table 5.2). Various degrees of tendon quality were exhibited among the location sites (Figure 5.2). Regardless of the presence of a tear, significantly more fatty infiltration at the myotendinous junction was observed compared to the insertion and mid-substance (Table 5.2, $p < 0.001$). Furthermore, tendons with a tear had twice as much fatty infiltration than intact tendons (Table 5.2, $p < 0.05$). No other histological parameters of tendon quality showed significant differences between location sites or tendon state.

Table 5.2: Histological Grades of Tendon Quality (Mean ± Standard Deviation)

	Fiber Organization	Nuclei Shape	Increased Cellularity	Fatty Infiltration	Sum
Insertion	2.5 ± 0.3	2.5 ± .03	0.6 ± 0.3	0.2 ± 0.2	5.9 ± 0.7
Mid-substance	2.4 ± 0.4	2.4 ± 0.4	0.6 ± 0.2	0.3 ± 0.3	5.6 ± 0.9
Junction	2.4 ± 0.3	2.4 ± 0.3	0.8 ± 0.4	0.9 ± 0.6	6.4 ± 1.1
p	0.349	0.168	0.616	**< 0.001**	0.051
Intact	2.5 ± 0.2	2.5 ± 0.3	0.6 ± 0.2	0.3 ± 0.3	5.9 ± 0.7
Torn	2.3 ± 0.4	2.4 ± 0.4	0.8 ± 0.3	0.6 ± 0.6	6.1 ± 1.2
p	0.328	0.546	0.163	**0.033**	0.476

The histological parameters of tendon quality at each individual location site showed poor tendon quality for tendons with a tear. At the mid-substance, overall tendon quality was graded to be 19% higher in torn tendons (6.4 ± 0.6) than intact tendons (5.4 ± 1.3) ($p < 0.05$). In addition, torn tendons had more fatty infiltration than intact tendons at the mid-substance, 0.5 ± 0.4 and 0.1 ± 0.1 respectively ($p < 0.05$). No significant difference was found between the intact and torn tendons for collagen fiber organization, cellularity, cell shape or fatty infiltration at the insertion site or myotendinous junction.

A total of three significant correlations between quantitative ultrasound measures and histological parameters were found (Table 5.1). A significant correlation was found at the insertion site between kurtosis and increased cellularity ($r = 0.724$, $p < 0.05$) (Figure 5.3). No correlation between quantitative ultrasound measures and histological parameters was found at the mid-substance. At the myotendinous junction, a significant inverse correlation between variance and fatty infiltration existed ($rho = -0.843$, $p < 0.01$) (Figure 5.4). When considering the entire tendon, a significant inverse correlation between variance and fatty infiltration was also found ($rho = -0.826$, $p < 0.05$) (Figure 5.4).

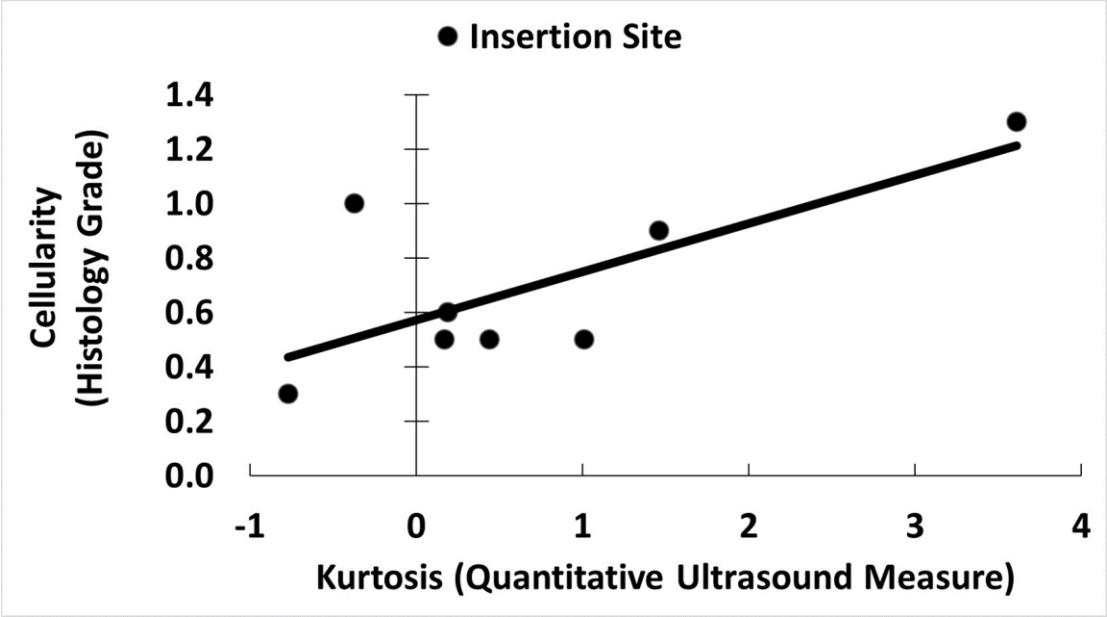

Figure 5.3: Positive correlation between kurtosis and cellulaity at the insertion site (r = 0.724, p < 0.05)

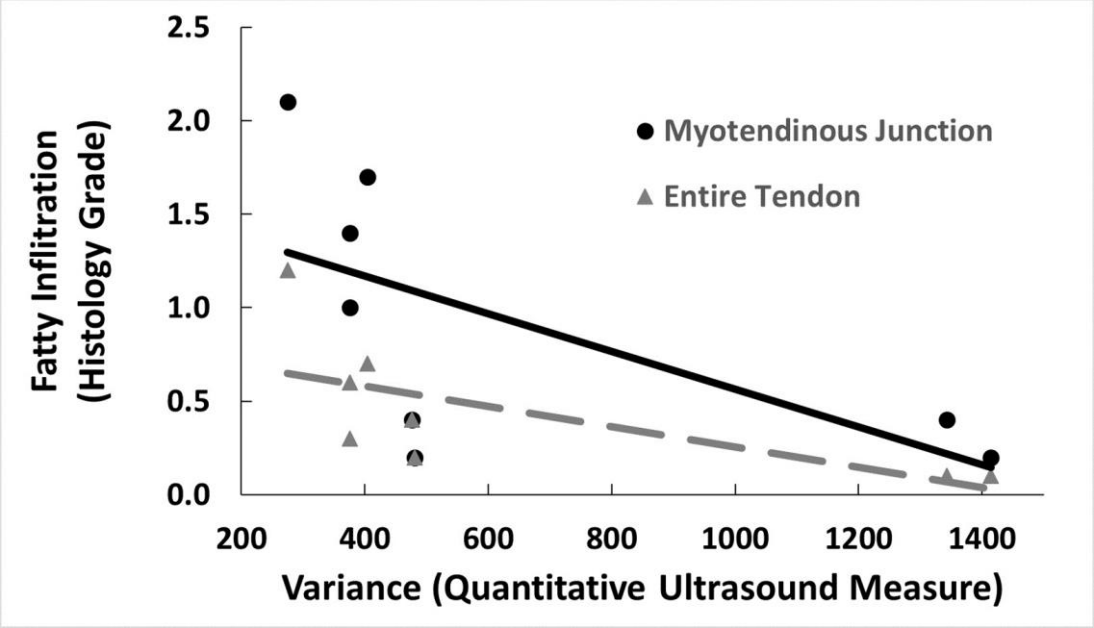

Figure 5.4: Strong inverse correlation between variance and fatty infiltration at both the myotendinous junction and the entire tendon (rho = -0.843 and rho = -0.825, respectively) (p < 0.05). Plotted data represents raw data rather than "ranked" data used for Spearman's rho calculation.

5.1.4 Discussion

The findings show the potential for using quantitative ultrasound measures to analyze the grayscale echotexture of an ultrasound image and assess changes in tendon quality as quantified through histology. Certain changes in tendon quality could be detected because of their effect on the echotexture of an ultrasound image (eg. fatty infiltration will make the ultrasound image have hyperechoic regions). While previous studies have shown quantitative ultrasound measures correlate to clinical pathologies (117, 119, 214), no direct evidence has been provided correlating quantitative ultrasound measurements to tendon morphology.

The quantitative ultrasound measures showed no statistically significant differences between the intact and torn tendons, but the trends observed were similar to previous studies in terms of healthier tendons exhibiting higher measures of variance and echogenicity as well as lower measures of kurtosis and skewness (117, 119). Comparisons of the raw values of each quantitative ultrasound measure to previous studies are not possible due to differences in ultrasound examiners and ultrasound settings (eg. frequency and gain). Nonetheless, with further development and analyses, quantitative ultrasound measures could be useful to assess tendon quality as long as a repeatable protocol is used to obtain repeatable images, and inter-examiner variability is eliminated (117-119, 213).

The strong positive correlation between cellularity and kurtosis indicate that a sharp peak in the grayscale histogram of the ultrasound image relate to hypercellular regions found in the tendon. The other correlations were between variance and fatty infiltration. Variance measures the spread of the grayscale values, while fatty infiltration indicates the amount of fatty infiltration. The correlations indicate that increased kurtosis and decreased variance are associated with increased

supraspinatus tendon degeneration, consistent with prior studies that found increased kurtosis and decreased variance correlated to poor supraspinatus and biceps tendon health (117). The correlations found suggest that quantitative ultrasound measures could be used to assess specific factors that affect tendon quality which can only be otherwise assessed through histology or magnetic resonance imaging. The ability for clinicians to evaluate the changes in tendon quality is important since material properties of the tendon may be reduced as a result, making rotator cuff tear initiation and propagation more likely (185, 218).

All tendons, regardless of their tendon state (ie. torn or intact) exhibited similar tendon quality. No statistical differences were found between the intact and torn group for the quantitative ultrasound measures. In addition, most histological parameters of degeneration (collagen fiber organization, nuclei shape and cellularity) showed no significant differences between the intact and torn tendons. Only fatty infiltration and overall tendon quality exhibited differences between the intact and torn tendons, which were similar to findings from previous histological studies (105, 183).

A limitation is that only the transverse view of the supraspinatus tendon was imaged by ultrasound, corresponding most closely to the insertion site of the tendon. Analysis of the supraspinatus tendon near the myotendinous junction using the transverse view is not possible due to interference from the acromion. This imaging protocol was previously verified to obtain repeatable images of the supraspinatus tendon for quantitative ultrasound measures analyses, while maximizing the amount of the tendon that can be imaged (118). The quantitative ultrasound measures are sensitive to the conventional B-mode image acquired. Care must be taken to thoroughly verify the repeatability of the ultrasound images acquired to account for the anisotropy of the supraspinatus tendon and the influence of the surrounding bones. Therefore, while a long-

axis view of the supraspinatus tendon may have provided more information about multiple tendon locations, an established repeatable protocol does not yet exist.

Based on the findings, further development of an imaging protocol for a long-axis supraspinatus tendon view may possibly reveal even more correlations to changes in tendon quality. In addition, only a small subset of factors that affect tendon quality could be investigated since only H&E staining was used. However, the use of additional staining techniques is not likely to change the results found for the subset of factors that altered tendon quality investigated. Future studies will utilize additional staining techniques to understand different factors that may affect tendon quality (eg. collagen content, fat and GAGs present in the extracellular matrix). To differentiate quantitative ultrasound measurements between intact and torn tendons, post-hoc power analysis showed 71 additional samples in each group were needed.

5.1.5 Conclusions

The foundation for a new methodology of quantitative ultrasound measures has been established for clinicians to use ultrasonography as a diagnostic tool to non-invasively and quantitatively evaluate tendon quality. With further development of this methodology, clinicians might be able to evaluate location specific changes in tendon quality non-invasively and monitor healing tendons in patients undergoing treatment.

5.2 ARFI Imaging of Musculoskeletal Tissues: An Experimental and Computational Approach

5.2.1 Introduction

Ultrasound is non-invasive, reliable and cost-effect tool often used by clinicians to diagnose and assess the severity musculoskeletal injuries (113). Currently, evaluation of tissue quality based on ultrasound images is predominantly qualitative and depends on the user. Acoustic Radiation Force Impulse (ARFI) imaging is an ultrasound technique that generates a localized force onto the tissue of interest at a precise location (ie. remote palpation) and the resulting tissue displacement is measured (120, 130). Information about the resulting tissue displacement may be able to predict the mechanical properties of the tissue and provide clinicians quantitative information about tissue quality. For example, during surgical repair of a rotator cuff tear, ARFI imaging can be used to evaluate tissue quality surrounding the tear, allowing clinicians to make a more informed decision as to where to place the sutures through the tendon.

ARFI imaging is primarily utilized for compliant, isotropic biological tissues such as breast, liver, and arteries where tissue displacements are less than 10 μm (120-125, 130). Clinically, ARFI imaging has been used to detect the presence of tumors based on the stiffness of the tissue (219, 220). For these elastic, isotropic tissues, the magnitude of this compressive ARFI displacement is assumed to be inversely proportional to the elastic modulus of the tissue (152). However, whether the clinical applications and assumptions can also be applied to musculoskeletal tissues which are much stiffer and anisotropic is still unknown. The tensile modulus in the linear region for muscles is on the order of hundreds of kilopascals to low megapascals, capsular tissue on the order of tens of megapascals, and tendons on the order of hundreds of megapascals (221-

224). Breast tissue on the other hand is much more compliant, with its tensile and compressive modulus on the order of kilopascals (225, 226).

Finite element method (FEM) models simulating ARFI imaging have been developed to better understand the effect of ultrasound transducer parameters, material properties and motion tracking algorithms on ARFI displacement measurements (152, 154-156). While some FEM models have investigate the role of anisotropy on ARFI displacement, the magnitude of the modulus of the tissues and phantoms being investigated are much lower than musculoskeletal tissues (155, 156). For anisotropic tissues, in order to obtain accurate and repeatable measures of ARFI displacement, it is essential to consider the orientation of the material when imaging (156).

The radiation force generated to push the tissue during ARFI imaging may not be strong enough to displace the stiff musculoskeletal tissues. The typical magnitude of force applied during ARFI imaging is on the order of dynes (121). Conventional ARFI imaging (full-frame) generally utilizes a single, focused, narrow beam to push onto the tissue, with this single beam repeated across the entire width of the transducer. However, the narrow beam limits the acoustic radiation force applied to the tissue. Mutli-foci beamforming is an ultrasound imaging technique that allows for a more powerful acoustic radiation force by dividing the ultrasound transducer into multiple sub-apertures and sending multiple beams at a specified location (227, 228). Multi-foci beam forming has been utilized to improve the efficiency of heating tissues for ultrasound-induced thermal strain imaging while using only a single transducer (229).

Overall, the utility of ARFI imaging is not fully understood for musculoskeletal tissues. Therefore, using an experimental and computational approach, the objective was to determine the utility of ARFI imaging to differentiate between different musculoskeletal tissues of varying moduli (eg. tendon, capsule and muscle) based on ARFI tissue displacement. In addition, the effect

of increasing the magnitude of the ARFI push force to allow for better differentiation between musculoskeletal tissues of high stiffness will also be investigated.

5.2.2 Methods: Effect of Tissue Modulus

15 fresh-frozen strips of tissues (5 pectoralis major muscle, 5 glenohumeral capsule, 5 biceps tendon) were harvested to a length of at least 10 cm from 8 cadaveric shoulder specimens (60.9 ± 4.9 years). All tissues were prepared for tensile testing and ARFI imaging of the tissue mid-substance. Two delrin beads (2 mm diameter) were superglued to the surface of each specimen to mark the mid-substance area. The cross-sectional area of the tissue mid-substance was determined using a laser scanner (Next Engine, Desktop 3D Scanner, Santa Monica, CA, USA). Specimens were kept moistened with physiologic saline solution to prevent dehydration during preparation and testing.

Each tissue underwent a uniaxial tensile testing protocol to determine the modulus of the toe and linear region of the stress-strain curve. The ends of the tissue were clamped with custom soft tissue clamps and aligned for tensile loading in the materials testing machine (Instron, Model 5965, Norwood, MA, USA) and the strain of the tissue mid-substance was measured by tracking the delrin beads with an optical tracking system (DMAS7, Spica Technology, Kihei, HI, USA) (Figure 5.5). The tissue was preloaded (tendon & capsule = 1N, muscle = 0.2N), preconditioned for 10 cycles (tendon = 1-10N, capsule = 1-5N, muscle = 0.2-2N) and then loaded (tendon = 100N, capsule = 50N, muscle = 5N). Loading levels were chosen based on preliminary tests that determined the loads required to reach the linear region of a stress-strain curve, but not result in tissue failure or clamp slippage.

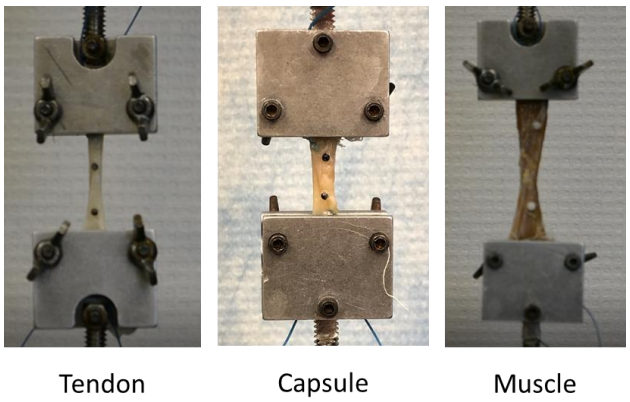

Figure 5.5: Tensile Test Setup for Musculoskeletal Tissues

Modulus of the toe region was determined by iteratively removing the first and last data points of the stress-strain curve from 0-1% strain until a linear regression fit of $r^2 \geq 0.99$ was achieved. Similar to the modulus of the toe region, the modulus of the linear region was determined by iteratively removing the first and last data points of the stress-strain curve from >1% strain until a linear regression fit of $r^2 \geq 0.99$ was achieved. A Kolmogrov-Smirnov test was performed to check the normality of the data. Based on the result of the Komogrov-Smirnov test, either a Kruskal-Wallis test or ANOVA with a post-hoc Bonferroni test was performed to evaluate the effect of tissue type on the modulus of the toe region and the modulus of the linear region.

Following tensile testing, each tissue was mounted into a custom tensioning jig and tensioned to 0.1MPa and embedded in gelatin. A Krackow stitch was applied to both ends of the tendon using a #2 suture (Ethibond*Excel, Ethicon Inc., Somerville, NJ, USA) to allow for tensile loading of the tendon in the custom tensioning jig. The gelatin mixture consisted of 1 liter of water, 5% concentration of gelatin from porcine skin (G2500, Sigma Aldrich, St. Louis, MO, USA) and 1% concentration of cellulose (S3504, Sigma Aldrich, St. Louis, MO, USA).

All ARFI testing was performed with the gel temperature at 20°C confirmed by a digital infrared thermometer and the tissue positioned at a 25 mm axial depth and centered laterally as

confirmed by a B-mode image (Figure 5.6B). A linear array transducer (ATL L7-4) connected to a research ultrasound platform (Vantage 128, Verasonics, Kirkland, WA, USA) was used to perform the entire full-frame ARFI sequence. The full-frame ARFI sequence first consists of a reference imaging pulse focused at the elevation focus of the transducer (25 mm axial depth). Then, an ARFI push is generated using a localized radiation force fired at an excitation voltage of 30V (F# = 1.3, push duration = 192 μs). After the ARFI push, a tracking pulse is fired (ie. imaging pulse identical to the reference imaging pulse). The process of imaging, pushing and tracking is repeated 64 times across the entire width of the transducer (Figure 5.6A). ARFI displacement due to the radiation force is calculated using the phase-based Loupas algorithm on the reference and tracking images (230). In total, 3 ARFI images were acquired for each specimen, where the average ARFI displacement was used for analysis (repeatability = 0.2 μm). A bi-linear translation stage (BiSlide MN10, Velmex, Bloomfield, NY, USA; accuracy = 0.003", repeatability = 0.0002") and probe holder was used to position the probe directly at tissue mid-substance (ie. halfway between the two beads marking the mid-substance).

ARFI displacement of the tissue was defined by a region of interest at the center area of the tissue which was manually selected to minimize boundary effects. Similarly, ARFI displacement of the surrounding gelatin was measured at the same axial depth. ARFI displacement of the tissue was normalized to the surrounding gel displacement. A Kolmogrov-Smirnov test was performed to check the normality of the data. Based on the results from the Komogrov-Smirnov test, either a Kruskal-Wallis test or ANOVA with a post-hoc Bonferroni test was performed to evaluate the effect of tissue type on the modulus of the toe region, modulus of the linear region and normalized ARFI displacement. Significance was set at $p < 0.05$.

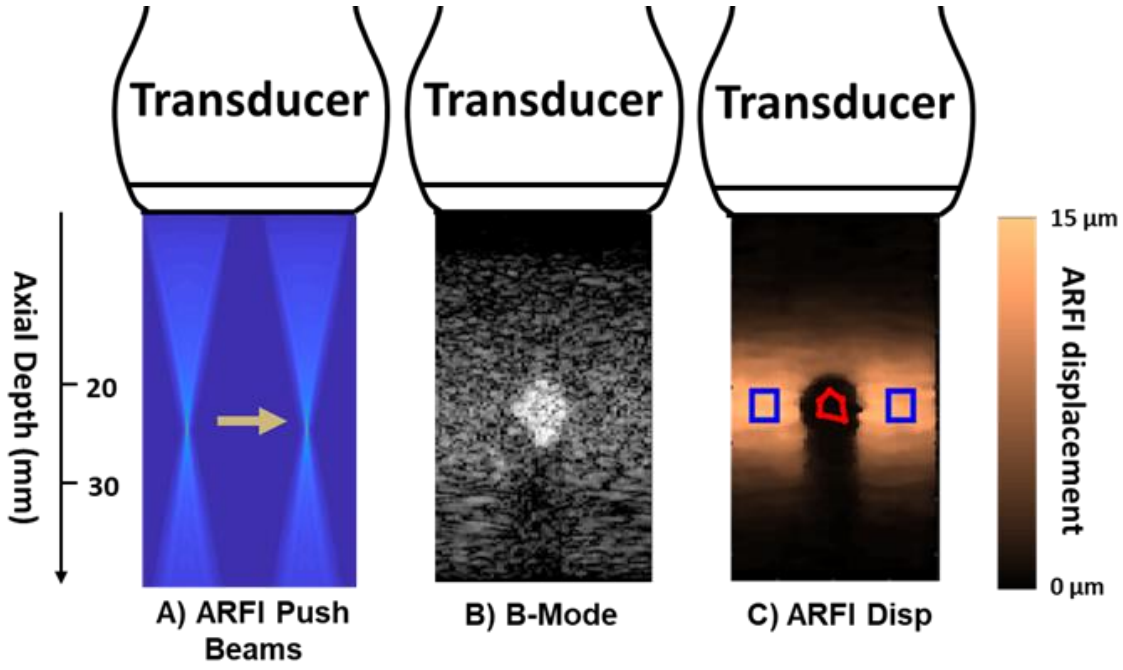

Figure 5.6: ARFI imaging overview. A) 64 ARFI push beams fired across the transducer aperture width. B) B-mode image of tissue embedded in gelatin. C) ARFI displacement image where tissue displacement (red region) was always lower and normalized to the softer surrounding gelatin

5.2.3 Results: Effect of Tissue Modulus

Tissue type had a significant effect on both the modulus of the linear region and the modulus of the toe region of the stress-strain curve ($p < 0.05$) (Figure 5.7). Large differences between the tendon, capsule and muscle were seen for both the modulus of the toe region and linear region. The modulus of the toe region for tendons (34.9 ± 27.7 MPa) was 35 times higher than muscle (1.0 ± 1.1 MPa) and 3.8 times higher than capsular tissue (9.8 ± 6.5 MPa). The modulus of the linear region for tendons (257.8 ± 124.1 MPa) was 103 times higher than muscle (2.5 ± 2.1 MPa) and 7 times higher than capsular tissue (36.3 ± 25.3 MPa). Significant differences were found between muscle-tendon and muscle-capsule, but not tendon-capsule for the modulus of both the toe and linear region (Figure 5.7). The ratio of the modulus of the linear region to the modulus of the toe region was highest for tendons and lowest for muscles (tendons = 7.3:1, capsule = 3.7:1 and muscle = 2.5:1).

For ARFI imaging, tissue displacement was always lower than the surrounding gelatin. Tissue type had a significant effect on normalized ARFI displacement ($p < 0.05$), however, post-hoc Bonferroni results showed no significant differences between the tendon, capsule and muscle groups (Figure 5.7). In general, the higher the modulus of the tissue the lower the normalized ARFI displacement Normalized ARFI displacement of muscle (0.60 ± 0.30) was highest, over double the values for capsule and tendon. Normalized ARFI displacement between tendon (0.26 ± 0.08) and capsule (0.27 ± 0.15) differed by less than 0.1.

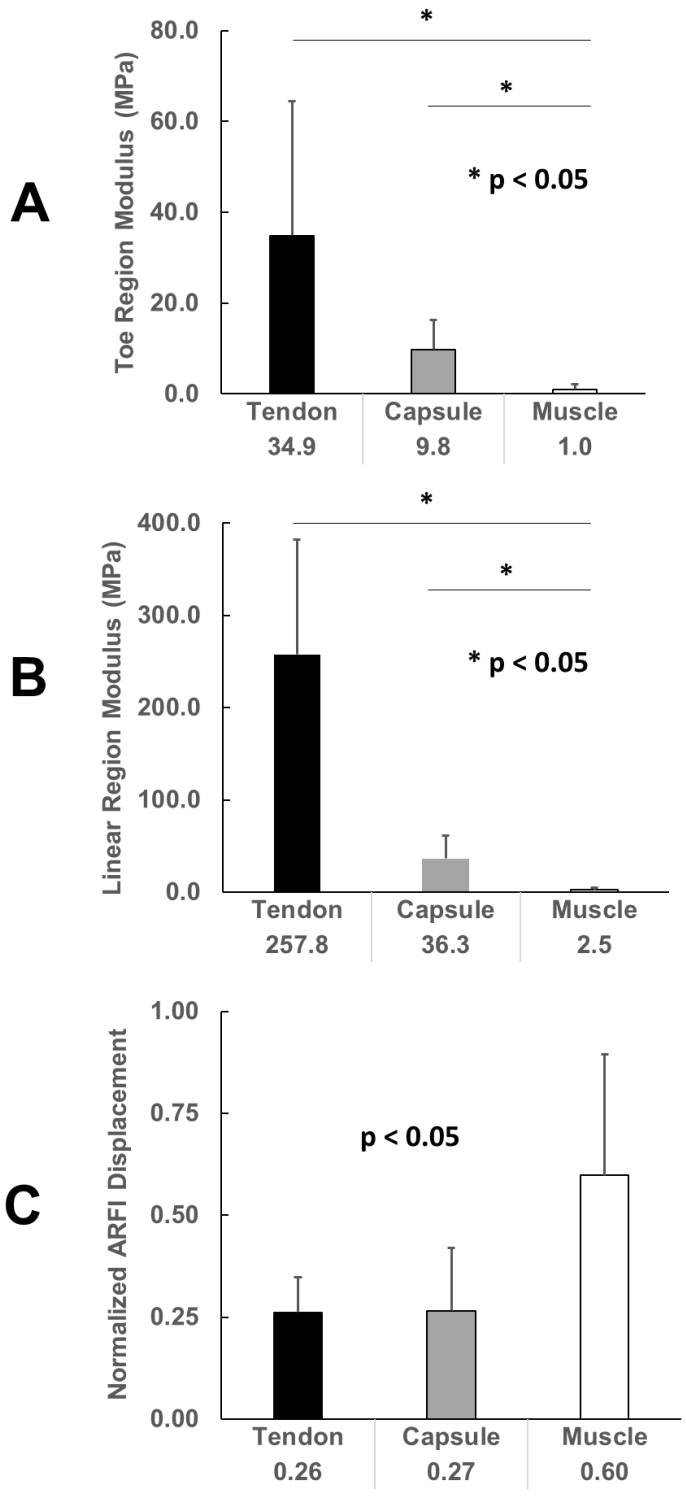

Figure 5.7: Modulus of toe region (A), linear region (B) and normalized ARFI displacement (C) for muscle, capsule and tendon specimens (mean ± SD).

5.2.4 Methods: Effect of ARFI Push Magnitude

Four fresh-frozen porcine knees were dissected and the anterior extensor tendons were harvested to a length of at least 10 cm and prepared for mechanical testing and ARFI imaging of the tendon mid-substance. Two delrin beads (2 mm diameter) were superglued to the surface of each specimen to mark the mid-substance area. The cross-sectional area of the tissue mid-substance was determined using a laser scanner (Next Engine, Desktop 3D Scanner, Santa Monica, CA, USA). Specimens were kept moist with physiologic saline to prevent dehydration during preparation and testing.

The ends of the tendon were clamped with custom soft tissue clamps and aligned for tensile loading in the materials testing machine (Instron, Model 5965, Norwood, MA, USA). Each tendon underwent a uniaxial tensile testing protocol (preload = 1N, preconditioning = 1-10N for 10 cycles, and load to 100N). Loading levels were chosen based on preliminary tests that non-destructively loaded the tendon into the linear region. Mid-substance strain in the tendon was measured with an optical tracking system (DMAS, Spica Technology, Kihei, HI, USA). Modulus of the linear region was determined by iteratively removing the first and last data points of the stress-strain curve from >1% strain until a linear regression fit of $r^2 \geq 0.99$ was achieved.

Following tensile testing, each tendon was wrapped with a layer of muscle and loaded into a custom tensioning jig immersed in distilled water to more closely mimic physiologic conditions. A Krackow stitch was applied to both ends of the tendon using a #2 suture (Ethibond*Excel, Ethicon Inc., Somerville, NJ, USA) to allow for tensile loading of the tendon in the custom tensioning jig. The tendon was loaded to five different stress levels (0.1, 0.25, 0.5, 0.75 and 1.0 MPa). At each stress level, 3 full-frame and 3 multi-foci based ARFI images were acquired using a linear array transducer (ATL L7-4) connected to a research ultrasound platform (Vantage 128, Verasonics, Kirkland, WA, USA).

The full-frame ARFI sequence first consists of a reference imaging pulse focused at the elevation focus of the transducer (25 mm axial depth). Then, an ARFI push is generated using a localized radiation force fired at an excitation voltage of 30V (F# = 1.3, push duration = 192 μs). After the ARFI push, a tracking pulse is fired (ie. imaging pulse identical to the reference imaging pulse). The process of imaging, pushing and tracking is repeated 64 times across the entire width of the transducer (Figure 5.8). For multi-foci imaging, a similar protocol is used, but with some key differences. A reference image is acquired using plane wave imaging rather than with conventional focused beams. Once the reference image was acquired a mulfi-foci ARFI push is introduced. The multi-foci push divides the transducer aperture into 3 foci, and targets the push to precise position (25 mm axial depth and 0 mm laterally) (Figure 5.8). The multi-foci ARFI push uses the same parameters (ie. excitation voltage, push duration) as full-frame ARFI imaging, but because 3 focused beams are used to target the same area, the magnitude of radiation force is 3 times larger. Following the ARFI push, tracking frames are acquired. ARFI displacement for both the full-frame and multi-foci approach is calculated using the phase-based Loupas algorithm on the reference and tracking images (230).

An additional test was performed to clarify the results found in the "effect of tissue modulus" section for higher ARFI forces. Cyclic compressive loading was applied to the tendon mid-substance to damage the tendon. Loading conditions were determined based on preliminary tests that resulted in a decrease in the modulus of the linear region by ~40%. After the damage protocol, the same mechanical testing and ARFI imaging protocol performed for the un-damaged tendon was repeated. A paired samples t-test was performed to assess the effect of ARFI technique (full-frame versus multi-foci) as well as injury (un-damaged versus damaged) on ARFI tendon displacement. Significance was set at $p < 0.05$.

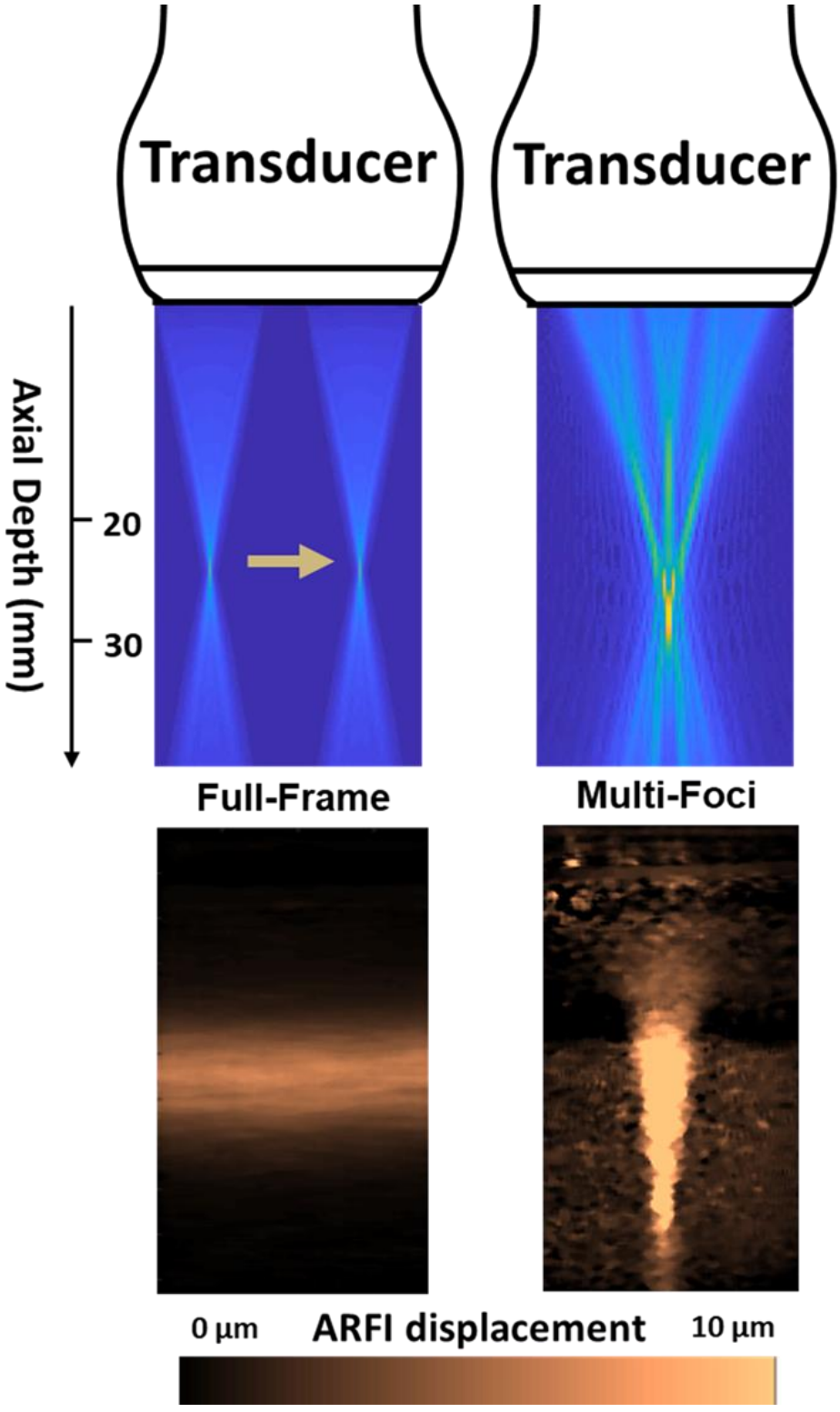

Figure 5.8: Full-frame and Multi-Foci ARFI Imaging

5.2.5 Results: Effect of ARFI Push Magnitude

Qualitatively, the multi-foci approach resulted in noise and worse image resolution making it difficult to identify the location of the tendon in the ARFI displacement images (Figure 5.9). As stress levels in the tendon increased, ARFI tendon displacement decreased, though the decrease was minimal. When increasing the stress level from 0.1 MPa to 1.0 MPa, ARFI tendon displacement decreased by only 0.24 μm for the full-frame approach and 0.58 μm for the multi-foci approach. Multi-foci ARFI imaging resulted in significantly more tendon displacement compared to full-frame ARFI imaging (Figure 5.10) ($p < 0.05$). Across both tendon injury states and all stress levels tested, multi-foci ARFI imaging was 2.7 times larger than the ARFI displacement measured using full-frame ARFI imaging (multi-foci = 1.6 ± 0.4 μm and full-frame = 0.6 ± 0.3 μm, $p < 0.001$).

The linear region modulus for the 4 un-damaged tendons was 347.0 ± 100.7 MPa. Following the mechanical testing damage protocol, the modulus of the linear region dropped by 43% (damaged tendons = 195.4 ± 47.8 MPa). The difference of ARFI tendon displacement between un-damaged and damaged tendons when using the multi-foci approach was < 0.24 μm. For the full-frame approach, the difference in ARFI tendon displacement between un-damaged and damaged tendons across all stress levels was < 0.1 μm (Figure 5.10). No significant difference in ARFI displacement was found between injury states ($p > 0.05$).

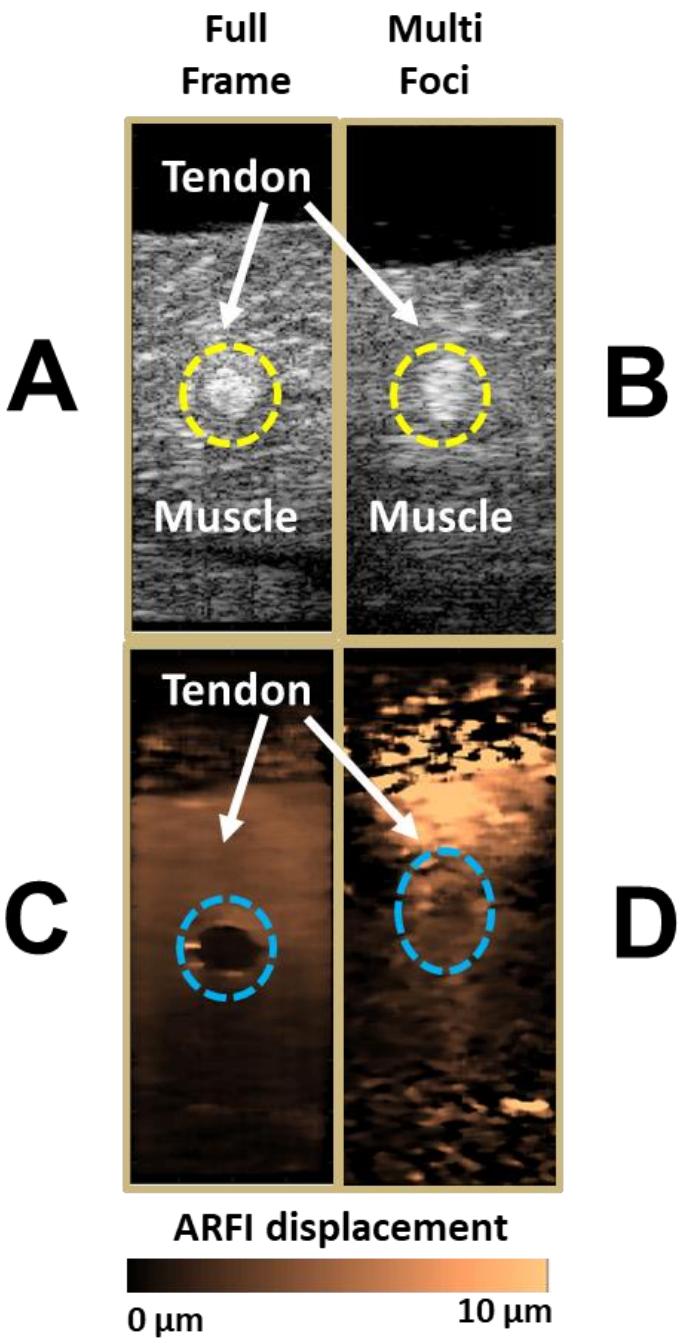

Figure 5.9: Full-Frame and Multi-Foci ARFI imaging of tendon wrapped with muscle. A & B are B-mode images using the Full-Frame and Multi-Foci technique respectively. C) Full-Frame: less ARFI displacement within stiff tendon than surrounding softer muscle. D) Multi-Foci: higher ARFI displacement, but worse image resolution.

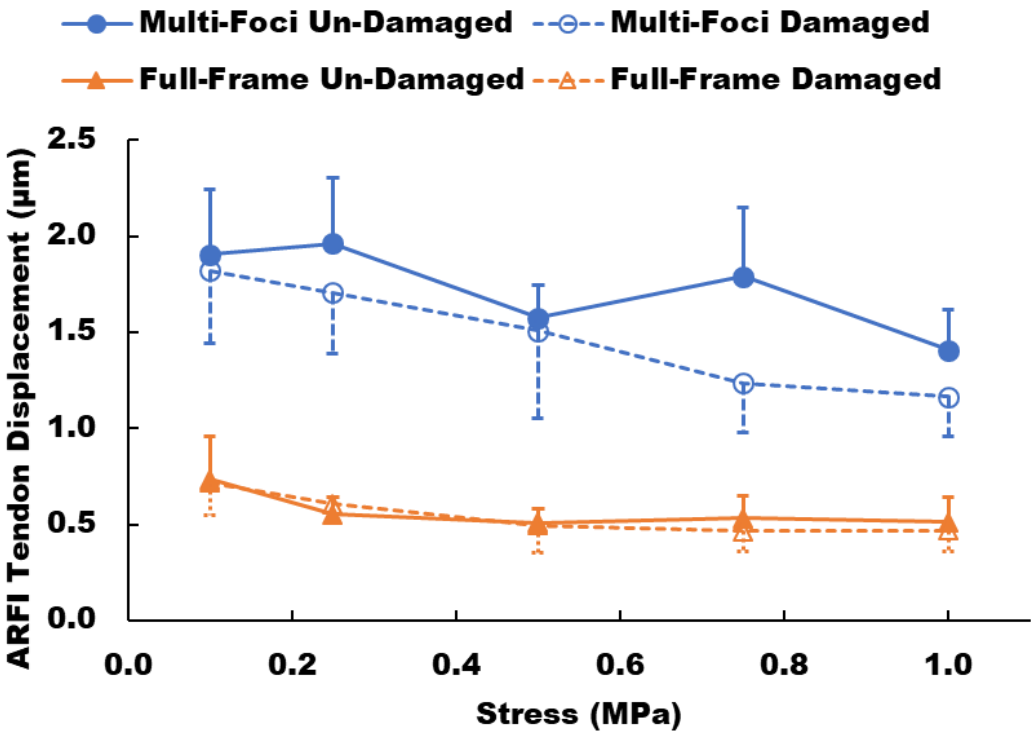

Figure 5.10: Full-Frame and Multi-Foci ARFI tendon displacement data (Avg ± SD).

5.2.6 Methods: FEM Model of ARFI Imaging

To corroborate and compare experimental findings, a FEM model of ARFI imaging with a tissue inclusion was developed. The goal of the computational analysis was to assess the effect of tissue modulus and the magnitude of ARFI push force on ARFI displacement measurements. A 3D, rectangular solid mesh was developed using 8-noded hexahedral elements to replicate the geometric shadow of the transducer (axial = 50 mm, lateral = 38 mm, elevation = 2.2 mm) (PreView, v2.1.4, febio.org) (Figure 5.11). A circular inclusion was modeled at the center of the mesh to represent the embedded tissue. A finer mesh density was used at the axial depth where the tissue was located. Additional mesh volume was included that surrounded the geometric shadow of the transducer to minimize wave reflection back into the region of interest caused by the impulsive ARFI pushing force. In total, the mesh extended 150 mm axially and 96 mm laterally with a 2.2 mm elevation depth. The mesh representing the geometric shadow of the transducer consisted of 7995 nodes and 5120 elements while the surrounding volume mesh consisted of 17,400 nodes and 11,2000 elements. A sensitivity analysis on the mesh size was performed until the difference in peak displacement predictions was <0.1 μm.

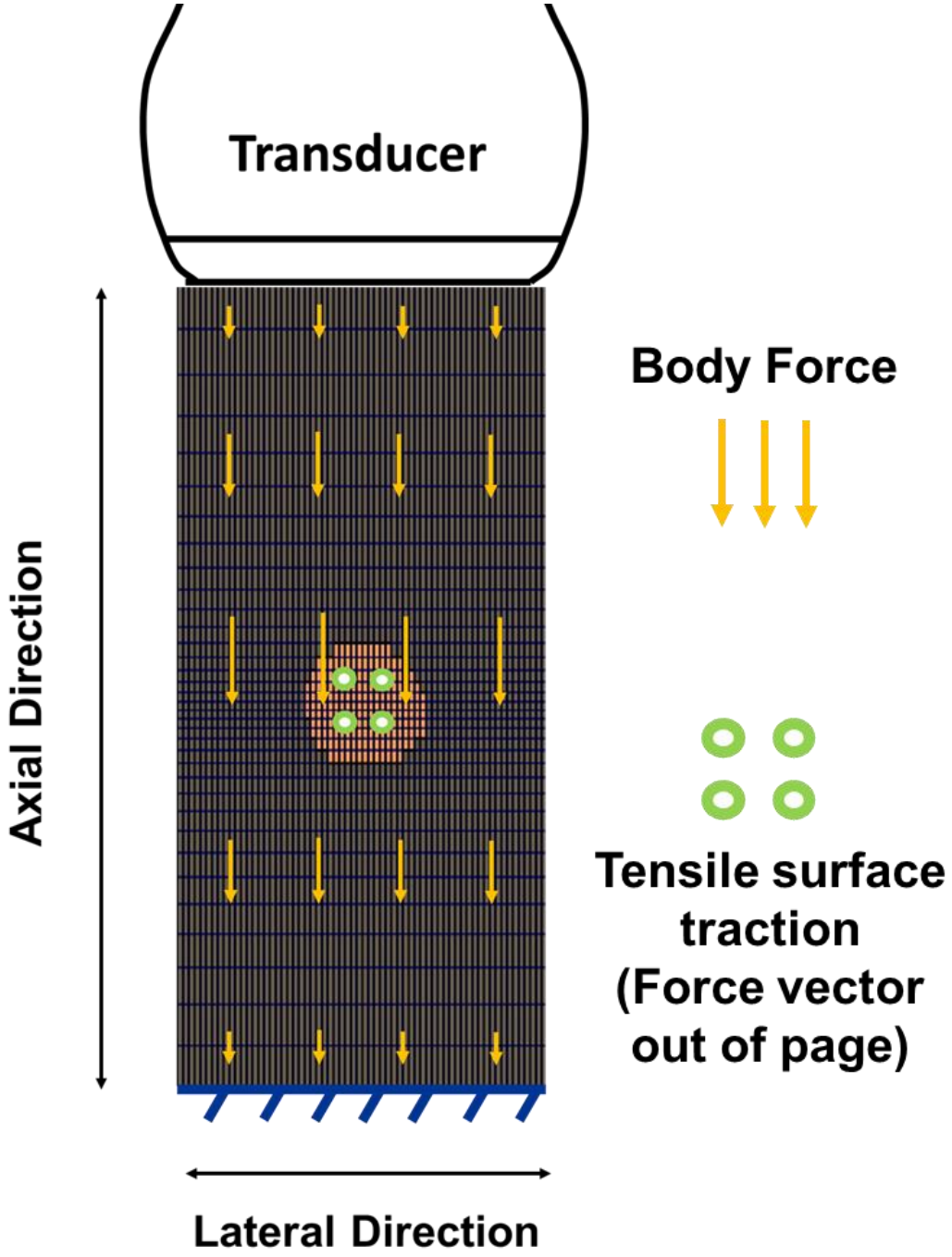

Figure 5.11: FEM Model of ARFI Imaging of the geometric shadow of the transducer. The yellow arrows represent the ARFI push, modeled as a depth dependent body force with the peak body force applied at the center of the tissue. The green circles represent the surface traction force applied to the tissue representing the 0.1MPa tensile force applied to the tissue experimentally. The bottom surface of the model was fixed in all degrees of freedom. The additional mesh volume used to mitigate the effect of wave reflection is not shown.

To minimize computational complexity and model the behavior of musculoskeletal tissues at very low loading conditions (< 0.1 N), the elements associated with the tissue were modeled as a neo-Hookean material with 2 material coefficients (v = Poisson's ratio; E = modulus). All other elements represented the surrounding gelatin and were also modeled as a neo-Hookean material. Poisson's ratio of 0.499 was used for both the tissue and the gelatin to represent near incompressibility. The modulus of the gelatin was set to 20 kPa based on the manufacturer's description of gel stiffness, unless specified otherwise. The bottom surface of the model (ie. opposite of the transducer contact) was fixed in all directions, the top surface (ie. in contact with the transducer) was fixed in the axial, and all other faces were unconstrained (Figure 5.11) (152). The surface traction load was applied to the tendon to represent the 0.1 MPa tensile loading done experimentally. Tied contact was used to model the interaction between the surfaces of the tissue and the gelatin.

The axially directed ARFI push force was modeled as a depth dependent body force with a gaussian distribution (154, 155),

$$\vec{F} = F_0(t)e^{\left(\frac{-y^2}{2\sigma^2}\right)} \quad \textbf{(5-1)}$$

where $F_0(t)$ is a time dependent force amplitude, σ = 1mm, and y represents the axial position. The model geometry was created so that the peak body force occurred at 25 mm axial depth (ie. elevation focus of transducer and centroid of tissue inclusion). The body force was applied as a step function and only during the excitation interval $0 < t < 192$ μs to mimic experimental ARFI methods. For reference, the ARFI push force magnitude based on our experimental conditions was 54 dynes/mm^3.

The main output parameter was the peak displacement of the node positioned at the centroid of the tissue inclusion. The effect of tissue modulus on ARFI displacement was investigated by changing material coefficient E of the tissue (range: 25 kPa – 1000 MPa). The effect of the ARFI push force magnitude was investigated by changing the peak magnitude of body force (range: 1-1000 dyne/mm^3). All simulations were performed using FEBio (v2.9.1, Musculoskeletal Research Laboratories, University of Utah, febio.org) and post-processing using PostView (v2.4.4, febio.org).

5.2.7 Results: FEM Model of ARFI Imaging

As tissue modulus increased, tissue ARFI displacement decreased (Table 5.3). The magnitude of the ARFI displacement for all cases was on the order of microns. Large differences in ARFI displacement were seen for tissues with a low modulus compared to tissues with high moduli. The ARFI displacement for a tissue with a modulus of 250 kPa was 6.13 μm smaller than a tissue with a modulus of 25 kPa (ie. overall decrease of 57%). For tissues with a higher modulus, ARFI displacement reached a plateau. The percent change in ARFI displacement from a tissue modulus of 10 MPa to 1000 MPa was only 1.3% (< 0.1 μm). Increasing the magnitude of the ARFI push by an order of magnitude, increases the resulting ARFI displacement by an order of magnitude regardless of the modulus of a tissue. For a 1000 dynes/mm^3 ARFI push, the difference in ARFI displacement for a tissue with a modulus of 100 MPa to 1000 MPa was < 0.1 μm (Table 5.3).

Table 5.3: Changes in tissue ARFI displacement based on tissue modulus and ARFI push magnitude

Tissue "E"	Tissue ARFI Displacement (10 dynes/mm^3 push)	Tissue ARFI Displacement (100 dynes/mm^3 push)
25 kPa	14.22 μm	142.23 μm
250 kPa	8.09 μm	80.96 μm
750 kPa	7.09 μm	70.98 μm
1 MPa	6.93 μm	69.33 μm
10 MPa	6.42 μm	64.24 μm
100 MPa	6.35 μm	63.56 μm
1000 MPa	6.34 μm	63.49 μm

5.2.8 Discussion

In general, higher stiffness tissues resulted in lower ARFI displacement. However, the change in ARFI displacement plateaus for high stiffness tissues. The difference in ARFI displacement was less than 1 μm for tissue with a modulus of 10 MPa and 1000 MPa, compared to over a 6 μm difference in ARFI displacement between a tissue with a modulus of 25 and 250 kPa. Experimentally, tissue type had a significant effect on normalized ARFI displacement, but minimal differences were observed for capsule and tendons (< 0.1). From tensile testing, almost an order of magnitude difference existed in the experimentally calculated modulus of the linear region for the tissues tested (muscle: <10 MPa, capsule: >10 but <100 MPa and tendon: >100 MPa). Similar statistically significant differences were also seen for the modulus of the toe region, with tendon and capsule being much stiffer than muscle. Furthermore, despite damaging the tendon which resulted in a change in the tendon modulus by over 40%, no significant differences in ARFI displacement were found. Thus, from the experimental tests, using ARFI imaging for high stiffness musculoskeletal tissues (eg. tendons) will be challenging, especially when discerning healthy and injured tendons.

The computational findings corroborate the experimental findings that ARFI imaging may not be able to differentiate between healthy and injured tendons. The modulus of most musculoskeletal tissues is greater than 1 megapascal and can reach up to hundreds of megapascals whereas tissues that are generally used for ARFI imaging (eg. breast, liver, nerves etc.) are on the order of kilopascals (130, 221-223, 231). From the model simulations, the difference between a tissue with a modulus of 1 MPa and 1000 MPa was <1 μm. Furthermore, the greatest change in ARFI displacement occurred for when the tissue modulus changed from 1 to 10 MPa (0.5 μm of that <1 μm difference). While damaged and healing tendons have been shown to have significantly

lower moduli than healthy tendons, the magnitude of the modulus is still relatively high (>10 MPa) (189, 232). Conversely, for low stiffness tissues, the difference in ARFI displacement for a tissue with a modulus of 25 kPa and 1 MPa was >7 μm. Large differences in ARFI tissue displacement for low stiffness tissues (kPa) and small differences in ARFI tissue displacement (>1 MPa), despite large differences in the modulus suggests that a larger ARFI push may be needed for highly stiff musculoskeletal tissues.

Current transducers available for ARFI imaging are limited on the magnitude of ARFI push that can be generated. The full-frame approach is the technique currently used for ARFI imaging. Using the full-frame approach, the effect of increasing the ARFI push force could not be performed experimentally without damaging our transducer (max magnitude of ARFI push = 54 dynes/mm^3). Therefore, a multi-foci approach was utilized to assess the effect of increasing the ARFI push force magnitude experimentally (227). Rather than a single beam pushing one at a time across the entire lateral width of the transducer, 3 simultaneous beams were used to push at one location, allowing for an ARFI push force magnitude 3 times larger than the full-frame approach.

The results demonstrate the utility of multi-foci ARFI imaging to generate larger tendon displacement compared to full-frame ARFI imaging. Across all stress levels, multi-foci ARFI imaging generated nearly 3 times more tendon displacement, proportional to the increase of ARFI push force magnitude multi-foci. For full-frame and multi-foci ARFI imaging can displace the tendon enough to be measured, though lower than the magnitude of displacement reported for breast and abdominal tissues (up to 10 μm) (130, 219). Experimentally, despite the increase in the ARFI push force and larger magnitude of ARFI displacement, differences between the damaged and un-damaged tendons were small and within the experimental repeatability of our ARFI displacement measurements (< 0.2 μm). Furthermore, the computational results substantiate the same findings found experimentally when investigating the effect of the ARFI push force

magnitude. Similar to what was observed experimentally, tendon displacement increased proportionally to the increase in ARFI push force magnitude. However, even with an ARFI push force much higher than currently capable (1000 dynes/mm^3), minimal differences still exist in ARFI displacement for high moduli tissues (eg. <1 μm for a tissue with modulus of 10 MPa to 1000 MPa). Despite increasing the ARFI push force magnitude to levels way beyond current capabilities, the force being applied may still be too small to generate any reasonable displacement (1000 dynes = 0.01 Newtons). Other factors may also influence the magnitude of displacement including the duration of the ARFI push, tension in the tissue and the stiffness of the surrounding material. Increasing the magnitude or duration of the ARFI push force too much would compromise the safety of ultrasound use due to cavitation or temperature changes in the tissue (233).

A limitation of the FEM model used was that although musculoskeletal tissues are anisotropic, the constitutive model used for the tissues did not account for anisotropy. The rationale for choosing a Neo-Hookean model was an assumption of the tendon behavior due to the low magnitude of the ARFI push as well as reducing computational complexity. At such low loads (54 dynes = 0.00054 Newtons), the collagen fibers are not being recruited and are playing a minimal role in resisting the ARFI force. Future work will aim to control localized damage to the fiber network or ECM within the same piece of tissue an established method such as thermal ablation (234). Thus, a better understanding of the capabilities of ARFI imaging to distinguish healthy versus injured areas within the same tissue based on ARFI displacement measurements.

Some of the findings may be relevant for the challenges of using shear wave elastography with musculoskeletal tissues to quantify mechanical properties (116, 138, 140), since the ARFI push is used to generate the shear waves. For shear wave elastography, shear wave speed is the main parameter of interest that describes the shear modulus of the tissue, but this relationship is

complex and not well understood. Shear wave speed is not only influenced by the mechanical properties of the tissue, but also the tension in the tissue and the stiffness surrounding media (235-237). The advantage of ARFI imaging is that it provides local information about the tissue properties whereas shear wave elastography is best suited to providing averaged information over the entire region where shear wave speed was measured.

5.2.9 Conclusions

Through an experimental and computational approach, valuable information about the necessary improvements needed to use ARFI imaging for musculoskeletal tissues are provided. The key findings suggest that ARFI imaging may be able to differentiate between low and high stiffness musculoskeletal tissues. However, for very stiff tissues (ie. modulus >10 MPa) discerning between healthy and injured tissues of high stiffness is difficult. Increasing the ARFI push magnitude may result in larger displacements, but there are still minimal differences for high moduli tissues. While ARFI imaging has great clinical potential to assess localized mechanical properties of musculoskeletal tissues, further understanding and development of this technology is needed.

5.3 ARFI Imaging to Quantify Mechanical Properties of Tendons

5.3.1 Introduction

Acoustic Radiation Force Impulse (ARFI) imaging is an ultrasound technique that generates a localized force onto the tissue of interest at a precise location (ie. remote palpation) and the resulting tissue displacement is measured (120, 130). Information about the resulting tissue displacement may be able to predict the mechanical properties of the tissue and provide clinicians quantitative information about tissue quality/health. For example, in the case of a surgical repair procedure for a rotator cuff tear, ARFI imaging has the potential to make precise measurement of tissue quality surrounding a tear, allowing the clinician to identify the best piece of tissue to use for repair.

ARFI imaging is primarily utilized for compliant, isotropic biological tissues such as breast, liver, and arteries where tissue displacements are less than 10 μm (120-125, 130). Clinically, ARFI imaging has been used to detect the presence of tumors based on the stiffness of the tissue (219, 220). For these elastic, isotropic tissues, the magnitude of compressive displacement is assumed to be inversely proportional to the elastic modulus of the tissue (152). However, whether the clinical applications and assumptions can also be applied to musculoskeletal tissues which are much stiffer and anisotropic is still unknown. The tensile modulus in the linear region for muscles is on the order of hundreds of kilopascals to low megapascals, capsular tissue on the order of tens of megapascals, and tendons on the order of hundreds of megapascals (221-224). Breast tissue on the other hand is much more compliant, with its compressive and tensile modulus on the order of kilopascals (225, 226).

Finite element method (FEM) models simulating ARFI imaging have been developed to better understand the effect of ultrasound transducer parameters, material properties and motion tracking algorithms on ARFI displacement measurements (152, 154-156). While some FEM models have investigate the role of anisotropy on ARFI displacement, the magnitude of the modulus of the tissues and phantoms being investigated are much lower than musculoskeletal tissues (155, 156). For anisotropic tissues, in order to obtain accurate and repeatable measures of ARFI displacement, it is essential to consider the orientation of the material when imaging (156).

While other ultrasound techniques such as shear wave elastography have been used to estimate the relative stiffness of the tissue based on shear wave speed, accurate quantification of tendon mechanical properties from shear wave speed has not yet been proven (116, 127, 138). The challenges present in shear wave elastography may be relevant for ARFI imaging because the ARFI push used in ARFI imaging is used to generate the shear waves in shear wave elastography.

Overall, the utility of ARFI imaging is not fully understood for stiff, anisotropic musculoskeletal tissues. Therefore, the objective of this section of the dissertation is twofold: 1) Determine if ARFI displacement correlates to tensile and compressive mechanical properties of the tendon. 2) Predict the modulus of the tissue based on ARFI displacement data.

5.3.2 Methods: Correlating ARFI Displacement to Mechanical Properties

Nine fresh-frozen strips of long head of biceps tendon were harvested from cadaveric shoulder specimens (71.4 ± 12.6 years). All tissues were prepared for tensile testing and ARFI imaging of the tissue mid-substance. Four of the nine specimens were also prepped for indentation testing of the tissue mid-substance. Two black delrin beads (2 mm diameter) were superglued to the surface of each specimen to mark the mid-substance area. Geometric measurements of the tendon's cross-sectional area and thickness at the mid-substance was determined using a laser scanner (Next Engine, Desktop 3D Scanner, Santa Monica, CA, USA). Specimens were kept moist with physiologic saline solution to prevent dehydration during preparation and testing.

Each tendon underwent a uniaxial tensile testing protocol to determine the tensile modulus of the toe and linear region of the stress-strain curve. The ends of the tissue were clamped with custom soft tissue clamps and aligned for tensile loading in the materials testing machine (Instron, Model 5965, Norwood, MA, USA) and the strain of the tissue mid-substance was measured by tracking the delrin beads with an optical tracking system (DMAS7, Spica Technology, Kihei, HI, USA) (Figure 5.12A). The tendon was preloaded to 1N, preconditioned from 1-10N for 10 cycles and loaded to 30N (Figure 5.12B). Loading levels were chosen based on preliminary tests that determined the loads required to achieve >1% tendon mid-substance strain, but not result in tissue failure or clamp slippage.

Each tendon also underwent an indentation testing protocol to determine the indentation modulus of the tendon. For indentation testing, the tendons were placed on sandpaper to avoid tendon slippage immersed a small dish filled with physiologic saline solution (238) (Figure 5.13A). A threaded, non-porous metal rod was used as the indenter. One end of the rod was attached to a 50N load cell (Honeywell Model 31 – 50N, Charlotte, NC, USA), while the other end which

contacts the tendon was filed to be smooth and have an approximate diameter of 4 mm. The indentation test consisted of a compressive preload of 0.1N, compressive preconditioning of 0.1-1N for 10 cycles and a compressive load to 2N (Figure 5.13B). A stress-strain curve of the indentation test was created from the compressive load-indentation displacement data where the stress was calculated by dividing the force with the cross-sectional area of the indenter (12.7 mm^2) and the strain was calculated based on the indentation displacement relative to the initial thickness of the tendon.

Tensile modulus of the toe region along the long-axis of the tendon was determined by iteratively removing the last data point of the tensile test stress-strain curve from 0-1% strain until a linear regression fit of $r^2 \geq 0.99$ was achieved. The tensile modulus of the linear region was determined by iteratively removing the minimum and maximum data points of the tensile stress-strain curve from >1% strain until a linear regression fit of $r^2 \geq 0.99$ was achieved. The indentation modulus of the tendon was calculated when compressively loaded to 2N. The minimum and maximum data points of the indentation test stress-strain curve were removed until a linear regression fit of $r^2 \geq 0.99$ was achieved.

Following mechanical testing, each tissue was mounted into a custom tensioning jig immersed in a tank filled with degassed, distilled water (Figure 5.14). A Krackow stitch was applied to both ends of the tendon using a #2 suture (Ethibond*Excel, Ethicon Inc., Somerville, NJ, USA) to allow for tensile loading of the tendon in the custom tensioning jig. ARFI imaging was performed with the tendon tensioned at 1N, 5N and 15N. A bi-linear translation stage (BiSlide MN10, Velmex, Bloomfield, NY, USA; accuracy = 0.003", repeatability = 0.0002") and probe holder was used to allow for repeatable imaging of the tissue mid-substance. All ARFI testing was performed with the tendon positioned at a 25 mm axial depth and centered laterally as confirmed by a B-mode image.

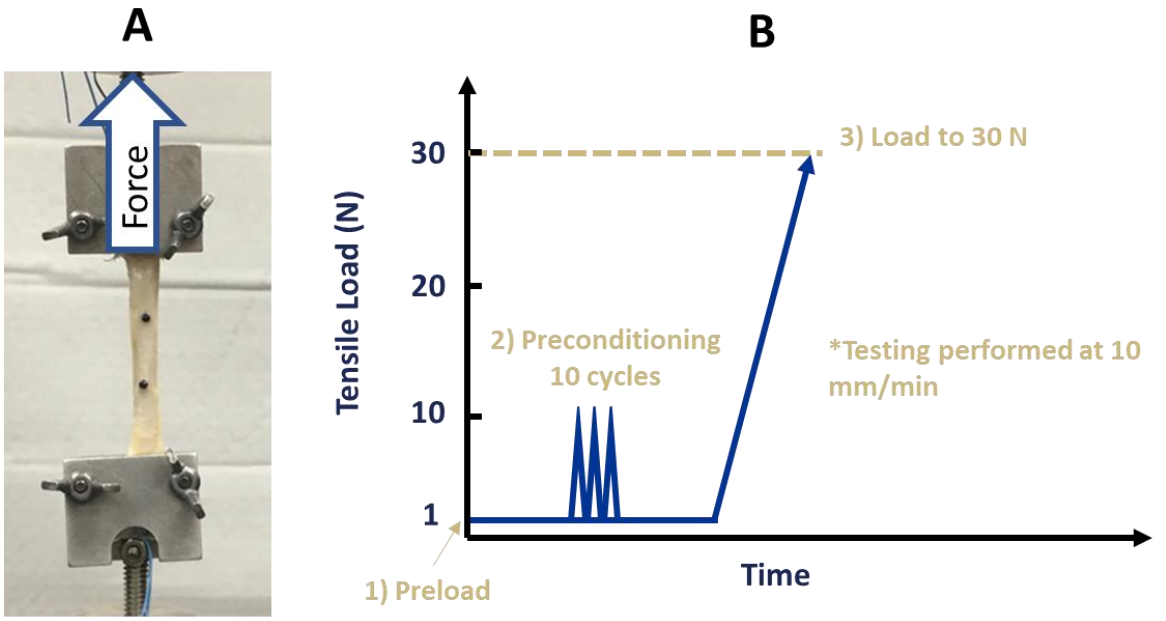

Figure 5.12: A) Tensile testing setup and B) tensile loading protocol. Tensile modulus was calculated when loaded to 30N (step 3).

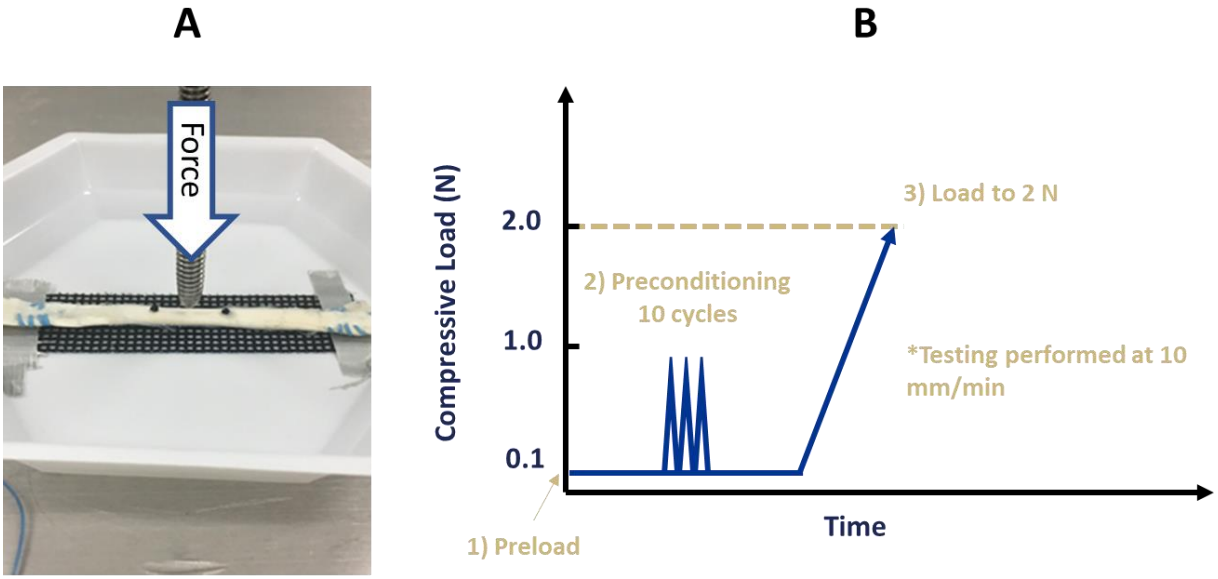

Figure 5.13: A) Indentation testing setup and B) indentation loading protocol. Indentation modulus was calculated when loaded to 2N (step 3).

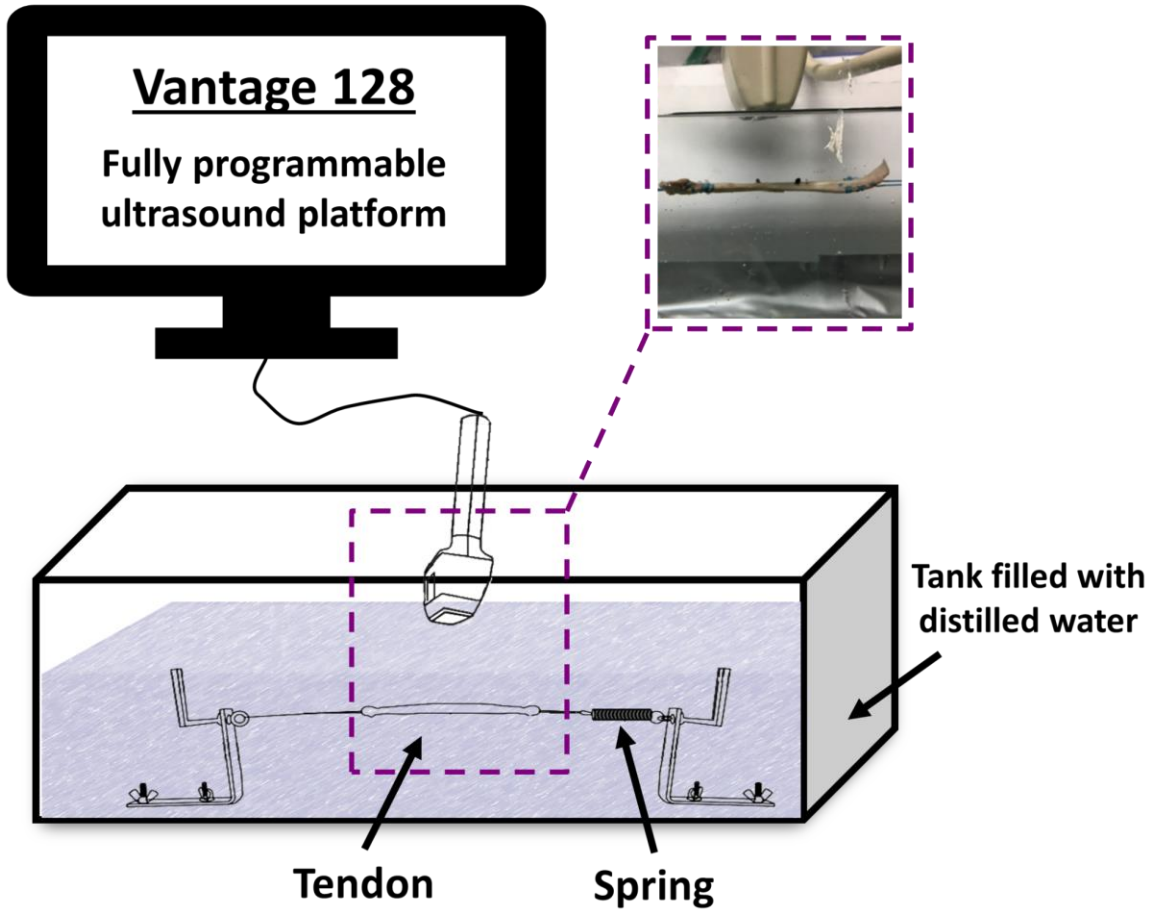

Figure 5.14: Experimental setup for ARFI imaging. The custom tensioning jig utilizes the prinicpal of "springs in series" where a spring of a known stiffness is connected in serires with the tendon of interest. By measuring the displacement of the spring, the force can be calculated using Hooke's law and therefore the force through the tendon is known. Furthermore, the stress in the tendon is known from cross-sectional area measurements from laser scanning.

A linear array transducer (ATL L7-4) connected to a research ultrasound platform (Vantage 128, Verasonics, Kirkland, WA, USA) was used to perform the entire full-frame ARFI sequence. The full-frame ARFI sequence first consists of a reference imaging. Then, an ARFI push is generated using a localized radiation force fired at an excitation voltage of 30V pulse aimed at the elevation focus of the transducer (25 mm axial depth) for 192 µs followed by a tracking pulse. The process of imaging, pushing and tracking is repeated 64 times across the entire width of the transducer. ARFI displacement due to the radiation force is calculated using the phase-based Loupas algorithm on the reference and tracking images (230). ARFI displacement of the tendon was defined by a region of interest at the center area of the tissue which was manually selected to minimize boundary effects and ensure the ARFI displacement measurement was of the tissue, not the tissue-gel interface (repeatability <0.2 µm).

A Kolmogrov-Smirnov test was performed to check the normality of the data. A repeated measures ANOVA with a post-hoc Bonferroni test was performed to evaluate the effect of tissue tension on ARFI displacement. Pearson's correlations were performed to correlate ARFI displacement with the long-axis modulus of the toe and linear region as well as the indentation modulus along the transverse axis of the tendon. Significance was set at $p < 0.05$.

5.3.3 Results: Correlating ARFI Displacement to Mechanical Properties

The tendons tested resulted in a wide range of stress-strain curves (Figure 5.15) and mechanical properties (Table 5.4). For the tensile test, when loaded to 30N of tension, a majority of the tendon mid-substances reached strain values of 1-2%. The tensile modulus of the toe region (0-0.5 MPa) was 67.3 ± 25.1 MPa, with the lowest calculated tensile modulus (40 MPa) 66% smaller than the largest tensile modulus of the toe region (117 MPa). The average tensile modulus of the linear region (131.1 MPa) was 49% larger than the average tensile modulus of the toe region. The modulus of the linear region also had a wide range of values, ranging from 89 to 196 MPa. For the indentation test, when compressive load of only 2N was applied, the compressive strain in the tendon exceeded 10% for all specimens. The highest indentation modulus of the 4 specimens (1.03 MPa) was 286% larger than the smallest indentation modulus (0.36 MPa). However, the indentation modulus for the other two specimens only differed by 0.01 MPa (0.83 and 0.84 MPa). The indentation modulus was an order of magnitude smaller than the tensile modulus.

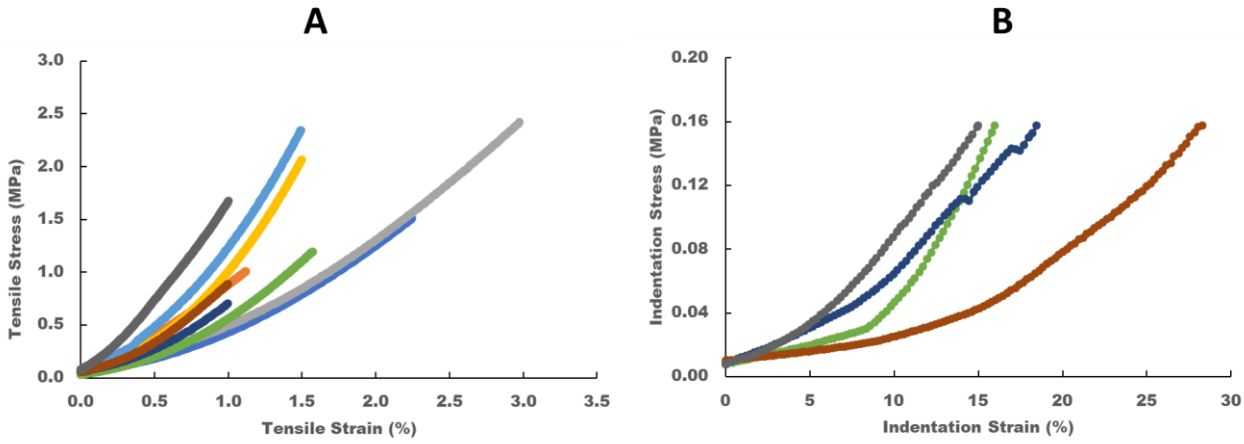

Figure 5.15: Stress-strain curves for all tendon specimens for (A) tensile loading to 30N and (B) indentation loading to 2N. Each color represents a unique tendon specimen.

Table 5.4: Tendon mechanical properties: indentation, toe and linear region modulus

	INDENTATION MODULUS (MPA)	TOE REGION MODULUS (MPA)	LINEAR REGION MODULUS (MPA)
TENDON 1	-	91.4	147.3
TENDON 2	-	40.5	89.3
TENDON 3	-	67.9	183.3
TENDON 4	-	78.1	100.5
TENDON 5	-	40.9	98.8
TENDON 6	0.84	49.8	109.3
TENDON 7	0.83	55.0	117.2
TENDON 8	0.36	65.3	137.6
TENDON 9	1.03	116.9	196.8

Qualitatively and quantitatively, with increasing tension, ARFI displacement decreased for all 9 specimens (Figure 5.16 and Figure 5.17). ARFI imaging in a tank of water resulted in noise in the surrounding water for both the B-mode images and ARFI displacement images (Figure 5.16). The noise in the B-mode image represented by the vertical white streaks are microbubbles being captured, whereas the speckled shadow around the tendon may be due to the reflection of the ultrasound waves off of the tank boundaries. In the ARFI displacement image, the displacement measurements observed in the surrounding water is due to the tracking of the microbubbles in the water and the subtle flow of the water in the tank.

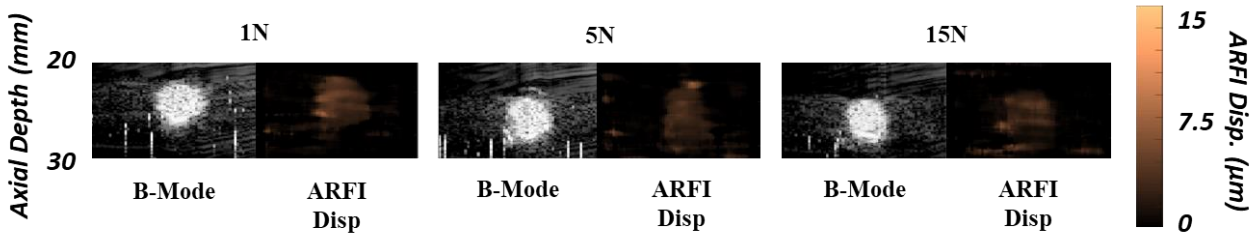

Figure 5.16: Representative B-mode and ARFI displacement images for a tendon at 1N, 5N and 15N of tension. With increasing tension, mangitude of ARFI displacement of tendon decreases.

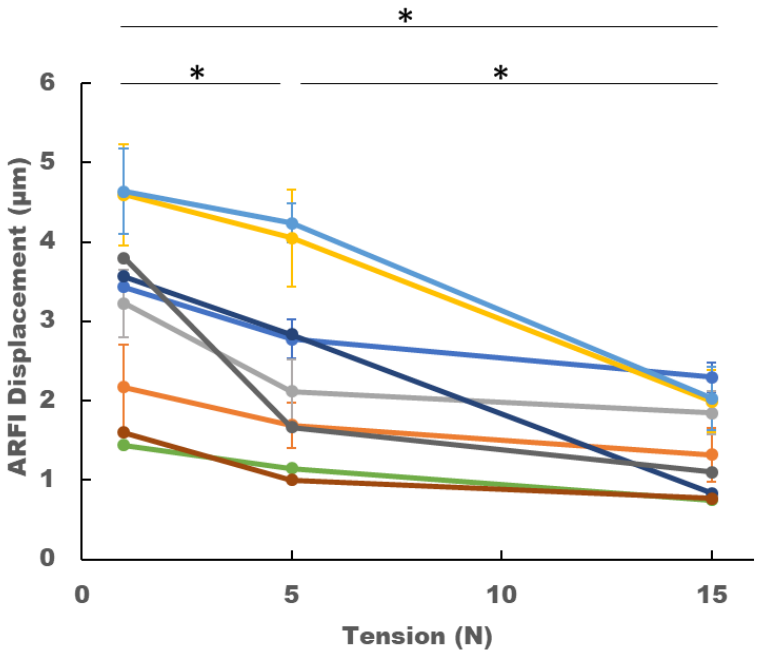

Figure 5.17: ARFI displacement for tendons tensioned at 1N, 5N and 15N. Each color represents a unique tendon specimen. Significant difference in ARFI displacement for all three tension levels.

On average, the magnitude of ARFI displacement for the tendon was >1 µm for all tension levels. Tension level had a significant effect on ARFI displacement, with all three tension levels (1N, 5N and 15N) all significantly different than each other ($p < 0.05$). ARFI displacement of the tendon at 1N (3.2 ± 1.2 µm) was 33% higher than the displacement at 5N (2.4 ± 1.2 µm), and 128% higher than at 15N (1.4 ± 0.6 µm). The range of tendon ARFI displacement at 15N of tension (1.5 µm) was 50% smaller than the range of tendon ARFI displacement at 1N and 5N of tension (3.0 µm and 3.2 µm, respectively). ARFI displacement of the tendon was not significantly correlated with any mechanical property measured (indentation modulus, toe region modulus and linear region modulus), when combining all tension levels or when analyzing each tension level separately ($p > 0.05$) (Figure 5.18 and Figure 5.19). Furthermore, both positive and negative correlations were observed, though the slope of most correlations remained flat (ie. slope of 0).

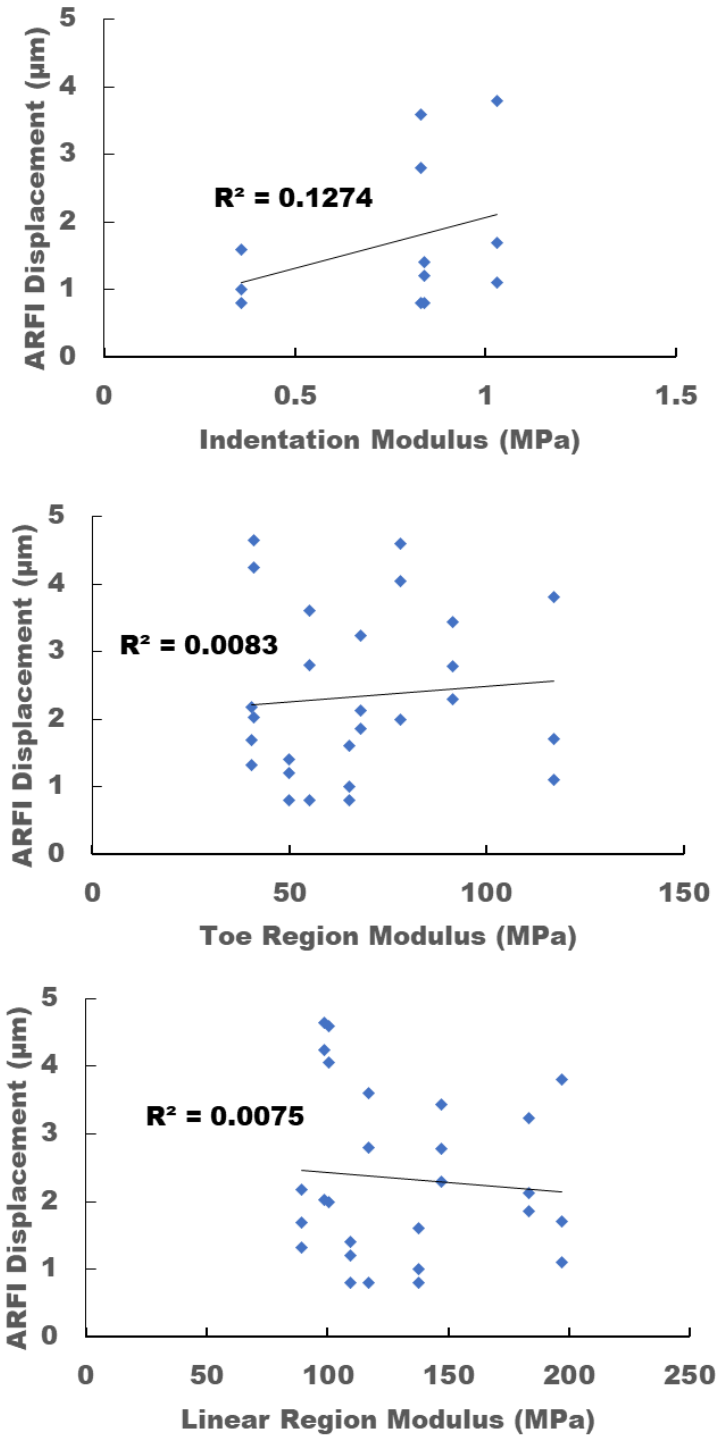

Figure 5.18: Correlation between tendon mechanical properties (indentation modulus, toe region modulus, and linear region modulus) and ARFI displacement combining all tension levels (1N, 5N and 15N). All correlations were not significant ($p > 0.05$).

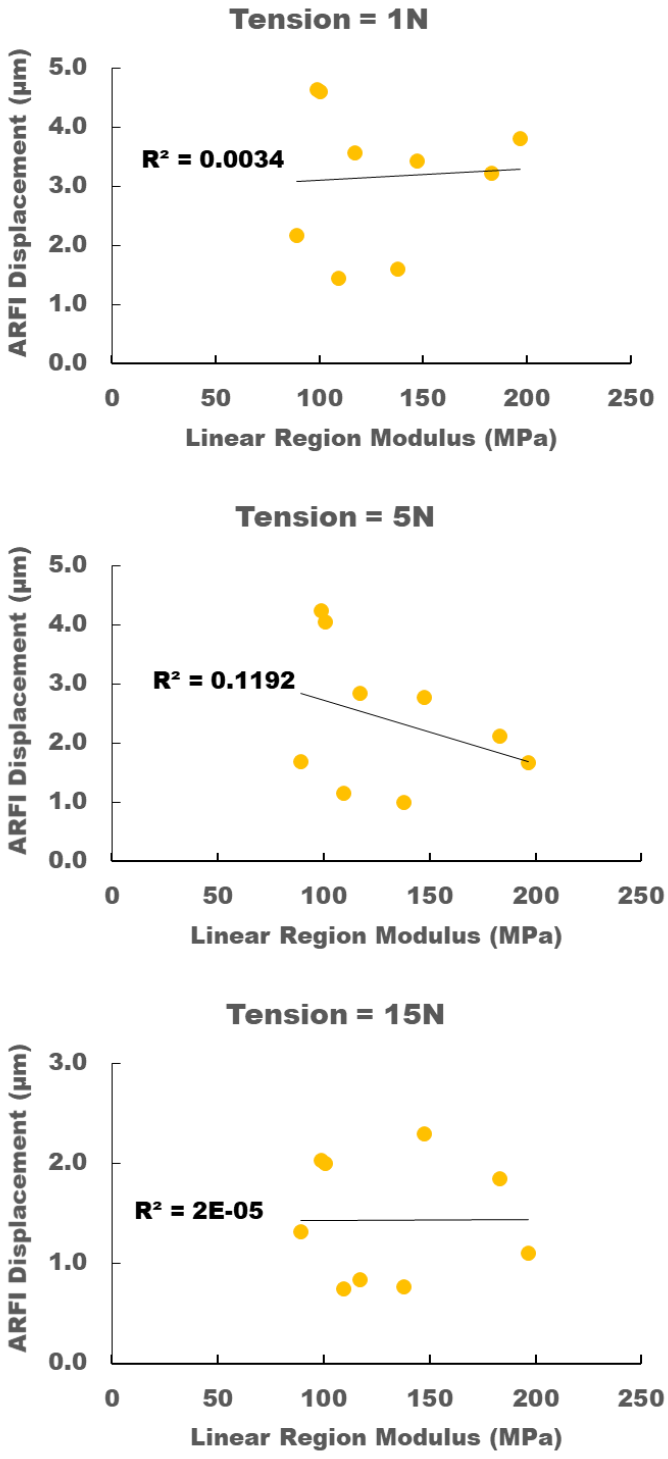

Figure 5.19: Correlation between the tensile modulus of the linear region and ARFI displacement at each tension level (1N, 5N and 15N). All correlations were insignificant ($p > 0.05$). Similar insigificant correlations were found for the modulus of the toe region and indentation modulus.

5.3.4 Discussion: Correlating ARFI Displacement to Mechanical Properties

Tendons with various degrees of degeneration were tested and account for the wide range of tensile and indentation moduli. ARFI displacements not correlating to the tensile modulus of the toe or linear region may be because tendons are transversely isotropic. Furthermore, the direction of the ARFI push is along the transverse-axis of the tendon, more closely approximating a compressive force. Indentation tests have been performed previously to provide an approximation of tendon stiffness in the transverse direction (238). However, the results show that ARFI displacement did not correlate to the indentation modulus of the tendon either. A possible explanation for the lack of the correlation may be due to the difference between an indentation force and an ARFI push force. The indentation test applies a surface force compared to a body force from an ARFI push.

The tension in the tissue was found to have a significant effect on ARFI displacement, where increasing tension in the tendon increases the stiffness along the long-axis, resulting in less displacement in the transverse-axis in response to an ARFI push. This finding supports previous findings for a comparable ultrasound technique, shear wave elastography, where increasing tension along the long-axis resulted in faster shear wave speed (235). In addition, at the highest tension level of the tendon, the range of ARFI displacement between the tendons was smallest, suggesting that differentiating between tissues of high stiffness based on ARFI displacement may be difficult. Therefore, ARFI displacement may more accurately measure the tension in the tissue rather than the actual mechanical properties of the tissue.

Clinically, quantification of the mechanical properties of the tissue is more valuable than detecting the amount of tension in the tissue, as information about mechanical properties describe the quality or health of the tissue. Specifically, prediction of the tensile modulus in tendons and

other musculoskeletal tissues is important since the primary function for most musculoskeletal tissues is in tension.

ARFI imaging in a water tank has some limitations. The decision to perform the experiment in a water tank was to allow for ARFI imaging at multiple loading conditions. Ultrasound waves pass very quickly through water (no attenuation) and may bounce off the tank boundaries and impact the ARFI displacement measurements of the tendon. However, the magnitude of the displacement from the reflections is expected to be minimal.

Overall, while a direct correlation of ARFI displacement to tendon mechanical properties was not found, ARFI displacement was clearly affected by the tension in the tissue. Thus, a singular measurement of ARFI displacement may be more representative of tendon loading than the actual mechanical properties of the tendon. When calculating tendon mechanical properties during tensile or compressive testing, the modulus is calculated from a stress-strain curve, not a singular value. Therefore, quantification of tendon mechanical properties using ARFI imaging may require understanding how the ARFI displacement values changes with increased tensile loading. However, based on preliminary tests, ARFI imaging at loading levels representative of the linear region of a tensile stress-strain curve is not feasible since the tendon becomes too stiff for the acoustic radiation force to generate any measurable displacement. Thus, experiments should be performed to attempt to quantify the tensile modulus of the linear region for tendons using ARFI imaging data collected at loading levels representative of the toe region of a tensile stress-strain curve.

5.3.5 Methods: Prediction of Linear Region Modulus

The data obtained from tensile testing and ARFI imaging of the nine cadaveric specimens in section 5.3.2 was used to accomplish the objective of this analysis. Specifically, the objective of this analysis is to predict the tensile modulus of the linear region for tendons using ARFI imaging data collected at loading levels representative of the toe region of a tensile stress-strain curve. To summarize, tensile testing of the tendon consisted of a preload to 1N, preconditioning from 1-10N for 10 cycles and loading 30N. The main outcome parameters from tensile testing was the stress-strain data. ARFI displacement of the tendon was collected with the tendon tensioned at 1N, 5N and 15N, loads corresponding to the toe region of a typical stress-strain curve for a tendon. The key outcome parameters from ARFI imaging was ARFI displacement data at each stress level (ie. stress level during ARFI imaging determined from tension in tendon and cross-sectional area measurement from laser scanning).

To predict the linear region modulus from ARFI imaging data, a novel methodology consisting of 4 steps was utilized: 1) Use ARFI tendon displacement data to predict the strain in the tendon. 2) Use predicted strain values and fit to the exponential approximation of a stress-strain curve to determine best fit model parameters. 3) Use model fit parameters to predict the modulus of the toe region. 4) Use toe region modulus to predict linear region modulus (Figure 5.20). To validate our predictions, 6 of the 9 specimens were randomly chosen to establish the relationships. The remaining 3 specimens were used to validate predictions with experimental results.

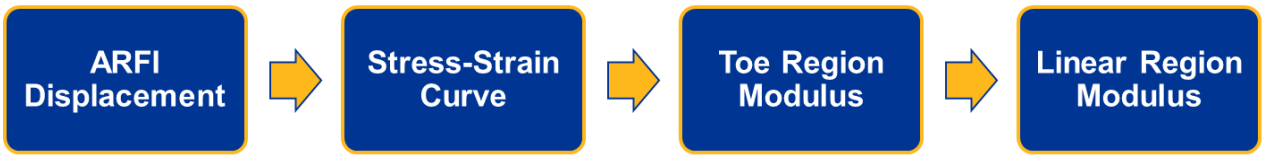

Figure 5.20: Overview of novel methodology used to predict linear region modulus of a tendon from ARFI displacement data collected at loading levels within the toe region of a stress-strain curve.

(1) Predict tendon strain from ARFI data: Using ARFI displacement data of the tendon, the parameter "ARFI strain" was calculated by describing the relationship between ARFI displacement with increasing stress:

$$\text{"ARFI Strain"} = \mathbf{1} - \frac{\boldsymbol{ARFI\ Displacement_{Applied\ Stress}}}{\boldsymbol{ARFI\ Displacement_{Lowest\ Applied\ Stress}}} \qquad \textbf{(5-2)}$$

Similar to the classic strain equation (change in length divided by original length), the "ARFI Strain" equation calculates the strain in the tendon by evaluating the change in ARFI displacement with increasing stress with respect to the ARFI displacement at the lowest applied stress. Since both ARFI imaging and the tensile test shared the same stress values, a direct relationship with "ARFI strain" and strain measured from tensile testing was made. Specifically, a linear regression was performed to determine the linear relationship between "ARFI strain" and the measured strain acquired during tensile testing.

(2 & 3) Stress-strain curve model fit of ARFI testing and relationship to toe region modulus: An exponential expression was used to represent the stress-strain (σ-ε) relationship for a tendon (239):

$$\boldsymbol{\sigma(\varepsilon) = A(e^{B\varepsilon} - 1)} \qquad \textbf{(5-3)}$$

Three data points were used to fit the exponential expression where σ represents the stress of the tendon during the 3 loading conditions during ARFI imaging and ε represents the predicted measured strain from tensile testing. A and B are constants that need to be determined, where A*B approximates the initial stiffness of a tissue (239). A linear regression was then performed to determine the relationship between parameter A*B to the modulus of the toe region calculated from tensile testing. Modulus of the toe region was determined with a linear fit of the data up until 1% strain, maximizing the number of data points such that $r^2 > 0.99$.

(4) Predict modulus of linear region: A dataset of 16 previously tested fresh-frozen cadaveric biceps tendons were utilized to determine the relationship between the modulus of the toe region modulus and the modulus of the linear region. All specimens were non-destructively tested in tension and the tendon mid-substance reached strain values >3%. The modulus of the linear region along the long-axis of the tendon was determined by iteratively removing the minimum and maximum data points of the stress-strain curve from >1% strain until a linear regression fit of $r^2 \geq 0.99$ was achieved. A linear regression was used to establish the relationship between toe and linear region modulus. Significance was set at $p < 0.05$ for all analyses.

5.3.6 Results: Prediction of Linear Region Modulus

Significant linear relationships were found for all 4 steps in the process of predicting the modulus of the linear region from ARFI data collected in the toe region ($p < 0.05$). "ARFI strain", which is measured along the transverse axis of the tendon was nearly two orders of magnitude larger than the experimentally measured strain from tensile testing. From the linear regression analyses of 6 of the 9 specimens, "ARFI Strain" was linearly related to the measured strain from tensile testing by a factor of 0.02 ($p < 0.05$, $r^2 = 0.562$) (Figure 5.21):

$$\textbf{Measured Strain from Tensile Testing} = \mathbf{0.02}(\text{ARFI Strain}) + \mathbf{0.001} \qquad \textbf{(5-4)}$$

Validation of the linear regression model using the remaining 3 specimens showed an average error of 37.0 ± 35.2% between predicted strain and measured strain. Predictions of measured strain resulted in both over and under estimation. The error for predicting strain at highest level of tensile stress in the tendon (54.6 ± 41.8%) was much higher than at lower levels of tensile stress (19.5 ± 20.7%).

All specimens were successfully fit to the exponential equation describing the stress-strain relationship of the tendon ($r^2 > 0.9$), in which parameters A and B were determined. For model fit parameter A*B, a representation of initial stiffness, all 3 specimens used for validation purposes underestimated the results from tensile testing (Table 5.5). The average magnitude of error for predicting model fit parameter A*B was 11.3 ± 10.9%.

Using 6 of the tendon specimens, prediction of the modulus of the toe region from model fit parameter A*B showed a strong and significant linear relationship ($p < 0.05$, $r^2 = 0.962$) (Figure 5.22):

$$\textbf{Toe Region Modulus} = \mathbf{1.21}(\text{Model Fit Parameter A*B}) + \mathbf{18.6} \qquad \textbf{(5-5)}$$

Modulus of the toe region was underestimated for 2 of the 3 specimens. The average error between experimental and model predictions was also higher than model fit parameter A*B, with an error 18.7 ± 10.2 %, corresponding to 14.1 ± 11.9 MPa (Table 5.5).

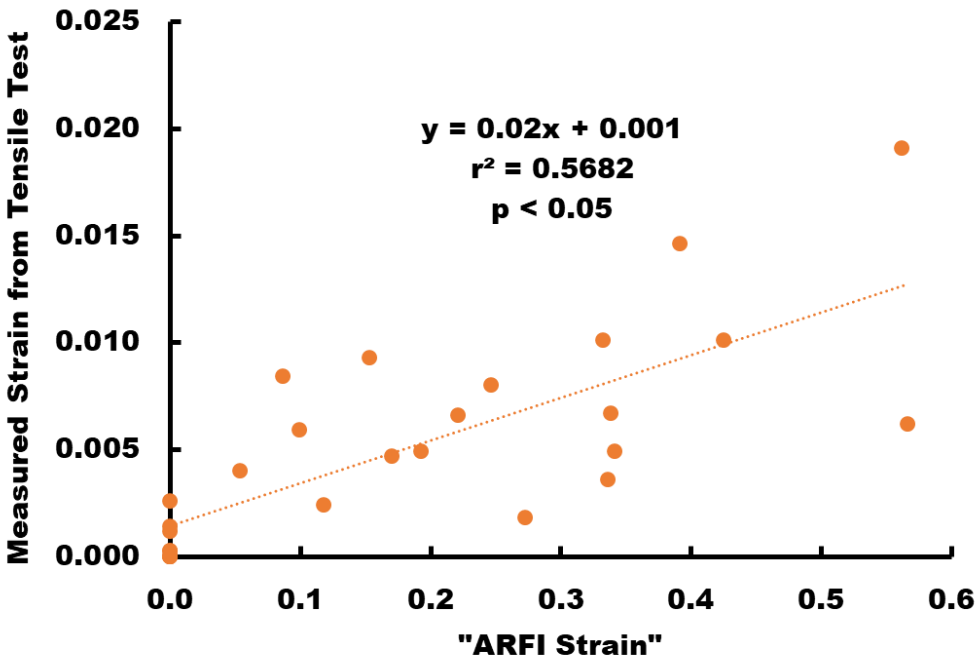

Figure 5.21: Predicting measured strain from tensile test from "ARFI Strain". Significant linear relationship found where *y* represents measured strain from tensile test and *x* represents "ARFI Strain".

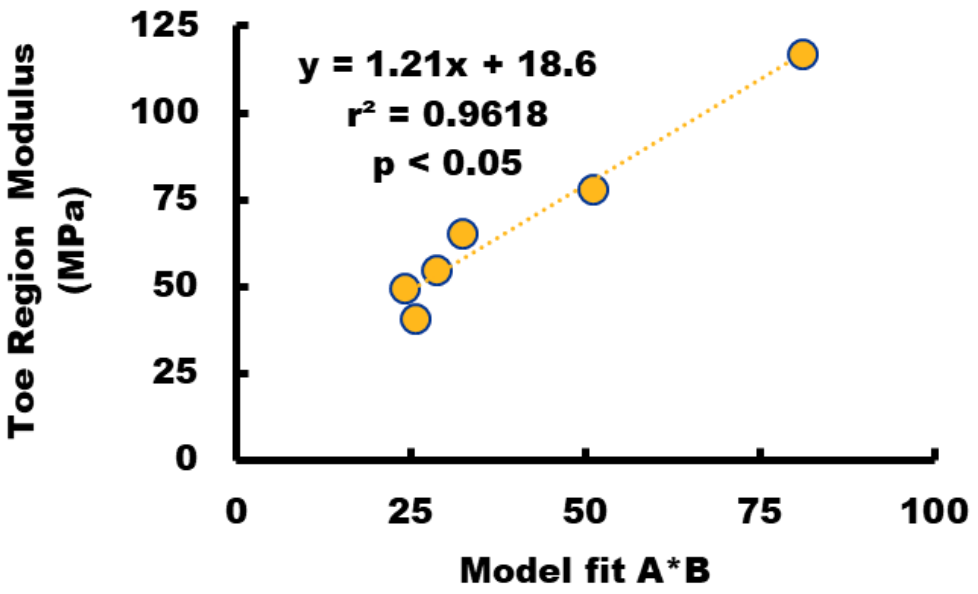

Figure 5.22: Prediction of toe region modulus from model fit parameter A*B. Significant linear relationship was found ($r^2 = 0.962$, $p < 0.05$) where y represents toe region modulus and x represents model fit parameter A*B.

Prediction of the modulus of the linear region from the modulus of the toe region also resulted in a significant strong relationship ($p < 0.05$, $r^2 = 0.872$) (Figure 5.23):

$$\textbf{Linear Region Modulus} = 4.5(\textbf{Toe Region Modulus}) - 14.7 \qquad \textbf{(5-6)}$$

The previously collected dataset used to derive the relationship between the modulus of the toe and linear region utilized tendons where the tendons were strained >3% during tensile testing. None of the 3 specimens used for validation purposes reached a tendon mid-substance strain of 3% when loaded to 30N. Prediction of the linear region modulus, greatly overestimated the

experimentally calculated values (Table 5.5) for all 3 specimens. On average, the predictions were off by 144 ± 49 MPa, corresponding to 134 ± 57%.

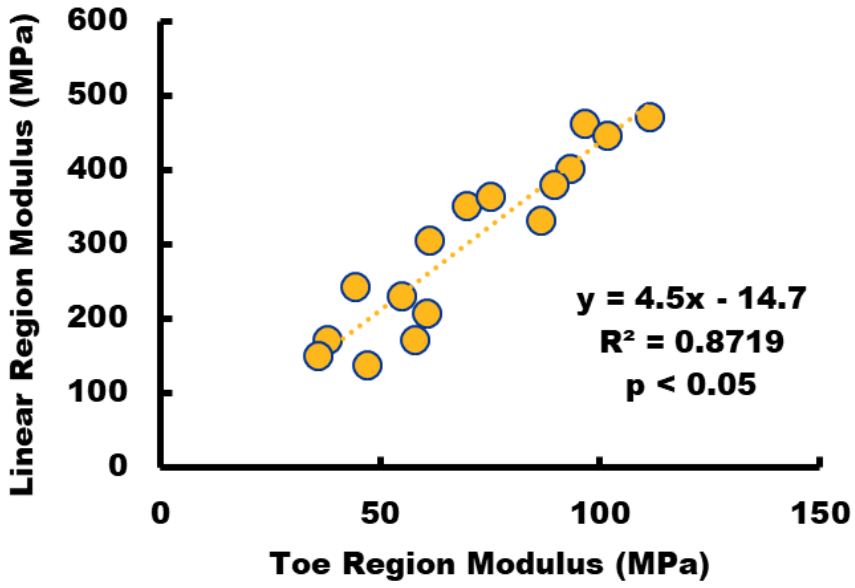

Figure 5.23: Prediction of linear region modulus from toe region modulus. Significant linear relationship was found (r^2 = 0.872, p < 0.05) where y represents linear region modulus and x represents toe region modulus.

Table 5.5: Comparison of experimental data and predictions from relationships derived from tendon ARFI displacement data

	A*B (MPa)		Toe Region Modulus (MPa)		Linear Region Modulus (MPa)	
	Predicted	*Experiment*	*Predicted*	*Experiment*	*Predicted*	*Experiment*
Tendon 1	34.8	38.8	63.7	91.4	273.9	147.3
Tendon 2	20.9	21.1	46.4	40.5	195.5	89.3
Tendon 3	39.4	50.9	69.4	78.1	299.7	100.5

5.3.7 Discussion: Prediction of Linear Region Modulus

The results demonstrate the inaccuracies of predicting the linear region modulus of tendons from ARFI imaging data collected in the toe region using only linear relationships. Final predictions of the tensile linear region modulus were off by a large margin (>100% error). Preliminary tests indicated that ARFI imaging in the linear region was not feasible because the tendon became too stiff for the acoustic radiation force to generate any measurable displacement.

Predicting tendon strain from ARFI displacement only had a moderate relationship (r^2 = 0.562), and had an average prediction error of nearly 40%. The large error is mostly likely attributed to the calculation of "ARFI Strain" to approximate tendon strain from ARFI displacement data with increasing stress. The "ARFI Strain" equation was chosen to estimate tendon strain from ARFI displacement data because it closely resembles the classic strain equation. In addition, the magnitude of the "ARFI strain" calculated values relative to tensile testing strain were physiologically reasonable. "ARFI Strain" describes the strain in the transverse direction, and studies have shown that transverse supraspinatus tendon properties can be 100-1000 times smaller than the long-axis properties (240). Therefore, a factor of 0.02 when comparing "ARFI strain", which is representative of strain in the transverse direction, to the long-axis tensile testing strain is reasonable.

Fitting the stress-strain relationship to the exponential expression using the 3 datapoints from ARFI imaging was successful for all cases ($r^2 > 0.9$). In addition, parameter A*B, which has the physical meaning of approximating the initial stiffness of the tissue (239), was closely related to the toe region modulus. This is evident by the slope of the relationship between model fit A*B and toe region modulus being close to 1 and having a high r^2 value of 0.962. Prediction of the toe

region modulus was the most accurate of all predictions, with an average magnitude of error being only 11%.

A strong relationship (r^2 = 0.872) was found predicting linear region modulus from toe region modulus, implying accurate assessment of the properties in the toe region of the tendon should provide accurate estimations of the properties of the tendon in the linear region. While the predicted values of linear region moduli were physiologically reasonable and within the range of values of previously tested tendons, the predicted linear region modulus for the 3 tendons used for validation were extremely overestimated compared to experimental results (error > 100%). However, this may be due to the differences between the dataset used to define the relationship between toe region modulus and linear region modulus, and the tendons used for validation. The tendons used to establish the relationship all achieved mid-substance strain >3%, while the tendons used for validation did not. Calculation of the toe region (<1% strain) and linear region (>1% strain) modulus were the same for both datasets. Since the 3 tendons used for validation purposed did not reach a strain value of 3%, the tendon may still be recruiting collagen fibers and the tendon behavior after 1% strain was more representative of the transition zone from the toe region into the linear region of a stress-strain curve. Thus, the experimentally calculated modulus of the linear region may be underestimated.

Overall, prediction of the tensile modulus of the linear region for tendons using ARFI imaging data collected at loading levels representative of the toe region of a tensile stress-strain curve was unsuccessful. Thus, an alternative strategy that should be investigated to understand the relationship between ARFI displacement and the mechanical properties would be to utilize the inverse finite element method (FEM). Using the inverse FEM approach, the optimal mechanical properties of the tendon to match the experimental data of ARFI displacement can be determined.

5.3.8 Methods: Inverse FEM

15 fresh-frozen strips of tissues (5 pectoralis major muscle, 5 glenohumeral capsule, 5 biceps tendon) with a length of at least 10 cm were harvested from 8 cadaveric shoulder specimens (60.9 ± 4.9 years). All tissues were prepared for tensile testing and ARFI imaging of the tissue mid-substance. Two delrin beads (2 mm diameter) were superglued to the surface of each specimen to mark the mid-substance area. The cross-sectional area of the tissue mid-substance was determined using a laser scanner (Next Engine, Desktop 3D Scanner, Santa Monica, CA, USA). Specimens were kept moistened with physiologic saline solution to prevent dehydration during preparation and testing.

Each tissue underwent a uniaxial tensile testing protocol to determine the modulus of the toe and linear region. The ends of the tissue were clamped with custom soft tissue clamps and aligned for tensile loading in the materials testing machine (Instron, Model 5965, Norwood, MA, USA) and the strain of the tissue mid-substance was measured by tracking the delrin beads with an optical tracking system (DMAS7, Spica Technology, Kihei, HI, USA). The tissue was preloaded (tendon & capsule = 1N, muscle = 0.2N), preconditioned for 10 cycles (tendon = 1-10N, capsule = 1-5N, muscle = 0.2-2N) and then loaded (tendon = 100N, capsule = 50N, muscle = 5N). Loading levels were chosen based on preliminary tests that determined the loads required to reach the linear region of a stress-strain curve, but not result in tissue failure or clamp slippage. Modulus of the toe region was determined by iteratively removing the first and last data points of the stress-strain curve from 0-1% strain until a linear regression fit of $r^2 \geq 0.99$ was achieved.

Following tensile testing, each tissue was mounted into a custom tensioning jig and tensioned to 0.1MPa. A Krackow stitch was applied to both ends of the tendon using a #2 suture (Ethibond*Excel, Ethicon Inc., Somerville, NJ, USA) to allow for tensile loading of the tendon in

the custom tensioning jig. Once appropriately tensioned, the tissue was embedded into a gelatin mixture. The gelatin mixture consisted of 1 liter of water, 5% concentration of gelatin from porcine skin (G2500, Sigma Aldrich, St. Louis, MO, USA) and 1% concentration of cellulose (S3504, Sigma Aldrich, St. Louis, MO, USA). A bi-linear translation stage (BiSlide MN10, Velmex, Bloomfield, NY, USA; accuracy = 0.003", repeatability = 0.0002") and probe holder was used to allow for repeatable imaging of the tissue mid-substance. All ARFI testing was performed with the gel temperature at 20°C confirmed by a digital infrared thermometer and the tissue positioned at a 25 mm axial depth and centered laterally as confirmed by a B-mode image (Figure 5.6).

A linear array transducer (ATL L7-4) connected to a research ultrasound platform (Vantage 128, Verasonics, Kirkland, WA, USA) was used to perform the entire full-frame ARFI sequence. The full-frame ARFI sequence first consists of a reference imaging pulse focused at the elevation focus of the transducer (25 mm axial depth). Then, an ARFI push is generated using a localized radiation force fired at an excitation voltage of 30V (push duration = 192 μs). After the ARFI push, a tracking pulse is fired (ie. imaging pulse identical to the reference imaging pulse). The process of imaging, pushing and tracking is repeated 64 times across the entire width of the transducer. ARFI displacement due to the radiation force is calculated using the phase-based Loupas algorithm on the reference and tracking images (230).

FEM Model Methods

A FEM model simulating ARFI imaging of a tissue inclusion surrounded by a homogenous gelatin phantom was developed. The goal of the computational analysis was to assess the effect of tissue modulus on ARFI tissue displacement measurements and predict tissue modulus based on experimental ARFI tissue displacement measurements. A 3D, rectangular solid mesh was developed using 8-noded hexahedral elements to replicate the geometric shadow of the transducer (axial = 50 mm, lateral = 38 mm, elevation = 2.2 mm) (PreView, v2.1.4, febio.org) (Figure 5.24). A circular inclusion was modeled at the center of the mesh to represent the embedded tissue. A finer mesh density was used at the axial depth where the tissue was located. Additional mesh volume was included that surrounded the geometric shadow of the transducer to minimize wave reflection back into the region of interest caused by the impulsive ARFI pushing force. In total, the mesh extended 150 mm axially and 96 mm laterally with a 2.2 mm elevation thickness. A sensitivity analysis on the mesh size was performed by increasing the size of the elements until the change in peak displacement predictions was <0.1 μm. The mesh representing the geometric shadow of the transducer consisted of 7995 nodes and 5120 elements while the surrounding volume mesh consisted of 17,400 nodes and 11,2000 elements.

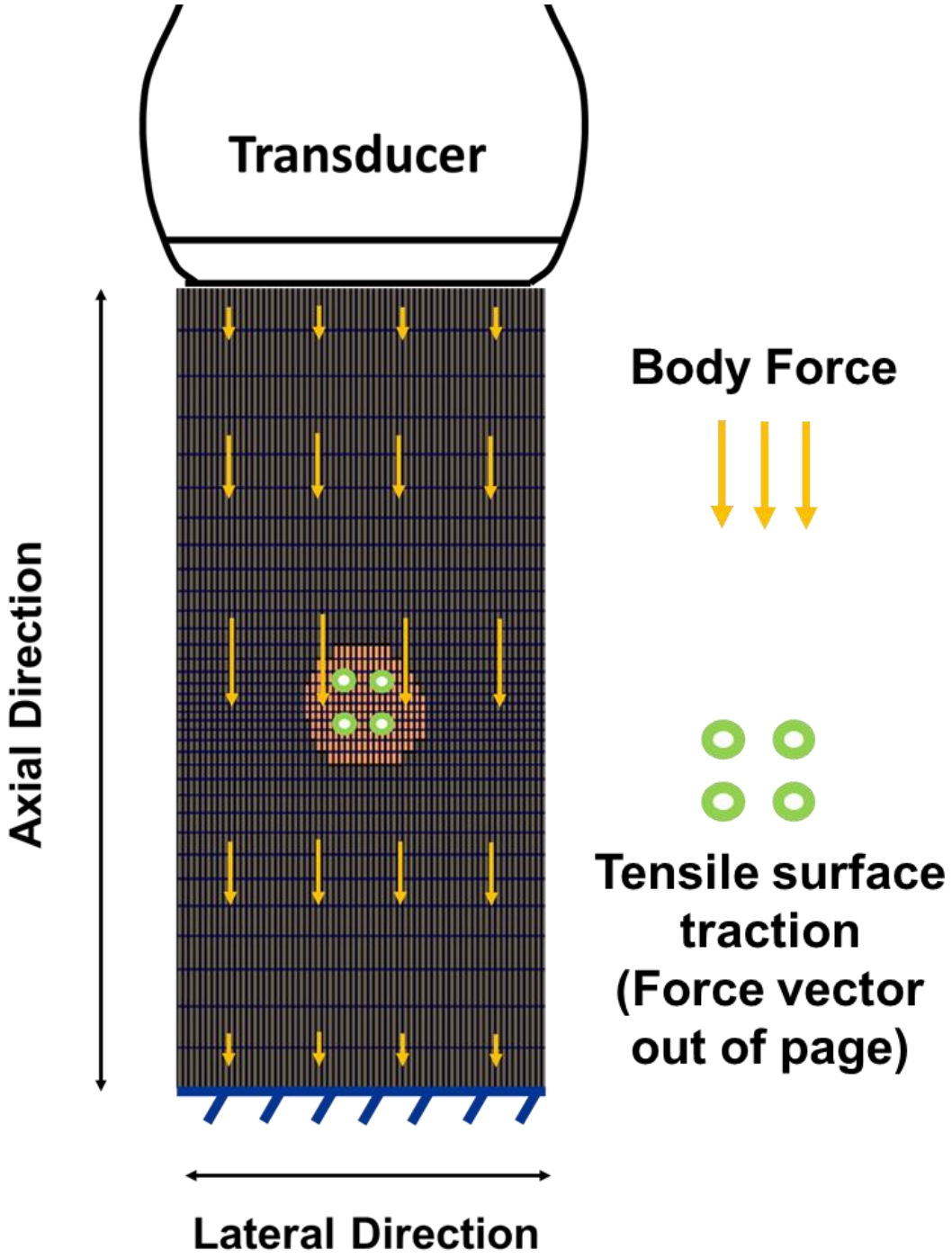

Figure 5.24: FEM Model of ARFI Imaging of the geometric shadow of the transducer. The yellow arrows represent the ARFI push, modeled as a depth dependent body force with the peak body force applied at the center of the tissue. The green circles represent the surface traction force applied to the tissue representing the 0.1MPa tensile force applied to the tissue experimentally. The bottom surface of the model was fixed in all degrees of freedom. The additional mesh volume used to mitigate the effect of wave reflection is not shown.

To minimize computational complexity and model the behavior of musculoskeletal tissues at low loading conditions (< 0.1 N), the elements associated with the tissue were modeled as a neo-Hookean material with 2 material coefficients (v = Poisson's ratio; E = modulus). Despite the anisotropy of tendons due to the alignment of collagen fibers, at such low loads, collagen fibers are not being recruited. Therefore, the tendon is most likely to behave like an isotropic material, supporting the choice of a neo-Hookean material model for this simulation. All other elements represented the gelatin and were also modeled as a neo-Hookean material. Poisson's ratio of 0.499 was used for both the tissue and the gelatin to represent near incompressibility.

The bottom surface of the model (ie. opposite of the transducer contact) was fixed in all directions, the top surface (ie. in contact with the transducer) was fixed in the axial direction, and all other faces were unconstrained (Figure 5.24) (152). The surface traction load was applied to the tendon to represent the 0.1 MPa tensile loading. The tied contact feature in FEBio was used to connect the surfaces of the tissue and gelatin together.

The axially directed ARFI push was modeled as a depth dependent body force with a gaussian distribution (154, 155):

$$\vec{F} = F_0(t)e^{\left(\frac{-y^2}{2\sigma^2}\right)} \quad \textbf{(5-7)}$$

where $F_0(t)$ is a time dependent force amplitude, σ = 1mm, and y represents the axial position. The model geometry was created so that the peak body force occurred at 25 mm axial depth (ie. elevation focus of transducer). The body force was applied as a step function and only during the excitation interval 0 < t < 192 μs to mimic experimental ARFI methods. The derived ARFI push force magnitude based on our experimental conditions was 54 dynes/mm^3 (Figure 5.25) and was used for our FEM model simulations.

$$P = \frac{V}{M} \Rightarrow I = \frac{P^2}{2\rho c} \Rightarrow F = \frac{2\alpha I}{c}$$

- **P = pressure**
- **V = measured voltage from 30V of excitation = 1.64 V**
- **M = hydrophone sensitivity = 0.223 V/MPa**
- **I = intensity**
- **c = speed of sound = 1540 m/s**
- **ρ = density = 1050 kg/m^3**
- **α = absorption coefficient = 25 Np/m**
- **F = body force (dynes/mm^3)**

Figure 5.25: Derivation of ARFI push force magnitude. First, pressure was determined from an experiment using a calibrated hydrophone. Knowing pressure, intensity could be determined and knowing intensity, the body force could be calculated. The derived body force was 54 dynes/mm^3. All constants were based on literature (241).

An inverse finite element optimization analysis built in FEBio (Levenberg-Marquardt) was performed by minimizing the objective function to determine the optimal material coefficient (E) for both the surrounding gel and tissue needed to match the experimental ARFI displacement data. Specifically, the data was fit based on the change of nodal position in the axial direction from the beginning of an ARFI push to the end of the ARFI push.

For the surrounding gel, an initial guess of 20 kPa was used based on the manufacturer's description of the gel stiffness, while constraining the values to be between 1 kPa and 200 kPa to ensure a reasonable approximation of the gel stiffness. For the musculoskeletal tissues, the material coefficient was constrained to be greater than 0 and less than 1000 MPa to ensure physiologically reasonable values. A modulus greater than 1000 MPa is considered unreasonable and well outside the range of previously calculated moduli of the toe region for musculoskeletal tissues. The optimized coefficients were compared to the modulus of the toe region determined from tensile testing. All simulations were performed using FEBio (v2.9.1, Musculoskeletal Research Laboratories, University of Utah, febio.org) and post-processing using PostView (v2.4.4).

5.3.9 Results: Inverse FEM

A detailed description of the experimental results has already been described in Section 4.2.3.1. To summarize the key results relevant for the analyses of using the inverse FEM approach to predict the modulus for musculoskeletal tissues, large differences between the tendon, capsule and muscle were seen for the modulus of the toe region. The modulus of the toe region for tendons (34.9 ± 27.7 MPa) was 35 times higher than muscle (1.0 ± 1.1 MPa) and 3.8 times higher than capsular tissue (9.8 ± 6.5 MPa). Significant differences were found between muscle/tendon and muscle/capsule, but not tendon/capsule for the modulus of the toe region.

The inverse FEM analysis was successful at optimizing the gelatin modulus for all specimens (Table 5.6). Higher gelatin modulus corresponded to less gelatin displacement, where the optimized gelatin modulus values ranged from 10.6 kPa to 28.4 kPa. Optimization of the tissue modulus was successful for only 2 of the 15 tissue specimens (Table 5.7). Both successful optimization procedures for the tissue modulus were for muscle tissue. The optimized tissue modulus for both specimens were within 3 MPa of the experimentally calculated toe region modulus from tensile testing. For the other tissues, the predicted displacement of the tissue from the FEM simulations, overestimated the experimentally measured ARFI displacements, even when simulating extremely stiff tissues (E = 1000 MPa) (Table 5.7).

Table 5.6: Surrounding gel modulus (E) based on ARFI displacement using inverse FEM optimization.Higher optimized gel modulus corresponded to lower surround gel ARFI displacement.

	Surrounding Gel ARFI Displacement (μm)	Optimized Gel Modulus (E) (kPa)
Tendon 1	19.6	22.1
Tendon 2	18.0	24.5
Tendon 3	28.0	14.2
Tendon 4	15.9	28.4
Tendon 5	21.1	20.1
Capsule 1	18.6	23.5
Capsule 2	20.9	20.4
Capsule 3	36.7	10.6
Capsule 4	16.9	26.4
Capsule 5	27.3	14.6
Muscle 1	23.0	18.1
Muscle 2	19.5	22.2
Muscle 3	20.7	20.6
Muscle 4	20.3	21.1
Muscle 5	24.1	17.1

Table 5.7: Predicted toe region modulus for tissue samples based on ARFI displacement data using inverse FEM optimization. Data shown is of the successfully optimized muscle tissues and a representative example of a tendon that did not converge. Optimized toe region modulus of muscle tissues and predicted displacement from an ARFI push closely matched experimental results. For the tendon example, tissue displacement was overestimated even when assuming a very high modulus.

	Experimental Modulus of Toe Region (MPa)	FEM E (MPa)	Experimental ARFI Displacement (μm)	Predicted FEM Displacement (μm)
Muscle 3	0.3	0.3	12.6	12.9
Muscle 4	2.8	4.9	12.9	12.1
Tendon 3	67.0	1000.0	9.2	14.3

5.3.10 Discussion: Inverse FEM

The modulus of the toe region for all musculoskeletal tissues is on the order of megapascals, whereas tissues generally used for ARFI imaging are on the order of kilopascals (225, 242). Even with large differences in the modulus of the toe region between capsule and tendon tissues (10 versus 35 MPa, respectively), minimal differences in ARFI displacement existed. Thus, for tissues with moduli greater than 10 MPa, the effect of the ARFI push is minimal. Despite the high stiffness of the musculoskeletal tissues relative to the stiffness of tissues generally used for ARFI imaging, the magnitude of ARFI displacement for the musculoskeletal tissues (up to 20 μm) is similar to the magnitude of ARFI displacement in previous studies (121). The similar magnitude of displacement seen experimentally may be because the magnitude of ARFI push used (54 dynes/mm^3) was larger than previous studies (121). Furthermore, the stiffness of the surrounding structures has an effect on ultrasound parameters such as shear wave speed and ARFI displacement (235).

The inverse FEM routine was successful at optimizing the gelatin to match the experimental ARFI displacement for all specimens. The optimized moduli of the gelatin (~15-30 kPa) has a similar modulus to tissues more commonly used for ARFI imaging (eg. breast, prostate, and arteries) (120, 123, 125). Only some muscles (2 out of 5), which were the least stiff musculoskeletal tissue tested, converged to physiologically reasonable modulus values. The optimized modulus values being similar to the experimental modulus of the toe region is an encouraging finding suggesting the constitutive model is appropriate. However, the optimization procedures for the capsule and tendon tissue specimens were unable to converge, suggesting that the modulus would need to be much higher than physiologically reasonable (>1000 MPa) to match

the experimental ARFI displacement measurements. Similar to the experimental findings, for high stiffness tissues (>10 MPa), the effect of the ARFI push is minimal.

The lack of convergence for these tissues is probably due to multiple reasons. One of the main reasons may be due the inability to distinguish tissue deformation or displacement experimentally. The stiffness of surrounding structures has a major effect on ARFI displacement measurements. If a tissue is surrounded by a stiff structure, ARFI displacement may be measuring tissue deformation. However, given the same tissue but surrounded by a much softer structure, ARFI displacement may be measuring the displacement of the tissue rather than the deformation. Therefore, future work is needed to understand whether experimental measurements are of tissue deformation or displacement in order to make accurate FEM model measurements. In addition, since ARFI displacement is dependent on the tension of the tissue, accurate loading conditions of the tension in the tissue is essential. In the FEM model, a uniform surface traction was applied to the tendon to simulate the tendon in tension, but it is possible that because the tendon ends were sutured rather than clamped, non-uniform loading could have occurred. Furthermore, a different constitutive model may be needed for the stiffer tissues that better distinguish the role of the ground matrix and collagen fibers since the ARFI push is most likely being resisted by the constituents in the ground matrix rather than the collagen fibers.

5.3.11 Conclusions: Quantifying Mechanical Properties with ARFI Imaging

The results of these analyses serve as the foundation of understanding the feasibility of using ARFI imaging to quantify mechanical properties of tendons and other musculoskeletal tissues. The ability to predict the modulus of the linear region is beneficial because other ultrasound techniques such as shear wave elastography have only been able to describe relative changes in tendon stiffness (116, 137). While ARFI displacement did not directly correlate to the mechanical properties of the tissues in the transverse or longitudinal direction, the results show that ARFI displacement is impacted by the tension in the tissue. Furthermore, prediction of the tensile modulus of the linear region for tendons using ARFI imaging data collected at loading levels representative of the toe region of a tensile stress-strain curve was highly inaccurate. Experimentally and computationally, the results show that the effect of the ARFI push is minimal for high stiffness tissues (>10 MPa) due to minimal differences in ARFI displacement with increasing tissue stiffness.

Our findings are relevant for the challenges of using shear wave elastography with musculoskeletal tissues, since the ARFI push is used to generate shear waves. An additional preliminary experiment was performed to substantiate our findings by using an ultrasound system equipped with shear wave elastography (Aplio i800, Canon Medical Systems, Otawara, Tochigi, Japan) to image an anterior extensor tendon from a porcine knee. From this additional analysis, tendon was found to be too stiff and exceeded the capabilities of the ultrasound machine to obtain a measurement (i.e. >400 kPa and >12 m/s). Future work will aim to understand the role of the collagen fiber network and ground matrix on ARFI displacement measurements. Furthermore, additional work is needed to understand when ARFI displacement measurement are of the tissue deforming or displacing.

6.0 Discussion

6.1 Relationship of Findings Between Aims

The findings from Aim 1 and 2 are linked because of the possible interplay that abnormal arthrokinematics due to unbalanced force couples may have on localized remodeling of the torn supraspinatus tendon. Abnormal glenohumeral arthrokinematics is indicative of joint instability. Joint instability may be as a result of unbalanced force couples, exposing the torn supraspinatus tendon to different loading conditions. For a tendon with a tear, heterogeneous stress distributions are observed throughout various locations a supraspinatus tendon with a tear (92, 101, 104, 143, 144, 147, 151). Tendon remodeling is known to be driven by mechanical stimuli, where a fine balance of the forces in the tendon can promote functional tissue remodeling or development of tendon degeneration due to overloading or underloading (191, 198). Thus, further understanding of the possible link of arthrokinematics affecting supraspinatus tendon loading that influences tendon remodeling can help identify patients susceptible to tear propagation.

From Aim 2, remodeling at the tear tips had the greatest influence on tear propagation. More specifically, increased stiffness at the tear tips lead to more tear propagation and a lower critical load. Therefore, the findings from Aims 2 and 3 are related because Aim 3 focuses on understanding the capabilities of current ultrasound techniques to measure tendon quality and mechanical properties. The continued development of ultrasound techniques such as QUS measures and ARFI imaging is essential towards advancing the diagnoses of patients with rotator cuff tears to predict whether they are susceptible to tear propagation. For example, targeted evaluation of key areas that influence of tear propagation (eg. tear tips), or locations used for suture

placement during surgery (eg. medial edge of tear) using ultrasound can help identify which individuals will fare well in exercise therapy or surgery.

The implications of the 3 aims together allow clinicians to better understand the causes of tear propagation in order to make a more informed treatment decision (eg. exercise therapy or surgery) for their patients with a rotator cuff tear (Figure 6.1). Localized changes in tendon mechanical properties is predictive of tear propagation (Aim 2). Localized changes in tendon mechanical properties can occur due to tendon remodeling driven by mechanical stimuli. There is a fine balance that promotes functional remodeling and tendon degeneration due to overloading or underloading. Glenohumeral arthrokinematics may be driven be driven by the balance of the force couples to stabilize the joint (Aim 1). As a result, the supraspinatus tendon may experience variable loading conditions depending on the force couple balance. There is a need to continue the development of new technologies to allow clinicians to measure localized changes in tendon mechanical properties non-invasively and accurately (Aim 3).

The two key factors of interest addressed in this dissertation to better understand rotator cuff tear propagation were abnormal glenohumeral arthrokinematics and localized changes in tendon mechanical properties. The combined findings from all three aims provide clinicians pertinent information toward understanding limitations of current exercise therapy programs to address abnormal glenohumeral arthrokinematics, the possible link between arthrokinematics and tendon remodeling, relevant localized changes in tendon mechanical properties that influence tear propagation, and the capabilities of current ultrasound techniques to measure tendon quality and mechanical properties.

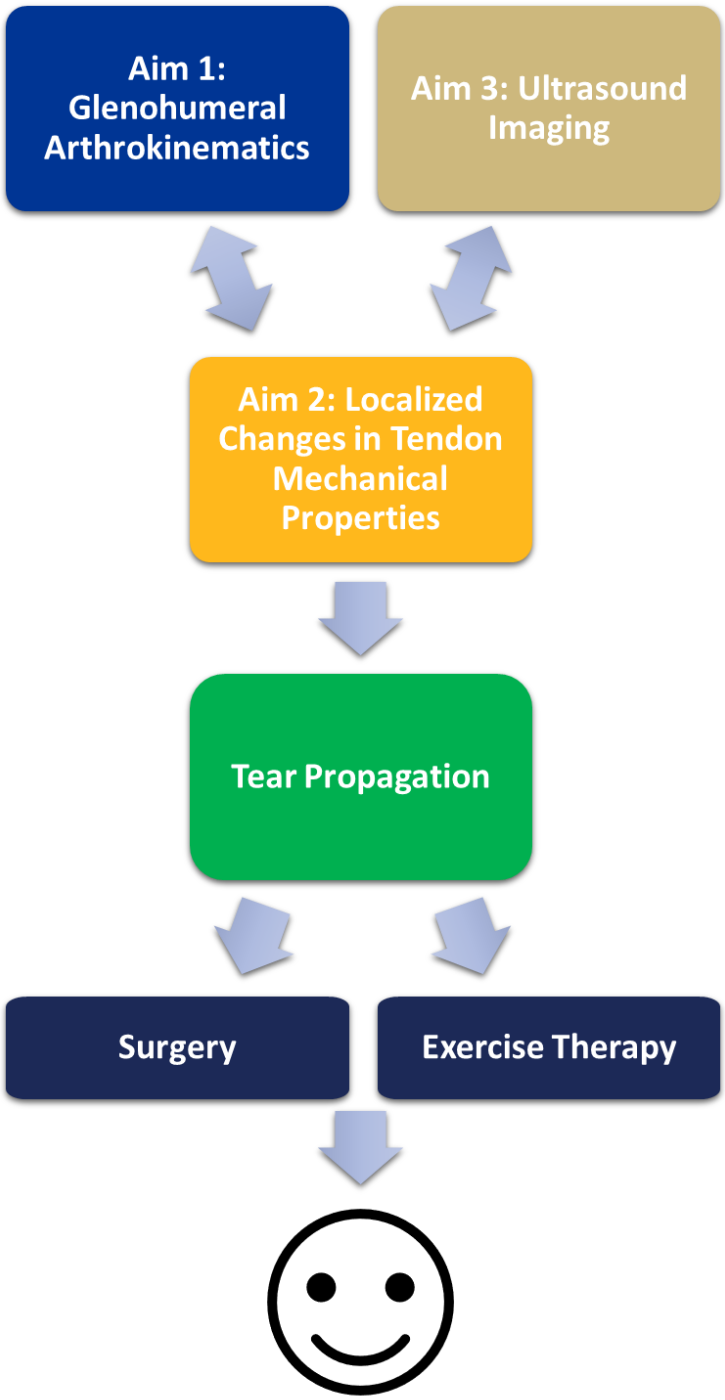

Figure 6.1: Overview of the relationship between the three Aims to better understand rotator cuff tear propagation and improve the decision making process for clinicians.

6.2 Future Directions

The work in this dissertation provides a better understanding of key biomechanical factors that influence rotator cuff tear propagation. In order to continually improve the understanding of factors behind rotator cuff tear propagation and utility of ultrasound techniques, several limitations related to the three aims should be addressed, and new avenues of research should be pursued.

From Aim 1, the effect of exercise therapy appears to be motion dependent, therefore future studies should investigate the changes in glenohumeral arthrokinematics for different arm positions that are representative of tasks common to daily living. Future studies should be conducted to obtain a better understanding on how specific exercises affect glenohumeral arthrokinematics so that exercise therapy can be adapted to emphasize the importance of improving glenohumeral arthrokinematics for multiple motions. In addition, the theory that abnormal glenohumeral arthrokinematics may be a result of unbalanced force couples, exposing the torn supraspinatus tendon to loads that increase the likelihood of tear propagation should be investigated. Alternatively, the thought that persistent abnormal arthrokinematics may injure the structures within the glenohumeral joint, thus promoting tear propagation should also be explored.

Glenohumeral arthrokinematics were only measured before and after therapy, with no knowledge about the long-term effects. Thus, future work should include long-term follow up studies to assess whether the inability to restore glenohumeral arthrokinematics would result in patients with rotator cuff tears eventually needing surgery. Furthermore, only 5 subjects were investigated, with no subject failing exercise therapy and pursuing surgery. Therefore, more subjects should be investigated in order to elucidate the factors that are associated with successful and failed non-operative treatment.

Two different ultrasound techniques were investigated in this dissertation (ie. QUS measures and ARFI Imaging). Both techniques are not without their limitations. For the quantitative ultrasound (QUS) measures, the raw values are very sensitive to the image acquired. The sensitivity of the image acquired limited our analyses to only using a transverse view of the supraspinatus tendon since the transverse view has been previously verified to be sufficiently repeatable (118). Quantitative ultrasound measures from a long-axis view of the supraspinatus tendon would be interesting to investigate in the future as long as a rigorous protocol that ensures repeatable images is established. In addition, only a small subset of factors that affect tendon quality was investigated with the H&E staining used. Future studies should correlate quantitative ultrasound measures to different factors associated with tendon quality by utilizing additional staining techniques (eg. collagen content, elastin, proteoglycans, etc.).

Despite the high clinical potential for ARFI imaging, limitations of this technique should be acknowledged in order to improve the future utility of ARFI imaging for musculoskeletal tissues. First and foremost, many of the findings for ARFI imaging are relevant and should be considered for the clinicians and other researchers that utilize shear wave elastography. A key consideration that must be accounted for before interpreting ARFI displacement in future studies is the tension in the tissue. Decreasing ARFI displacement measurements may be a result of the tension of the tissue rather than the modulus of the tissue. In addition, the minimal differences in ARFI displacement for high stiffness tissues suggest that the magnitude of the ARFI push may not be large enough to produce any reasonable displacement for stiff musculoskeletal tissues. It is possible, that something other than the modulus of the tissue impacts the magnitude of ARFI displacement. Future studies should be performed to identify the key factors that affect ARFI displacement for musculoskeletal tissues. For example, controlled localized damage/changes to

the collagen fiber network or extracellular matrix (ECM) can be investigated to understand the key constituents of the tendon that influences ARFI displacement measurements.

Prediction of tendon mechanical properties using ARFI imaging remains difficult. The work performed in Aim 2 demonstrated the feasibility of predicting the linear region modulus of tendons from ARFI imaging data collected in the toe region using only linear relationships. While the predicted modulus of the linear region was severely underestimated, future analyses should use tendons that were mechanically tested to greater than 3%. By matching the dataset used to define the relationship between toe region and linear region modulus more accurate predictions may be found.

Prediction of the modulus for musculoskeletal tissues using an inverse FEM approach was largely unsuccessful. A limitation of the ARFI imaging FEM model used was that although musculoskeletal tissues are anisotropic, the constitutive model used for the tissues did not account for anisotropy. The rationale for choosing a Neo-Hookean model was an assumption of the tendon behavior due to the low magnitude of the ARFI push as well as reducing computational complexity. At such miniscule loads (50 dynes = 0.0005 Newtons), the collagen fibers are not being recruited and are playing a minimal role in resisting the ARFI force. Alternative constitutive models (eg. transversely isotropic Mooney-Rivlin) should be investigated in the future to better understand the role of the extracellular matrix and collagen fibers in resisting the ARFI push. Differentiating the role of the extracellular matrix and collagen fibers may also allow for accurate predictions of material coefficients using the inverse FEM approach for the very stiff musculoskeletal tissues. Development of a tool such as ARFI imaging for clinicians to quantitatively and non-invasively assess tendon mechanical properties at precise locations would be especially useful based on the findings from Aim 3, where localized remodeling at the tear tips are predictive of the amount of tear propagation.

Based on the findings from Aim 3, future work should aim to identify the ideal loading condition that would promote maintaining tendon strength while minimizing the increase of tendon stiffness at a localized level. Mechanical stimulus has a large effect on the mechanical properties of musculoskeletal tissues, causing both increases and decreases in tissue stiffness (189, 201, 202). A fine balance is needed because too much loading may induce tear propagation while not enough loading may result in global degeneration throughout the entire tendon.

Currently, the subject-specific finite element model used in Aim 3 is limited because it is not representative of the general population. Therefore, a library of subject-specific models should be developed in order to account for the variability in the geometry and mechanical properties of the simulations. Furthermore, other improvements should also be considered to represent different structures and behaviors of the tendon. For example, specific properties of the tendon enthesis and rotator cable, as well as quantification of the collagen fiber organization and direction. In addition, the current model only utilized cohesive elements to simulate tear propagation in the anterior-posterior direction. Future models may consider including cohesive elements in multiple directions in order to better represent tear retraction as well as tear propagation into different tear shapes (eg. L-shaped, crescent, U-shape) (243, 244). Lastly, the model may even be useful for physical therapists in determining the exercises and loading levels a patient with a rotator cuff can undergo without inducing tear propagation.

6.3 Summary

Rotator cuff tears are extremely prevalent and have a negative impact on the quality of life for those with this injury. Billions of dollars are being spent annually in the United States alone to treat rotator cuff tears. The desire to improve the quality of life and productivity for those with rotator cuff tears in an aging population highlights the importance of being judicious in choosing the most effective treatment. Tear propagation is a key factor that may explain high failure rates of treatment as larger tears are more difficult to treat and have been associated with worse clinical outcomes.

The key finding from Aim 1 was that glenohumeral arthrokinematics for internal/external rotation with the arm at the side did not lead to any significant changes despite significant clinical improvements in terms of shoulder strength and patient-reported outcomes. The glenohumeral arthrokinematics for internal/external rotation showed increased translations compared to healthy subjects, indicating joint instability (75, 86, 245). Joint instability may be as a result of unbalanced force couples, which may expose the torn supraspinatus tendon to loads that increase the likelihood of tear propagation. While the initial clinical outcomes appear positive in terms of increased shoulder strength and improved patient reported outcomes, it is unclear whether these satisfactory clinical outcomes will remain.

Persistent abnormal arthrokinematics may injure the structures within the glenohumeral joint resulting in a larger tear and therefore increased pain and loss of shoulder function (13, 79). Furthermore, the results show that the effect of exercise therapy on glenohumeral arthrokinematics may depend on the type of motion. In a previous study that looked at glenohumeral joint arthrokinematics for coronal plane abduction, glenohumeral arthrokinematics were improved in

terms of less glenohumeral joint translation following therapy (6). Thus, exercise therapy should be adapted to emphasize the importance of improving glenohumeral arthrokinematics for multiple motions, in addition to restoring range of motion, increasing shoulder strength, and reducing pain.

Aim 2 was essential in the development and understanding of how different ultrasound techniques can be utilized for assessment of tendon quality as well as the quantification of tendon mechanical properties. The first ultrasound technique investigated utilized quantitative ultrasound (QUS) measures to assess tendon quality based on the grayscale echotexture of a traditional B-mode ultrasound image. The key finding was that quantitative ultrasound measures was correlated to measures of tendon quality as quantified through histology. The correlations found between QUS measures and histological grades of tendon quality suggest that quantitative ultrasound measures could be used to assess specific factors that affect tendon quality which can only be otherwise assessed through histology. The ability for clinicians to evaluate the changes in tendon quality is important since material properties of the tendon may be reduced as a result, making rotator cuff tear propagation more likely (185, 218). While previous studies have shown quantitative ultrasound measures correlate to clinical pathologies (117, 119, 214), no direct evidence had been provided correlating quantitative ultrasound measurements to tendon quality.

However, there are several factors that must be considered if quantitative ultrasound measures were to be used. The raw values of each quantitative ultrasound measure are very sensitive to the B-mode image acquired. A comprehensive imaging protocol is required to ensure repeatable images are acquired. Thus, direct comparisons of the raw values of each quantitative ultrasound measure to previous studies is not possible if different ultrasound examiners and ultrasound settings (eg. frequency and gain) are used. Nonetheless, the findings provide a foundation for a new methodology of quantitative ultrasound measures to be used by clinicians as

a diagnostic tool to non-invasively and quantitatively evaluate tendon quality. With further development and analyses, quantitative ultrasound measures could be useful to assess tendon quality as long as a repeatable protocol is used to obtain repeatable images, and inter-examiner variability is eliminated (117-119, 213).

The second ultrasound technique investigated for Aim 2 was ARFI imaging. ARFI imaging is an exciting ultrasound technique that works like "remote palpation", where localized radiation forces push onto the tissue and the resulting displacement is measured. The magnitude of ARFI displacement had been shown to be associated with the stiffness of the tissue, but the traditional tissues used for ARFI imaging (eg. breast, liver) are a lot more compliant than musculoskeletal tissues such as tendons. The development of ARFI imaging for tendons would advantageous because it would allow for precise measurements of tendon mechanical properties. For example, information about localized tendon mechanical properties could be helpful for surgical repair of rotator cuff tears. Re-tears following surgery typically occur at the suture-tendon interface (61, 64); therefore, surgeons could use ARFI imaging to identify the healthiest/strongest piece of tissue to place the sutures through to minimize the occurrence of the suture pulling through the tendon. Non-operatively, ARFI imaging could also be used by physical therapists to monitor the progress of tendon healing. In addition, ARFI imaging has the potential to be impactful in other settings as well, such as athletics. ARFI imaging can be used by clinicians to identify when an athlete is at an increased risk of tendon injury due to overuse and adjusting the athlete's workload (eg. deciding when to take a baseball pitcher out from the game) to proactively treat tendon overuse injuries.

The key findings from our investigation of ARFI imaging on musculoskeletal tissues were supported both experimentally and computationally. In general, stiffer tissues resulted in lower ARFI displacement. However, the change in ARFI displacement was dependent on the stiffness

of the tissue, with minimal differences in ARFI displacement observed for tissues of high stiffness (>10 MPa). Small differences in ARFI displacement despite large differences in the modulus of the tissues suggest a larger ARFI push is needed for stiff musculoskeletal tissues. ARFI displacement was found to increase proportionally to the increase in the ARFI push force magnitude. However, even with an ARFI push force much higher than what is currently capable, minimal differences (< 1μm) exist in ARFI displacement for high stiffness tissues. In addition, the magnitude of ARFI displacement was found to be dependent on the tension in the tissue, consistent with shear wave elastography, where increasing tension along the long-axis resulted in faster shear wave speed (235). Therefore, care must be taken when interpreting the magnitude of ARFI displacement or shear wave speed for shear wave elastography, since the measurements may reflect the tension in the tissue rather than the actual mechanical properties.

Direct assessment of tendon mechanical properties along the long-axis or transverse-axis based on the magnitude of ARFI displacement was not possible. However, this work demonstrated the feasibility of predicting the modulus of the linear region for tendons from ARFI imaging data collected in the toe region using only linear relationships. The ability to predict the modulus of the linear region is beneficial because other ultrasound techniques such as shear wave elastography have only been able to describe relative changes in tendon stiffness (116, 137). The development of a FEM model of ARFI imaging allowed for unique opportunity to re-create the experiments and infer the mechanical properties needed to match the experimental results using an inverse FEM approach. The inverse FEM routine was successful at optimizing the gelatin, whose moduli (~15-30 kPa) is similar to tissues more commonly used for ARFI imaging (eg. breast, prostate, and arteries) (120, 123, 125). However, for high stiffness tissues (eg. capsule and tendon), the effect of the ARFI push is minimal. The work presented in this dissertation has provided valuable

information about the limitations and necessary improvements needed to use ARFI imaging for musculoskeletal tissues. Furthermore, the findings may also explain the challenges of using shear wave elastography with musculoskeletal tissues, since the ARFI push is used to generate shear waves.

The final aim of this dissertation focused on the effect of location specific tendon remodeling on tear propagation using a validated subject-specific finite element model of a supraspinatus tendon. A key finding was that remodeling at the tear tips had the greatest influence on tear propagation. More specifically, increased stiffness at the tear tips lead to more tear propagation and a lower critical load. This finding is interesting because previous studies using the same model showed tendon degeneration across the entire tendon was associated with a greater risk of tear propagation (92). From these findings, clinicians may be more inclined to monitor the changes in tissue quality directly at the anterior/posterior tear tips, and suggest a more aggressive treatment such as surgery if the tear is believed to be susceptible to tear propagation. However, the results may not be generalizable since the results were specific to the tendon geometry, mechanical properties, boundary and loading conditions used.

By better understanding tear propagation, appropriate treatment decisions can be made to minimize the likelihood of failed treatment. Specifically, this dissertation focused on glenohumeral arthrokinematics and location specific mechanical properties. In addition, the assessment of different ultrasound techniques to be used by clinicians to evaluate tendon quality and quantify tendon mechanical properties was also investigated. Ultimately, delineating the effect of the factors influencing tear propagation will enable clinicians to better determine which patients should be treated non-operatively or be referred for immediate surgical repair.

Appendix A – Aim 1

This appendix includes additional information regarding data processing, raw data and presentations.

Appendix A.1 MATLAB Code – Interpolation of Kinematic Data

```
% Subject 4 - RIGHT Shoulder
%Import kinematic data
clear;
clc;

workbookFile = 'C:\Users\gferr\Documents\Grad School\ORL\Research in ORL\RC
Kinematics IntExtRotation\Tracking&KinematicsData\04\RC-04_Data_Rot.xlsx';
data = importData(workbookFile,'Pre1','A2:F73');
Axial = data(:,1);
SI = data(:,2);
AP = data(:,3);
SIContact = data(:,4);
APContact = data(:,5);
MinWidthStoH = data(:,6);

axi = -72:1:1;
SI_i=interp1(Axial,SI,axi);
AP_i=interp1(Axial,AP,axi);
SIContact_i=interp1(Axial,SIContact,axi);
APContact_i=interp1(Axial,APContact,axi);
AHD_i=interp1(Axial,MinWidthStoH,axi);

interpdata = zeros(length(axi),6);
interpdata(:,1) = axi.';
interpdata(:,2) = SI_i.';
interpdata(:,3) = AP_i.';
interpdata(:,4) = SIContact_i.';
interpdata(:,5) = APContact_i.';
interpdata(:,6) = AHD_i.';
xlswrite('Interpolated.xlsx',interpdata,'Pre1','A2:F75')
heading=[{'Axial'}
,{'SI Translation'},{'AP Translation'},{'SI Contact Path'},{'AP Contact
Path'},{'Minimum AHD'}];
xlswrite('Interpolated.xlsx',heading,'Pre1','A1:F1')

%%
%Import kinematic data
```

```
workbookFile = 'C:\Users\gferr\Documents\Grad School\ORL\Research in ORL\RC
Kinematics IntExtRotation\Tracking&KinematicsData\04\RC-04_Data_Rot.xlsx';
data = importData(workbookFile,'Pre2','A2:F80');
Axial = data(:,1);
SI = data(:,2);
AP = data(:,3);
SIContact = data(:,4);
APContact = data(:,5);
MinWidthStoH = data(:,6);

axi = -66:1:20;
SI_i=interp1(Axial,SI,axi);
AP_i=interp1(Axial,AP,axi);
SIContact_i=interp1(Axial,SIContact,axi);
APContact_i=interp1(Axial,APContact,axi);
AHD_i=interp1(Axial,MinWidthStoH,axi);

interpdata = zeros(length(axi),6);
interpdata(:,1) = axi.';
interpdata(:,2) = SI_i.';
interpdata(:,3) = AP_i.';
interpdata(:,4) = SIContact_i.';
interpdata(:,5) = APContact_i.';
interpdata(:,6) = AHD_i.';
xlswrite('Interpolated.xlsx',interpdata,'Pre2','A2:F88')
heading=[{'Axial'},{'SI Translation'},{'AP Translation'},{'SI Contact
Path'},{'AP Contact Path'},{'Minimum AHD'}];
xlswrite('Interpolated.xlsx',heading,'Pre2','A1:F1')

%%
%Import kinematic data
workbookFile = 'C:\Users\gferr\Documents\Grad School\ORL\Research in ORL\RC
Kinematics IntExtRotation\Tracking&KinematicsData\04\RC-04_Data_Rot.xlsx';
data = importData(workbookFile,'Pre3','A2:F83');
Axial = data(:,1);
SI = data(:,2);
AP = data(:,3);
SIContact = data(:,4);
APContact = data(:,5);
MinWidthStoH = data(:,6);

axi = -66:1:17;
SI_i=interp1(Axial,SI,axi);
AP_i=interp1(Axial,AP,axi);
SIContact_i=interp1(Axial,SIContact,axi);
APContact_i=interp1(Axial,APContact,axi);
AHD_i=interp1(Axial,MinWidthStoH,axi);

interpdata = zeros(length(axi),6);
interpdata(:,1) = axi.';
interpdata(:,2) = SI_i.';
interpdata(:,3) = AP_i.';
interpdata(:,4) = SIContact_i.';
interpdata(:,5) = APContact_i.';
interpdata(:,6) = AHD_i.';
xlswrite('Interpolated.xlsx',interpdata,'Pre3','A2:F85')
```

```
heading=[{'Axial'},{'SI Translation'},{'AP Translation'},{'SI Contact
Path'},{'AP Contact Path'},{'Minimum AHD'}];
xlswrite('Interpolated.xlsx',heading,'Pre3','A1:F1')

% %%
%Import kinematic data
workbookFile = 'C:\Users\gferr\Documents\Grad School\ORL\Research in ORL\RC
Kinematics IntExtRotation\Tracking&KinematicsData\04\RC-04_Data_Rot.xlsx';
data = importData(workbookFile,'Post1','A2:F77');
Axial = data(:,1);
SI = data(:,2);
AP = data(:,3);
SIContact = data(:,4);
APContact = data(:,5);
MinWidthStoH = data(:,6);

axi = -66:1:9;
SI_i=interp1(Axial,SI,axi);
AP_i=interp1(Axial,AP,axi);
SIContact_i=interp1(Axial,SIContact,axi);
APContact_i=interp1(Axial,APContact,axi);
AHD_i=interp1(Axial,MinWidthStoH,axi);

interpdata = zeros(length(axi),6);
interpdata(:,1) = axi.';
interpdata(:,2) = SI_i.';
interpdata(:,3) = AP_i.';
interpdata(:,4) = SIContact_i.';
interpdata(:,5) = APContact_i.';
interpdata(:,6) = AHD_i.';
xlswrite('Interpolated.xlsx',interpdata,'Post1','A2:F77')
heading=[{'Axial'},{'SI Translation'},{'AP Translation'},{'SI Contact
Path'},{'AP Contact Path'},{'Minimum AHD'}];
xlswrite('Interpolated.xlsx',heading,'Post1','A1:F1')

%%
%Import kinematic data
workbookFile = 'C:\Users\gferr\Documents\Grad School\ORL\Research in ORL\RC
Kinematics IntExtRotation\Tracking&KinematicsData\04\RC-04_Data_Rot.xlsx';
data = importData(workbookFile,'Post2','A2:F85');
Axial = data(:,1);
SI = data(:,2);
AP = data(:,3);
SIContact = data(:,4);
APContact = data(:,5);
MinWidthStoH = data(:,6);

axi = -59:1:15;
SI_i=interp1(Axial,SI,axi);
AP_i=interp1(Axial,AP,axi);
SIContact_i=interp1(Axial,SIContact,axi);
APContact_i=interp1(Axial,APContact,axi);
AHD_i=interp1(Axial,MinWidthStoH,axi);

interpdata = zeros(length(axi),6);
interpdata(:,1) = axi.';
interpdata(:,2) = SI_i.';
```

```
interpdata(:,3) = AP_i.';
interpdata(:,4) = SIContact_i.';
interpdata(:,5) = APContact_i.';
interpdata(:,6) = AHD_i.';
xlswrite('Interpolated.xlsx',interpdata,'Post2','A2:F76')
heading=[{'Axial'},{'SI Translation'},{'AP Translation'},{'SI Contact
Path'},{'AP Contact Path'},{'Minimum AHD'}];
xlswrite('Interpolated.xlsx',heading,'Post2','A1:F1')

%%
%Import kinematic data
workbookFile = 'C:\Users\gferr\Documents\Grad School\ORL\Research in ORL\RC
Kinematics IntExtRotation\Tracking&KinematicsData\04\RC-04_Data_Rot.xlsx';
data = importData(workbookFile,'Post3','A2:F81');
Axial = data(:,1);
SI = data(:,2);
AP = data(:,3);
SIContact = data(:,4);
APContact = data(:,5);
MinWidthStoH = data(:,6);

axi = -68:1:10;
SI_i=interp1(Axial,SI,axi);
AP_i=interp1(Axial,AP,axi);
SIContact_i=interp1(Axial,SIContact,axi);
APContact_i=interp1(Axial,APContact,axi);
AHD_i=interp1(Axial,MinWidthStoH,axi);

interpdata = zeros(length(axi),6);
interpdata(:,1) = axi.';
interpdata(:,2) = SI_i.';
interpdata(:,3) = AP_i.';
interpdata(:,4) = SIContact_i.';
interpdata(:,5) = APContact_i.';
interpdata(:,6) = AHD_i.';
xlswrite('Interpolated.xlsx',interpdata,'Post3','A2:F80')
heading=[{'Axial'},{'SI Translation'},{'AP Translation'},{'SI Contact
Path'},{'AP Contact Path'},{'Minimum AHD'}];
xlswrite('Interpolated.xlsx',heading,'Post3','A1:F1')
```

Appendix A.2 MATLAB Code – Euler Angle Calculations

```
%% Humerus to Lab Rotation Matrix calculation
clear;
clc;

%% Load Data
hum2lab = csvread('C:\Users\gferr\Documents\Grad School\ORL\Research in
ORL\RC Kinematics
IntExtRotation\Tracking&KinematicsData\04\post\02\HomoTransMatrices_Humerus-
to-Lab.csv',1,1);
hum2lab_time = hum2lab(:,1);
lab2scap = csvread('C:\Users\gferr\Documents\Grad School\ORL\Research in
ORL\RC Kinematics
IntExtRotation\Tracking&KinematicsData\04\post\02\HomoTransMatrices_Lab-to-
Scapula.csv',1,1);
lab2scap_time(:,1) = lab2scap(:,1);

%% Humerus to Lab Rotation Matrix calculation

for Z = 1:length(hum2lab_time)
    j = 1;
    k = 1;
    l = 1;
    m = 1;
    for i = 2:17
        if i <= 5
           rot_hum2lab(j,1) = hum2lab(Z,i);
           j = j+1;
        elseif i <= 9
           rot_hum2lab(k,2) = hum2lab(Z,i);
           k = k+1;
        elseif i <= 13
           rot_hum2lab(l,3) = hum2lab(Z,i);
           l = l+1;
        else
           rot_hum2lab(m,4) = hum2lab(Z,i);
           m = m+1;
        end
    end


    %%  Lab to Sacpula Rotation Matrix calculation
    j = 1;
    k = 1;
    l = 1;
    m = 1;
    for i = 2:17
        if i <= 5
           rot_lab2scap(j,1) = lab2scap(Z,i);
           j = j+1;
        elseif i <= 9
           rot_lab2scap(k,2) = lab2scap(Z,i);
           k = k+1;
```

```
        elseif i <= 13
            rot_lab2scap(l,3) = lab2scap(Z,i);
            l = l+1;
        else
            rot_lab2scap(m,4) = lab2scap(Z,i);
            m = m+1;
        end
    end

    %%  Humerus to Scapula Rotation Matrix

    rot_hum2scap = rot_hum2lab * rot_lab2scap;

    %% Euler Angle Decomposition for YXY rotation

    Pole(Z,1) = atan2d(rot_hum2scap(1,2),rot_hum2scap(3,2));
  % Pole(Z,3) = atand(rot_hum2scap(1,2)/rot_hum2scap(3,2));
    Elevation(Z,1) = acosd(rot_hum2scap(2,2));
    Axial(Z,1) = atan2d(-rot_hum2scap(2,1),rot_hum2scap(2,3));
  % Axial(Z,3) = atand(-rot_hum2scap(2,1)/rot_hum2scap(2,3));

end

%% Fix Axial degree values
 for g = 1:length(Axial)
    if Axial(g,1)<0
        Axial(g,1) = Axial(g,1)+180;
    else
        Axial(g,1) = Axial(g,1)-180;
    end
 end

%   for g = 1:length(Axial)
%     if Pole(g,1)<0
%         Pole(g,2) = Pole(g,1)+180;
%     else
%         Pole(g,2) = Pole(g,1)-180;
%     end
%   end

%% Right shoulder - flip pole and axial so that ER = +
Axial = -Axial;
Pole = -Pole;

%% Write EXCEL file for Euler Angles
xlswrite('EulerAngleDecomp_postrot0402.xlsx',{'Time'}x,'ANGLES','A1:A1');
xlswrite('EulerAngleDecomp_postrot0402.xlsx',{'Pole'},'ANGLES','B1:B1');
xlswrite('EulerAngleDecomp_postrot0402.xlsx',{'Elevation'},'ANGLES','C1:C1');
xlswrite('EulerAngleDecomp_postrot0402.xlsx',{'Axial'},'ANGLES','D1:D1');

xlswrite('EulerAngleDecomp_postrot0402.xlsx',lab2scap_time,'ANGLES','A2:A102'
);
xlswrite('EulerAngleDecomp_postrot0402.xlsx',Pole,'ANGLES','B2:B102');
xlswrite('EulerAngleDecomp_postrot0402.xlsx',Elevation,'ANGLES','C2:C102');
xlswrite('EulerAngleDecomp_postrot0402.xlsx',Axial,'ANGLES','D2:D102');
```

Appendix A.3 – Relevant Raw Data for Each Subject

Subject 1:

	Pre 1	Pre 2	Pre 3	Post 1	Post 2	Post 3	Shared
Max IR (°)	26	61	N/A	55	N/A	N/A	26
Max ER (°)	78	89	N/A	25	N/A	N/A	25

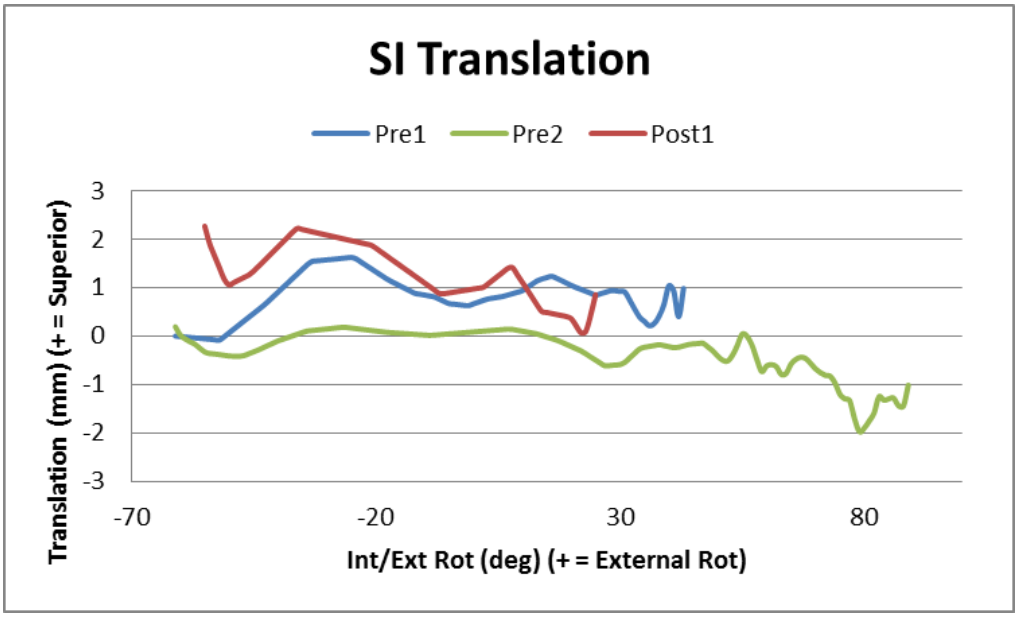

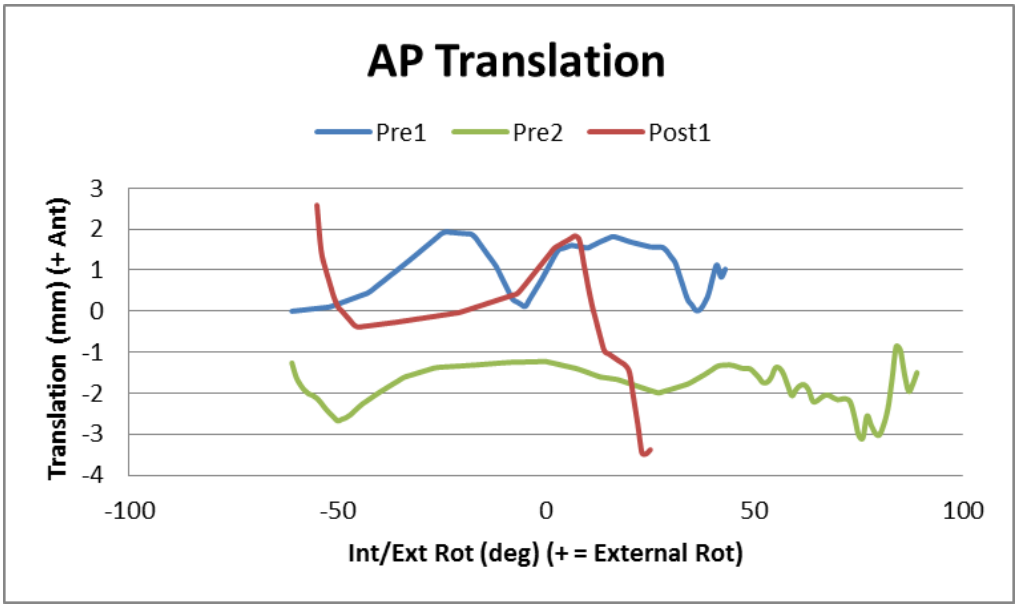

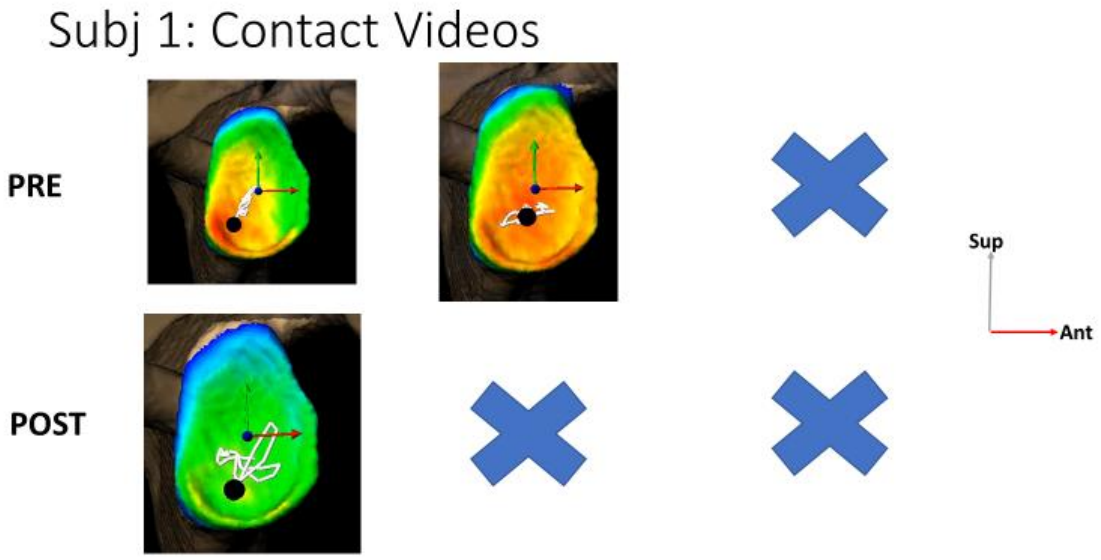
Subj 1: Contact Videos
PRE
POST
Sup
Ant

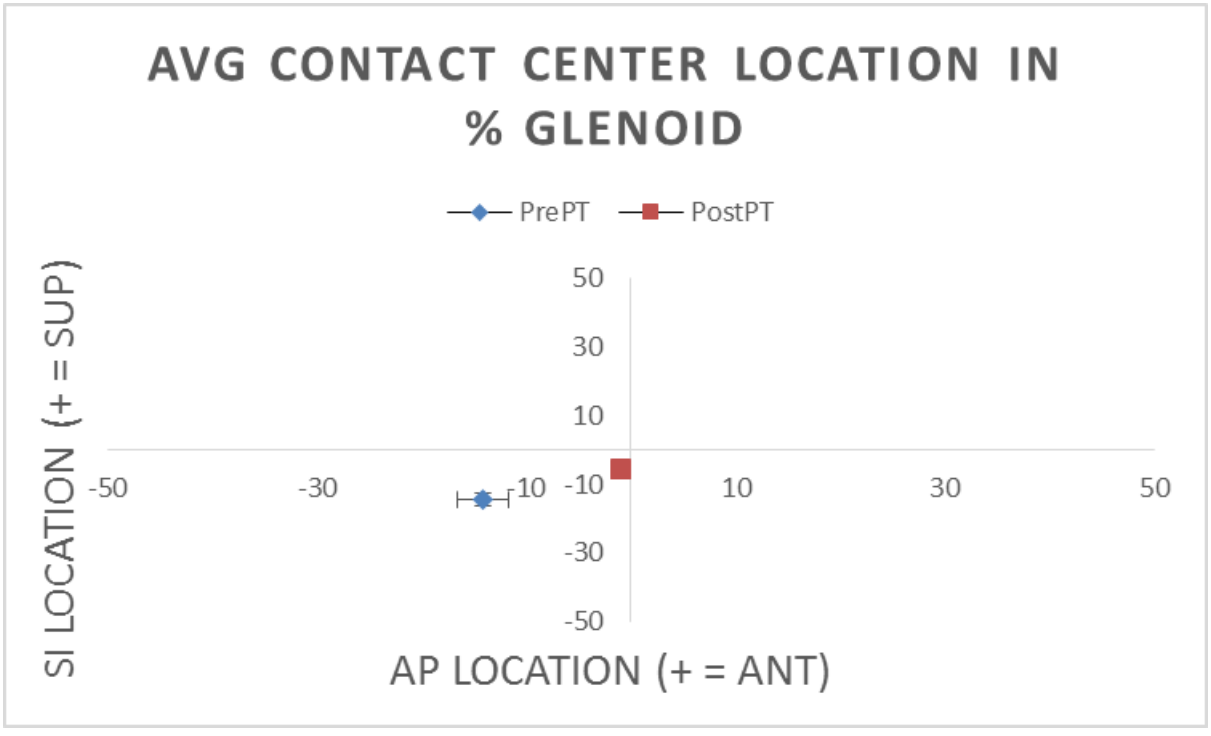
AVG CONTACT CENTER LOCATION IN % GLENOID
PrePT
PostPT
SI LOCATION (+ = SUP)
AP LOCATION (+ = ANT)
50
30
10
-10
-30
-50
-50
-30
-10
10
30
50

Subject 2:

	Pre 1	Pre 2	Pre 3	Post 1	Post 2	Post 3	Shared
Max IR (°)	86	89	85	75	N/A	N/A	**75**
Max ER (°)	87	103	105	92	100	98	**87**

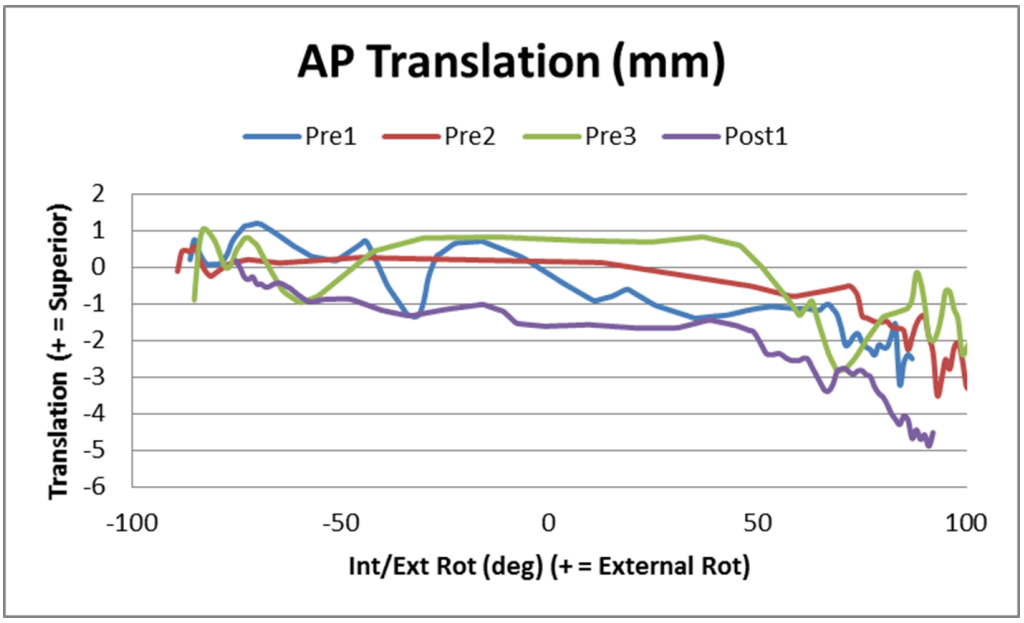

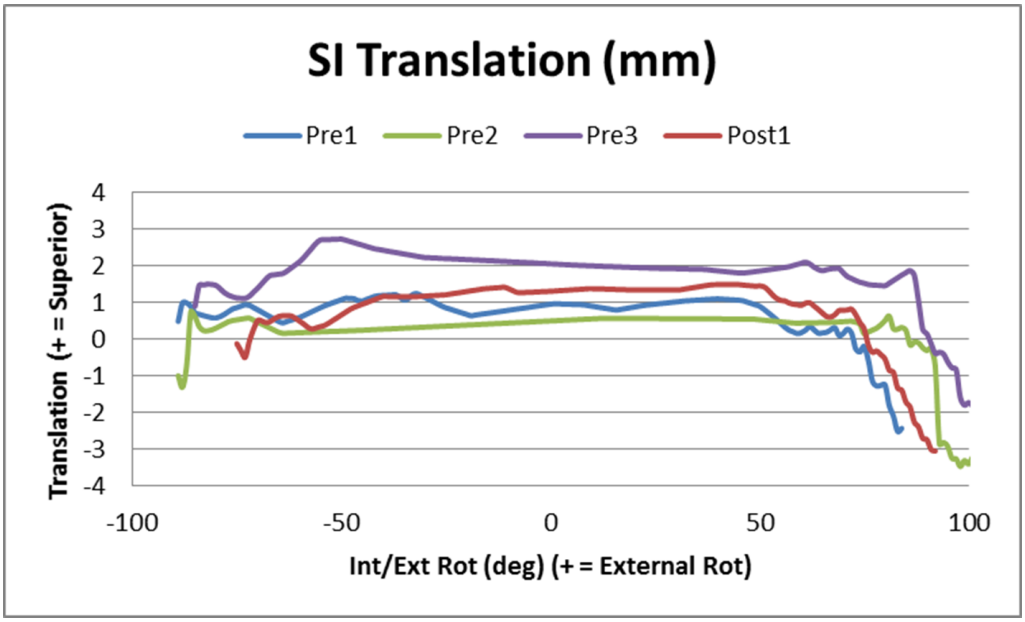

Subj 2: Contact Videos

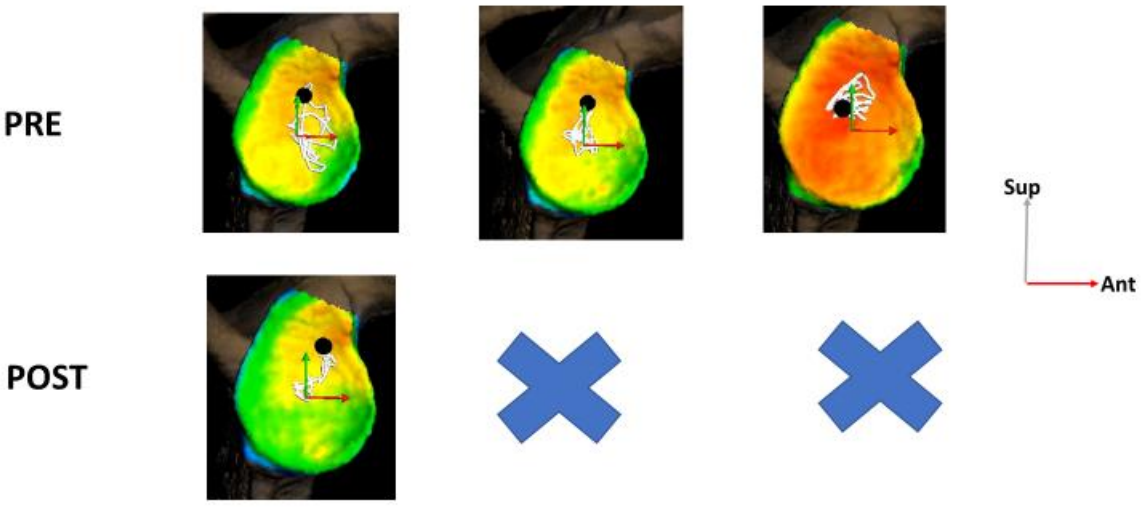

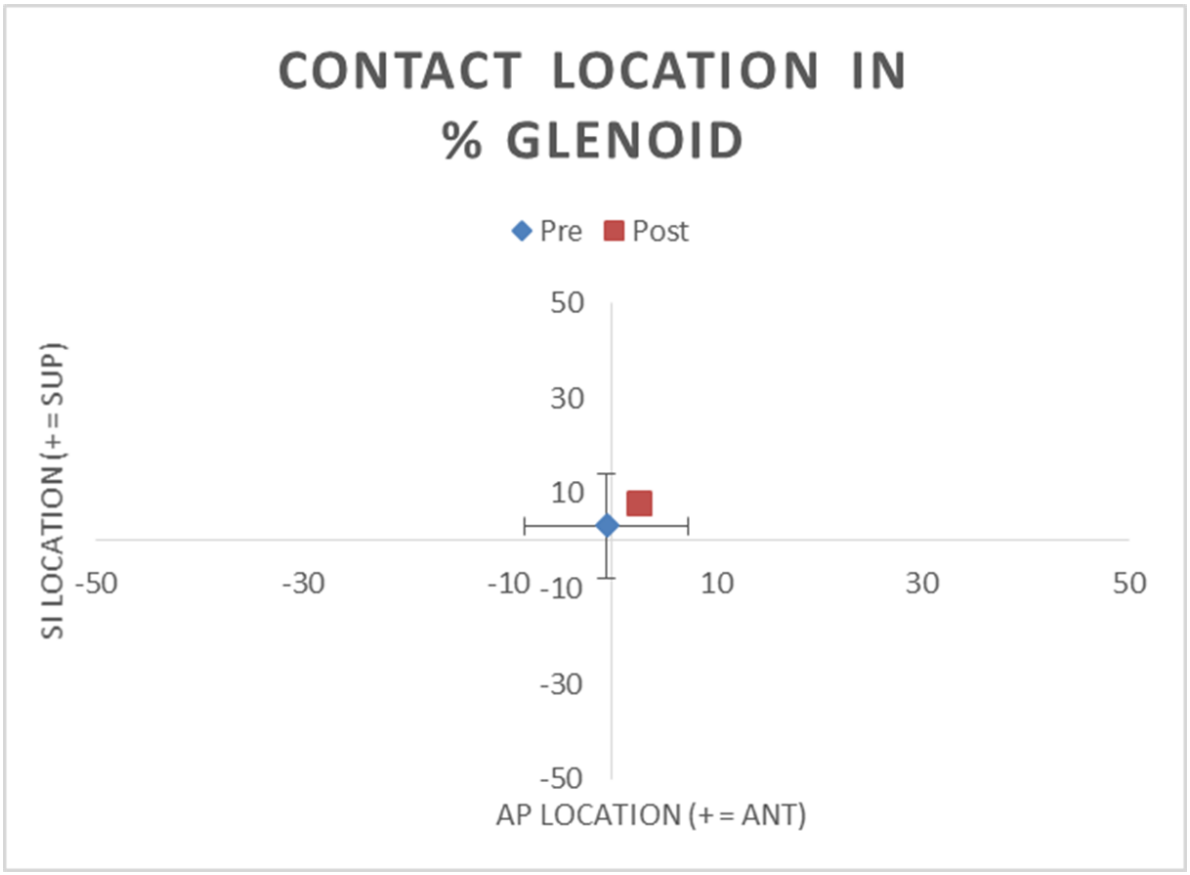

Subject 3:

	Pre 1	Pre 2	Pre 3	Post 1	Post 2	Post 3	Shared
Max IR (°)	64	59	67	57	67	30	**30**
Max ER (°)	118	102	114	90	88	94	**88**

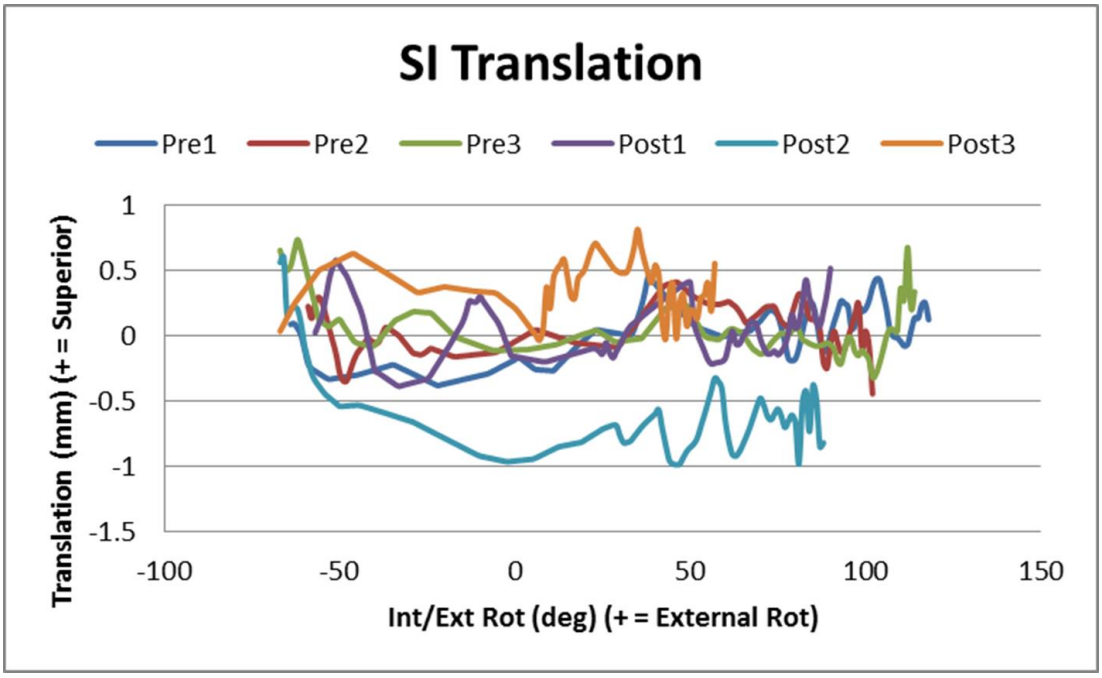

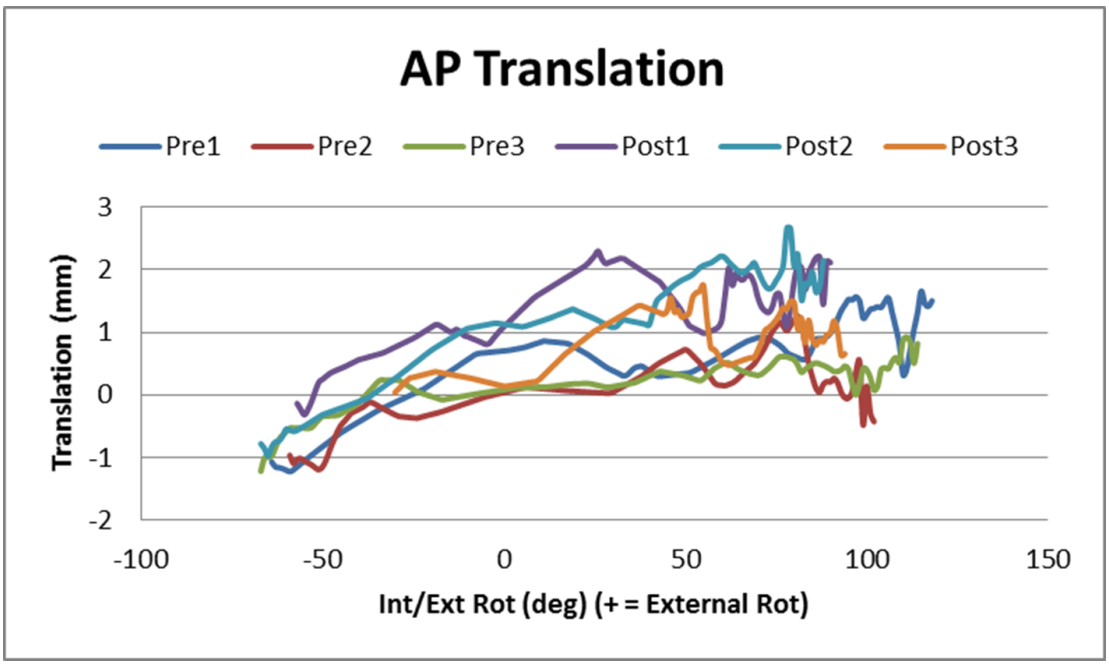

Subj 3: Contact Videos

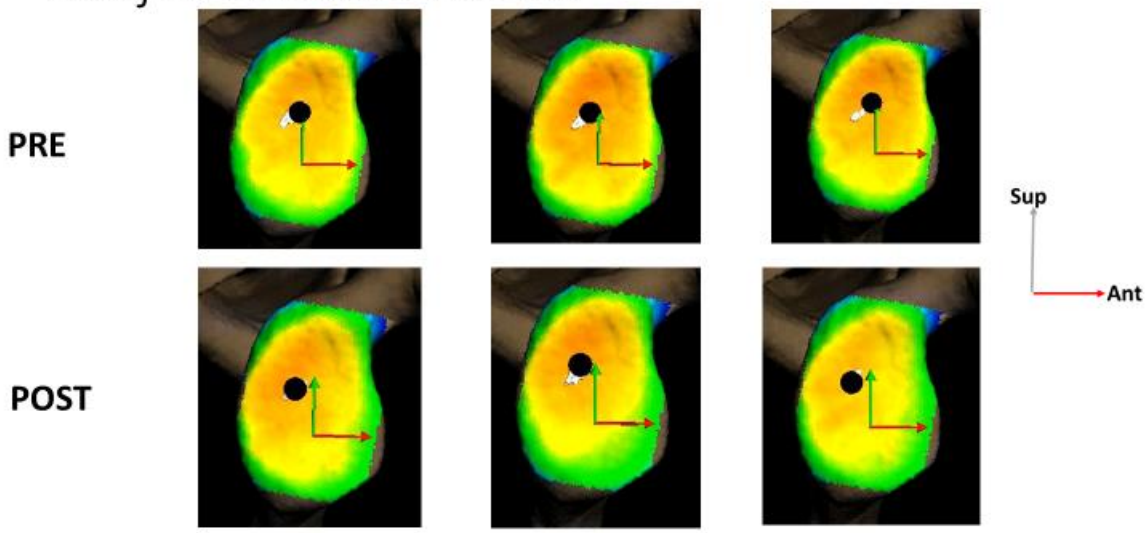

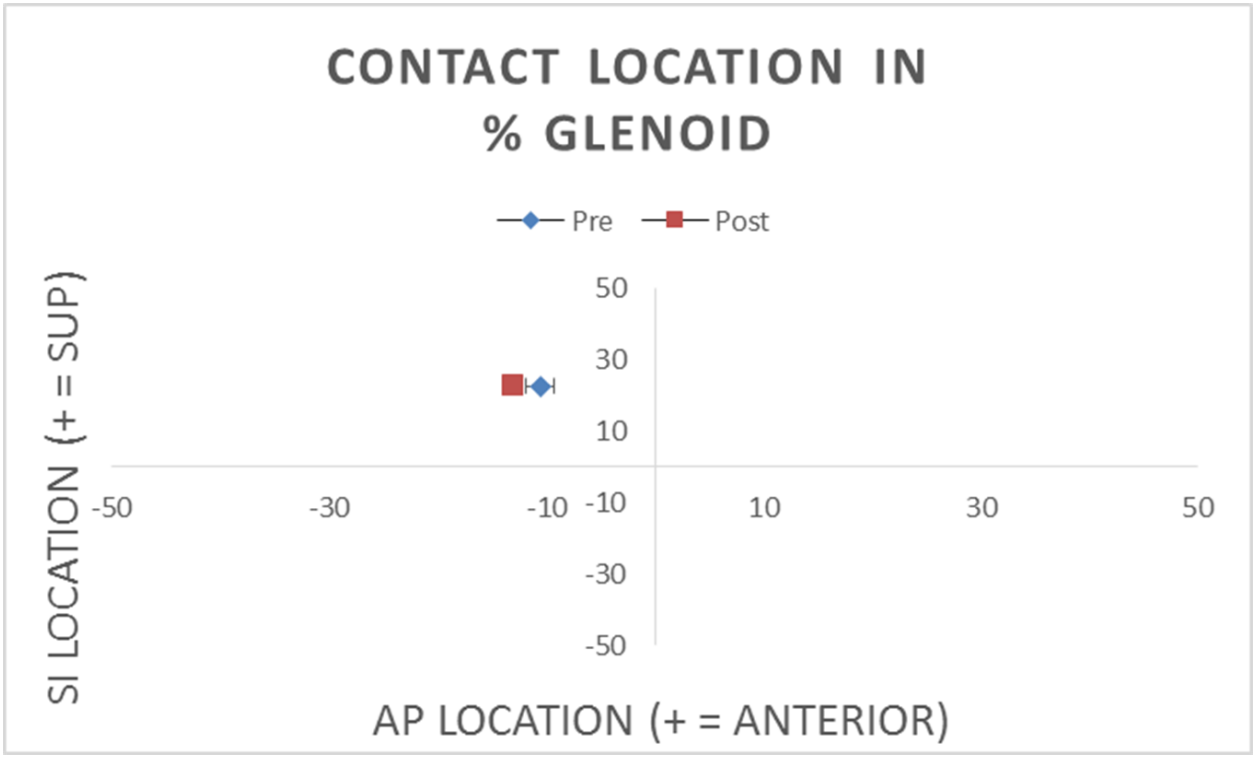

Subject 4:

	Pre 1	Pre 2	Pre 3	Post 1	Post 2	Post 3	Shared
Max IR (°)	72	66	66	66	59	68	59
Max ER (°)	1	20	17	9	15	10	1

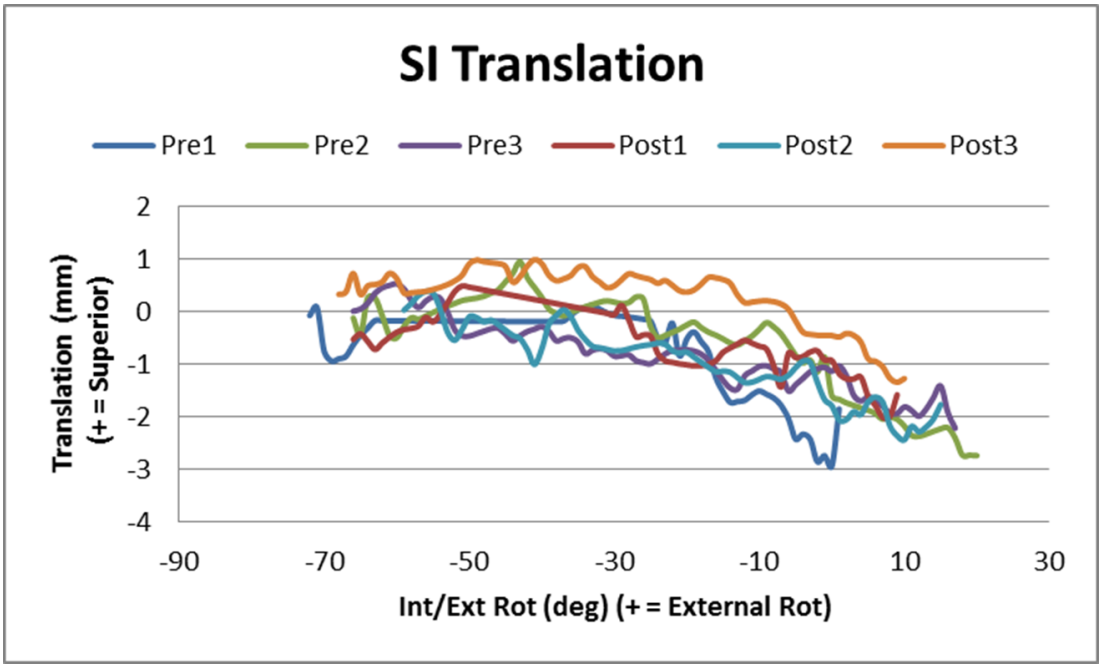

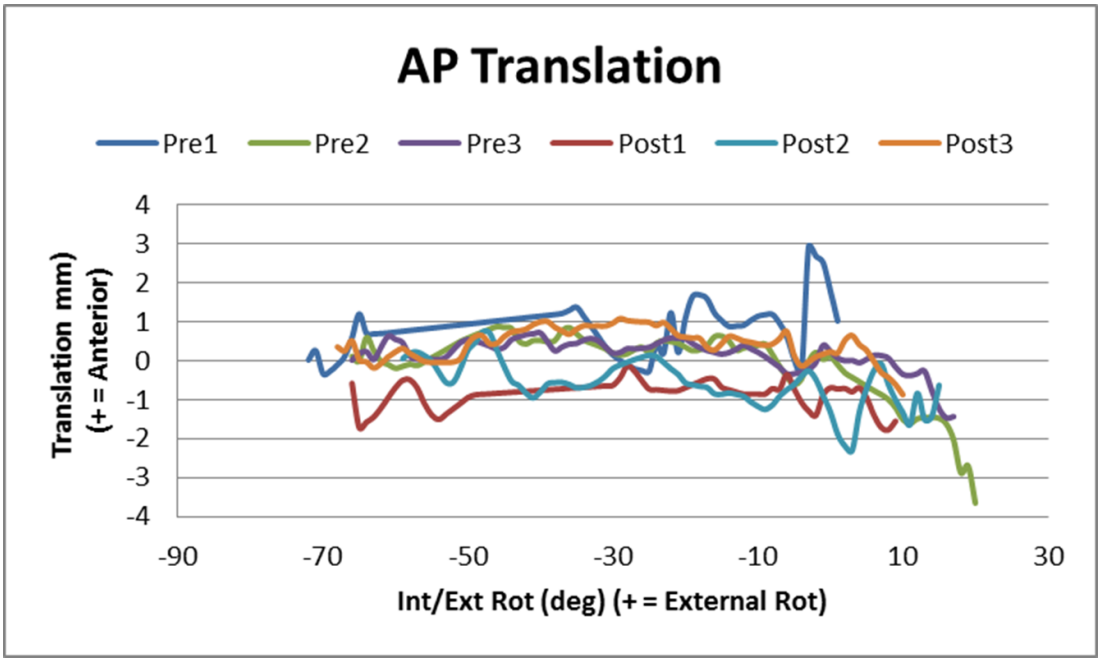

Subj 4: Contact Videos

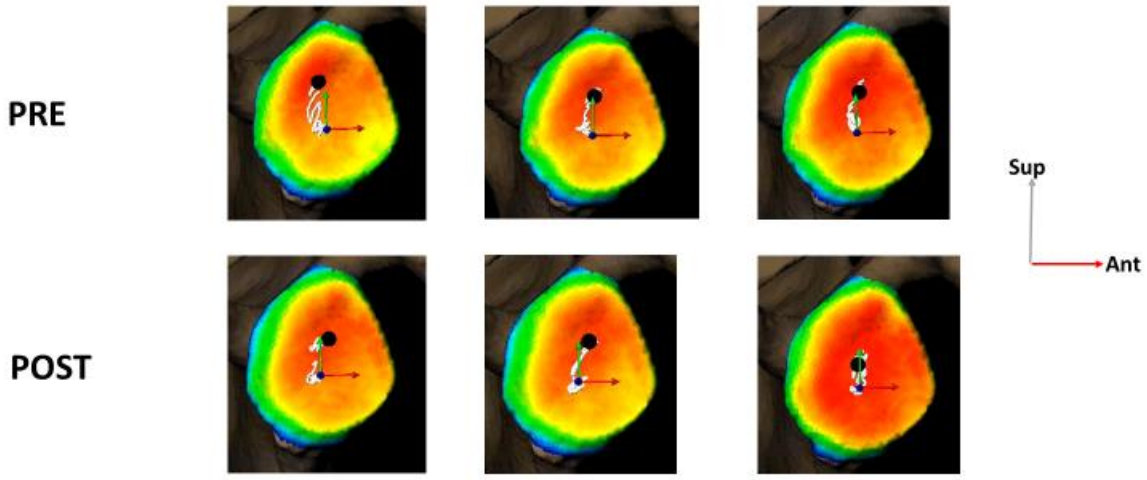

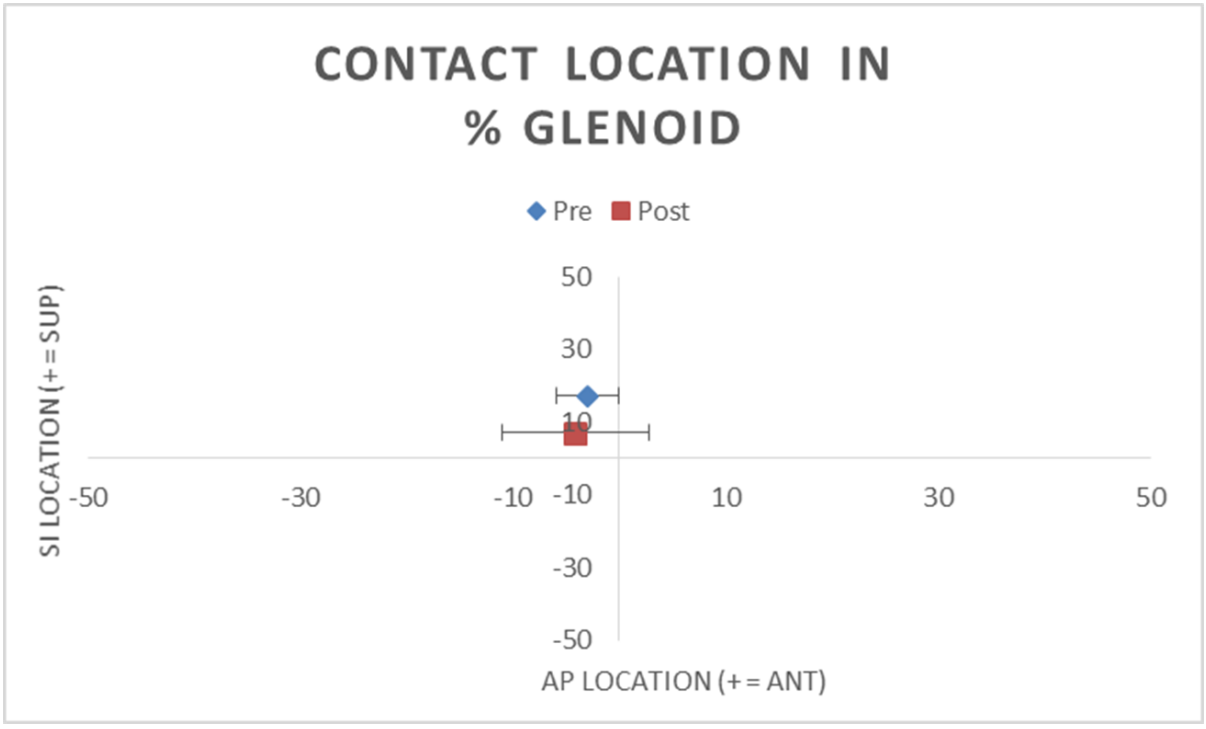

Subject 5:

	Pre 1	Pre 2	Pre 3	Post 1	Post 2	Post 3	Shared
Max IR (°)	71	75	69	73	77	76	**69**
Max ER (°)	50	51	51	51	51	51	**50**

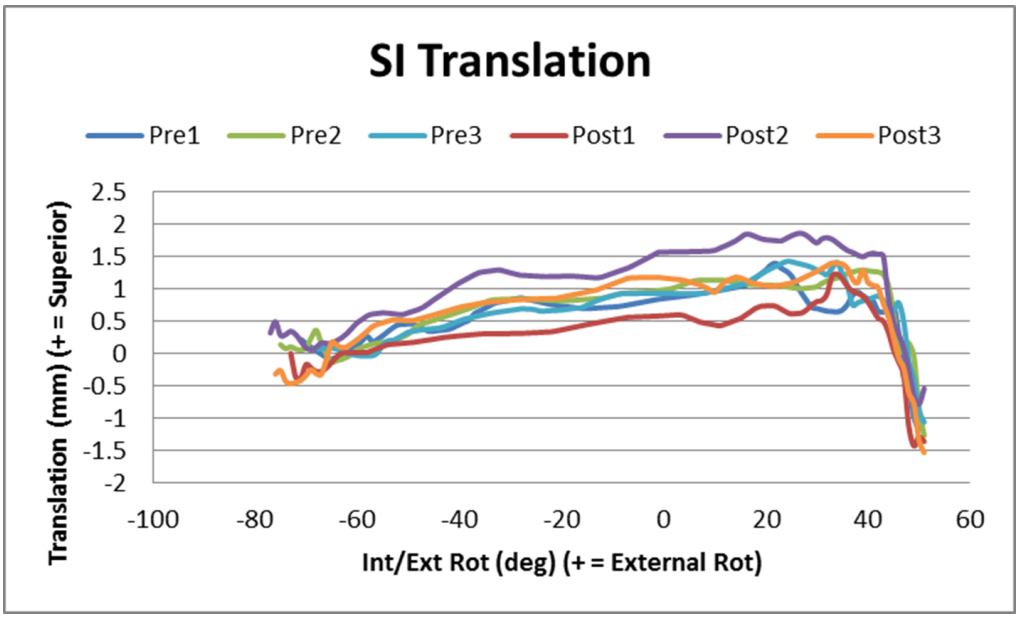

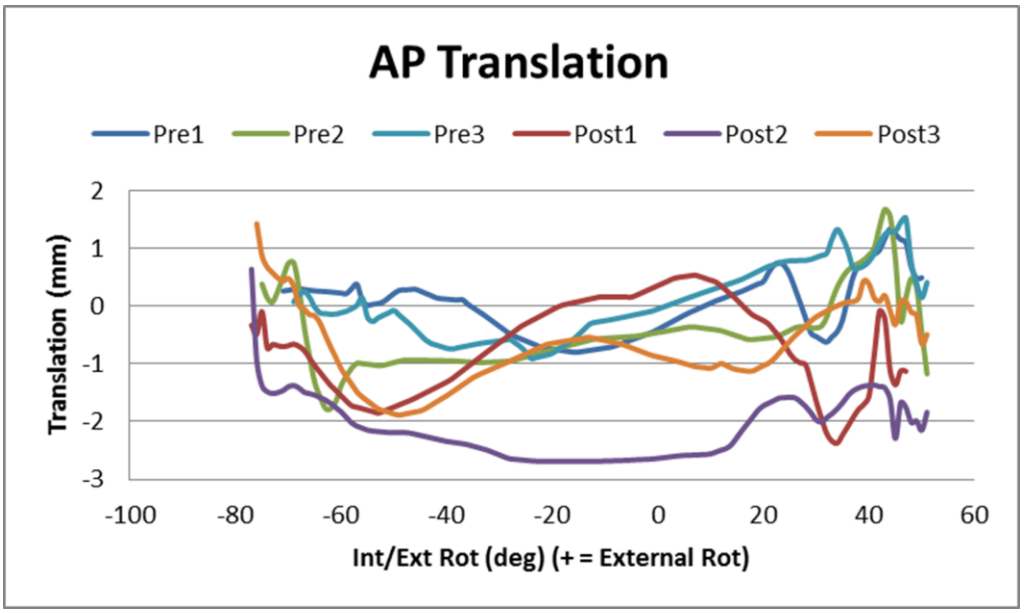

Subj 5: Contact Videos

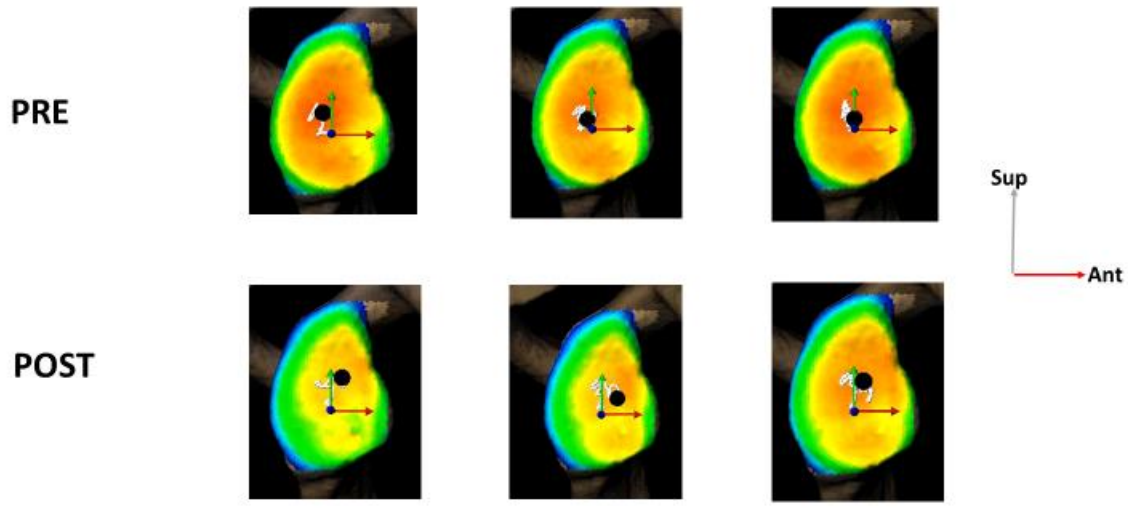

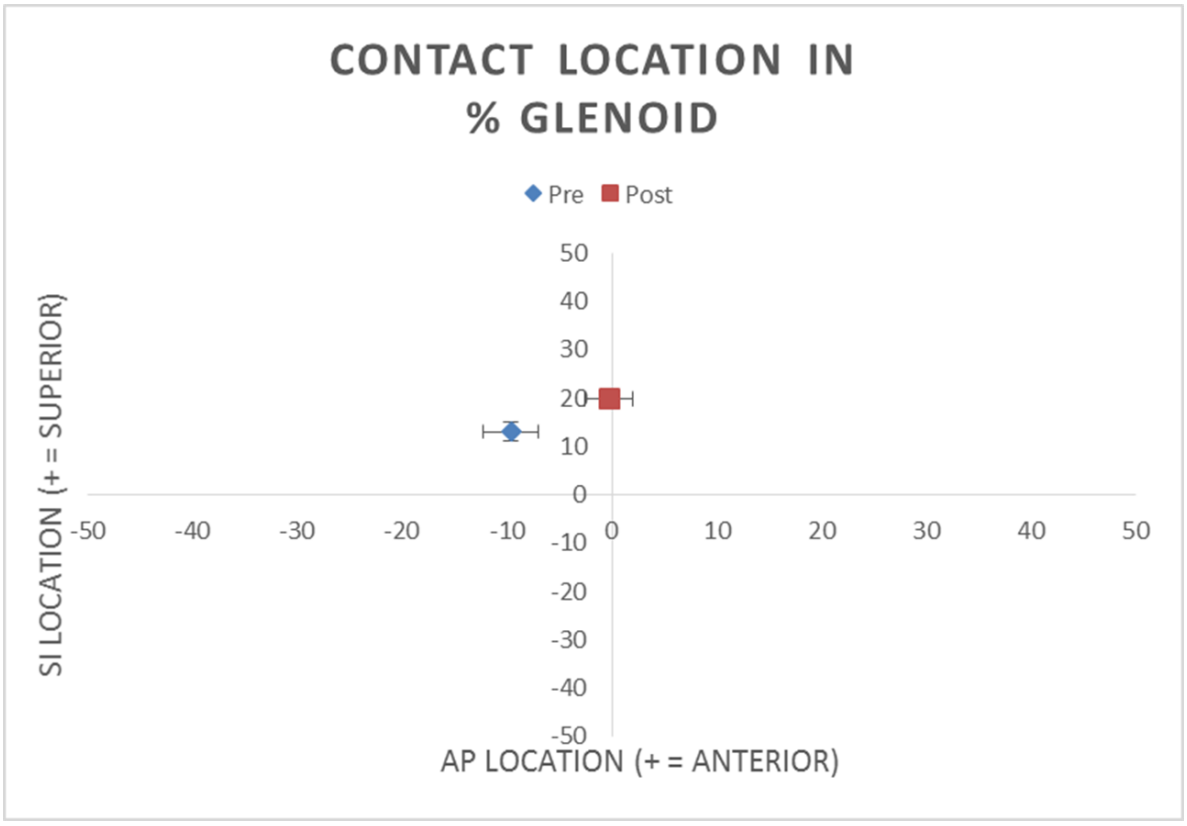

Appendix B – Aim 2

Running of the FEM model for tear propagation required 4 data files (Geometry Data ".dat", Material Model Parameters ".mat", Fibers Direction Vectors ".fiber", and Loading Conditions ".load"). An example of each file will be shown in this appendix.

Appendix B.1 Example .dat file defining the model geometry data

1. Top heading shows information including
    a. number of nodes
    b. number of elements
    c. number of imposed boundary conditions (numimp)
    d. number of materials for volumetric elements (numatv)
    e. number of elements with an imposed traction condition (ntracel)
    f. number of traction conditions (ntracv)
2. The first block shows node number and associated nodal coordinates
3. The second block shows volumetric element connectivity
    a. First number is element number
    b. Second number is type of element (e.g. 3 is tetrahedral)
    c. Third number is the number of nodes in the element (e.g. 4 nodes for a linear tetrahedral element)
    d. Fourth number is the associated material
    e. Last numbers are the nodes associated with that element
4. The next blocks show applied nodal boundary conditions, surface element connectivity for traction boundary condition, traction vector, reaction node list, etc.

In the following example, "…" represents a continued list of similar data in the file in order to minimize the number of pages

```
nodes    elements    numelc    numpair   numimp    numatv    numatc   numelvp
npmark  ntracel  ntracv
33092   150626  2652    0   2549    99  3   0   0   1026    1
coordinates
    1 1.577209e-02 -6.918577e-02 -4.465969e-02 1
    2 1.622827e-02 -6.973315e-02 -4.502367e-02 1
    3 1.591206e-02 -6.930559e-02 -4.525494e-02 1
    4 1.641208e-02 -6.902694e-02 -4.462640e-02 1
    5 2.034799e-02 -9.258102e-02 -4.358105e-02 1
...
    33085 2.572673e-02 -9.189395e-02 -4.273124e-02 1
    33086 2.745740e-02 -8.931210e-02 -4.285277e-02 1
    33087 2.637966e-02 -8.614617e-02 -4.907586e-02 1
    33088 2.747286e-02 -8.530143e-02 -4.220868e-02 1
    33089 2.746879e-02 -8.479415e-02 -4.217055e-02 1
    33090 2.556579e-02 -9.183578e-02 -4.997494e-02 1
    33091 2.636546e-02 -8.565999e-02 -4.910737e-02 1
    33092 2.633718e-02 -8.468888e-02 -4.919711e-02 1
volumetric element connectivity
1  3  4  2  1  2  3  4
2   3   4  19   5   6   7   8
3   3   4  40   9  10  11  12
4   3   4   3  13  14  15  16
5   3   4   3  17  18  19  20
6   3   4   3  21  22  23  24
...
150617       3       4      67   32225   32407   32263   32224
150618       3       4      48   33080   12475   14349   32832
150619       3       4      98   32748   32854   32852   32983
150620       3       4      64   32187   32282   32220   32184
150621       3       4      19   14204   32742   32549   33076
150622       3       4      19   32547   32548    6153   32422
150623       3       4      38   32799   32541   32965   32998
150624       3       4      98   32615   14000   32613   14523
150625       3       4      98   32748   32854   32342   32852
150626       3       4      50   33080   12475   14344   14349
cohesive element connectivity
1      7      3      2    575    576    577  29224  26392  28889
2      7      3      3   1177   1178   1179  30407  30326  27000
3      7      3      3   3058   1192   3059  27023  24343  24983
4      7      3      3   3058   3059   3518  27023  24983  30438
5      7      3      2   3753    587    576  22404  26327  26392
...
2646      7      3      1  11106  11107  13346  29815  26218  29792
2647      7      3      1  13787  10639  13435  28821  28822  22658
2648      7      3      1   5261   8519   5260  26204  25097  29360
2649      7      3      1   9562  10961   9561  29334  29330  25701
2650      7      3      1  14173  14178  14177  29995  25621  25622
2651      7      3      1  11233   7375  10692  29826  26952  26954
2652      7      3      1   8012   7721  10365  25614  24470  24471
periodic boundary pairs
nodes with imposed BC
 102 1111
 103 1111
 203 1111
 207 1111
 429 1111
```

```
...
30670 2207
30716 2207
30721 2207
31848 2207
element connectivity for pressure loading
nodes with imposed load and load value
0
Surface element connectivity for traction BC
   1  7  3  2    21557    21559    21558
   2  7  3  2    22122    22123    22124
   3  7  3  2    22292    22294    22293
   4  7  3  2    22432    22433    21348
   5  7  3  2    22584    22585    22586
 ...
1019  7  3  2    24675    30151    16077
1020  7  3  2    30782    26480    30402
1021  7  3  2    23986    24359    22864
1022  7  3  2    26098    26462    26473
1023  7  3  2    26031    26032    24780
1024  7  3  2    27427    26487    27428
1025  7  3  2    26219    25827    26220
1026  7  3  2    26031    24780    25793
Traction vector
1 6.334000e+04 1.997000e+04 -6.877000e+04
Reaction node list
   533
    1 30654
    2 30655
    3 30657
    4 30656
    5 30659
    6 24102
    7 30664
    8 30670
    9 30362
   10 30354
   11 30353
   12 30355
...
  527 18775
  528 29548
  529 27858
  530 22483
  531 29547
  532 26560
  533 26905
```

Appendix B.2 Example .mat file defining material parameters

1. Parameters k1 and k2 will be output to represent properties of the collagen fibers (strength and stiffness)
2. The values for the Lame parameters (lambda and mu) are calculated based on estimated values of elastic modulus and Poisson's ratio for the matrix

In the following example, "…" represents a continued list of similar data in the file in order to minimize the number of pages

```
list Mattype lambda mu sigmay para1 para2
1 3161 1.8e+07 2e+06 2e+15 0 0 8.91e+06 0.3243
2 3161 1.8e+07 2e+06 2e+15 0 0 8.91e+06 0.3243
3 3161 1.8e+07 2e+06 2e+15 0 0 8.91e+06 0.3243
4 3161 1.8e+07 2e+06 2e+15 0 0 8.9276e+06 0.33578
5 3161 1.8e+07 2e+06 2e+15 0 0 9.0683e+06 0.42783
6 3161 1.8e+07 2e+06 2e+15 0 0 9.209e+06 0.51988
7 3161 1.8e+07 2e+06 2e+15 0 0 9.3497e+06 0.61193
…
92 3161 1.8e+07 2e+06 2e+15 0 0 1.5095e+07 4.2604
93 3161 1.8e+07 2e+06 2e+15 0 0 1.5119e+07 4.3859
94 3161 1.8e+07 2e+06 2e+15 0 0 1.5193e+07 4.3595
95 3161 1.8e+07 2e+06 2e+15 0 0 1.5259e+07 4.478
96 3161 1.8e+07 2e+06 2e+15 0 0 1.529e+07 4.4586
97 3161 1.8e+07 2e+06 2e+15 0 0 1.5388e+07 4.5576
98 3161 1.8e+07 2e+06 2e+15 0 0 1.54e+07 4.57
99 3161 1.8e+07 2e+06 2e+15 0 0 1.54e+07 4.57
s_max_normal delta_max_normal s_max_shear delta_max_shear initial_damage
5.78e+06 0.00064 5.78e+06 0.00064 0.98 0
5.81e+06 0.00053 5.81e+06 0.00053 0.98 0
4.25e+06 0.00057 4.25e+06 0.00057 0.98 0
Bulk Damage Variables
list DamageType DamagePara1 DamagePara2 DamagePara3
1 0 1e-07 0.2 1
2 0 1e-07 0.2 1
3 0 1e-07 0.2 1
4 0 1e-07 0.2 1
…
91 0 1e-07 0.2 1
92 0 1e-07 0.2 1
93 0 1e-07 0.2 1
94 0 1e-07 0.2 1
95 0 1e-07 0.2 1
96 0 1e-07 0.2 1
97 0 1e-07 0.2 1
98 0 1e-07 0.2 1
99 0 1e-07 0.2 1
```

Appendix B.3 Example .fiber and .load data files

1. Direction of fibers is aligned with axis of loading

```
Number of fibers and then the fiber direction vectors
1
  1   .939693 0 -0.34202
```

1. Define x,y,z displacement vector based on desired displacement
    a. Multiply the displacement by a unit vector that represents the axis of loading (e.g. if the +x axis is aligned with the long axis of the humerus and the +z axis points toward the bursal side of the tendon, multiply by [1,0,0] for the displacement at 90 deg and by [0.94,0,-0.34] for 70 deg) – use this vector as the displacement loading condition

```
"imposed maximum x,y,z-disp (loading_disp_max))"
0.0047  0   0.0017
imposed maximum y-disp (loading_disp_max)
0.0  0.0  0.0
0.0  0.0  0.0
0.0  0.0  0.0
Pressure marker and values
minimum number of load steps
100
pressure
0
```

Appendix C – Aim 3

This section provides additional information about data processing and raw data.

Appendix C.1 MATLAB Code: Calculation of Quantitative Ultrasound Measures

```
%% Calculation of Quantitative Ultrasound Measurse (Skewness, Variance,
Kurtosis, and Echogenicity)

clear;
clc;

%import histogram data from ImageJ
filename = uigetfile('*.xls');
[value,count] = importHistogram(filename,2, 257);


%calculate length of data vector
sum(count);
data=zeros(length(count),1);

n=1; %index for writing to data vector
for i=1:length(count)
    if count(i) > 0
        for j=1:count(i)
            data(n)=value(i);
            n=n+1;
        end
    end
end

%Plot histogram fitted
histfit(data);

%Skewness, Kurtosis, and Variance Calculations
SKV(1) = skewness(data);
SKV(2) = kurtosis(data)-3; %Normalizes to 0 instead of 3
SKV(3) = var(data);
SKV(4) = mean(data);

%Auto-create an EXCEL file of calculated variables
name = filename(1:end-9);
xlswrite('Skewness_Kurtosis_Variance_MasterCopy.xlsx',{'Skewness'},name,'A1:A
1')
xlswrite('Skewness_Kurtosis_Variance_MasterCopy.xlsx',{'Kurtosis'},name,'A2:A
2')
```

```
xlswrite('Skewness_Kurtosis_Variance_MasterCopy.xlsx',{'Variance'},name,'A3:A
3')
xlswrite('Skewness_Kurtosis_Variance_MasterCopy.xlsx',{'Echogenecity'},name,'
A4:A4')
xlswrite('Skewness_Kurtosis_Variance_MasterCopy.xlsx',SKV(1),name,'B1:B1')
xlswrite('Skewness_Kurtosis_Variance_MasterCopy.xlsx',SKV(2),name,'B2:B2')
xlswrite('Skewness_Kurtosis_Variance_MasterCopy.xlsx',SKV(3),name,'B3:B3')
xlswrite('Skewness_Kurtosis_Variance_MasterCopy.xlsx',SKV(4),name,'B4:B4')
```

Appendix C.2 Raw data images and values for QUS measures

AZ13062963R

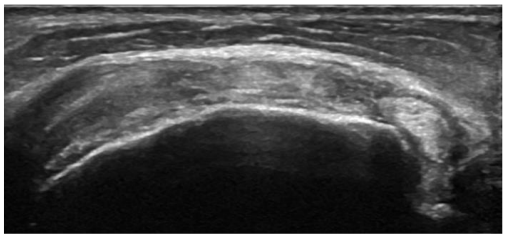

- No tear
- Skewness = 0.20
- Kurtosis = -0.23

- Variance = 817.06
- Thickness = 4.8 mm

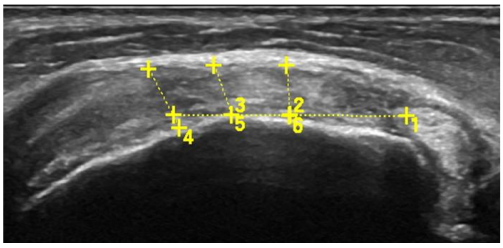

NJ13071433L

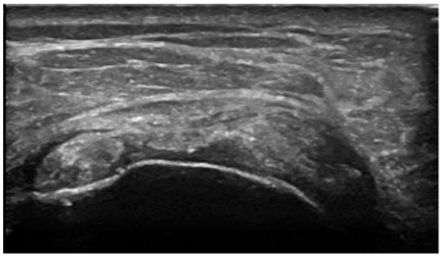

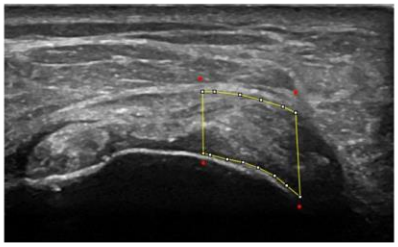

- No tear
- Skewness = 0.14
- Kurtosis = -0.37

- Variance = 1342.92
- Thickness = 6.4 mm

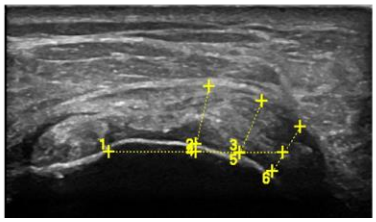

MD13071637R

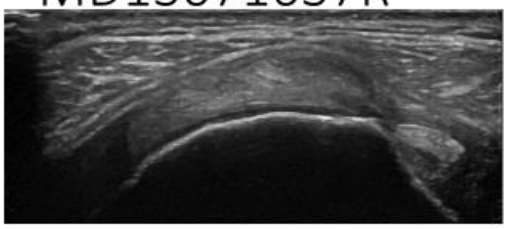

- No tear
- Skewness = 0.23
- Kurtosis = 0.60

- Variance = 407.83
- Thickness = 5.7 mm

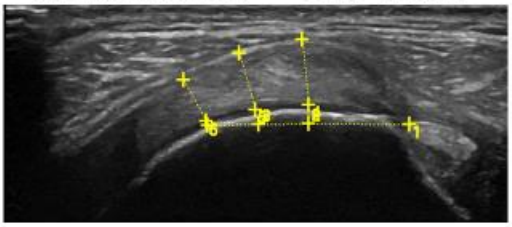

VA13070613L

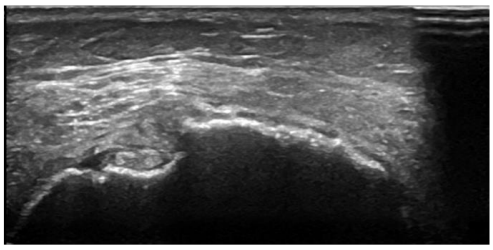

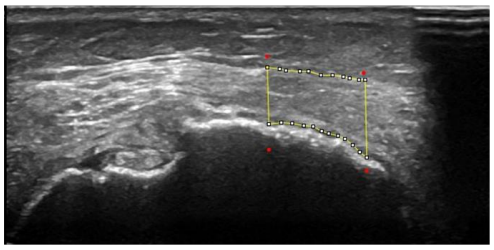

- No Tear
- Skewness = 0.68
- Kurtosis = 0.55

- Variance = 412.36
- Thickness = 6.4 mm

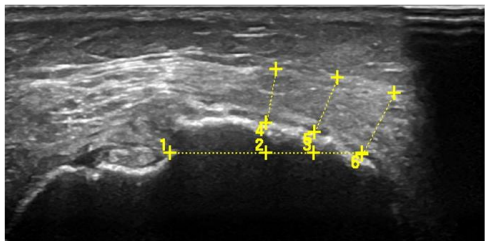

MD13070509R

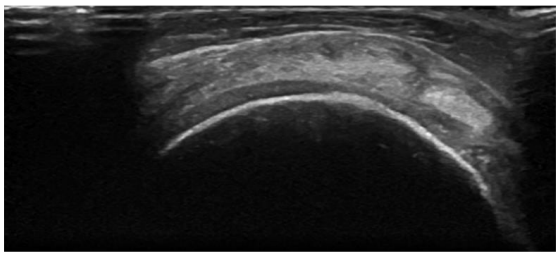

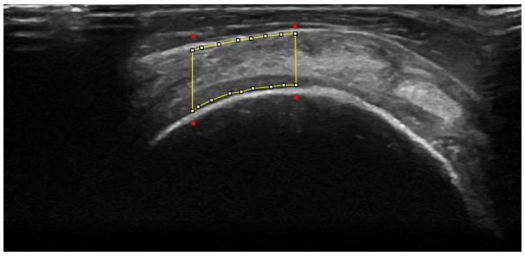

- No Tear
- Skewness = 0.36
- Kurtosis = -0.65

- Variance = 544.55
- Thickness = 5.6 mm

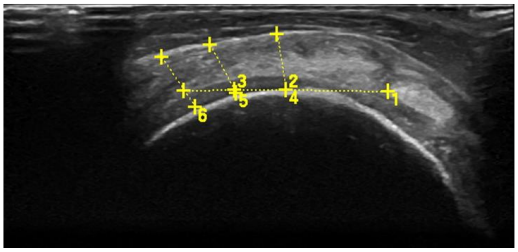

MD14071742L

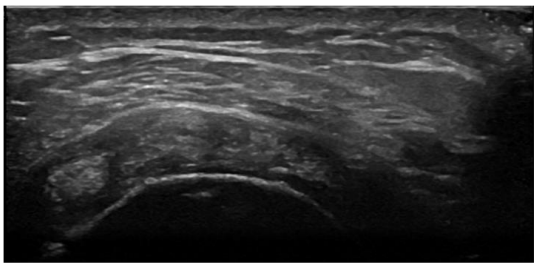

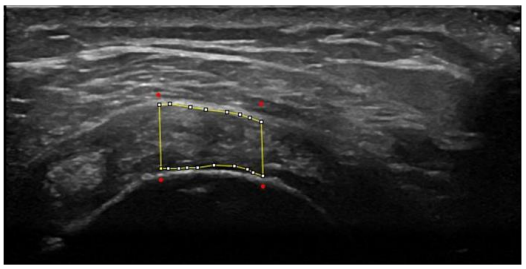

- No Tear
- Skewness = 0.60
- Kurtosis = 0.37

- Variance = 604.35
- Thickness = 5.1 mm

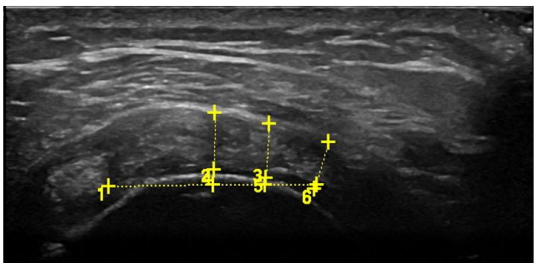

VA13071125L

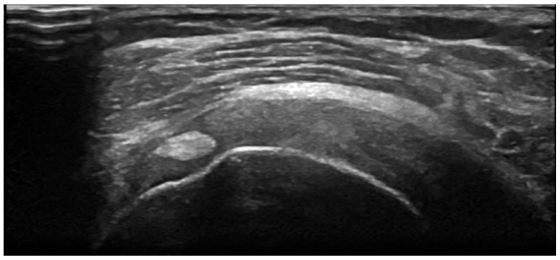

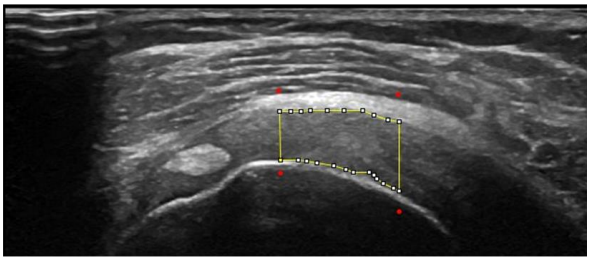

- No Tear
- Skewness = 0.14
- Kurtosis = 0.17

- Variance = 376.11
- Thickness = 5.5 mm

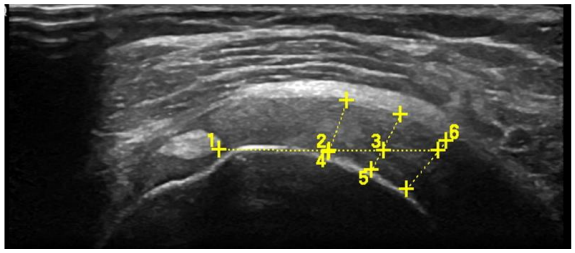

VA13071125R

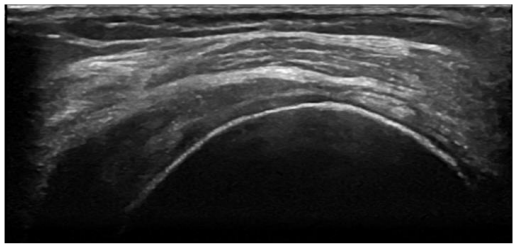

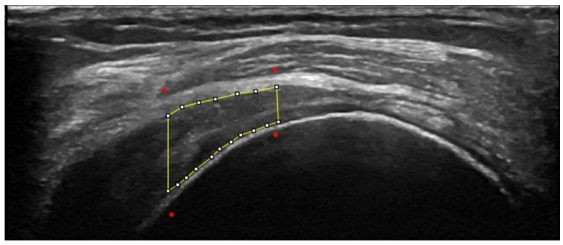

- No Tear
- Skewness = 0.43
- Kurtosis = 1.24

- Variance = 352.05
- Thickness = 4.2 mm

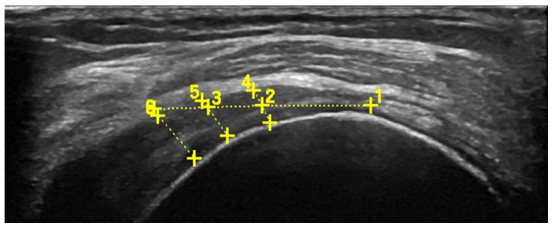

NY13062448L

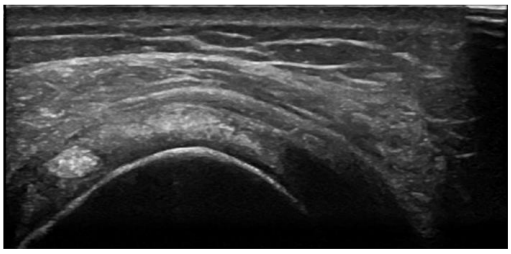

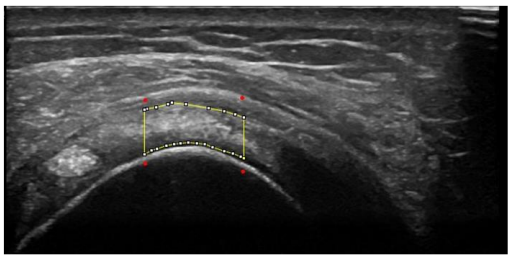

- No Tear
- Skewness = -0.11
- Kurtosis = -0.77

- Variance = 1414.27
- Thickness = 4.0 mm

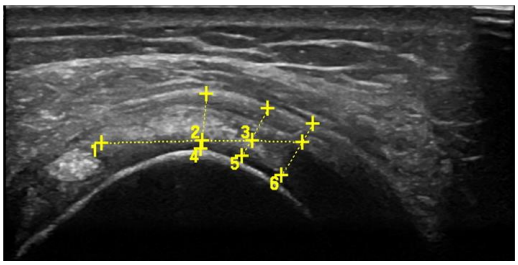

C150042L

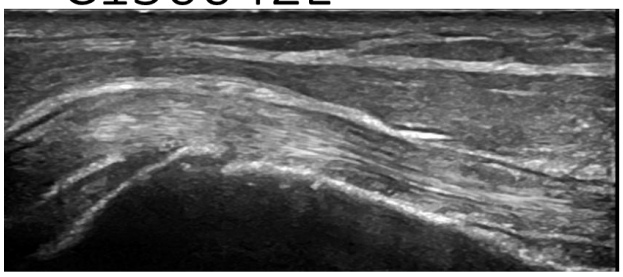

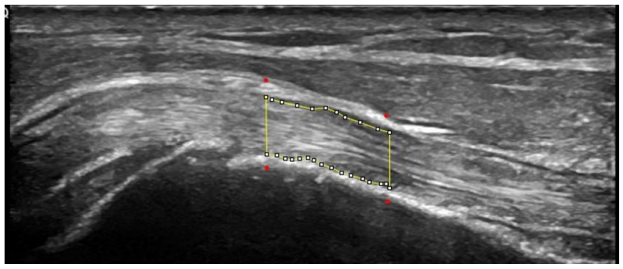

- No Tear
- Skewness = 0.16
- Kurtosis = -0.50

- Variance = 1258.63
- Thickness = 4.7 mm

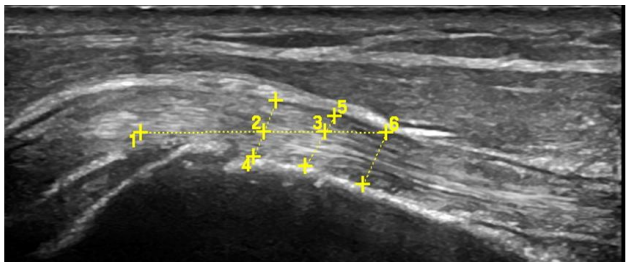

FL14072154L

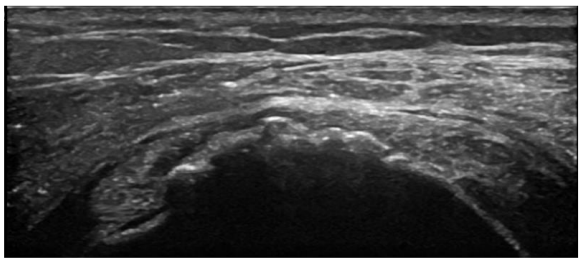

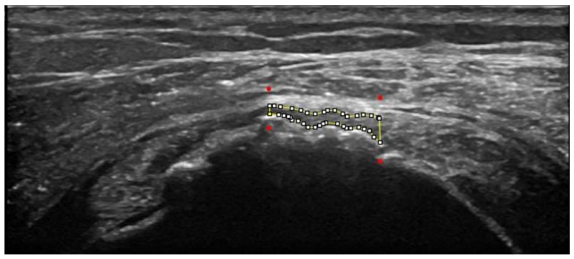

- No Tear
- Skewness = 0.38
- Kurtosis = -0.04

- Variance = 404.79
- Thickness = 1.8 mm

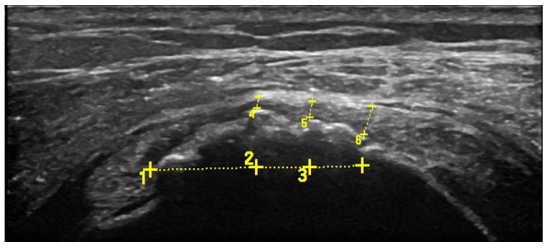

FL14072154R

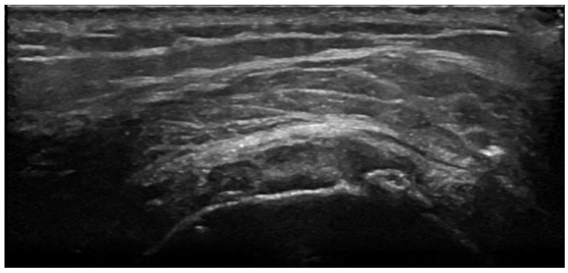

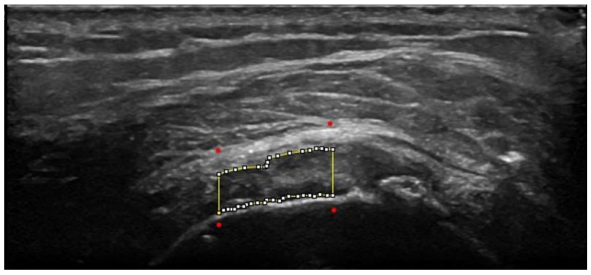

- No Tear
- Skewness = 0.71
- Kurtosis = 0.51

- Variance = 541.86
- Thickness = 3.5 mm

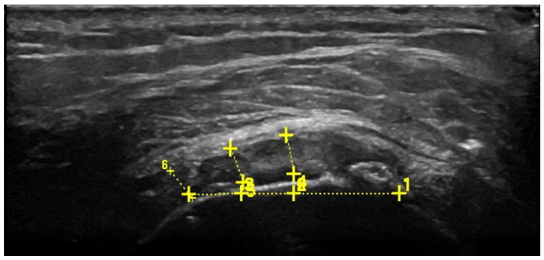

MD13071637L

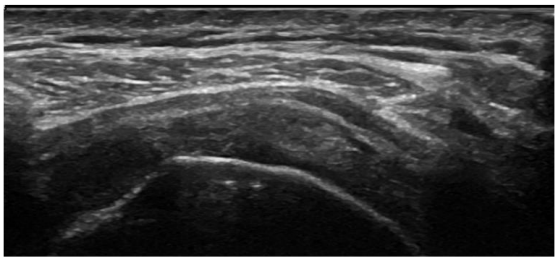

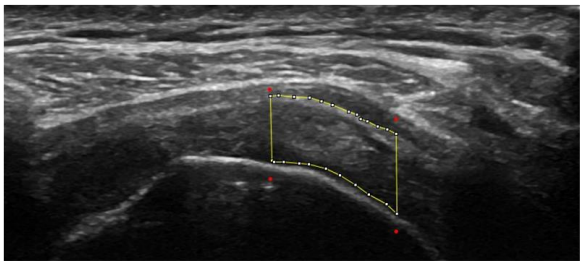

- No Tear
- Skewness = 0.77
- Kurtosis = 0.51

- Variance = 857.35
- Thickness = 4.4 mm

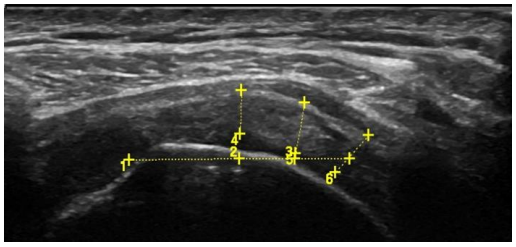

MD14070714L

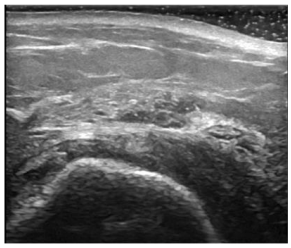

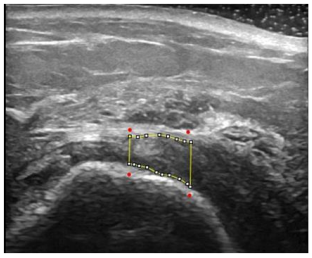

- No Tear
- Skewness = 0.69
- Kurtosis = -0.35

- Variance = 1009.19
- Thickness = 5.2 mm

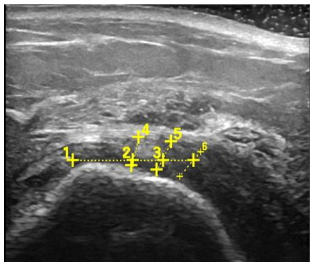

MD14071742R

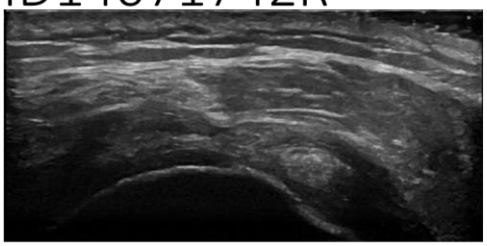

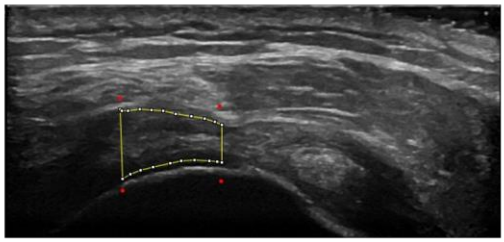

- No Tear
- Skewness = 1.15
- Kurtosis = 2.47

- Variance = 350.25
- Thickness = 5.4 mm

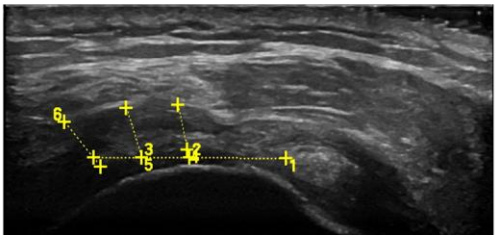

PA14070511L

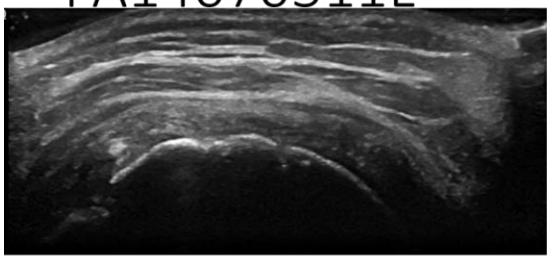

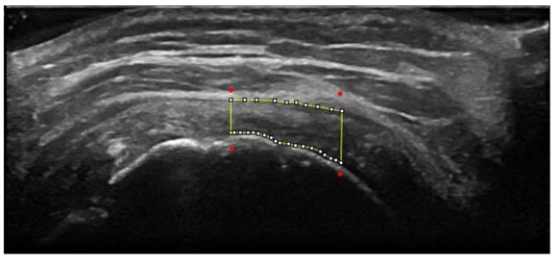

- No Tear
- Skewness = 0.56
- Kurtosis = -0.56

- Variance = 746.31
- Thickness = 3.7 mm

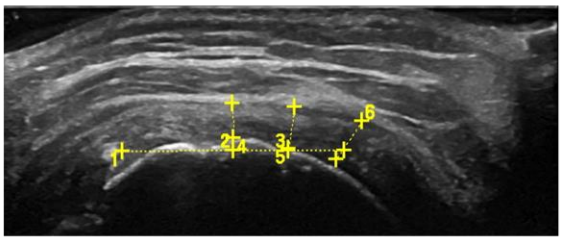

C141074R

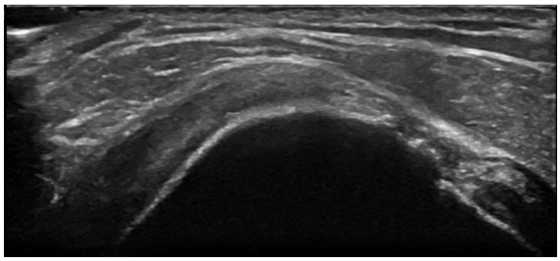

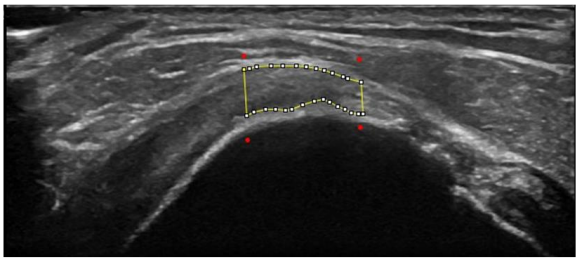

- No Tear
- Skewness = 0.38
- Kurtosis = 0.10

- Variance = 329.51
- Thickness = 3.2 mm

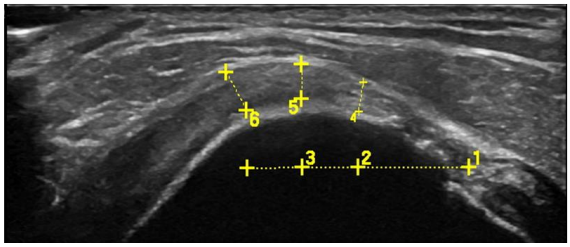

C150313R

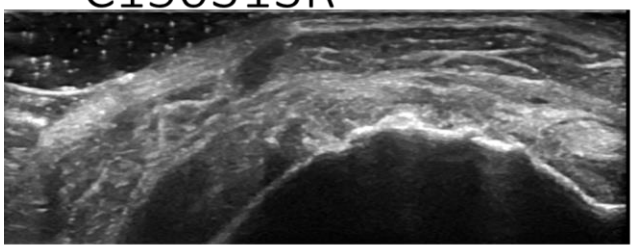

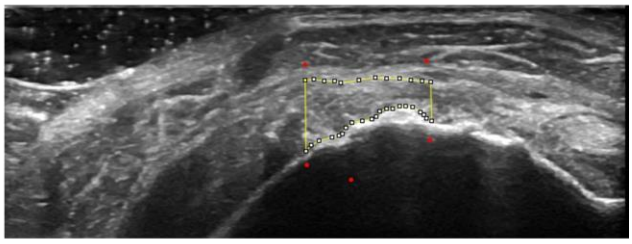

- No Tear
- Skewness = 0.29
- Kurtosis = -0.35

- Variance = 796.65
- Thickness = 3.5 mm

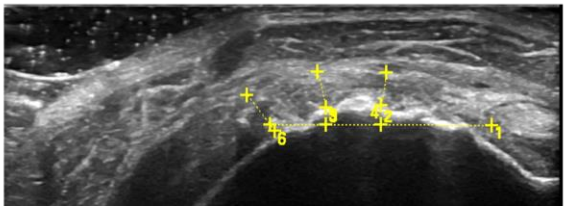

NY13062448R

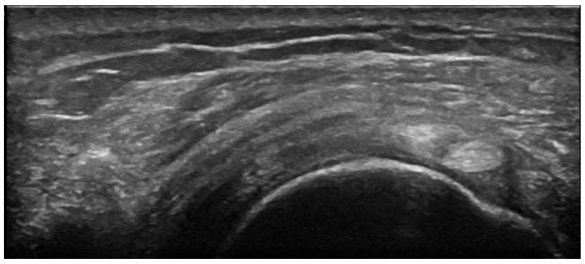

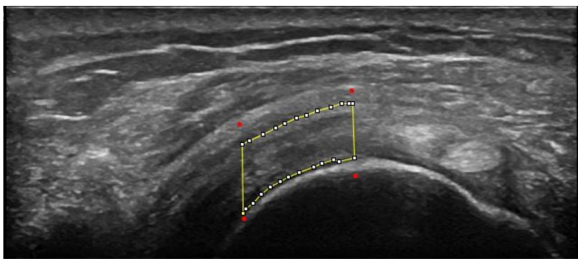

- No Tear
- Skewness = 0.15
- Kurtosis = 0.44

- Variance = 481.21
- Thickness = 4.5 mm

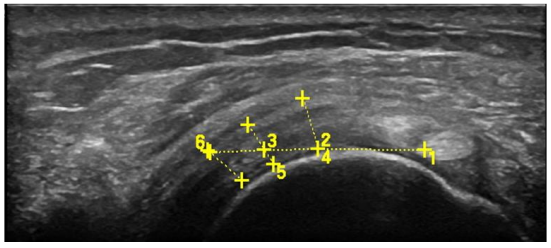

BRC1008061R

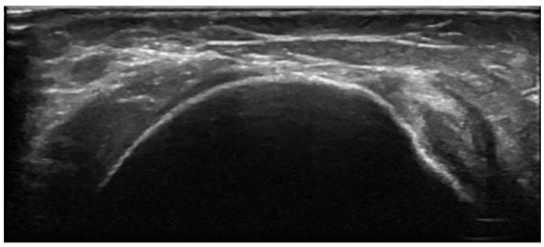

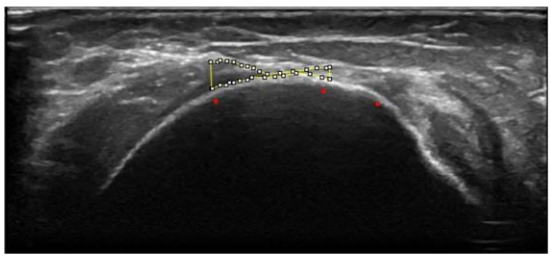

- Tear
- Skewness = 0.54
- Kurtosis = -0.35

- Variance = 1498.96
- Thickness = 2.2 mm

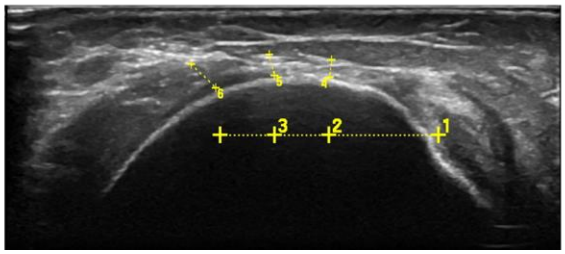

NJ13071433R

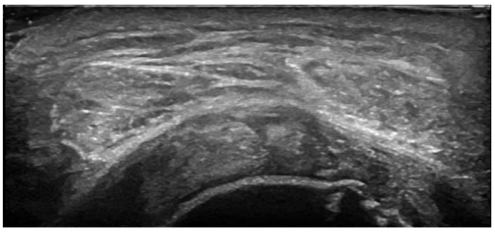

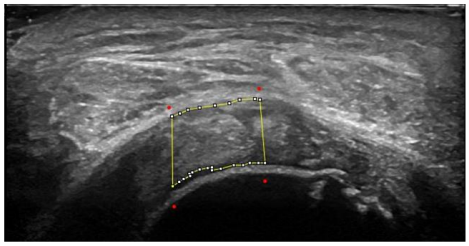

- Partial Tear (art)
- Skewness = 0.27
- Kurtosis = -0.11

- Variance = 729.57
- Thickness = 5.5 mm

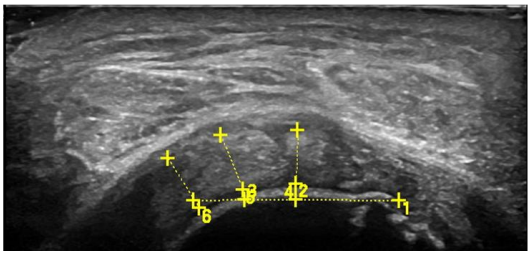

C150313L

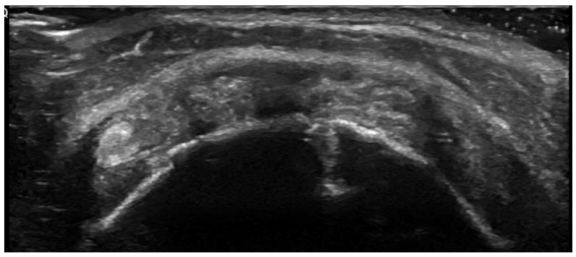

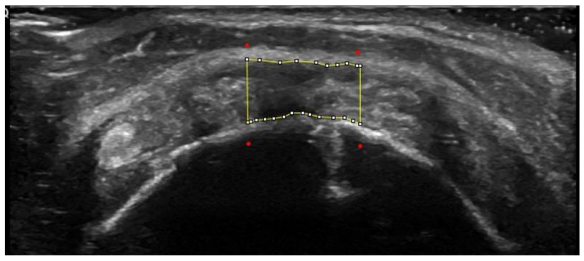

- Partial Tear (Burs)
- Skewness = 0.61
- Kurtosis = 0.11

- Variance = 680.65
- Thickness = 5.2 mm

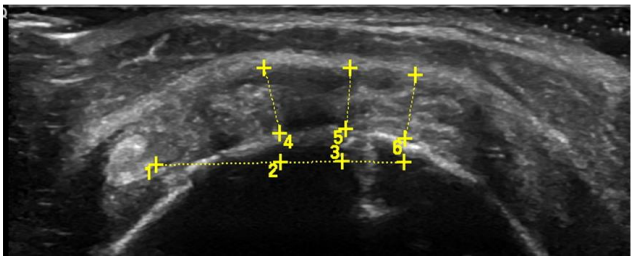

PA12060622R

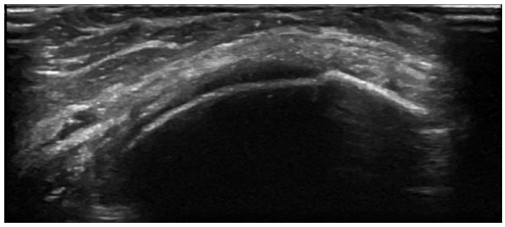

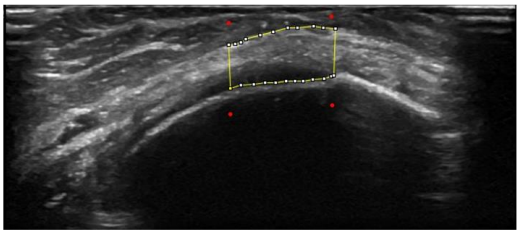

- Tear
- Skewness = 0.20
- Kurtosis = 0.11

- Variance = 1184.55
- Thickness = 3.7 mm

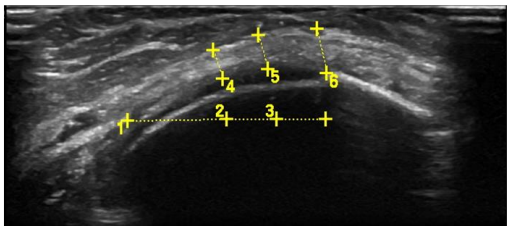

VA13070613R

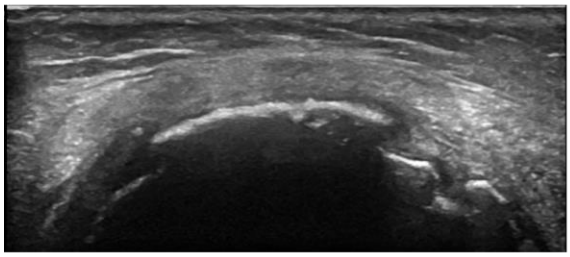

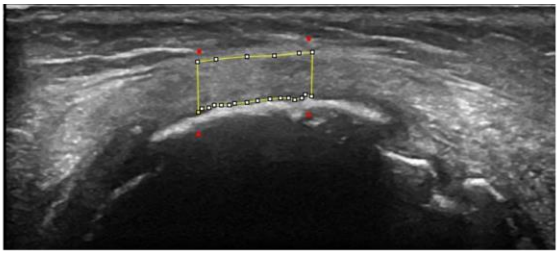

- Tear
- Skewness = 0.14
- Kurtosis = 0.19

- Variance = 274.55
- Thickness = 4.1 mm

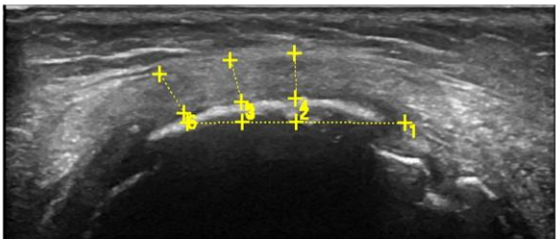

Summary of all QUS measures for all specimens

	No Tear (n = 19)	Full Tear (n = 3)	Partial Tear (n=2)
Thickness (mm)	4.6 ± 1.2	3.3 ± 1.0	5.4 ± 0.2
Skewness	0.42 ± 0.30	0.29 ± 0.22	0.44 ± 0.24
Kurtosis	0.17 ± 0.77	-0.02 ± 0.29	0.00 ± 0.16
Variance	686.70 ± 351.57	986.02 ± 635.89	705.11 ± 34.59
Echogenicity	89.94 ± 26.36	98.83 ± 17.58	78.66 ± 20.28

List of specimens used for correlation of QUS measures and histology section

Histo ID	Specimen ID	Side	Group	Age	Sex
1	VA13071125	Left	Intact	47	F
2	NJ13071433	Left	Intact	73	M
3	NY13062448	Left	Intact	51	F
4	VA13070613	Right	Torn	58	F
5	NY13062448	Right	Intact	51	F
6	09-06278	Left	Torn	73	F
7	09-06278	Right	Torn	73	F
8	BRC1006037	Left	Torn	78	M

Appendix C.3 ARFI Imaging Raw Data

Raw data for 9 specimens tested in a water tank at 1N, 5N and 15N of tension. Specimens 6 through 9 were also underwent ARFI imaging at 0.1, 0.25 and 0.5 MPa of tension

Specimen 1

1N

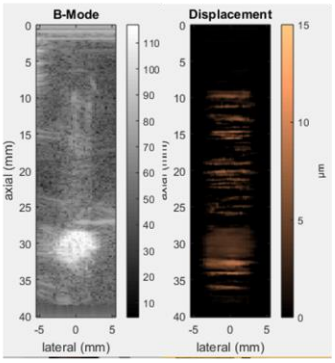

3.4 ± 0.2 μm

5N

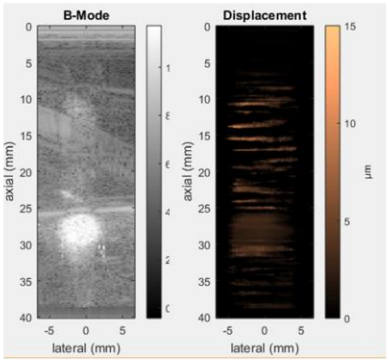

2.8 ± 0.2 μm

15N

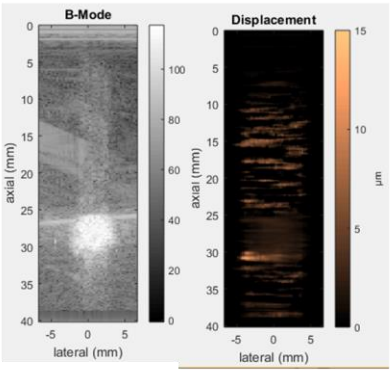

2.3 ± 0.2 μm

Specimen 2

1N

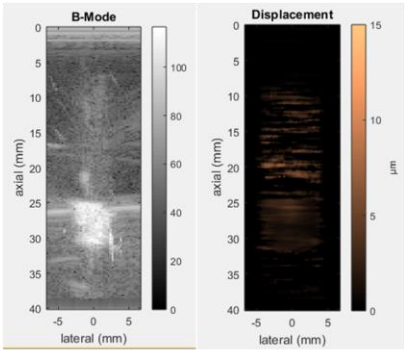

2.2 ± 0.5 μm

5N

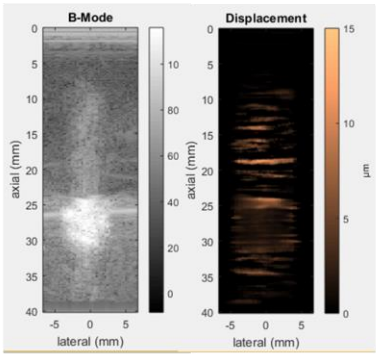

1.7 ± 0.3 μm

15N

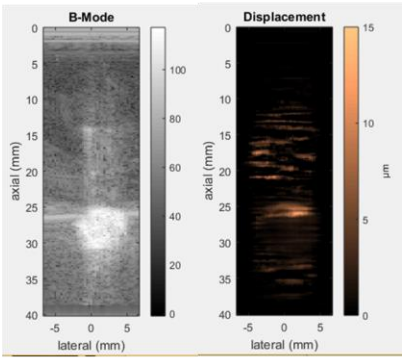

1.3 ± 0.3 μm

Specimen 3

1N

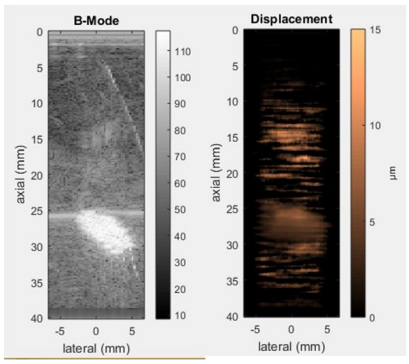

4.6 ± 0.6 μm

5N

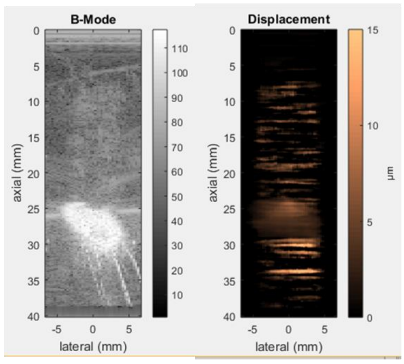

4.1 ± 0.6 μm

15N

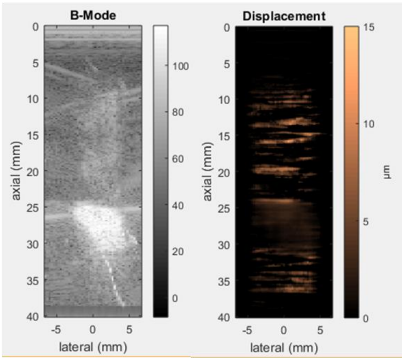

2.0 ± 0.4 μm

Specimen 4

1N

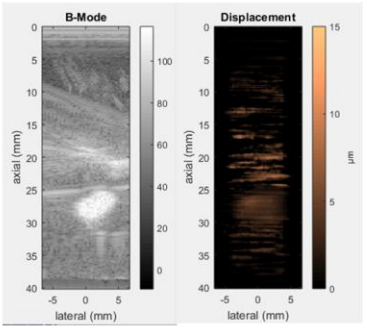

3.2 ± 0.4 μm

5N

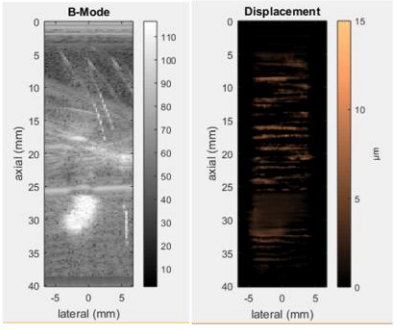

2.1 ± 0.4 μm

15N

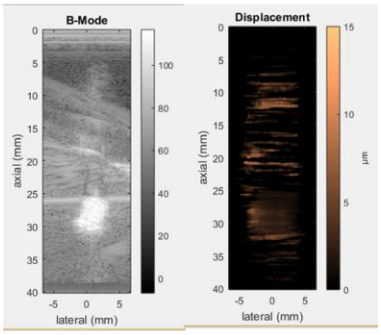

1.8 ± 0.3 μm

Specimen 5

1N

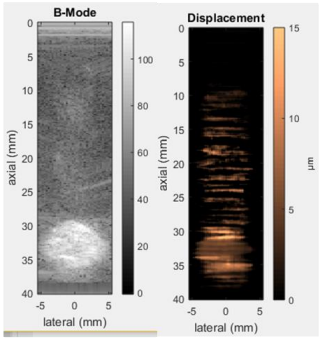

4.6 ± 0.5 μm

5N

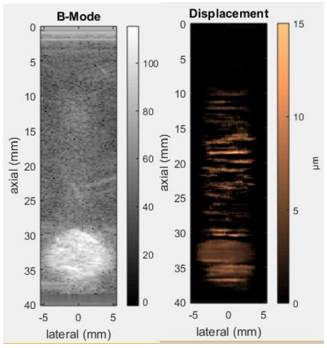

4.2 ± 0.3 μm

15N

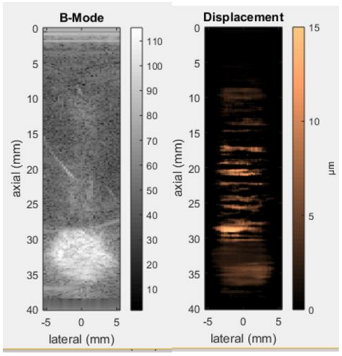

2.0 ± 0.4 μm

Specimen 6

1N

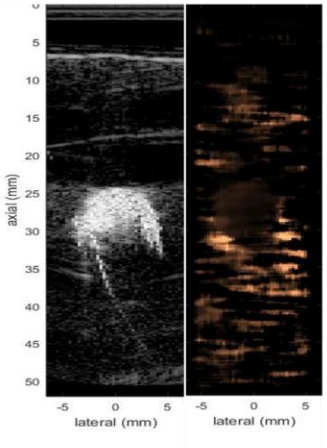

1.4 ± 0.3 μm

5N

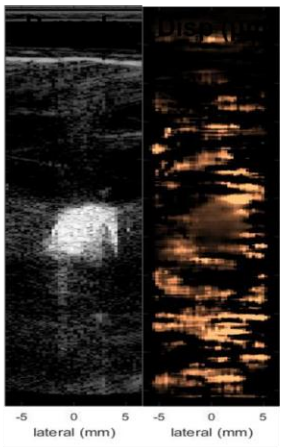

1.1 ± 0.3 μm

15N

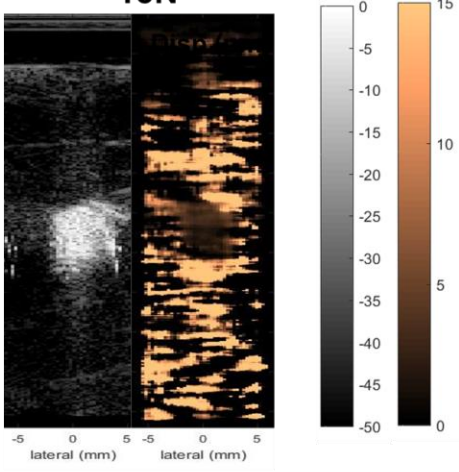

0.8 ± 0.2 μm

Specimen 6

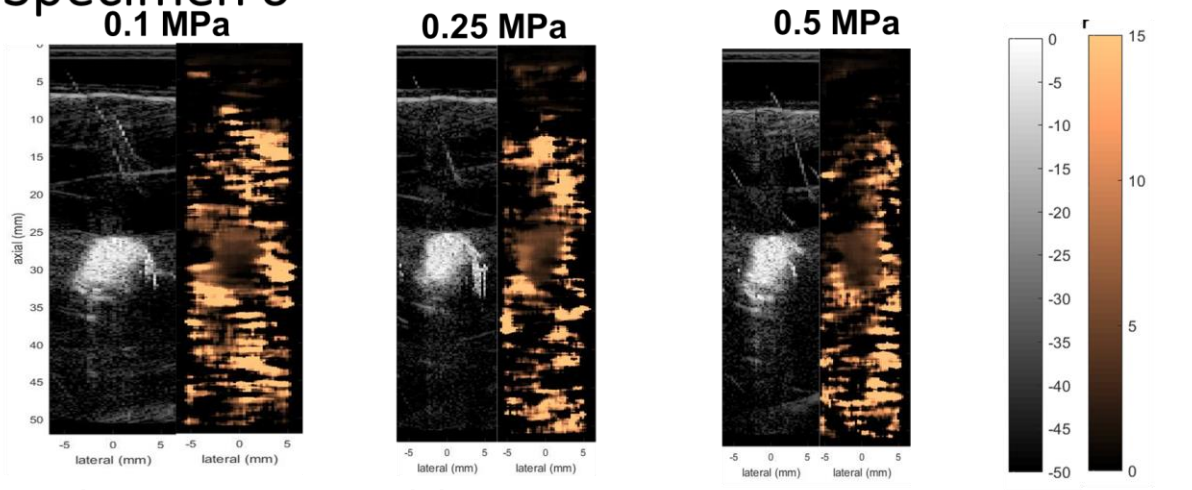

1.2 ± 0.3 µm

1.1 ± 0.2 µm

1.0 ± 0.2 µm

Specimen 7

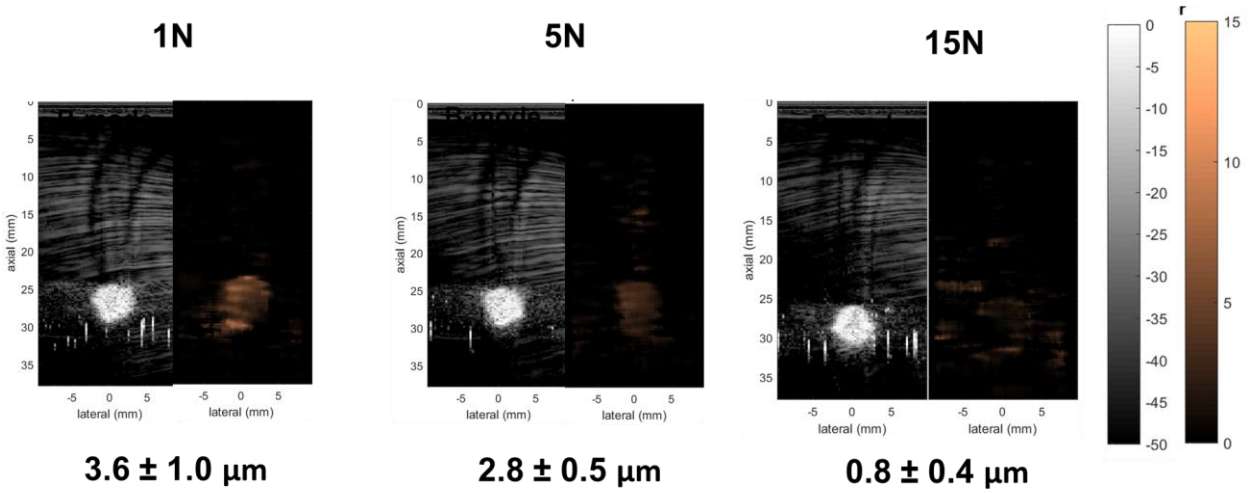

3.6 ± 1.0 µm

2.8 ± 0.5 µm

0.8 ± 0.4 µm

Specimen 7

0.1 MPa

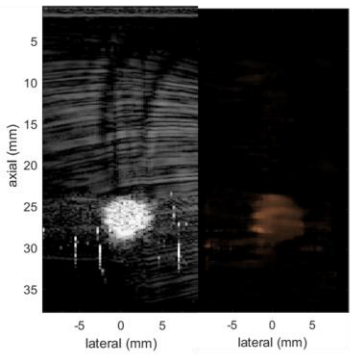

3.5 ± 0.7 µm

0.25 MPa

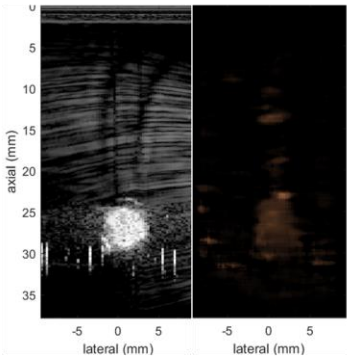

2.9 ± 0.4 µm

0.5 MPa

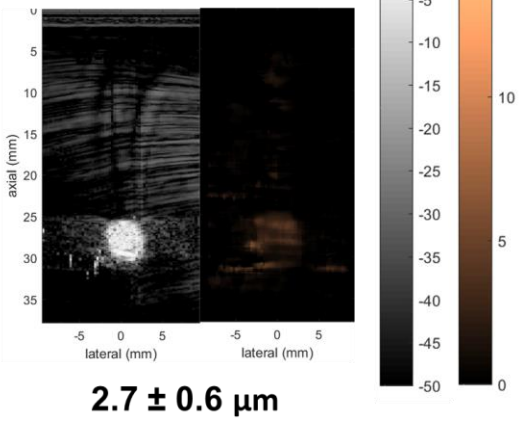

2.7 ± 0.6 µm

Specimen 8

1N

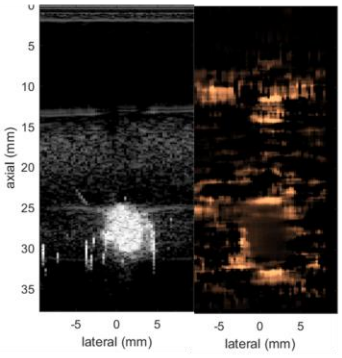

1.6 ± 0.3 µm

5N

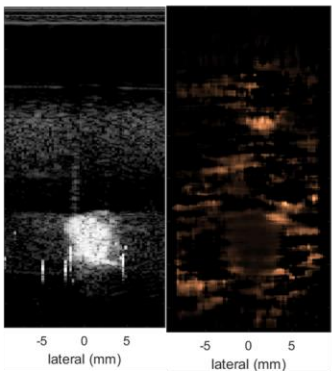

1.0 ± 0.2 µm

15N

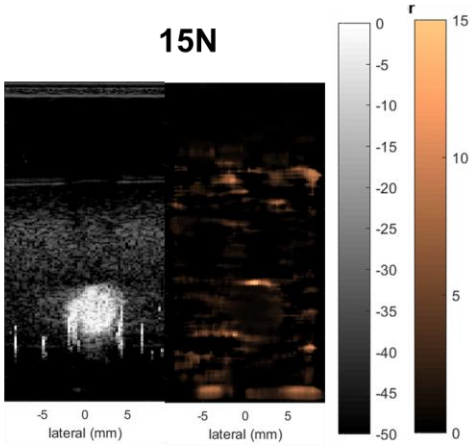

0.8 ± 0.1 µm

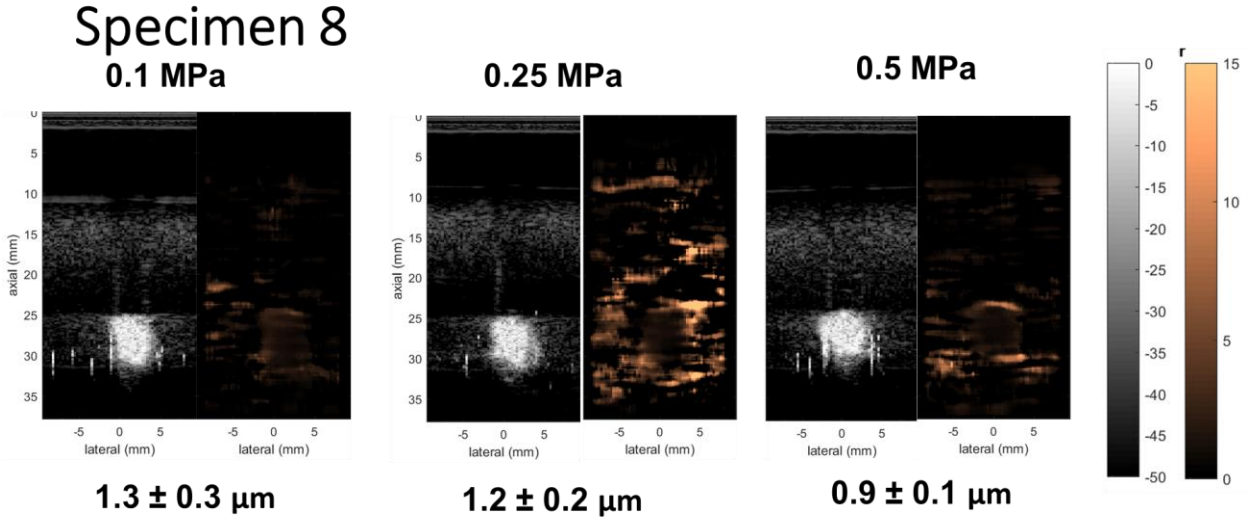
Specimen 8
0.1 MPa
0.25 MPa
0.5 MPa
axial (mm)
lateral (mm)
r
1.3 ± 0.3 µm
1.2 ± 0.2 µm
0.9 ± 0.1 µm

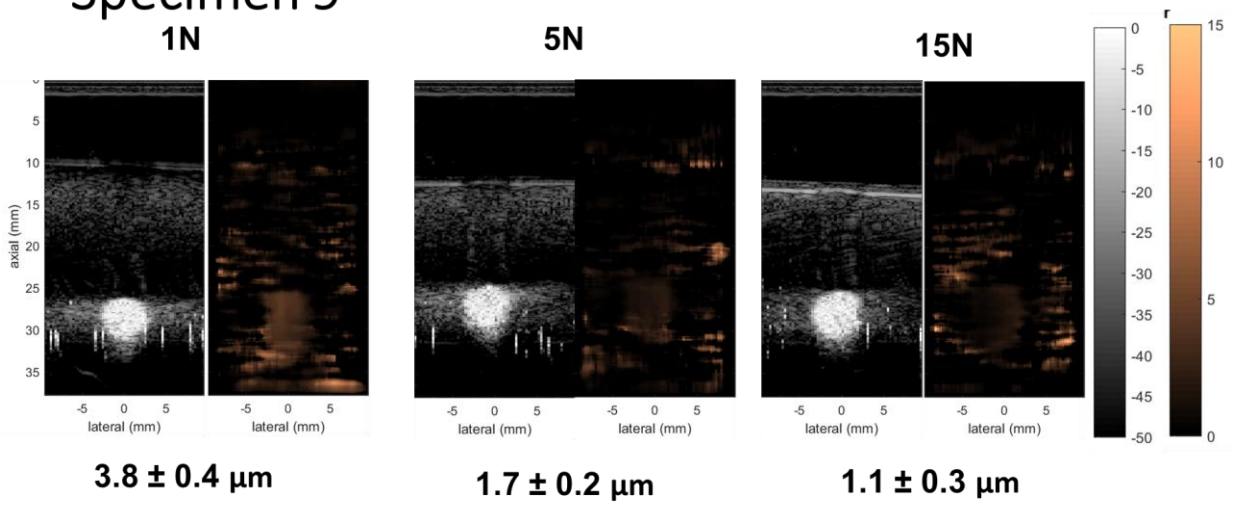
Specimen 9
1N
5N
15N
axial (mm)
lateral (mm)
r
3.8 ± 0.4 µm
1.7 ± 0.2 µm
1.1 ± 0.3 µm

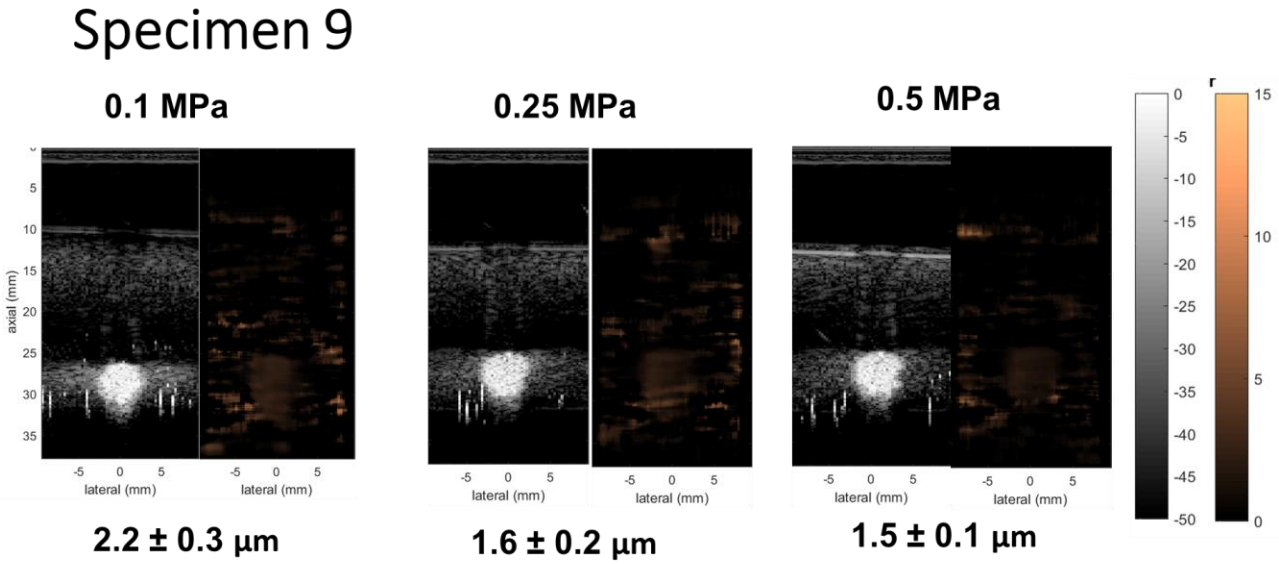

Summary of tensile and compressive (indentation test) properties as well as ARFI displacement data for all 9 specimens

	Ind Stiff	Toe Region Modulus	Linear Region Modulus	1N	5N	15N	0.1Mpa	0.25MPa	0.5MPa
VA15071335L		91.36	147.29	3.4 ± 0.2	2.8 ± 0.2	2.3 ± 0.2			
C141074R		40.49	89.25	2.2 ± 0.5	1.7 ± 0.3	1.3 ± 0.3			
MD13071637L		67.92	183.29	3.2 ± 0.4	2.1 ± 0.4	1.9 ± 0.3			
C150313L		78.11	100.53	4.6 ± 0.6	4.1 ± 0.6	2.0 ± 0.4			
FL14072154L		40.87	98.83	4.6 ± 0.5	4.2 ± 0.3	2.0 ± 0.4			
15-0431R	0.84	49.76	109.28	1.4 ± 0.3	1.2 ± 0.4	0.8 ± 0.2	1.2 ± 0.3	1.1 ± 0.2	1.0 ± 0.2
15-0890L	0.83	55.04	117.16	3.6 ± 1.1	2.8 ± 0.5	0.8 ± 0.4	3.5 ± 0.7	2.9 ± 0.4	2.7 ± 0.6
15-0577R	0.36	65.28	137.64	1.6 ± 0.3	1.0 ± 0.2	0.8 ± 0.1	1.3 ± 0.3	1.2 ± 0.2	0.9 ± 0.1
15-0949R	1.03	116.95	196.75	3.8 ± 0.4	1.7 ± 0.2	1.1 ± 0.3	2.2 ± 0.3	1.6 ± 0.2	1.5 ± 0.1

Raw data for full-frame versus multi-foci ARFI imaging at 0.1, 0.25, 0.5, 0.75 and 1MPa of tension for 4 tendons, before and after damaging through compressive loading

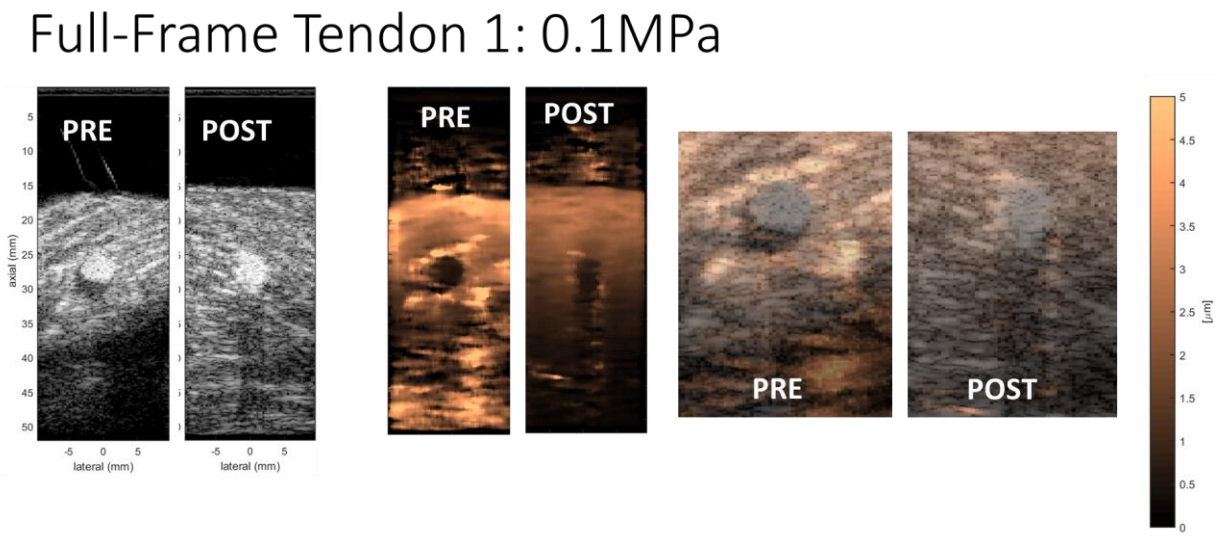

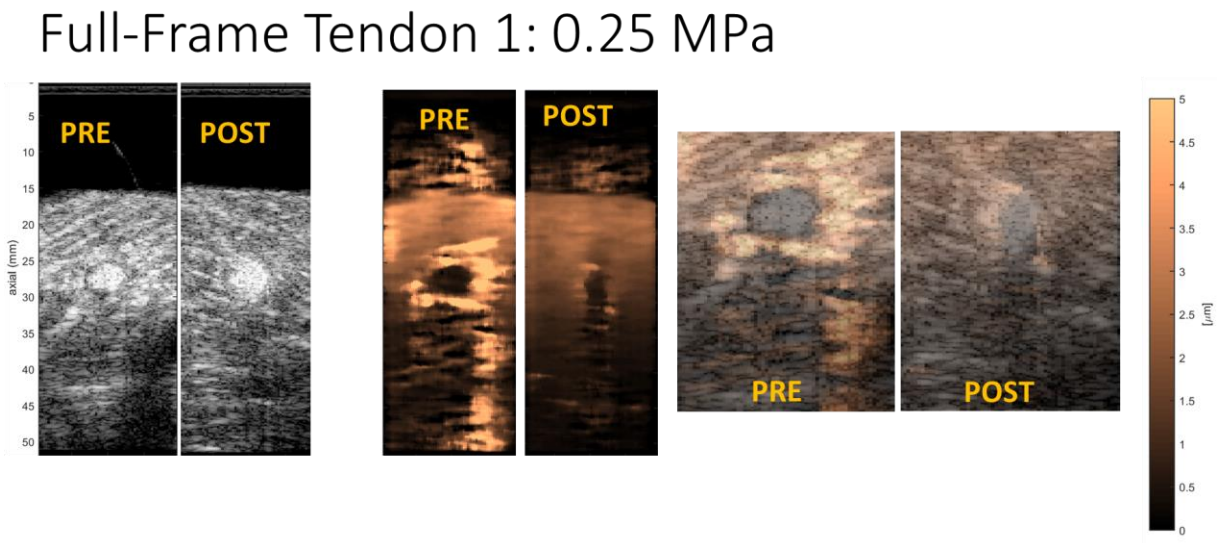

Full-Frame Tendon 1: 0.5 MPa

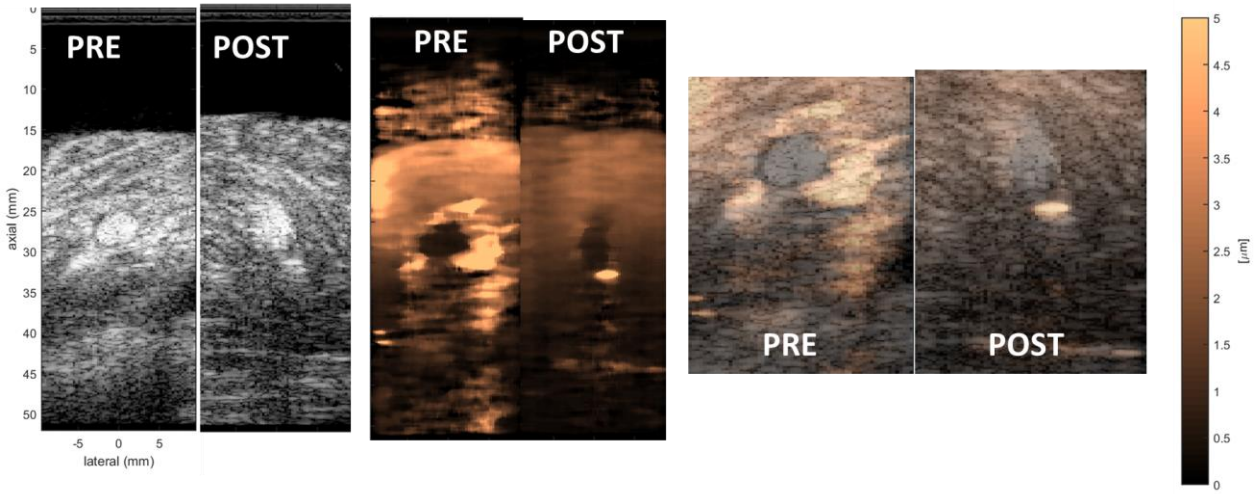

Full-Frame Tendon 1: 0.75 MPa

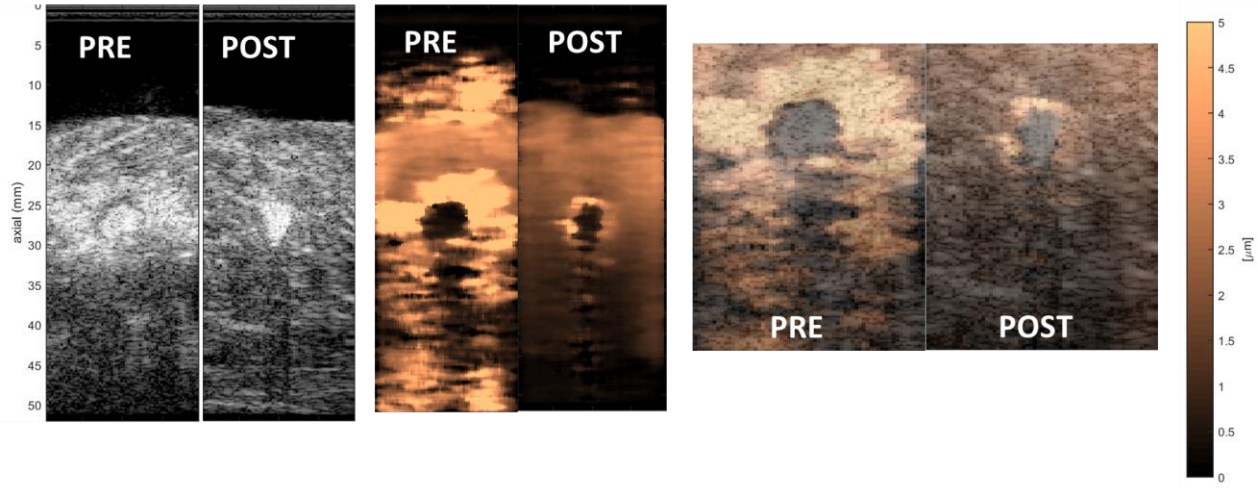

Full-Frame Tendon 1: 1 MPa

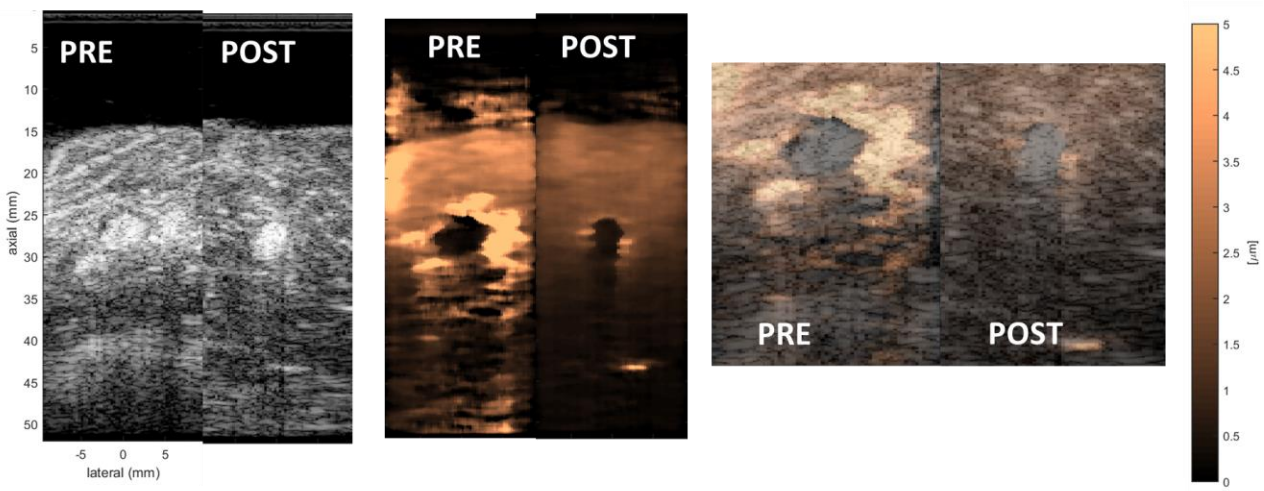

Multi-Foci Tendon 1: 0.1MPa

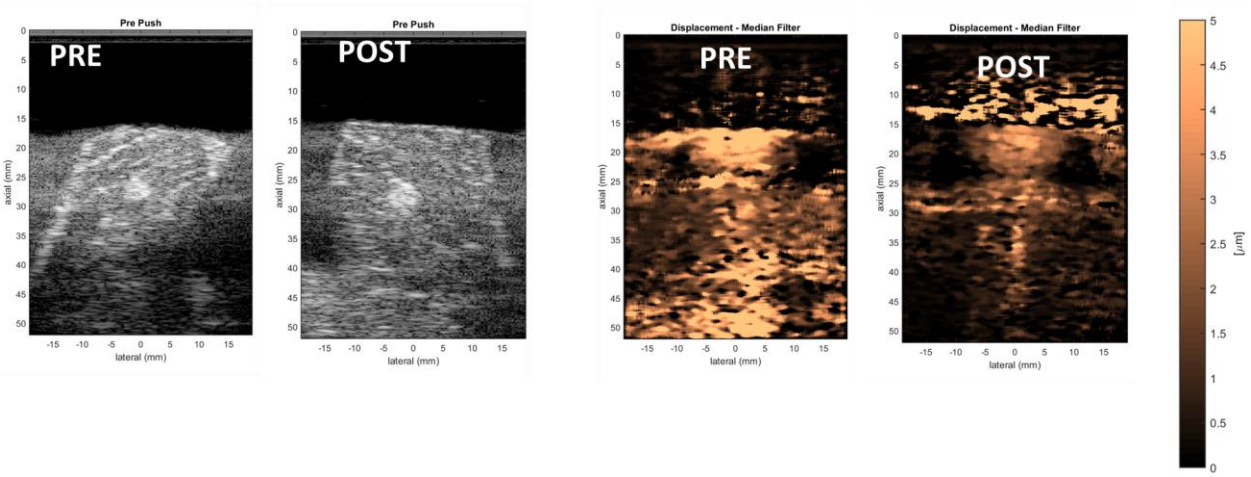

Multi-Foci Tendon 1: 0.25 MPa

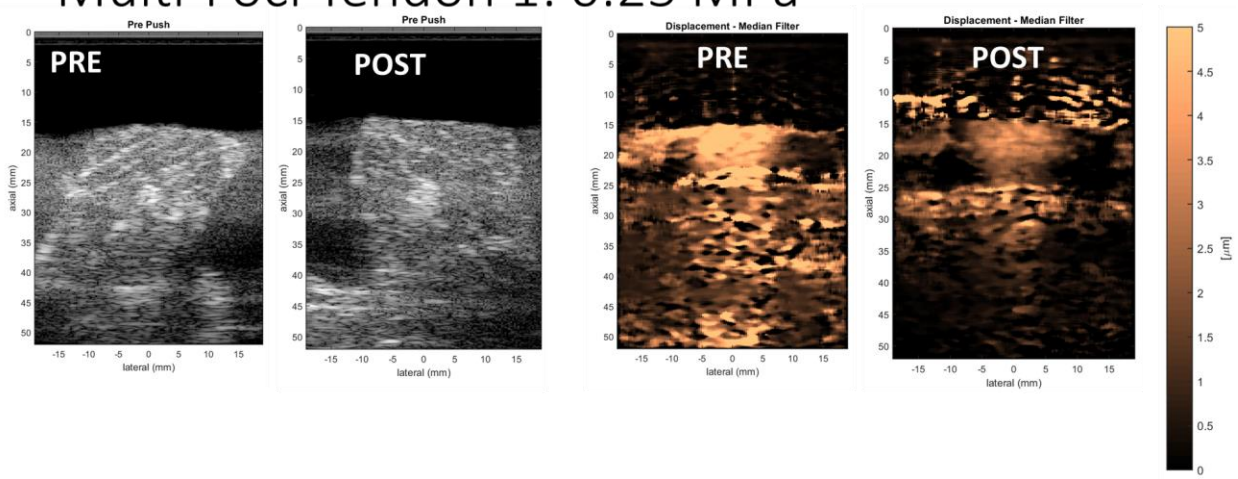

Multi-Foci Tendon 1: 0.5 MPa

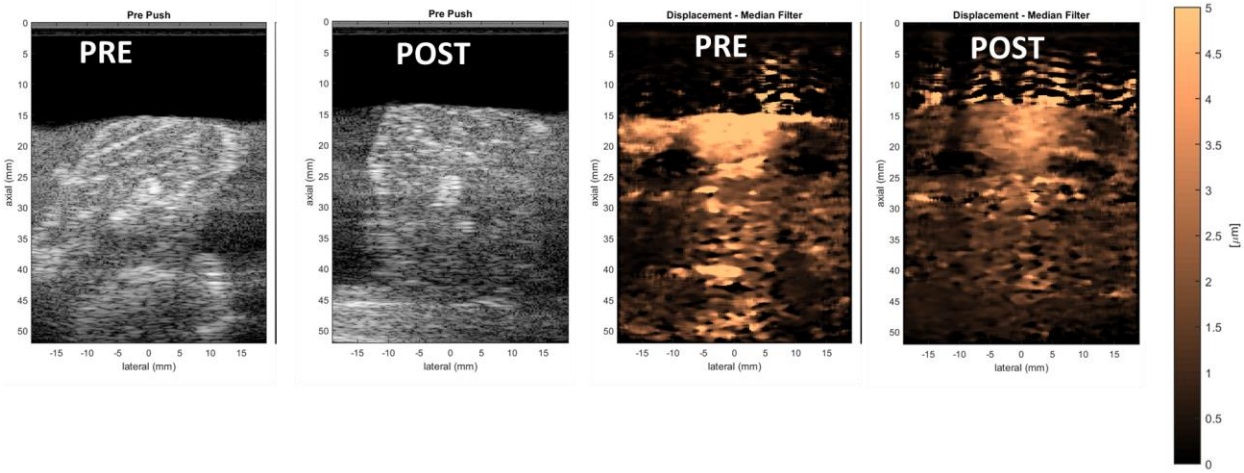

Multi-Foci Tendon 1: 0.75 MPa

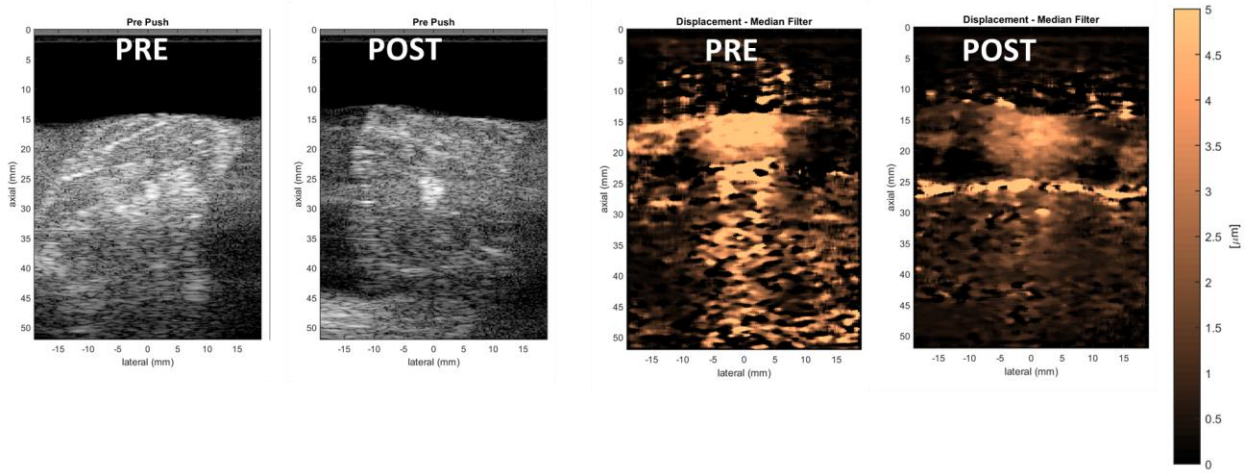

Multi-Foci Tendon 1: 1 MPa

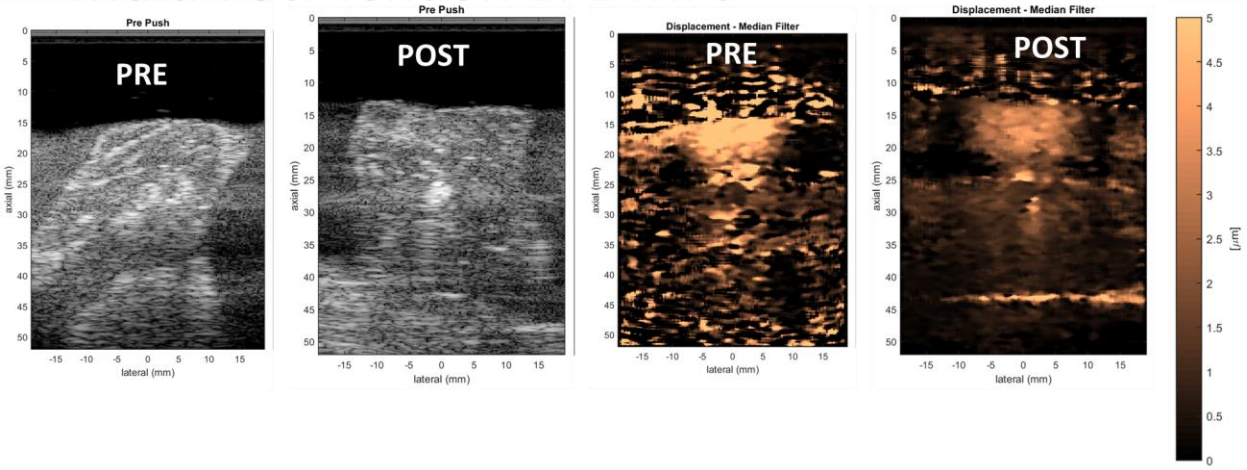

Tendon 1 Results

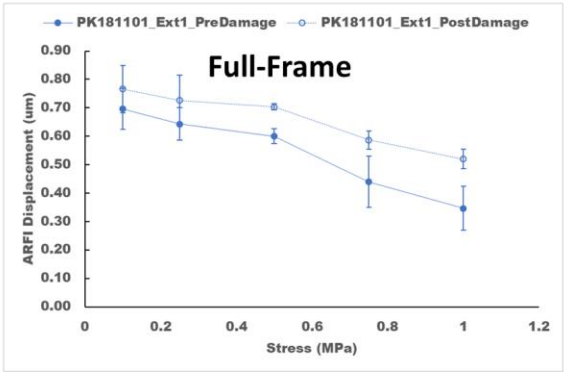

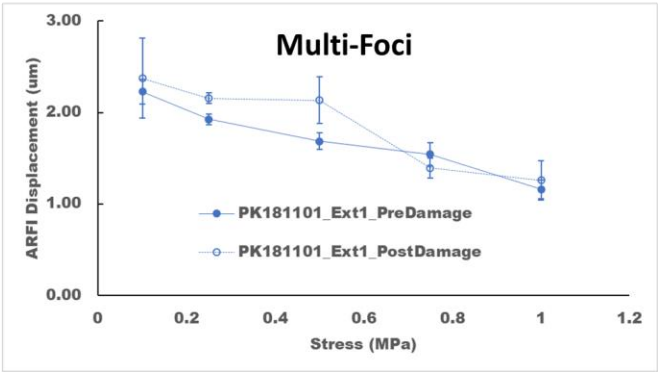

Full-Frame Tendon 2: 0.1 MPa

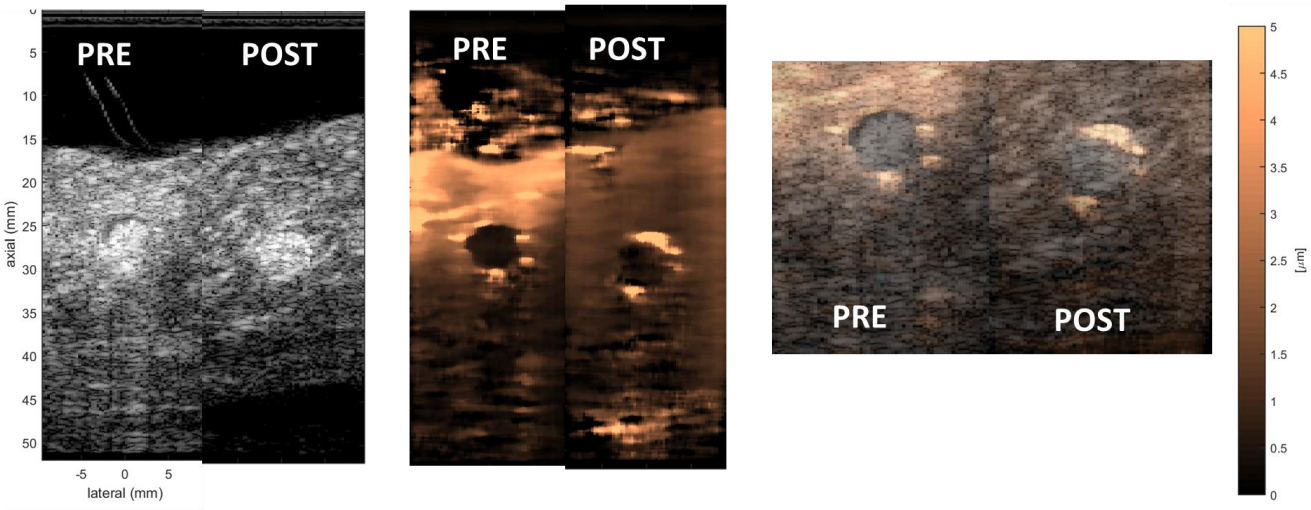

Full-Frame Tendon 2: 0.25 MPa

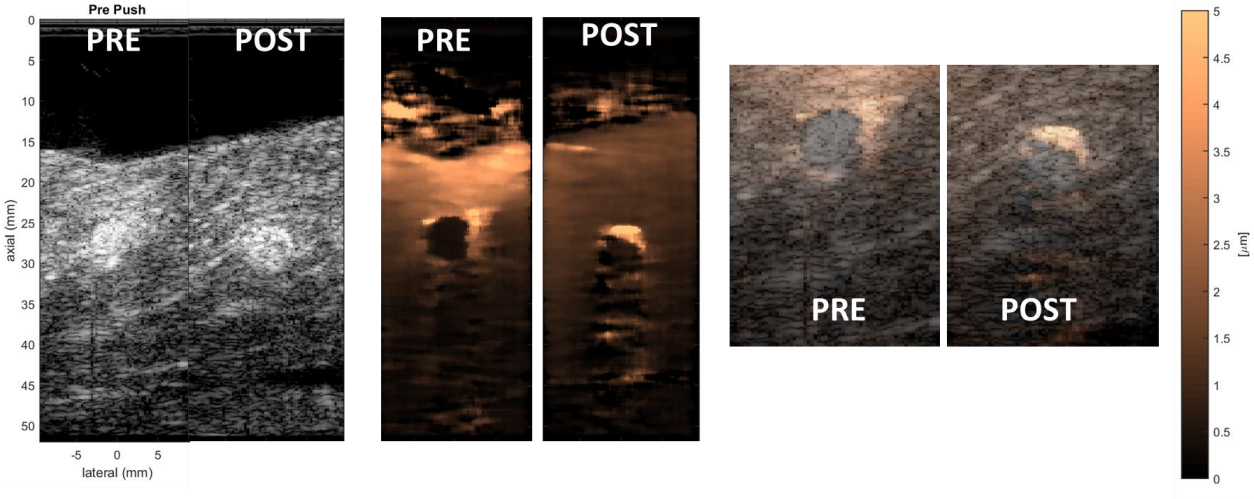

Full-Frame Tendon 2: 0.5 MPa

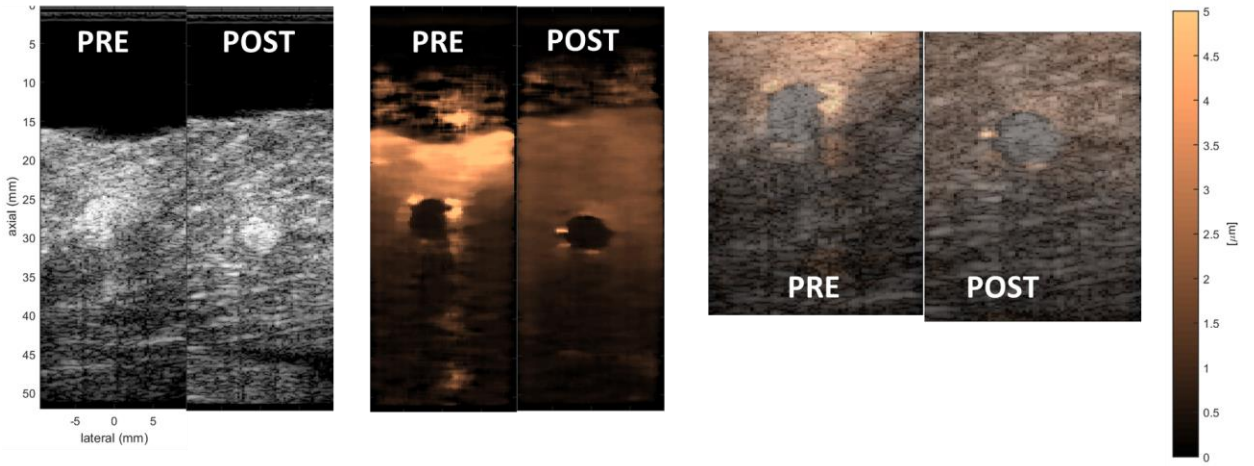

Full-Frame Tendon 2: 0.75 MPa

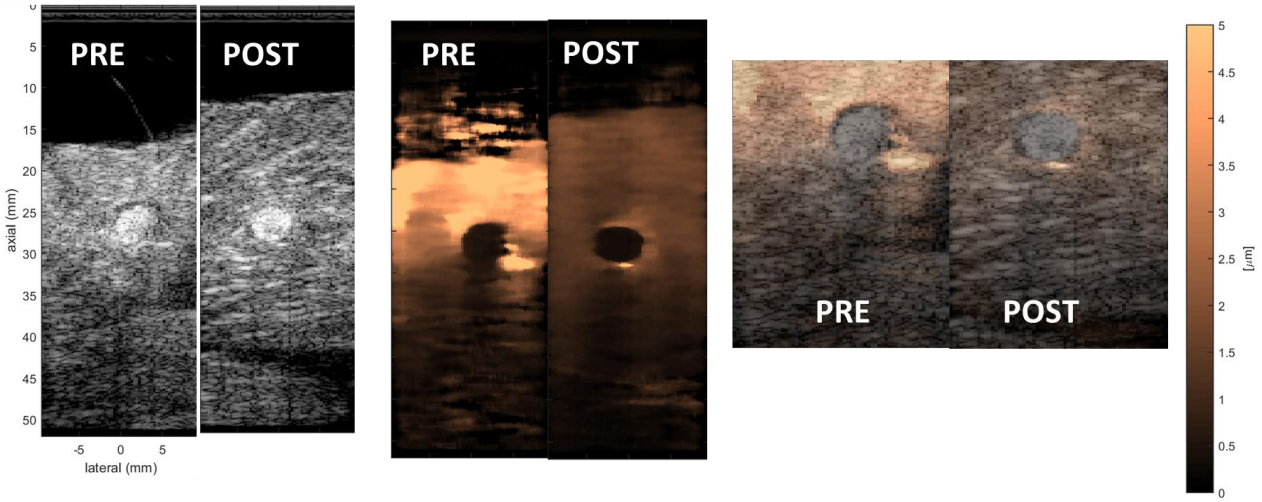

Full-Frame Tendon 2: 1 MPa

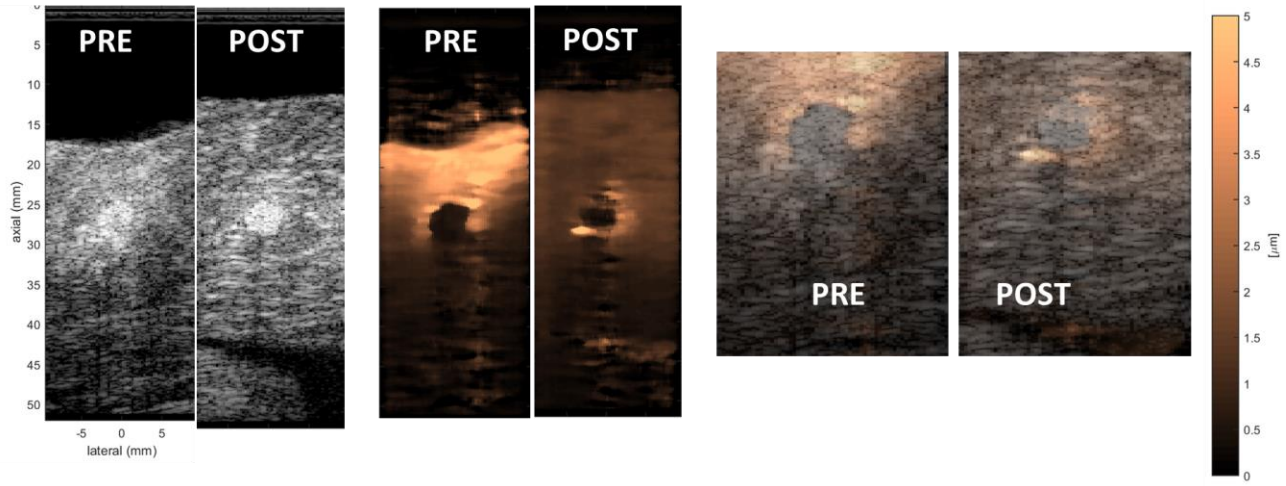

Multi-Foci Tendon 2: 0.1MPa

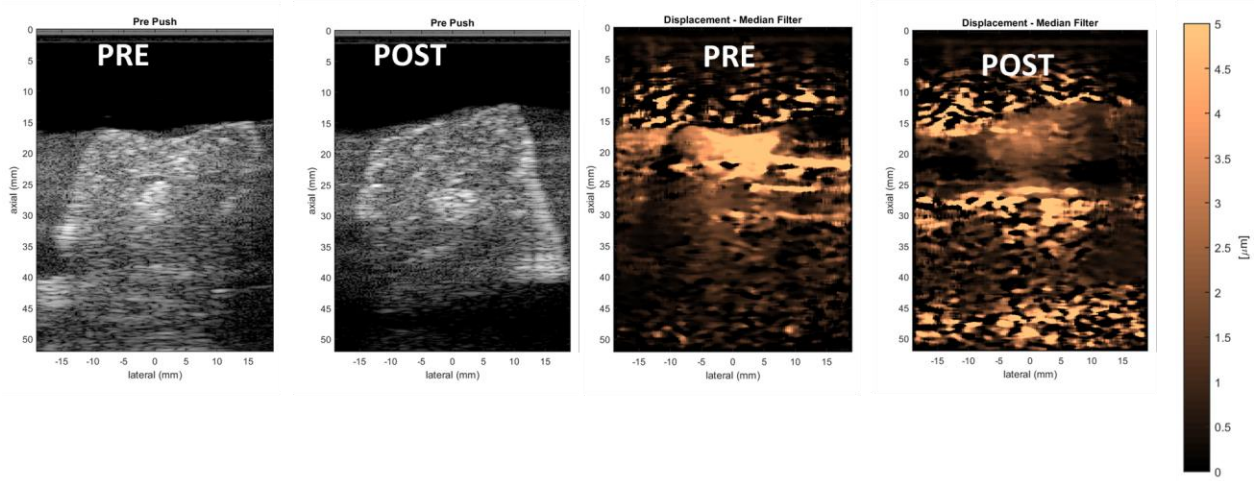

Multi-Foci Tendon 2: 0.25 MPa

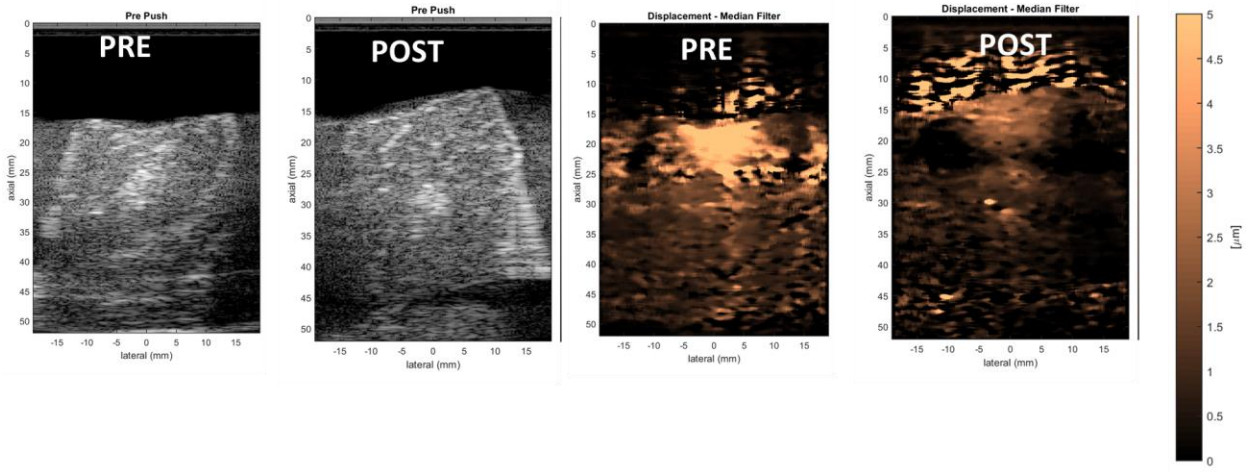

Multi-Foci Tendon 2: 0.5 MPa

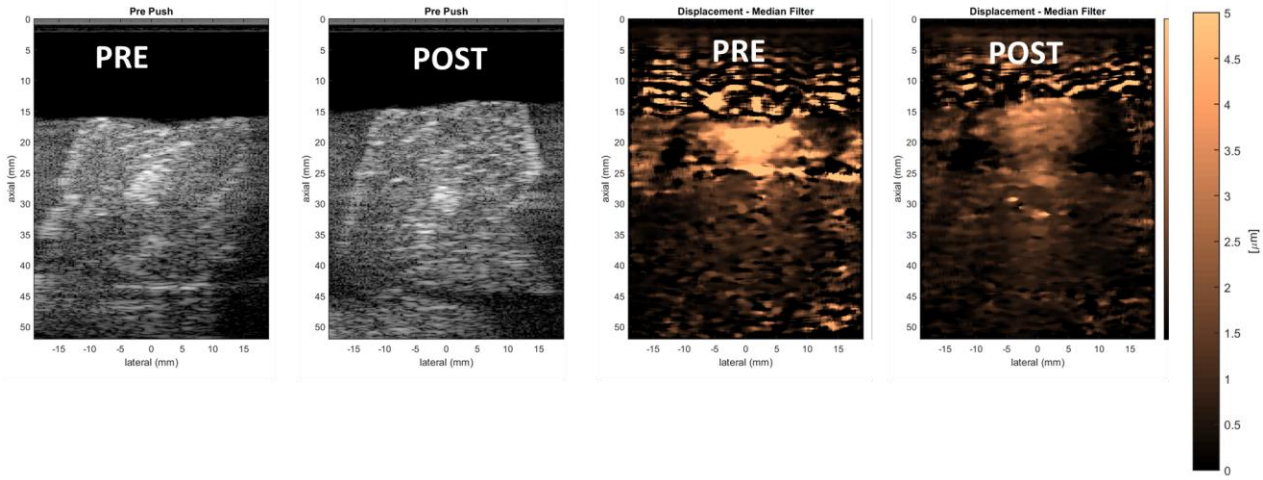

Multi-Foci Tendon 2: 0.75 MPa

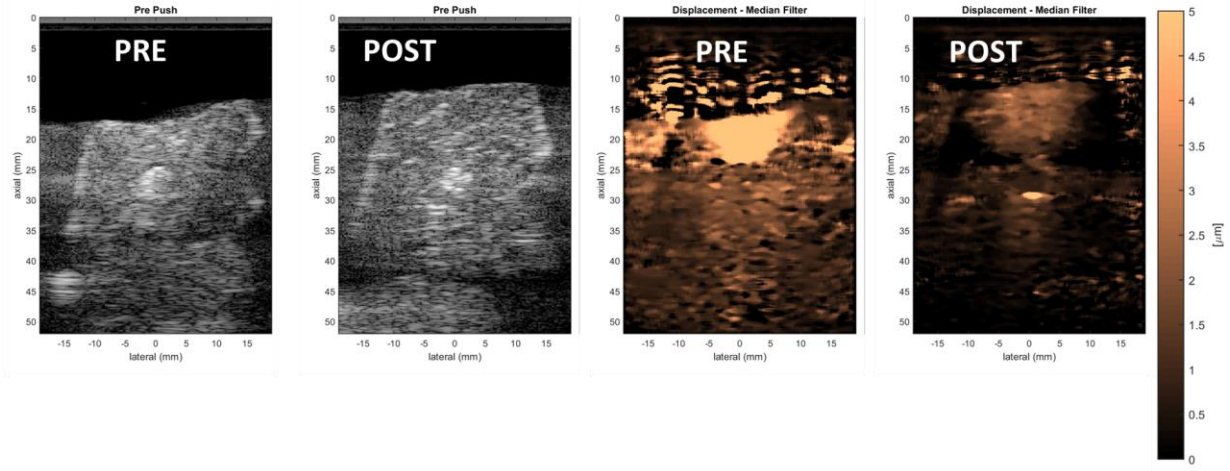

Multi-Foci Tendon 2: 1 MPa

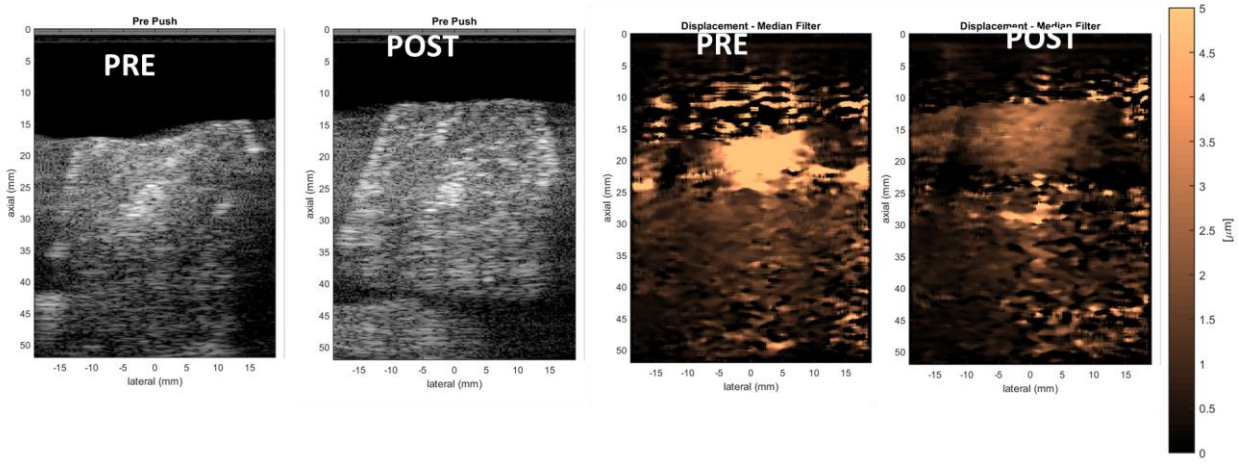

Tendon 2 Results

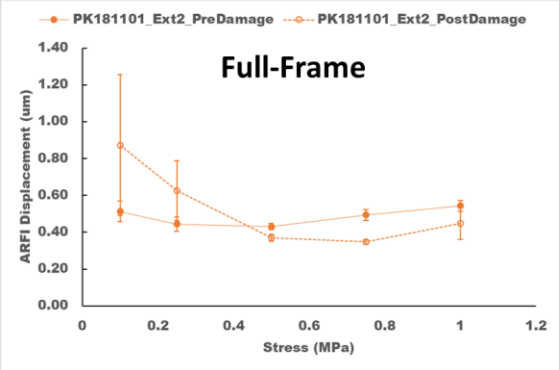

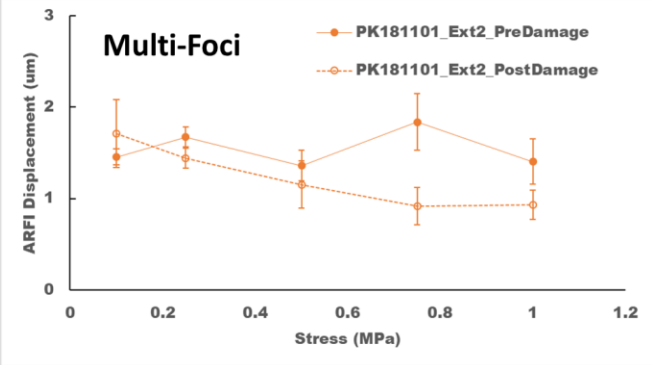

Full-Frame Tendon 3: 0.1 MPa

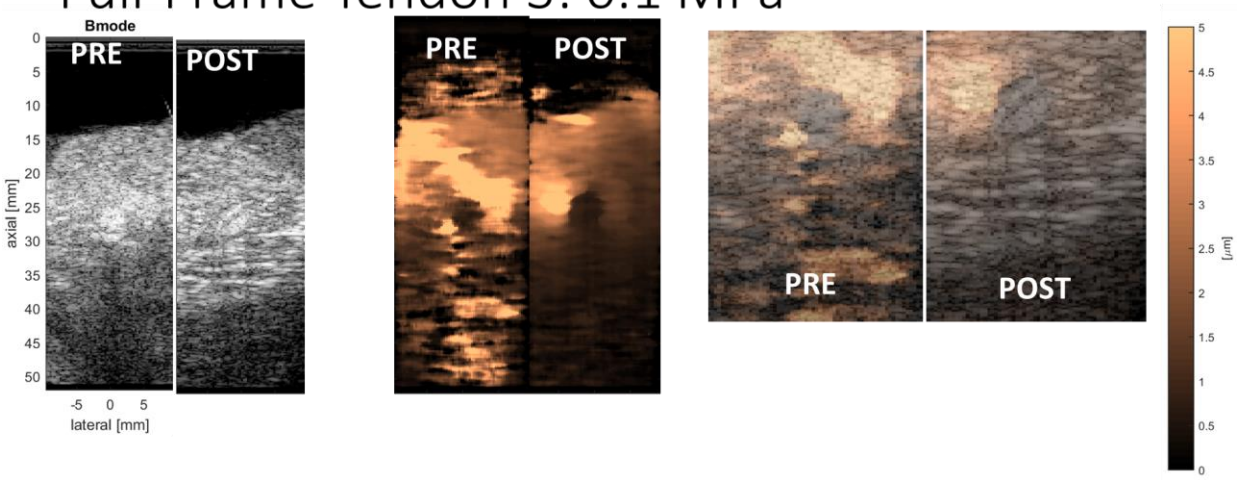

Full-Frame Tendon 3: 0.25 MPa

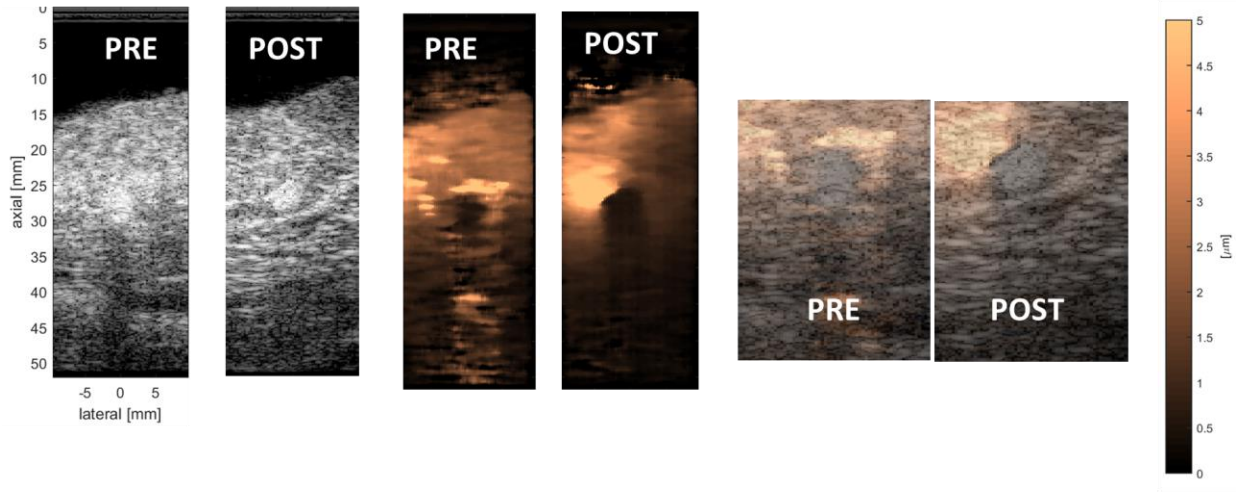

Full-Frame Tendon 3: 0.5 MPa

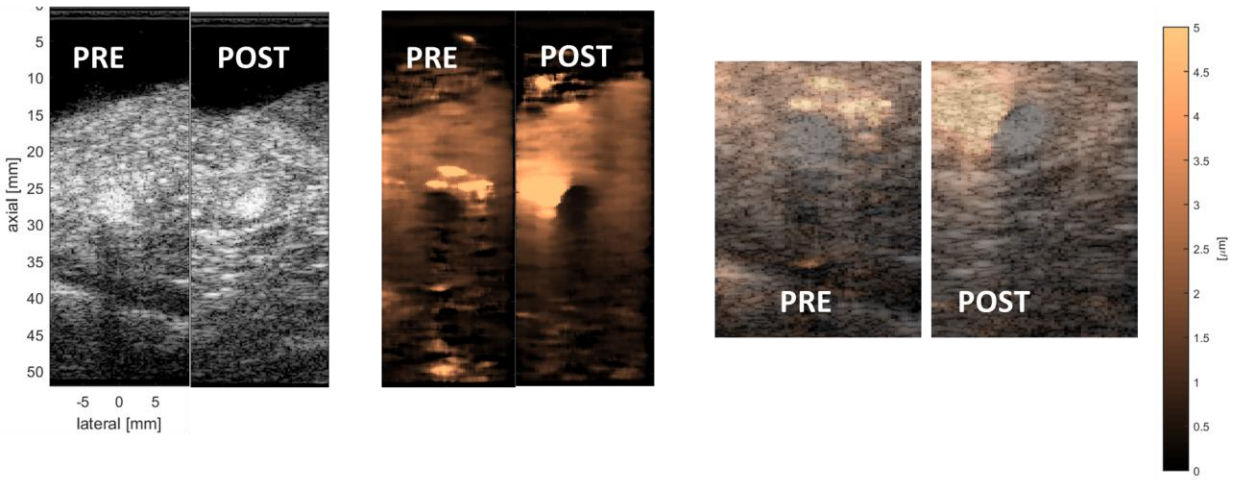

Full-Frame Tendon 3: 0.75 MPa

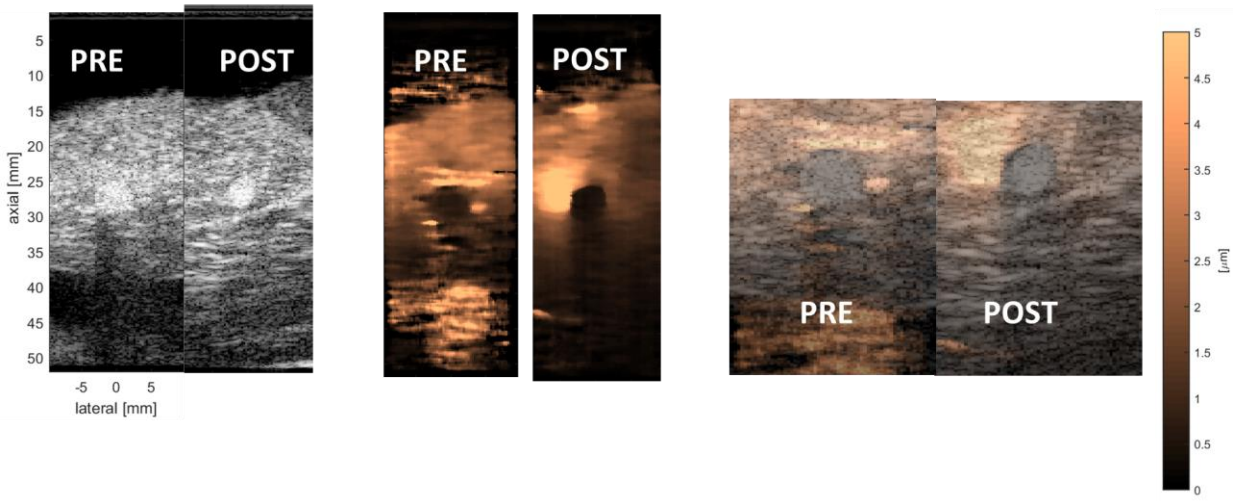

Full-Frame Tendon 3: 1 MPa

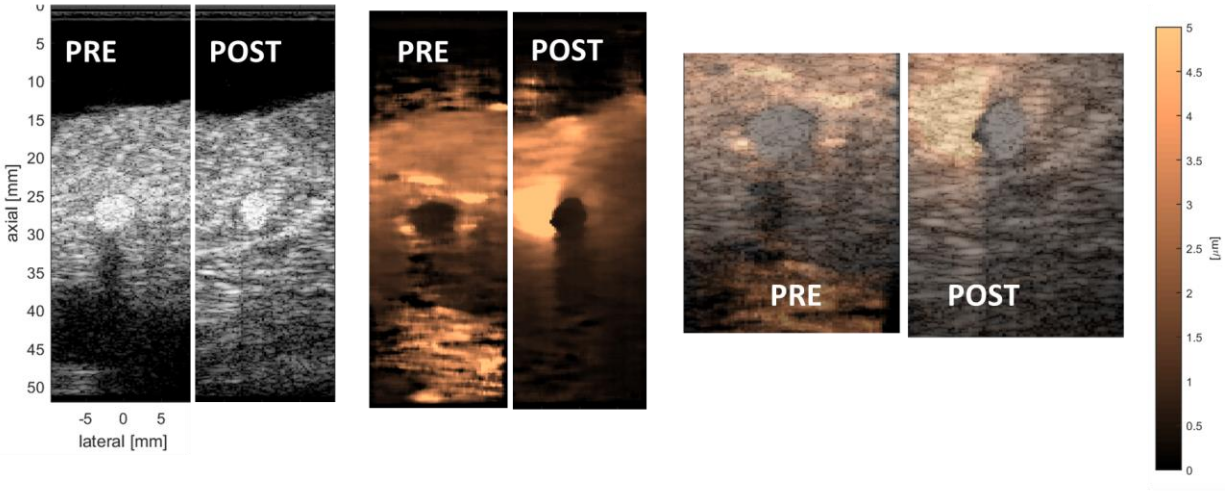

Multi-Foci Tendon 3: 0.1MPa

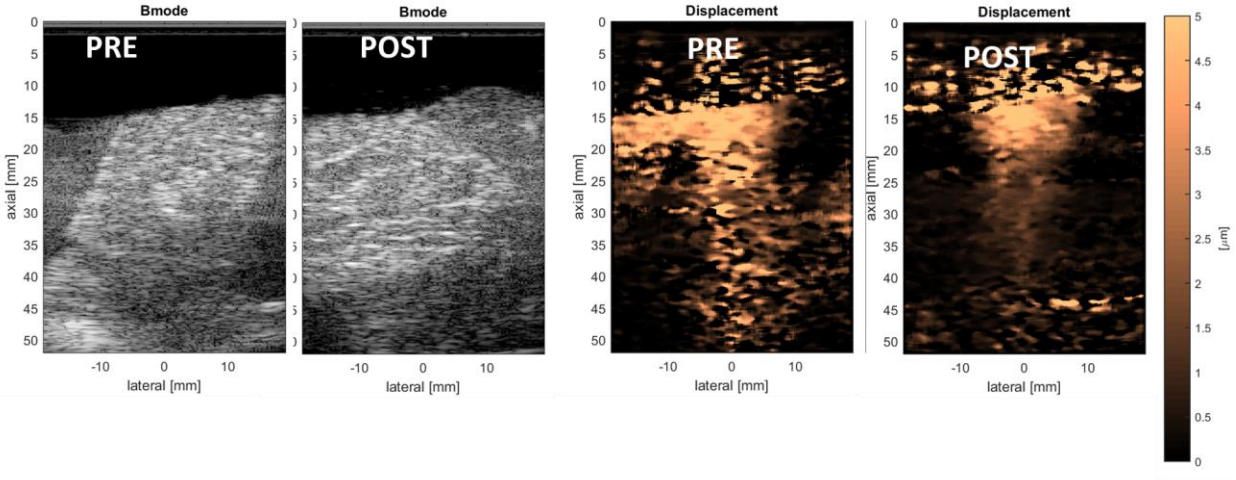

Multi-Foci Tendon 3: 0.25 MPa

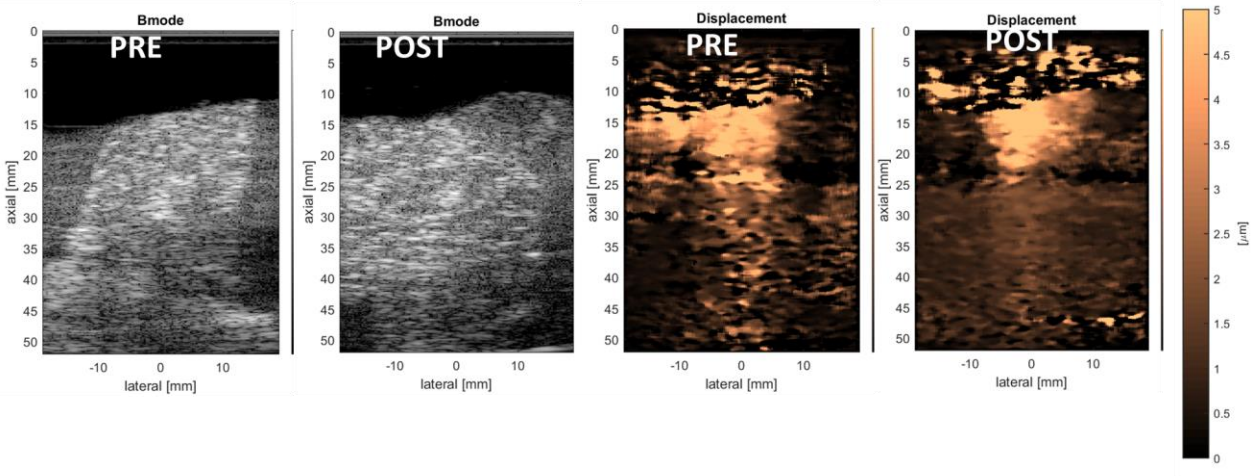

Multi-Foci Tendon 3: 0.5 MPa

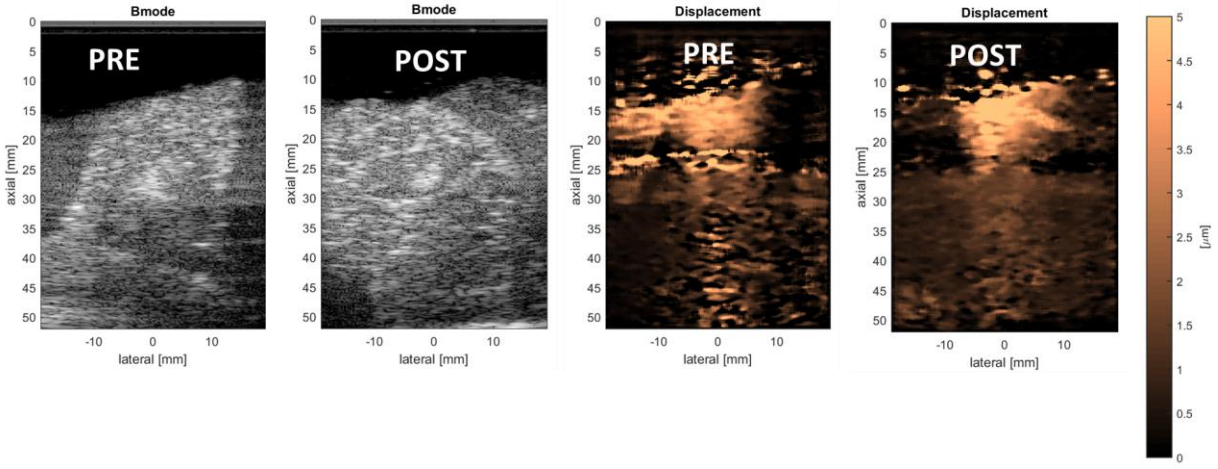

Multi-Foci Tendon 3: 0.75 MPa

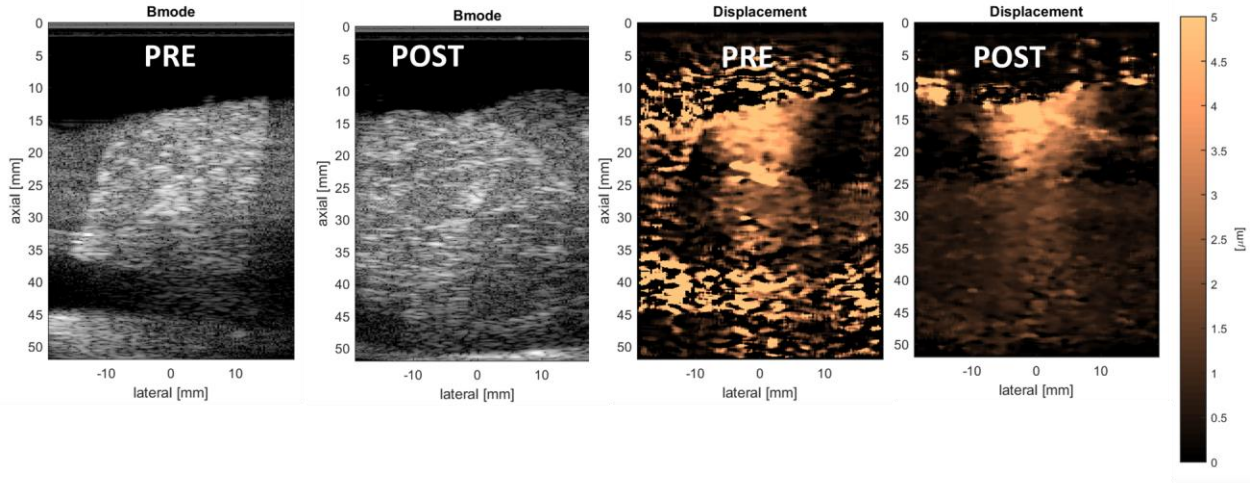

Multi-Foci Tendon 3: 1 MPa

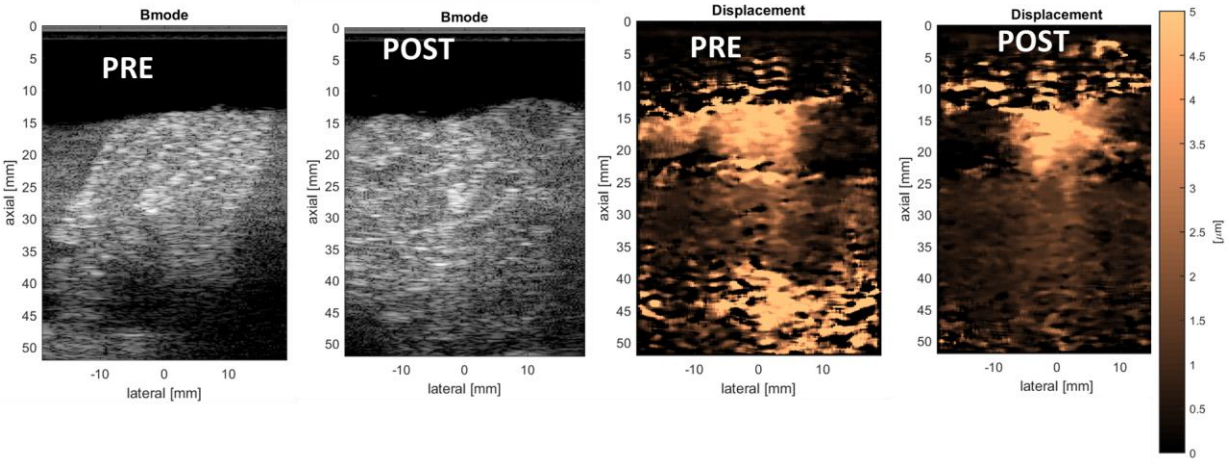

Tendon 3 Results

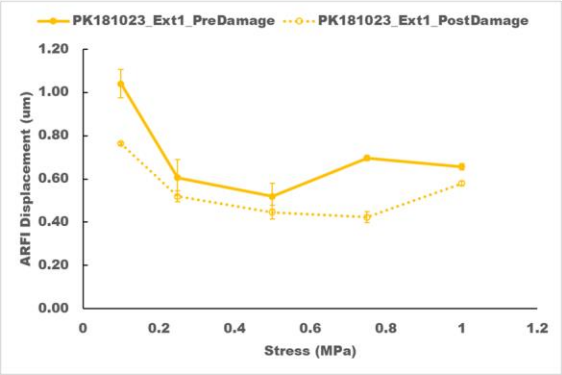

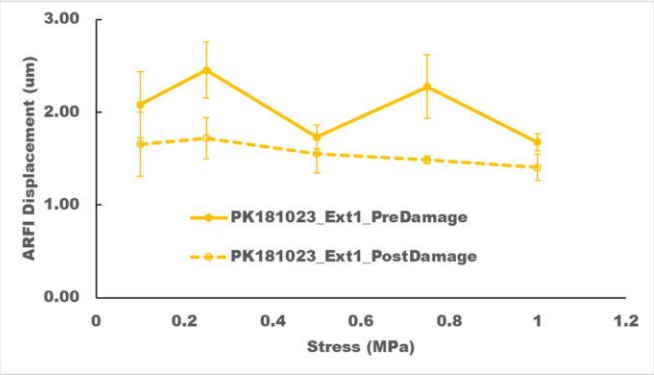

Full-Frame Tendon 4: 0.1 MPa

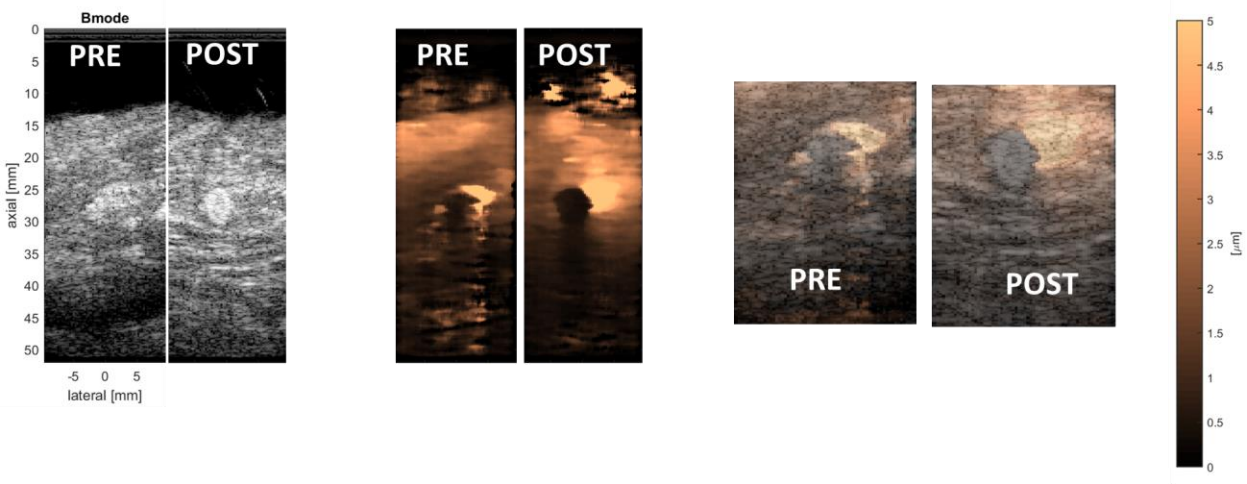

Full-Frame Tendon 4: 0.25 MPa

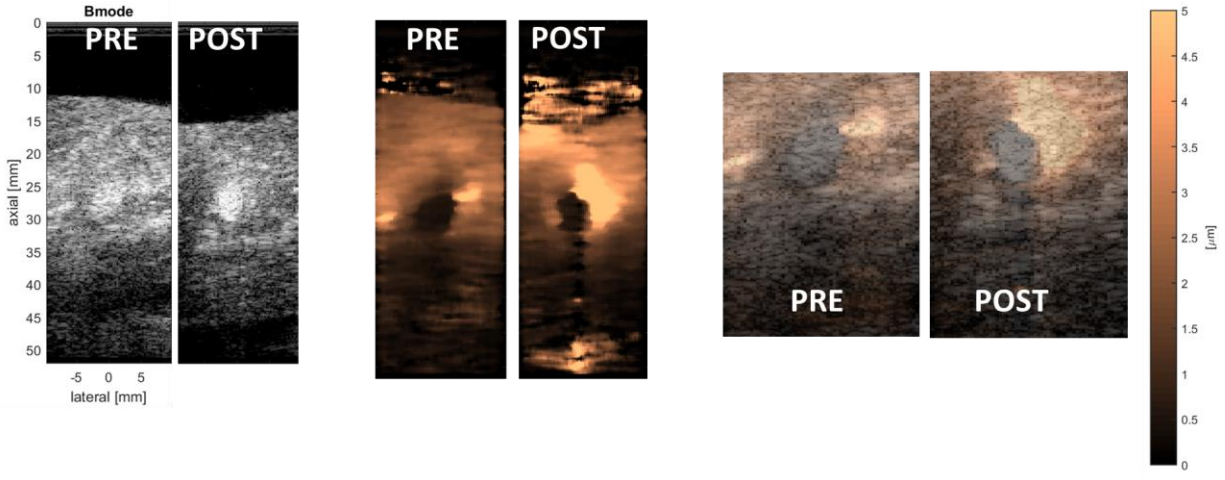

Full-Frame Tendon 4: 0.5 MPa

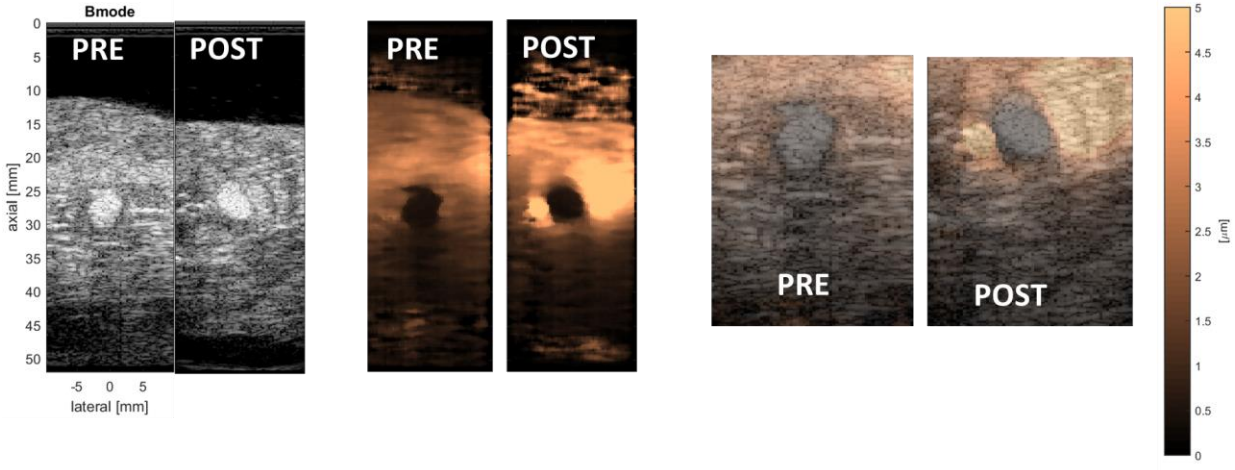

Full-Frame Tendon 4: 0.75 MPa

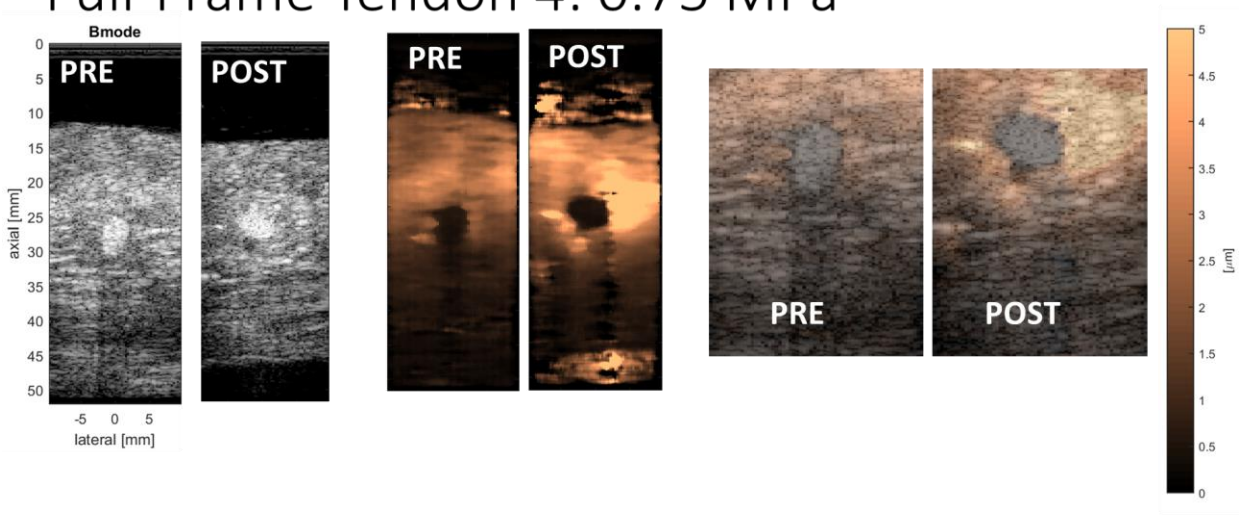

Full-Frame Tendon 4: 1 MPa

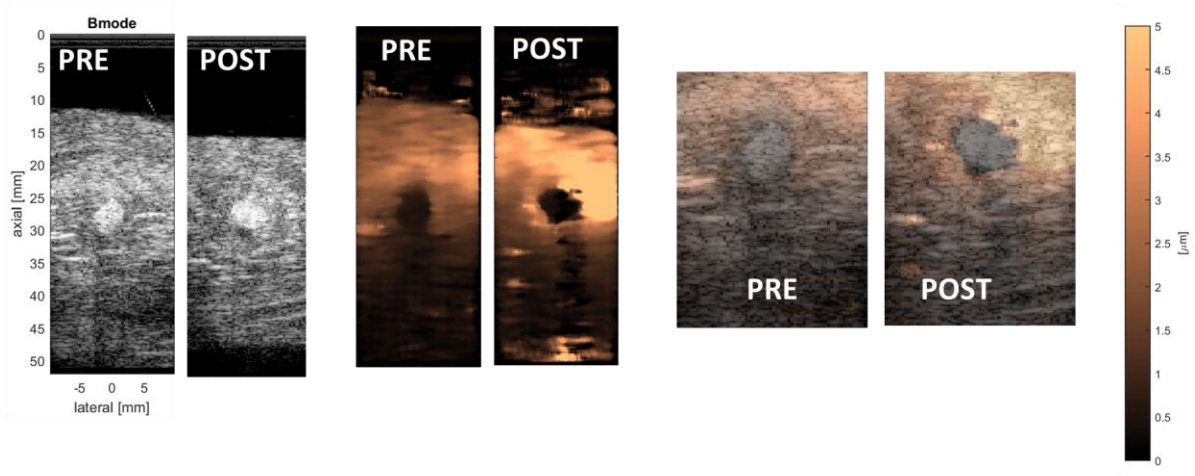

Multi-Foci Tendon 4: 0.1MPa

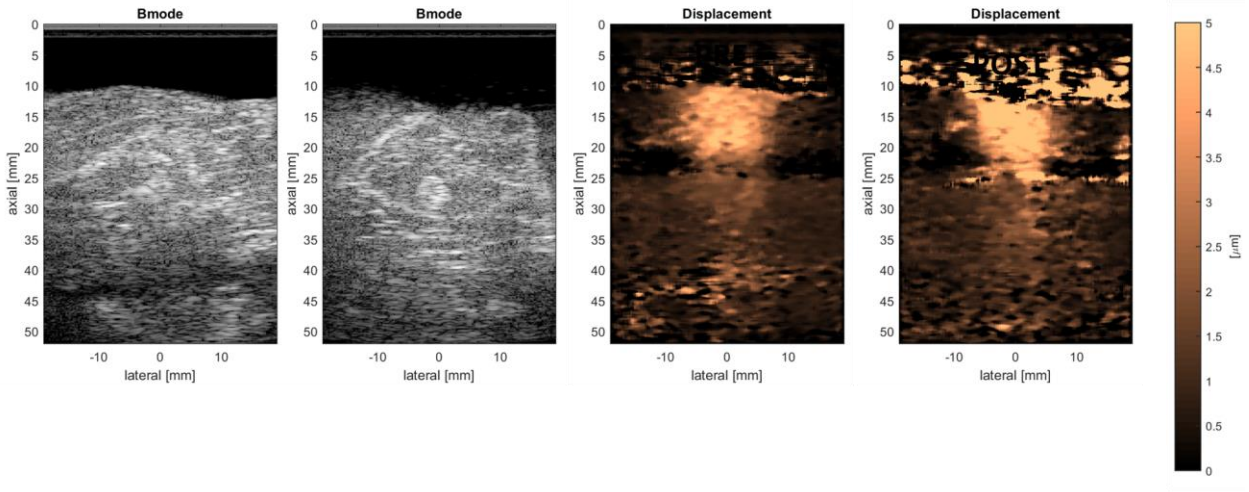

Multi-Foci Tendon 4: 0.25 MPa

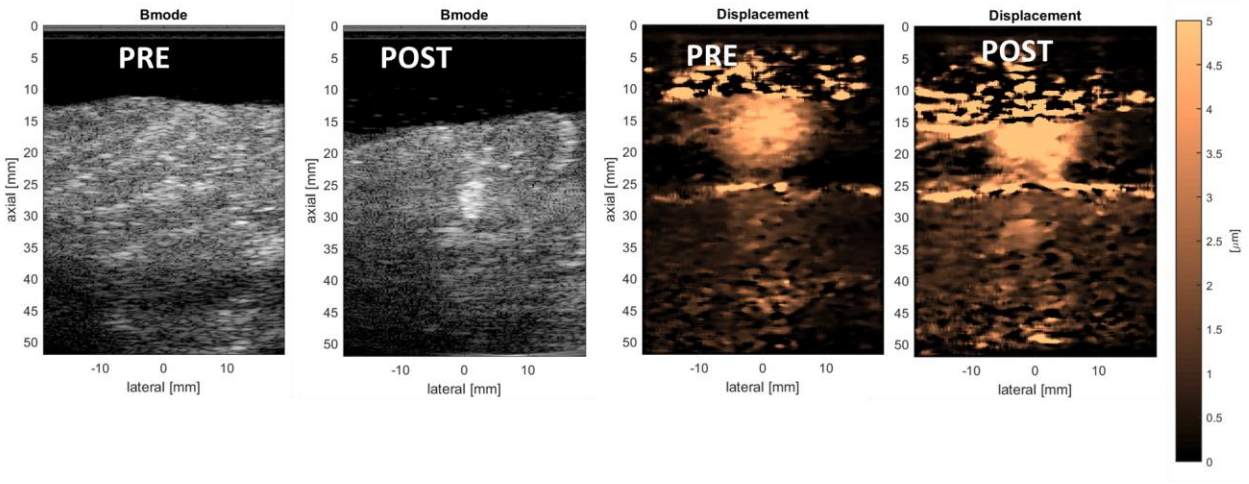

Multi-Foci Tendon 4: 0.5 MPa

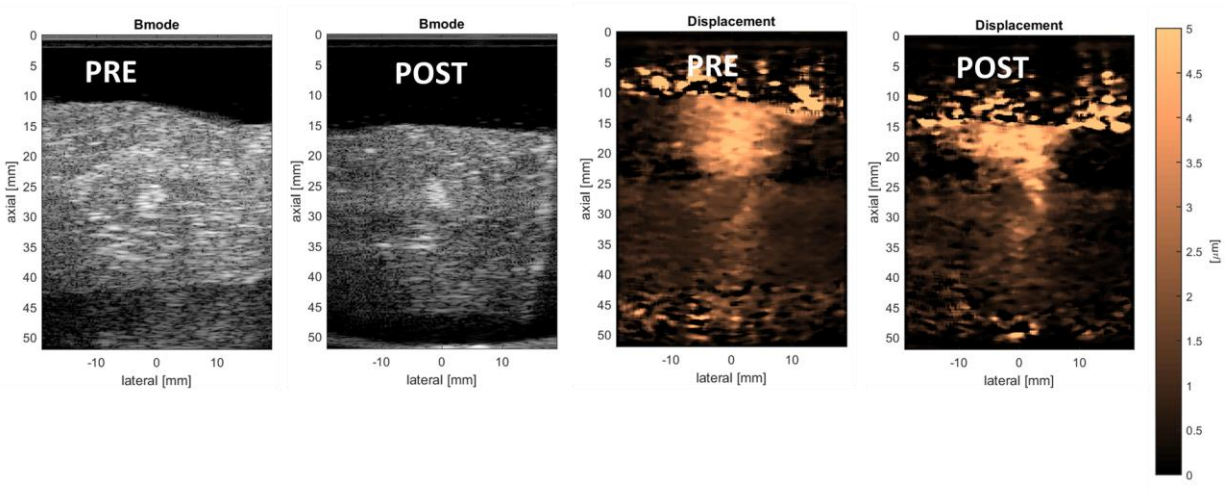

Multi-Foci Tendon 4: 0.75 MPa

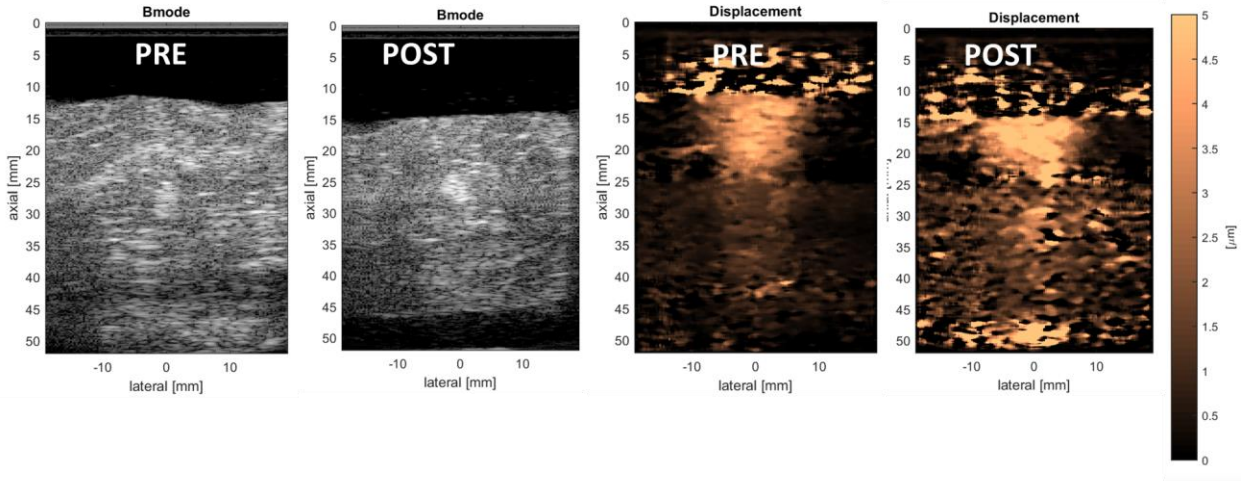

Multi-Foci Tendon 4: 1 MPa

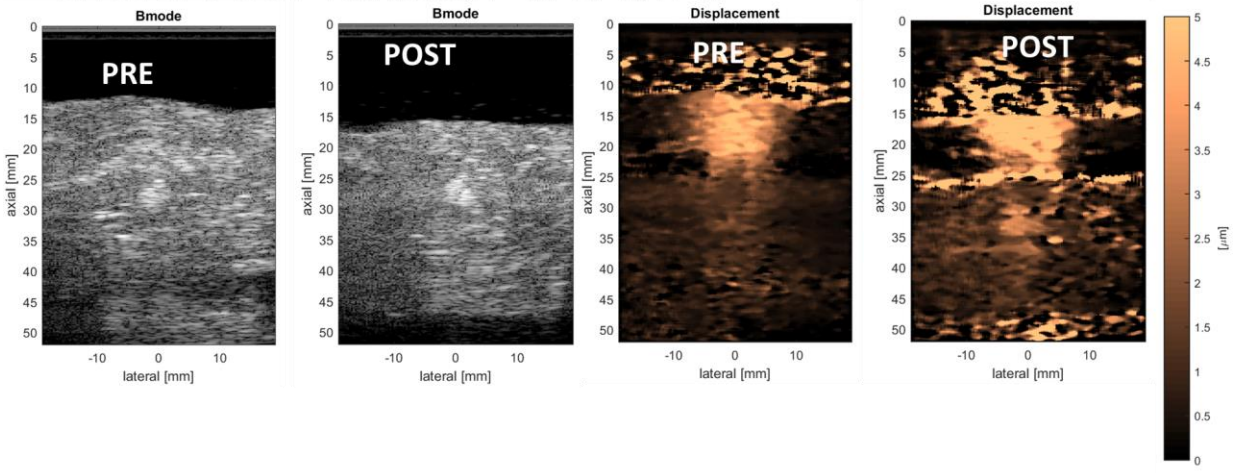

Tendon 4 Results

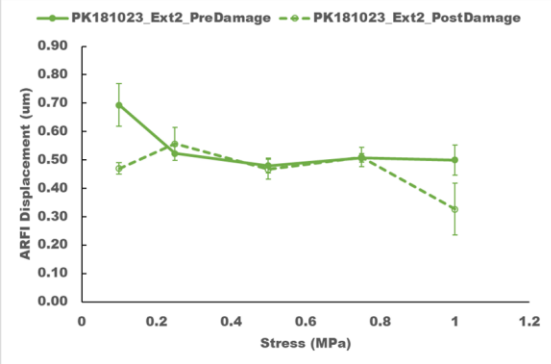

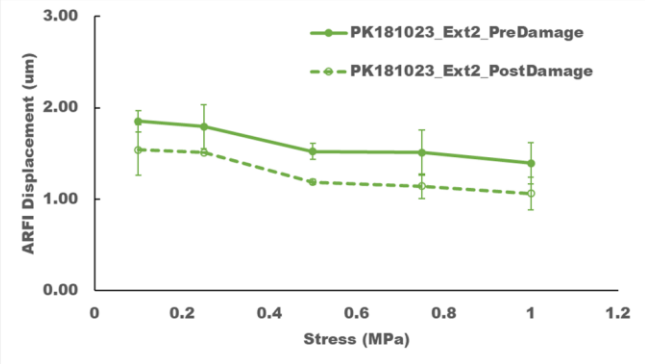

Raw data images for muscle, tendon, capsule experiment. Tissues were embedded in a gelatin phantom when tensioned at 0.1MPa

Tendon 1

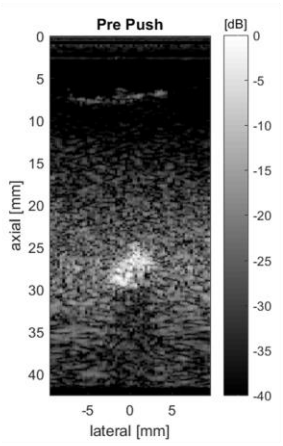

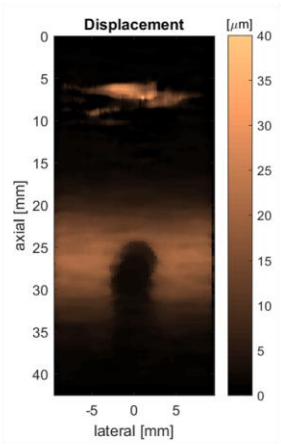

Modulus (MPa)	Norm Disp	Tissue (um)	Gel (um)
309.4	0.16	3.1	19.6

Tendon 2

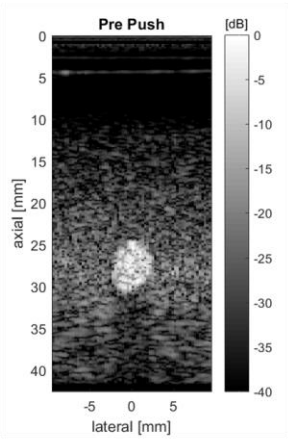

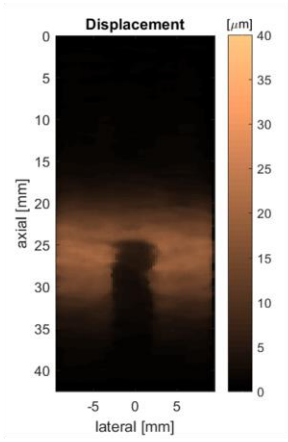

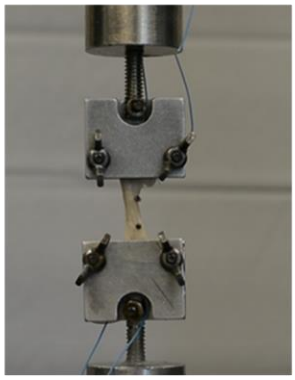

Modulus (MPa)	Norm Disp	Tissue (um)	Gel (um)
134.8	0.3	5.5	18.0

Tendon 3

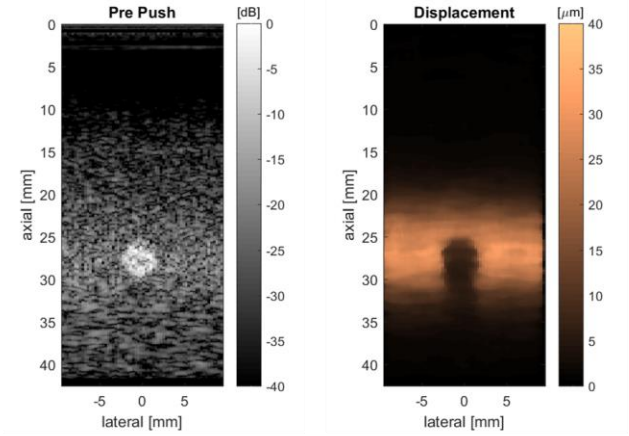

Modulus (MPa)	Norm Disp	Tissue (um)	Gel (um)
430.2	0.33	9.2	28.0

Tendon 4

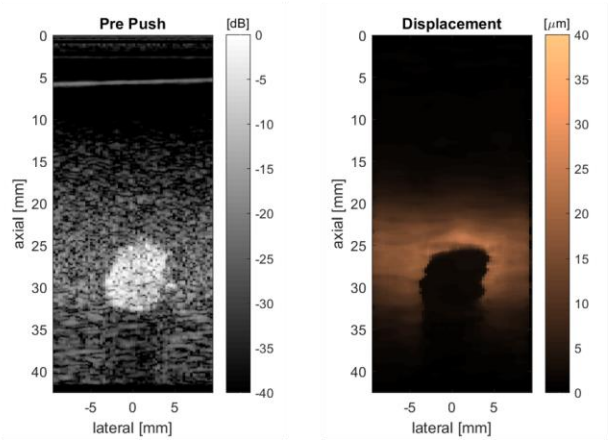

Modulus (MPa)	Norm Disp	Tissue (um)	Gel (um)
140.4	0.34	2.8	15.9

Tendon 5

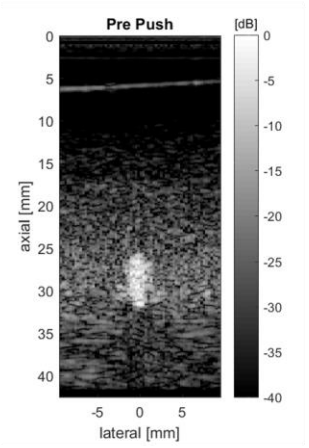

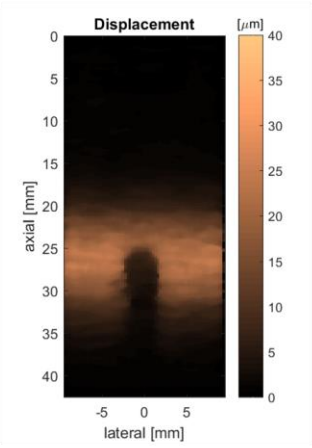

Modulus (MPa)	Norm Disp	Tissue (um)	Gel (um)
274.3	0.34	7.2	21.1

Capsule 1

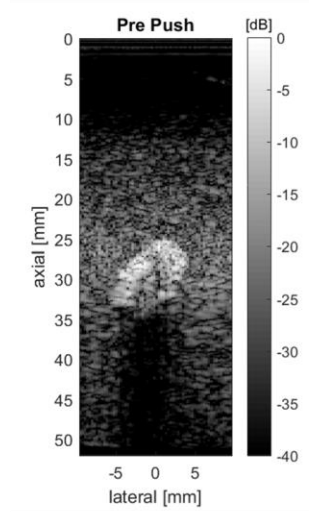

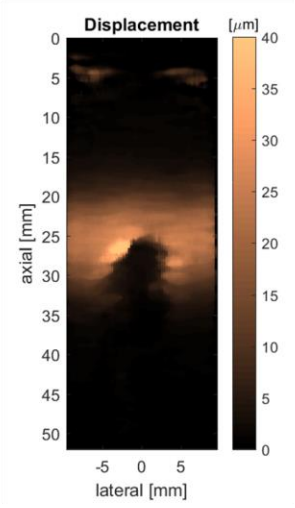

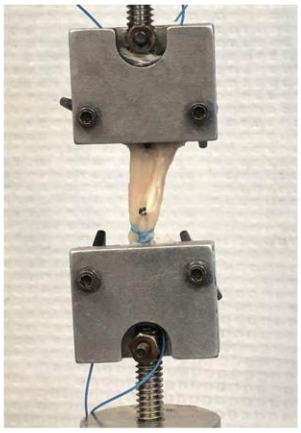

Modulus (MPa)	Norm Disp	Tissue (um)	Gel (um)
9.0	0.14	2.6	18.6

Capsule 2

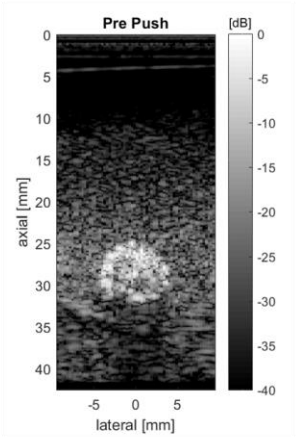

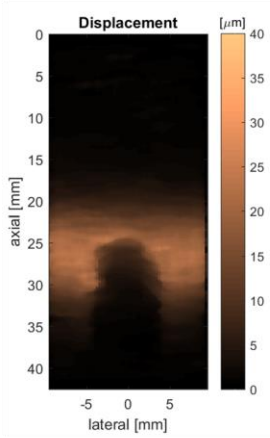

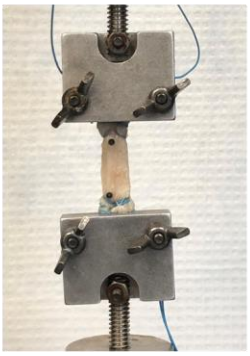

Modulus (MPa)	Norm Disp	Tissue (um)	Gel (um)
66.6	0.45	9.3	20.9

Capsule 3

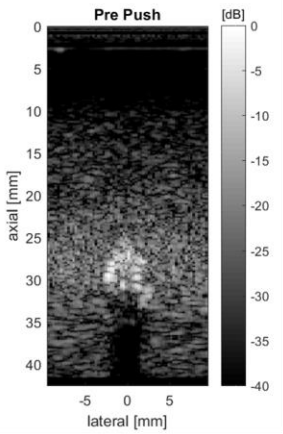

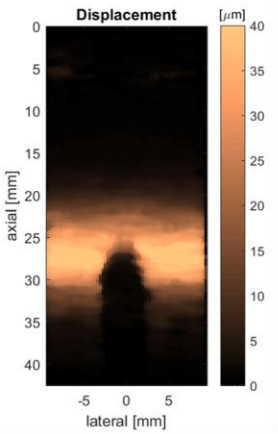

Modulus (MPa)	Norm Disp	Tissue (um)	Gel (um)
28.0	0.08	3.0	36.7

Capsule 4

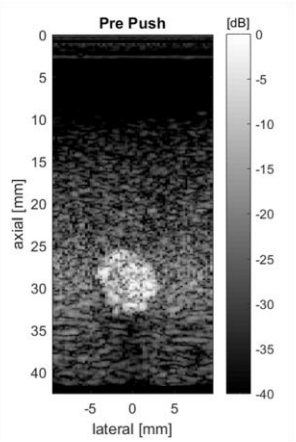

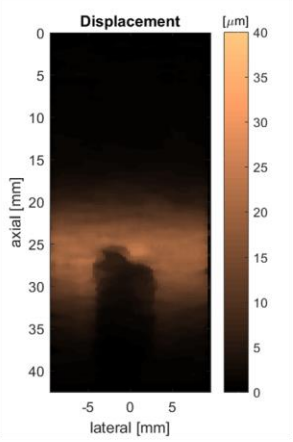

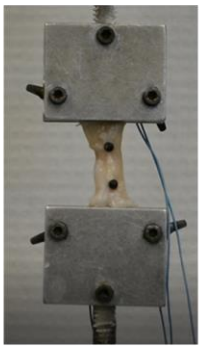

Modulus (MPa)	Norm Disp	Tissue (um)	Gel (um)
18.9	0.35	5.9	16.9

Capsule 5

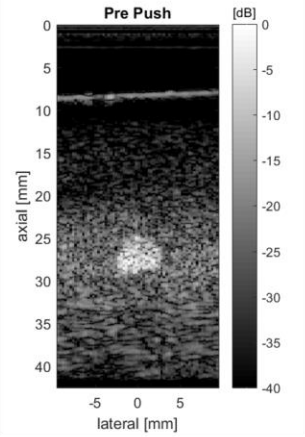

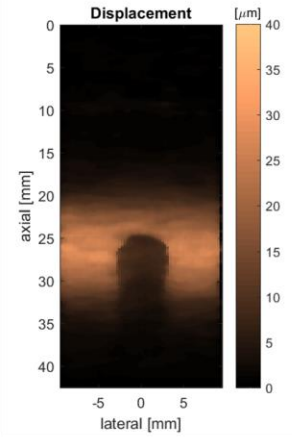

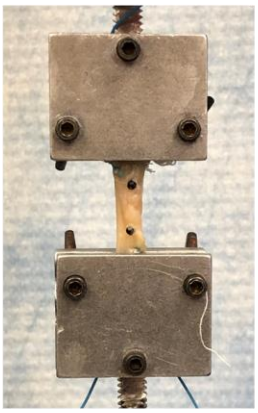

Modulus (MPa)	Norm Disp	Tissue (um)	Gel (um)
59.2	0.31	6.0	27.3

Muscle 1

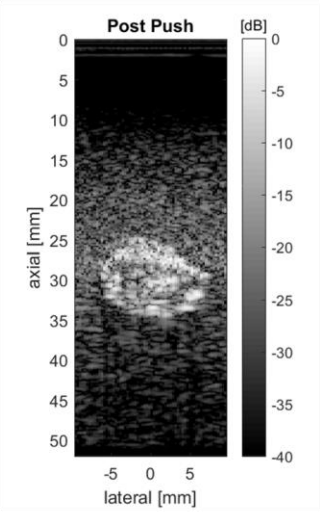

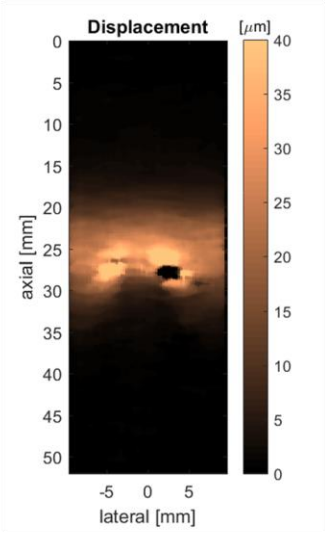

Modulus (MPa)	Norm Disp	Tissue (um)	Gel (um)
1.4	1.06	24.3	23

Muscle 2

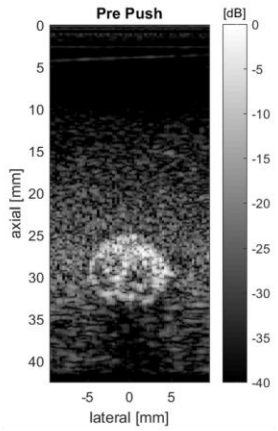

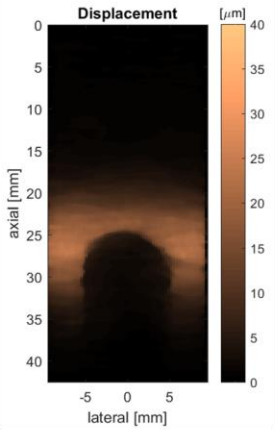

Modulus (MPa)	Norm Disp	Tissue	Gel
3.3	0.28	5.4	19.5

Muscle 3

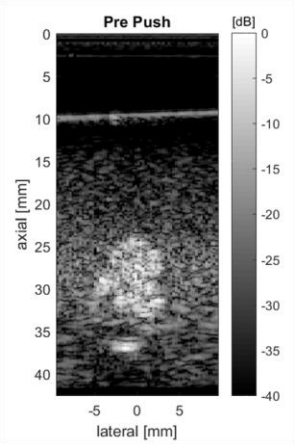

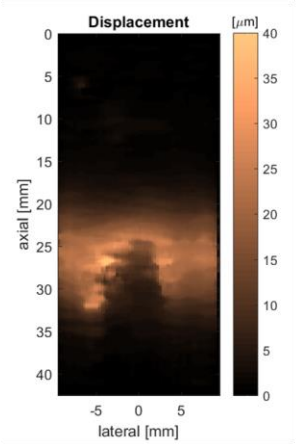

Modulus (MPa)	Norm Disp	Tissue	Gel
1.1	0.61	12.6	20.7

Muscle 4

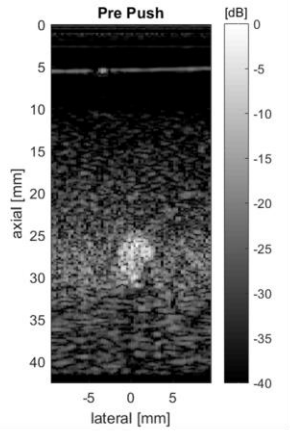

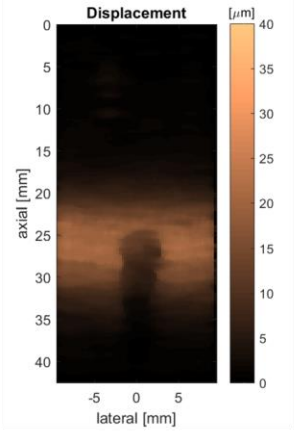

Modulus (MPa)	Norm Disp	Tissue	Gel
5.9	0.63	12.9	20.3

Muscle 5

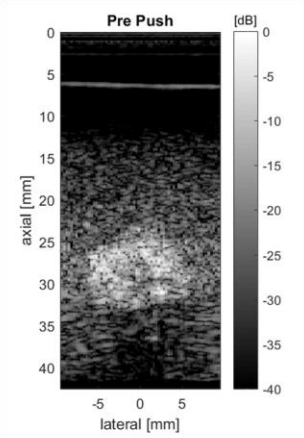

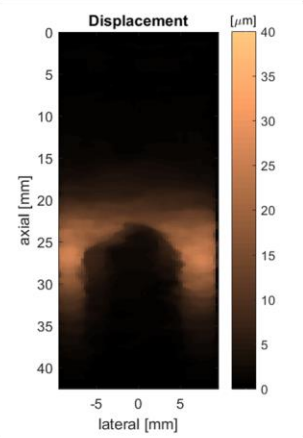

Modulus (MPa)	Norm Disp	Tissue	Gel
0.75	0.41	9.8	24.1

Summary of tensile mechanical properties and ARFI displacement measurements

	Linear Region Modulus (Mpa)	Toe Region Modulus (Mpa)	Tissue ARFI Displacement (um)	Surrounding Gel ARFI Displacement (um)	Norm
Tendon 3	430.2	67	9.18	28	0.33
Tendon 1	309.4	63	3.1	19.6	0.16
Tendon 5	274.3	18	7.2	21.1	0.34
Tendon 4	140.4	10.2	2.81	15.9	0.18
Tendon 2	134.8	16.3	5.47	18	0.3
Capsule 2	66.6	17	9.3	20.9	0.45
Capsule 5	59.2	16.5	6	27.3	0.31
Capsule 3	28	6.5	3	36.7	0.08
Capsule 4	18.9	4.9	5.87	16.9	0.35
Capsule 1	9	3.9	2.6	18.6	0.14
Muscle 4	5.9	2.8	12.9	20.3	0.63
Muscle 2	3.3	1.6	5.4	19.5	0.28
Muscle 1	1.4	0.3	24.3	23	1.06
Muscle 3	1.1	0.32	12.6	20.7	0.61
Muscle 5	0.75	0.2	9.8	24.1	0.41

Appendix C.4 ARFI Imaging FEM Model Details

Example section of the loading details for FEBio input file. Specifically, a surface traction was applied to model the tissue in tension and a depth dependent body force to model the ARFI push.

```
<Loads>
        <surface_load type="traction" surface="SurfaceTraction1">
            <scale lc="2">1</scale>
            <traction>0,0,0.1</traction>
        </surface_load>
        <surface_load type="traction" surface="SurfaceTraction2">
            <scale lc="3">1</scale>
            <traction>0,0,-0.1</traction>
        </surface_load>
        <body_load type="non-const" elem_set="Part412">
            <x lc="1">0</x>
            <y lc="1">5.4e-4*exp(-(Y^2)/2)</y>
            <z lc="1">0</z>
        </body_load>
        <body_load type="non-const" elem_set="Part1">
            <x lc="1">0</x>
            <y lc="1">5.4e-4*exp(-(Y^2)/2)</y>
            <z lc="1">0</z>
        </body_load>
    </Loads>
    <Contact>
        <contact type="tied-node-on-facet" name="TiedContact1" surface_pair="TiedContact1">
            <laugon>0</laugon>
            <tolerance>0.2</tolerance>
            <penalty>1</penalty>
            <minaug>0</minaug>
            <maxaug>10</maxaug>
        </contact>
    </Contact>
    <LoadData>
        <loadcurve id="1" type="step">
            <point>0,0</point>
            <point>775,0</point>
            <point>776,1</point>
            <point>968,1</point>
            <point>969,0</point>
        </loadcurve>
        <loadcurve id="2" type="step">
            <point>0,0</point>
            <point>1,1</point>
        </loadcurve>
        <loadcurve id="3" type="step">
            <point>0,0</point>
            <point>1,1</point>
        </loadcurve>
    </LoadData>
```

Example optimization file for inverse FEM approach to optimize the gel modulus (E) based on ARFI displacement.

```
<?xml version="1.0"?>
<febio_optimize version="2.0">
    <Options type="levmar">
        <obj_tol>0.001</obj_tol>
        <f_diff_scale>0.001</f_diff_scale>
        <log_level>LOG_FILE_AND_SCREEN</log_level>
    </Options>
    <Parameters>
        <param name="fem.material('Material1').E">0.02, 0.001, 0.2</param>
    </Parameters>
    <Objective type="data-fit">
        <fnc type="parameter">
            <param name="fem.mesh.node[60].position.y"/>
        </fnc>
        <data>
            <point>0,0</point>
            <point>192,-0.0241</point>
        </data>
    </Objective>
</febio_optimize>
```

Bibliography

1. Terry GC, Chopp TM. Functional anatomy of the shoulder. J Athl Train. 2000;35(3):248-55. Epub 2006/03/25. PubMed PMID: 16558636; PMCID: PMC1323385.

2. Rugg CM, Hettrich CM, Ortiz S, Wolf BR, Zhang AL. Surgical stabilization for first-time shoulder dislocators: a multicenter analysis. Journal of shoulder and elbow surgery. 2018;27(4):674-85. Epub 2018/01/13. doi: 10.1016/j.jse.2017.10.041. PubMed PMID: 29321108.

3. Clark JM, Harryman DT, 2nd. Tendons, ligaments, and capsule of the rotator cuff. Gross and microscopic anatomy. J Bone Joint Surg Am. 1992;74(5):713-25. PubMed PMID: 1624486.

4. Yamamoto A, Takagishi K, Osawa T, Yanagawa T, Nakajima D, Shitara H, Kobayashi T. Prevalence and risk factors of a rotator cuff tear in the general population. Journal of shoulder and elbow surgery. 2010;19(1):116-20. Epub 2009/06/23. doi: 10.1016/j.jse.2009.04.006. PubMed PMID: 19540777.

5. Reilly P, Macleod I, Macfarlane R, Windley J, Emery RJ. Dead men and radiologists don't lie: a review of cadaveric and radiological studies of rotator cuff tear prevalence. Annals of the Royal College of Surgeons of England. 2006;88(2):116-21. Epub 2006/03/23. doi: 10.1308/003588406x94968. PubMed PMID: 16551396; PMCID: PMC1964063.

6. Yamaguchi K, Ditsios K, Middleton WD, Hildebolt CF, Galatz LM, Teefey SA. The demographic and morphological features of rotator cuff disease. A comparison of asymptomatic and symptomatic shoulders. The Journal of bone and joint surgery American volume. 2006;88(8):1699-704. Epub 2006/08/03. doi: 10.2106/jbjs.e.00835. PubMed PMID: 16882890.

7. Bey MJ, Derwin KA. Measurement of in vivo tendon function. Journal of shoulder and elbow surgery. 2012;21(2):149-57. Epub 2012/01/17. doi: 10.1016/j.jse.2011.10.023. PubMed PMID: 22244057.

8. Baydar M, Akalin E, El O, Gulbahar S, Bircan C, Akgul O, Manisali M, Torun Orhan B, Kizil R. The efficacy of conservative treatment in patients with full-thickness rotator cuff tears. Rheumatology international. 2009;29(6):623-8. Epub 2008/10/14. doi: 10.1007/s00296-008-0733-2. PubMed PMID: 18850322.

9. Itoi E. Rotator cuff tear: physical examination and conservative treatment. Journal of orthopaedic science : official journal of the Japanese Orthopaedic Association. 2013;18(2):197-204. Epub 2013/01/12. doi: 10.1007/s00776-012-0345-2. PubMed PMID: 23306597; PMCID: PMC3607722.

10. Kukkonen J, Kauko T, Virolainen P, Aarimaa V. The effect of tear size on the treatment outcome of operatively treated rotator cuff tears. Knee surgery, sports traumatology, arthroscopy : official journal of the ESSKA. 2015;23(2):567-72. Epub 2013/09/03. doi: 10.1007/s00167-013-2647-0. PubMed PMID: 23996071.

11. Cho NS, Rhee YG. The factors affecting the clinical outcome and integrity of arthroscopically repaired rotator cuff tears of the shoulder. Clin Orthop Surg. 2009;1(2):96-104. Epub 2009/11/04. doi: 10.4055/cios.2009.1.2.96. PubMed PMID: 19885061; PMCID: PMC2766755.

12. Kuhn JE, Dunn WR, Sanders R, An Q, Baumgarten KM, Bishop JY, Brophy RH, Carey JL, Holloway BG, Jones GL, Ma CB, Marx RG, McCarty EC, Poddar SK, Smith MV, Spencer EE, Vidal AF, Wolf BR, Wright RW. Effectiveness of physical therapy in treating atraumatic full-thickness rotator cuff tears: a multicenter prospective cohort study. Journal of shoulder and elbow surgery. 2013;22(10):1371-9. Epub 2013/04/02. doi: 10.1016/j.jse.2013.01.026. PubMed PMID: 23540577; PMCID: PMC3748251.

13. Huegel J, Williams AA, Soslowsky LJ. Rotator cuff biology and biomechanics: a review of normal and pathological conditions. Curr Rheumatol Rep. 2015;17(1):476. Epub 2014/12/06. doi: 10.1007/s11926-014-0476-x. PubMed PMID: 25475598.

14. Safran O, Schroeder J, Bloom R, Weil Y, Milgrom C. Natural history of nonoperatively treated symptomatic rotator cuff tears in patients 60 years old or younger. The American journal of sports medicine. 2011;39(4):710-4. Epub 2011/02/12. doi: 10.1177/0363546510393944. PubMed PMID: 21310940.

15. Kijima T, Matsuki K, Ochiai N, Yamaguchi T, Sasaki Y, Hashimoto E, Sasaki Y, Yamazaki H, Kenmoku T, Yamaguchi S, Masuda Y, Umekita H, Banks SA, Takahashi K. In vivo 3-dimensional analysis of scapular and glenohumeral kinematics: comparison of symptomatic or asymptomatic shoulders with rotator cuff tears and healthy shoulders. Journal of shoulder and elbow surgery. 2015;24(11):1817-26. Epub 2015/08/04. doi: 10.1016/j.jse.2015.06.003. PubMed PMID: 26234667.

16. Miniato MA, Varacallo M. Anatomy, Shoulder and Upper Limb, Shoulder. StatPearls. Treasure Island (FL): StatPearls Publishing
StatPearls Publishing LLC.; 2019.

17. Lugo R, Kung P, Ma CB. Shoulder biomechanics. European journal of radiology. 2008;68(1):16-24. Epub 2008/05/31. doi: 10.1016/j.ejrad.2008.02.051. PubMed PMID: 18511227.

18. Soslowsky LJ, Flatow EL, Bigliani LU, Pawluk RJ, Ateshian GA, Mow VC. Quantitation of in situ contact areas at the glenohumeral joint: a biomechanical study. Journal of orthopaedic research : official publication of the Orthopaedic Research Society. 1992;10(4):524-34. Epub 1992/07/01. doi: 10.1002/jor.1100100407. PubMed PMID: 1613626.

19. McMahon PJ, Debski RE, Thompson WO, Warner JJ, Fu FH, Woo SL. Shoulder muscle forces and tendon excursions during glenohumeral abduction in the scapular plane. Journal of shoulder and elbow surgery. 1995;4(3):199-208. Epub 1995/05/01. doi: 10.1016/s1058-2746(05)80052-7. PubMed PMID: 7552678.

20. Poppen NK, Walker PS. Normal and abnormal motion of the shoulder. The Journal of bone and joint surgery American volume. 1976;58(2):195-201. Epub 1976/03/01. PubMed PMID: 1254624.

21. Soslowsky LJ, Flatow EL, Bigliani LU, Mow VC. Articular geometry of the glenohumeral joint. Clinical orthopaedics and related research. 1992(285):181-90. Epub 1992/12/01. PubMed PMID: 1446435.

22. Howell SM, Galinat BJ. The glenoid-labral socket. A constrained articular surface. Clinical orthopaedics and related research. 1989(243):122-5. Epub 1989/06/01. PubMed PMID: 2721051.

23. Cooper DE, Arnoczky SP, O'Brien SJ, Warren RF, DiCarlo E, Allen AA. Anatomy, histology, and vascularity of the glenoid labrum. An anatomical study. The Journal of bone and joint surgery American volume. 1992;74(1):46-52. Epub 1992/01/01. PubMed PMID: 1734013.

24. O'Brien SJ, Neves MC, Arnoczky SP, Rozbruck SR, Dicarlo EF, Warren RF, Schwartz R, Wickiewicz TL. The anatomy and histology of the inferior glenohumeral ligament complex of the shoulder. The American journal of sports medicine. 1990;18(5):449-56. Epub 1990/09/01. doi: 10.1177/036354659001800501. PubMed PMID: 2252083.

25. Voycheck CA. Characterizing the Effects of Simulated Injury on the Structure and Function of the Glenohumeral Capsule. 2011.

26. Moore SM, Ellis B, Weiss JA, McMahon PJ, Debski RE. The glenohumeral capsule should be evaluated as a sheet of fibrous tissue: a validated finite element model. Annals of biomedical engineering. 2010;38(1):66-76. Epub 2009/11/17. doi: 10.1007/s10439-009-9834-7. PubMed PMID: 19911278; PMCID: PMC2819238.

27. Halder AM, Itoi E, An KN. Anatomy and biomechanics of the shoulder. Orthop Clin North Am. 2000;31(2):159-76. Epub 2000/03/29. doi: 10.1016/s0030-5898(05)70138-3. PubMed PMID: 10736387.

28. Debski RE, Sakone M, Woo SL, Wong EK, Fu FH, Warner JJ. Contribution of the passive properties of the rotator cuff to glenohumeral stability during anterior-posterior loading. Journal of shoulder and elbow surgery. 1999;8(4):324-9. doi: 10.1016/s1058-2746(99)90154-4. PubMed PMID: 10472004.

29. Inman VT, deC. M. Saunders JB, Abbott LC. OBSERVATIONS ON THE FUNCTION OF THE SHOULDER JOINT. JBJS. 1944;26(1):1-30. PubMed PMID: 00401515-194426010-00001.

30. Saha AK. Theory of shoulder mechanism: descriptive and applied: Thomas; 1961.

31. Lo IK, Burkhart SS. Current concepts in arthroscopic rotator cuff repair. The American journal of sports medicine. 2003;31(2):308-24. Epub 2003/03/19. doi: 10.1177/03635465030310022701. PubMed PMID: 12642271.

32. Yamaguchi K, Sher JS, Andersen WK, Garretson R, Uribe JW, Hechtman K, Neviaser RJ. Glenohumeral motion in patients with rotator cuff tears: a comparison of asymptomatic and symptomatic shoulders. Journal of shoulder and elbow surgery. 2000;9(1):6-11. Epub 2000/03/16. doi: 10.1016/s1058-2746(00)90002-8. PubMed PMID: 10717855.

33. Liu J, Hughes RE, Smutz WP, Niebur G, Nan-An K. Roles of deltoid and rotator cuff muscles in shoulder elevation. Clinical biomechanics (Bristol, Avon). 1997;12(1):32-8. Epub 1997/01/01. doi: 10.1016/s0268-0033(96)00047-2. PubMed PMID: 11415669.

34. Minagawa H, Itoi E, Konno N, Kido T, Sano A, Urayama M, Sato K. Humeral attachment of the supraspinatus and infraspinatus tendons: an anatomic study. Arthroscopy : the journal of arthroscopic & related surgery : official publication of the Arthroscopy Association of North America and the International Arthroscopy Association. 1998;14(3):302-6. Epub 1998/05/20. doi: 10.1016/s0749-8063(98)70147-1. PubMed PMID: 9586977.

35. Kuechle DK, Newman SR, Itoi E, Morrey BF, An KN. Shoulder muscle moment arms during horizontal flexion and elevation. Journal of shoulder and elbow surgery. 1997;6(5):429-39. Epub 1997/11/14. doi: 10.1016/s1058-2746(97)70049-1. PubMed PMID: 9356931.

36. Colachis SC, Jr., Strohm BR, Brechner VL. Effects of axillary nerve block on muscle force in the upper extremity. Arch Phys Med Rehabil. 1969;50(11):647-54. Epub 1969/11/01. PubMed PMID: 5360326.

37. Ovesen J, Nielsen S. Anterior and posterior shoulder instability. A cadaver study. Acta Orthop Scand. 1986;57(4):324-7. Epub 1986/08/01. doi: 10.3109/17453678608994402. PubMed PMID: 3788495.

38. Oh LS, Wolf BR, Hall MP, Levy BA, Marx RG. Indications for rotator cuff repair: a systematic review. Clinical orthopaedics and related research. 2007;455:52-63. Epub 2006/12/21. doi: 10.1097/BLO.0b013e31802fc175. PubMed PMID: 17179786.

39. Meislin RJ, Sperling JW, Stitik TP. Persistent shoulder pain: epidemiology, pathophysiology, and diagnosis. Am J Orthop (Belle Mead NJ). 2005;34(12 Suppl):5-9. Epub 2006/02/03. PubMed PMID: 16450690.

40. Matsen FA, 3rd. Clinical practice. Rotator-cuff failure. The New England journal of medicine. 2008;358(20):2138-47. Epub 2008/05/16. doi: 10.1056/NEJMcp0800814. PubMed PMID: 18480206.

41. Tashjian RZ. Epidemiology, natural history, and indications for treatment of rotator cuff tears. Clin Sports Med. 2012;31(4):589-604. Epub 2012/10/09. doi: 10.1016/j.csm.2012.07.001. PubMed PMID: 23040548.

42. Lehman C, Cuomo F, Kummer FJ, Zuckerman JD. The incidence of full thickness rotator cuff tears in a large cadaveric population. Bull Hosp Jt Dis. 1995;54(1):30-1. Epub 1995/01/01. PubMed PMID: 8541777.

43. Piper CC, Hughes AJ, Ma Y, Wang H, Neviaser AS. Operative versus nonoperative treatment for the management of full-thickness rotator cuff tears: a systematic review and meta-analysis. Journal of shoulder and elbow surgery. 2018;27(3):572-6. Epub 2017/11/25. doi: 10.1016/j.jse.2017.09.032. PubMed PMID: 29169957.

44. Saltychev M, Aarimaa V, Virolainen P, Laimi K. Conservative treatment or surgery for shoulder impingement: systematic review and meta-analysis. Disabil Rehabil. 2015;37(1):1-8. Epub 2014/04/04. doi: 10.3109/09638288.2014.907364. PubMed PMID: 24694286.

45. Koester MC, Dunn WR, Kuhn JE, Spindler KP. The efficacy of subacromial corticosteroid injection in the treatment of rotator cuff disease: A systematic review. The Journal of the American Academy of Orthopaedic Surgeons. 2007;15(1):3-11. Epub 2007/01/11. doi: 10.5435/00124635-200701000-00002. PubMed PMID: 17213378.

46. Kukkonen J, Joukainen A, Lehtinen J, Mattila KT, Tuominen EK, Kauko T, Aarimaa V. Treatment of Nontraumatic Rotator Cuff Tears: A Randomized Controlled Trial with Two Years of Clinical and Imaging Follow-up. The Journal of bone and joint surgery American volume. 2015;97(21):1729-37. Epub 2015/11/06. doi: 10.2106/jbjs.N.01051. PubMed PMID: 26537160.

47. Agout C, Berhouet J, Spiry C, Bonnevialle N, Joudet T, Favard L. Functional outcomes after non-operative treatment of irreparable massive rotator cuff tears: Prospective multicenter study in 68 patients. Orthop Traumatol Surg Res. 2018;104(8s):S189-s92. Epub 2018/08/06. doi: 10.1016/j.otsr.2018.08.003. PubMed PMID: 30077657.

48. Escamilla RF, Yamashiro K, Paulos L, Andrews JR. Shoulder muscle activity and function in common shoulder rehabilitation exercises. Sports medicine (Auckland, NZ). 2009;39(8):663-85. Epub 2009/09/23. doi: 10.2165/00007256-200939080-00004. PubMed PMID: 19769415.

49. Millett PJ, Wilcox RB, 3rd, O'Holleran JD, Warner JJ. Rehabilitation of the rotator cuff: an evaluation-based approach. The Journal of the American Academy of Orthopaedic Surgeons. 2006;14(11):599-609. Epub 2006/10/13. doi: 10.5435/00124635-200610000-00002. PubMed PMID: 17030593.

50. Chang KV, Mezian K, Nanka O, Wu WT, Lin CP, Ozcakar L. Ultrasound-guided interventions for painful shoulder: from anatomy to evidence. J Pain Res. 2018;11:2311-22. Epub 2018/10/24. doi: 10.2147/jpr.S169434. PubMed PMID: 30349357; PMCID: PMC6188188.

51. Petri M, Ettinger M, Brand S, Stuebig T, Krettek C, Omar M. Non-Operative Management of Rotator Cuff Tears. Open Orthop J. 2016;10:349-56. Epub 2016/10/07. doi: 10.2174/1874325001610010349. PubMed PMID: 27708737; PMCID: PMC5041208.

52. Goldberg BA, Nowinski RJ, Matsen FA, 3rd. Outcome of nonoperative management of full-thickness rotator cuff tears. Clinical orthopaedics and related research. 2001(382):99-107. Epub 2001/01/12. PubMed PMID: 11154011.

53. Zingg PO, Jost B, Sukthankar A, Buhler M, Pfirrmann CW, Gerber C. Clinical and structural outcomes of nonoperative management of massive rotator cuff tears. The Journal of bone and joint surgery American volume. 2007;89(9):1928-34. Epub 2007/09/05. doi: 10.2106/jbjs.F.01073. PubMed PMID: 17768188.

54. Maman E, Harris C, White L, Tomlinson G, Shashank M, Boynton E. Outcome of nonoperative treatment of symptomatic rotator cuff tears monitored by magnetic resonance imaging. The Journal of bone and joint surgery American volume. 2009;91(8):1898-906. Epub 2009/08/05. doi: 10.2106/jbjs.G.01335. PubMed PMID: 19651947.

55. Depres-Tremblay G, Chevrier A, Snow M, Hurtig MB, Rodeo S, Buschmann MD. Rotator cuff repair: a review of surgical techniques, animal models, and new technologies under development. Journal of shoulder and elbow surgery. 2016;25(12):2078-85. Epub 2016/08/25. doi: 10.1016/j.jse.2016.06.009. PubMed PMID: 27554609.

56. Duquin TR, Buyea C, Bisson LJ. Which method of rotator cuff repair leads to the highest rate of structural healing? A systematic review. The American journal of sports medicine. 2010;38(4):835-41. Epub 2010/04/02. doi: 10.1177/0363546509359679. PubMed PMID: 20357403.

57. Galatz LM, Ball CM, Teefey SA, Middleton WD, Yamaguchi K. The outcome and repair integrity of completely arthroscopically repaired large and massive rotator cuff tears. The Journal of bone and joint surgery American volume. 2004;86-a(2):219-24. Epub 2004/02/13. PubMed PMID: 14960664.

58. Greenspoon JA, Petri M, Warth RJ, Millett PJ. Massive rotator cuff tears: pathomechanics, current treatment options, and clinical outcomes. Journal of shoulder and elbow surgery. 2015;24(9):1493-505. Epub 2015/07/02. doi: 10.1016/j.jse.2015.04.005. PubMed PMID: 26129871.

59. Yamaguchi K, Tetro AM, Blam O, Evanoff BA, Teefey SA, Middleton WD. Natural history of asymptomatic rotator cuff tears: a longitudinal analysis of asymptomatic tears detected sonographically. Journal of shoulder and elbow surgery. 2001;10(3):199-203. Epub 2001/06/16. doi: 10.1067/mse.2001.113086. PubMed PMID: 11408898.

60. Rashid MS, Cooper C, Cook J, Cooper D, Dakin SG, Snelling S, Carr AJ. Increasing age and tear size reduce rotator cuff repair healing rate at 1 year. Acta Orthop. 2017;88(6):606-11. Epub 2017/09/08. doi: 10.1080/17453674.2017.1370844. PubMed PMID: 28880113; PMCID: PMC5694804.

61. Ponce BA, Hosemann CD, Raghava P, Tate JP, Sheppard ED, Eberhardt AW. A biomechanical analysis of controllable intraoperative variables affecting the strength of rotator cuff repairs at the suture-tendon interface. Am J Sports Med. 2013;41(10):2256-61. doi: 10.1177/0363546513499228. PubMed PMID: 23950108.

62. Thomazeau H, Boukobza E, Morcet N, Chaperon J, Langlais F. Prediction of rotator cuff repair results by magnetic resonance imaging. Clin Orthop Relat Res. 1997(344):275-83. PubMed PMID: 9372778.

63. Schneeberger AG, von Roll A, Kalberer F, Jacob HA, Gerber C. Mechanical strength of arthroscopic rotator cuff repair techniques: an in vitro study. J Bone Joint Surg Am. 2002;84-A(12):2152-60. PubMed PMID: 12473702.

64. Gerber C, Schneeberger AG, Beck M, Schlegel U. Mechanical strength of repairs of the rotator cuff. J Bone Joint Surg Br. 1994;76(3):371-80. PubMed PMID: 8175836.

65. Gimbel JA, Van Kleunen JP, Lake SP, Williams GR, Soslowsky LJ. The role of repair tension on tendon to bone healing in an animal model of chronic rotator cuff tears. J Biomech. 2007;40(3):561-8. doi: 10.1016/j.jbiomech.2006.02.010. PubMed PMID: 16600252.

66. Burkhart SS, Diaz Pagan JL, Wirth MA, Athanasiou KA. Cyclic loading of anchor-based rotator cuff repairs: confirmation of the tension overload phenomenon and comparison of suture anchor fixation with transosseous fixation. Arthroscopy : the journal of arthroscopic & related surgery : official publication of the Arthroscopy Association of North America and the International Arthroscopy Association. 1997;13(6):720-4. Epub 1998/01/27. PubMed PMID: 9442325.

67. Denard PJ, Burkhart SS. Techniques for managing poor quality tissue and bone during arthroscopic rotator cuff repair. Arthroscopy. 2011;27(10):1409-21. doi: 10.1016/j.arthro.2011.05.015. PubMed PMID: 21872421.

68. Burkhart SS, Fischer SP, Nottage WM, Esch JC, Barber FA, Doctor D, Ferrier J. Tissue fixation security in transosseous rotator cuff repairs: a mechanical comparison of simple versus mattress sutures. Arthroscopy. 1996;12(6):704-8. PubMed PMID: 9115559.

69. Cummins CA, Murrell GA. Mode of failure for rotator cuff repair with suture anchors identified at revision surgery. Journal of shoulder and elbow surgery. 2003;12(2):128-33. Epub 2003/04/18. doi: 10.1067/mse.2003.21. PubMed PMID: 12700563.

70. Seitz AL, McClure PW, Finucane S, Boardman ND, 3rd, Michener LA. Mechanisms of rotator cuff tendinopathy: intrinsic, extrinsic, or both? Clinical biomechanics (Bristol, Avon). 2011;26(1):1-12. Epub 2010/09/16. doi: 10.1016/j.clinbiomech.2010.08.001. PubMed PMID: 20846766.

71. Neer CS, 2nd. Impingement lesions. Clinical orthopaedics and related research. 1983(173):70-7. PubMed PMID: 6825348.

72. Reuther KE, Thomas SJ, Tucker JJ, Sarver JJ, Gray CF, Rooney SI, Glaser DL, Soslowsky LJ. Disruption of the anterior-posterior rotator cuff force balance alters joint function and leads to joint damage in a rat model. J Orthop Res. 2014;32(5):638-44. doi: 10.1002/jor.22586. PubMed PMID: 24464961; PMCID: 4006275.

73. Hsu JE, Reuther KE, Sarver JJ, Lee CS, Thomas SJ, Glaser DL, Soslowsky LJ. Restoration of anterior-posterior rotator cuff force balance improves shoulder function in a rat model of chronic massive tears. Journal of orthopaedic research : official publication of the Orthopaedic Research Society. 2011;29(7):1028-33. Epub 2011/02/11. doi: 10.1002/jor.21361. PubMed PMID: 21308755; PMCID: Pmc3094494.

74. Millett PJ, Giphart JE, Wilson KJ, Kagnes K, Greenspoon JA. Alterations in Glenohumeral Kinematics in Patients With Rotator Cuff Tears Measured With Biplane Fluoroscopy. Arthroscopy : the journal of arthroscopic & related surgery : official publication of the Arthroscopy Association of North America and the International Arthroscopy Association. 2016;32(3):446-51. Epub 2015/11/26. doi: 10.1016/j.arthro.2015.08.031. PubMed PMID: 26603825.

75. Bey MJ, Kline SK, Zauel R, Lock TR, Kolowich PA. Measuring dynamic in-vivo glenohumeral joint kinematics: technique and preliminary results. Journal of biomechanics. 2008;41(3):711-4. Epub 2007/11/09. doi: 10.1016/j.jbiomech.2007.09.029. PubMed PMID: 17996874.

76. Graichen H, Hinterwimmer S, von Eisenhart-Rothe R, Vogl T, Englmeier K-H, Eckstein F. Effect of abducting and adducting muscle acitivity on glenohumeral translation, scapular kinematics and subacromial space width in vivo. Journal of biomechanics. 2005;38(4):755-60.

77. Graichen H, Stammberger T, Bonel H, Englmeier K-H, Reiser M, Eckstein F. Glenohumeral translation during active and passive elevation of the shoulder—a 3D open-MRI study. Journal of biomechanics. 2000;33(5):609-13.

78. von Eisenhart-Rothe RM, Jager A, Englmeier KH, Vogl TJ, Graichen H. Relevance of arm position and muscle activity on three-dimensional glenohumeral translation in patients with traumatic and atraumatic shoulder instability. The American journal of sports medicine. 2002;30(4):514-22. Epub 2002/07/20. PubMed PMID: 12130406.

79. Parsons IM, Apreleva M, Fu FH, Woo SL. The effect of rotator cuff tears on reaction forces at the glenohumeral joint. Journal of orthopaedic research : official publication of the Orthopaedic Research Society. 2002;20(3):439-46. Epub 2002/06/01. doi: 10.1016/s0736-0266(01)00137-1. PubMed PMID: 12038616.

80. Bey MJ, Kline SK, Zauel R, Lock TR, Kolowich PA. Measuring dynamic in-vivo glenohumeral joint kinematics: technique and preliminary results. J Biomech. 2008;41(3):711-4. Epub 2007/11/13. doi: http://dx.doi.org/10.1016/j.jbiomech.2007.09.029. PubMed PMID: 17996874.

81. Giphart JE, van der Meijden OA, Millett PJ. The effects of arm elevation on the 3-dimensional acromiohumeral distance: a biplane fluoroscopy study with normative data. J Shoulder Elbow Surg. 2012;21(11):1593-600. Epub 2012/03/01. doi: http://dx.doi.org/10.1016/j.jse.2011.11.023. PubMed PMID: 22361718.

82. Massimini DF, Boyer PJ, Papannagari R, Gill TJ, Warner JP, Li G. In-vivo glenohumeral translation and ligament elongation during abduction and abduction with internal and external rotation. Journal of orthopaedic surgery and research. 2012;7:29. Epub 2012/06/30. doi: 10.1186/1749-799x-7-29. PubMed PMID: 22741601; PMCID: Pmc3403937.

83. Peltz CD, Haladik JA, Hoffman SE, McDonald M, Ramo N, Moutzouros V, Bey MJ. Associations among shoulder strength, glenohumeral joint motion, and clinical outcome after rotator cuff repair. Am J Orthop (Belle Mead NJ). 2014;43(5):220-6. Epub 2014/05/20. PubMed PMID: 24839628.

84. Baumer TG, Chan D, Mende V, Dischler J, Zauel R, van Holsbeeck M, Siegal DS, Divine G, Moutzouros V, Bey MJ. Effects of Rotator Cuff Pathology and Physical Therapy on In Vivo Shoulder Motion and Clinical Outcomes in Patients With a Symptomatic Full-Thickness Rotator Cuff Tear. Orthopaedic journal of sports medicine. 2016;4(9):2325967116666506. Epub 2016/10/14. doi: 10.1177/2325967116666506. PubMed PMID: 27734020; PMCID: PMC5040201.

85. Tempelaere C, Pierrart J, Lefevre-Colau MM, Vuillemin V, Cuenod CA, Hansen U, Mir O, Skalli W, Gregory T. Dynamic Three-Dimensional Shoulder Mri during Active Motion for Investigation of Rotator Cuff Diseases. PloS one. 2016;11(7):e0158563. Epub 2016/07/21. doi: 10.1371/journal.pone.0158563. PubMed PMID: 27434235; PMCID: PMC4951034.

86. Kozono N, Okada T, Takeuchi N, Hamai S, Higaki H, Ikebe S, Shimoto T, Miake G, Nakanishi Y, Iwamoto Y. In vivo kinematic analysis of the glenohumeral joint during dynamic full axial rotation and scapular plane full abduction in healthy shoulders. Knee surgery, sports traumatology, arthroscopy : official journal of the ESSKA. 2017;25(7):2032-40. Epub 2016/08/12. doi: 10.1007/s00167-016-4263-2. PubMed PMID: 27511218.

87. Miller RM, Popchak A, Vyas D, Tashman S, Irrgang JJ, Musahl V, Debski RE. Effects of exercise therapy for the treatment of symptomatic full-thickness supraspinatus tears on in vivo

glenohumeral kinematics. Journal of shoulder and elbow surgery. 2016;25(4):641-9. Epub 2015/12/02. doi: 10.1016/j.jse.2015.08.048. PubMed PMID: 26620280.

88. Itoi E, Berglund LJ, Grabowski JJ, Schultz FM, Growney ES, Morrey BF, An KN. Tensile properties of the supraspinatus tendon. Journal of orthopaedic research : official publication of the Orthopaedic Research Society. 1995;13(4):578-84. Epub 1995/07/01. doi: 10.1002/jor.1100130413. PubMed PMID: 7674074.

89. Matsuhashi T, Hooke AW, Zhao KD, Goto A, Sperling JW, Steinmann SP, An K-N. Tensile properties of a morphologically split supraspinatus tendon. Clin Anat. 2014;27(5):702-6. Epub 2013/11/08. doi: 10.1002/ca.22322. PubMed PMID: 24214830.

90. Araki D, Miller RM, Fujimaki Y, Hoshino Y, Musahl V, Debski RE. Effect of tear location on propagation of isolated supraspinatus tendon tears during increasing levels of cyclic loading. The Journal of bone and joint surgery American volume. 2015;97(4):273-8. Epub 2015/02/20. doi: 10.2106/jbjs.n.00062. PubMed PMID: 25695976.

91. Miller RM, Fujimaki Y, Araki D, Musahl V, Debski RE. Strain distribution due to propagation of tears in the anterior supraspinatus tendon. Journal of orthopaedic research : official publication of the Orthopaedic Research Society. 2014;32(10):1283-9. Epub 2014/07/06. doi: 10.1002/jor.22675. PubMed PMID: 24985532.

92. Miller RM, Thunes J, Maiti S, Musahl V, Debski RE. Effects of Tendon Degeneration on Predictions of Supraspinatus Tear Propagation. Annals of biomedical engineering. 2019;47(1):154-61. Epub 2018/09/21. doi: 10.1007/s10439-018-02132-w. PubMed PMID: 30242532.

93. Thorpe CT, Screen HRC. Tendon Structure and Composition. In: Ackermann PW, Hart DA, editors. Metabolic Influences on Risk for Tendon Disorders. Cham: Springer International Publishing; 2016. p. 3-10.

94. Yoon JH, Halper J. Tendon proteoglycans: biochemistry and function. J Musculoskelet Neuronal Interact. 2005;5(1):22-34. PubMed PMID: 15788868.

95. Derwin KA, Soslowsky LJ, Kimura JH, Plaas AH. Proteoglycans and glycosaminoglycan fine structure in the mouse tail tendon fascicle. Journal of orthopaedic research : official publication of the Orthopaedic Research Society. 2001;19(2):269-77. doi: 10.1016/S0736-0266(00)00032-2. PubMed PMID: 11347701.

96. Danielson KG, Baribault H, Holmes DF, Graham H, Kadler KE, Iozzo RV. Targeted disruption of decorin leads to abnormal collagen fibril morphology and skin fragility. J Cell Biol. 1997;136(3):729-43. doi: 10.1083/jcb.136.3.729. PubMed PMID: 9024701.

97. Curwin SL, Vailas AC, Wood J. Immature tendon adaptation to strenuous exercise. Journal of applied physiology (Bethesda, Md : 1985). 1988;65(5):2297-301. doi: 10.1152/jappl.1988.65.5.2297. PubMed PMID: 3209575.

98. Hae Yoon J, Brooks R, Hwan Kim Y, Terada M, Halper J. Proteoglycans in chicken gastrocnemius tendons change with exercise. Arch Biochem Biophys. 2003;412(2):279-86. doi: 10.1016/s0003-9861(03)00064-x. PubMed PMID: 12667493.

99. Anderson DR, Weiss JA, Takai S, Ohland KJ, Woo SL. Healing of the medial collateral ligament following a triad injury: a biomechanical and histological study of the knee in rabbits. Journal of orthopaedic research : official publication of the Orthopaedic Research Society. 1992;10(4):485-95. doi: 10.1002/jor.1100100404. PubMed PMID: 1613624.

100. Scheffler SU, Clineff TD, Papageorgiou CD, Debski RE, Ma CB, Woo SL. Structure and function of the healing medial collateral ligament in a goat model. Annals of biomedical engineering. 2001;29(2):173-80. doi: 10.1114/1.1349701. PubMed PMID: 11284672.

101. Sano H, Hatta T, Yamamoto N, Itoi E. Stress distribution within rotator cuff tendons with a crescent-shaped and an L-shaped tear. The American journal of sports medicine. 2013;41(10):2262-9. Epub 2013/08/03. doi: 10.1177/0363546513497565. PubMed PMID: 23907331.

102. Bey MJ, Song HK, Wehrli FW, Soslowsky LJ. Intratendinous strain fields of the intact supraspinatus tendon: the effect of glenohumeral joint position and tendon region. Journal of orthopaedic research : official publication of the Orthopaedic Research Society. 2002;20(4):869-74. Epub 2002/08/10. doi: 10.1016/s0736-0266(01)00177-2. PubMed PMID: 12168680.

103. Bey MJ, Ramsey ML, Soslowsky LJ. Intratendinous strain fields of the supraspinatus tendon: effect of a surgically created articular-surface rotator cuff tear. Journal of shoulder and elbow surgery. 2002;11(6):562-9. Epub 2002/12/07. doi: 10.1067/mse.2002.126767. PubMed PMID: 12469080.

104. Thunes J, Matthew Miller R, Pal S, Damle S, Debski RE, Maiti S. The Effect of Size and Location of Tears in the Supraspinatus Tendon on Potential Tear Propagation. Journal of biomechanical engineering. 2015;137(8):081012. Epub 2015/06/05. doi: 10.1115/1.4030745. PubMed PMID: 26043431.

105. Sano H, Ishii H, Yeadon A, Backman DS, Brunet JA, Uhthoff HK. Degeneration at the insertion weakens the tensile strength of the supraspinatus tendon: a comparative mechanical and histologic study of the bone-tendon complex. Journal of orthopaedic research : official publication of the Orthopaedic Research Society. 1997;15(5):719-26. Epub 1998/01/08. doi: 10.1002/jor.1100150514. PubMed PMID: 9420602.

106. Gimbel JA, Van Kleunen JP, Mehta S, Perry SM, Williams GR, Soslowsky LJ. Supraspinatus tendon organizational and mechanical properties in a chronic rotator cuff tear animal model. Journal of biomechanics. 2004;37(5):739-49. Epub 2004/03/30. doi: 10.1016/j.jbiomech.2003.09.019. PubMed PMID: 15047003.

107. Andarawis-Puri N, Ricchetti ET, Soslowsky LJ. Rotator cuff tendon strain correlates with tear propagation. Journal of biomechanics. 2009;42(2):158-63. Epub 2008/12/10. doi: 10.1016/j.jbiomech.2008.10.020. PubMed PMID: 19064267; PMCID: PMC2775924.

108. Reilly P, Amis AA, Wallace AL, Emery RJ. Mechanical factors in the initiation and propagation of tears of the rotator cuff. Quantification of strains of the supraspinatus tendon in vitro. The Journal of bone and joint surgery British volume. 2003;85(4):594-9. Epub 2003/06/10. PubMed PMID: 12793570.

109. Reilly P, Amis AA, Wallace AL, Emery RJ. Supraspinatus tears: propagation and strain alteration. Journal of shoulder and elbow surgery. 2003;12(2):134-8. Epub 2003/04/18. doi: 10.1067/mse.2003.7. PubMed PMID: 12700564.

110. Teefey SA, Middleton WD, Payne WT, Yamaguchi K. Detection and measurement of rotator cuff tears with sonography: analysis of diagnostic errors. AJR American journal of roentgenology. 2005;184(6):1768-73. Epub 2005/05/24. doi: 10.2214/ajr.184.6.01841768. PubMed PMID: 15908528.

111. Prickett WD, Teefey SA, Galatz LM, Calfee RP, Middleton WD, Yamaguchi K. Accuracy of ultrasound imaging of the rotator cuff in shoulders that are painful postoperatively. The Journal of bone and joint surgery American volume. 2003;85-a(6):1084-9. Epub 2003/06/05. PubMed PMID: 12784007.

112. Teefey SA, Hasan SA, Middleton WD, Patel M, Wright RW, Yamaguchi K. Ultrasonography of the rotator cuff. A comparison of ultrasonographic and arthroscopic findings in one hundred consecutive cases. The Journal of bone and joint surgery American volume. 2000;82(4):498-504. Epub 2000/04/13. PubMed PMID: 10761940.

113. Teefey SA, Rubin DA, Middleton WD, Hildebolt CF, Leibold RA, Yamaguchi K. Detection and quantification of rotator cuff tears. Comparison of ultrasonographic, magnetic resonance imaging, and arthroscopic findings in seventy-one consecutive cases. The Journal of bone and joint surgery American volume. 2004;86-a(4):708-16. Epub 2004/04/08. PubMed PMID: 15069134.

114. Sipola P, Niemitukia L, Kroger H, Hofling I, Vaatainen U. Detection and quantification of rotator cuff tears with ultrasonography and magnetic resonance imaging - a prospective study in 77 consecutive patients with a surgical reference. Ultrasound in medicine & biology. 2010;36(12):1981-9. Epub 2010/10/23. doi: 10.1016/j.ultrasmedbio.2010.09.001. PubMed PMID: 20965645.

115. Fotiadou AN, Vlychou M, Papadopoulos P, Karataglis DS, Palladas P, Fezoulidis IV. Ultrasonography of symptomatic rotator cuff tears compared with MR imaging and surgery. European journal of radiology. 2008;68(1):174-9. Epub 2007/12/28. doi: 10.1016/j.ejrad.2007.11.002. PubMed PMID: 18160242.

116. Baumer TG, Davis L, Dischler J, Siegal DS, van Holsbeeck M, Moutzouros V, Bey MJ. Shear wave elastography of the supraspinatus muscle and tendon: Repeatability and preliminary findings. Journal of biomechanics. 2017;53:201-4. Epub 2017/01/24. doi: 10.1016/j.jbiomech.2017.01.008. PubMed PMID: 28110933.

117. Collinger JL, Fullerton B, Impink BG, Koontz AM, Boninger ML. Validation of grayscale-based quantitative ultrasound in manual wheelchair users: relationship to established clinical measures of shoulder pathology. American journal of physical medicine & rehabilitation. 2010;89(5):390-400. Epub 2010/04/22. doi: 10.1097/PHM.0b013e3181d8a238. PubMed PMID: 20407304; PMCID: PMC2859462.

118. Collinger JL, Gagnon D, Jacobson J, Impink BG, Boninger ML. Reliability of quantitative ultrasound measures of the biceps and supraspinatus tendons. Academic radiology. 2009;16(11):1424-32. Epub 2009/07/15. doi: 10.1016/j.acra.2009.05.001. PubMed PMID: 19596592; PMCID: PMC2764004.

119. Collinger JL, Impink BG, Ozawa H, Boninger ML. Effect of an intense wheelchair propulsion task on quantitative ultrasound of shoulder tendons. PM & R : the journal of injury, function, and rehabilitation. 2010;2(10):920-5. Epub 2010/10/26. doi: 10.1016/j.pmrj.2010.06.007. PubMed PMID: 20970761.

120. Nightingale K, Soo MS, Nightingale R, Trahey G. Acoustic radiation force impulse imaging: in vivo demonstration of clinical feasibility. Ultrasound in medicine & biology. 2002;28(2):227-35. Epub 2002/04/09. PubMed PMID: 11937286.

121. Nightingale K. Acoustic Radiation Force Impulse (ARFI) Imaging: a Review. Current medical imaging reviews. 2011;7(4):328-39. Epub 2012/05/01. doi: 10.2174/157340511798038657. PubMed PMID: 22545033; PMCID: PMC3337770.

122. Palmeri ML, Dahl JJ, MacLeod DB, Grant SA, Nightingale KR. On the feasibility of imaging peripheral nerves using acoustic radiation force impulse imaging. Ultrasonic imaging. 2009;31(3):172-82. Epub 2009/09/24. doi: 10.1177/016173460903100303. PubMed PMID: 19771960; PMCID: PMC2810513.

123. Trahey GE, Palmeri ML, Bentley RC, Nightingale KR. Acoustic radiation force impulse imaging of the mechanical properties of arteries: in vivo and ex vivo results. Ultrasound in medicine & biology. 2004;30(9):1163-71. Epub 2004/11/20. doi: 10.1016/j.ultrasmedbio.2004.07.022. PubMed PMID: 15550320.

124. Zhai L, Madden J, Foo WC, Palmeri ML, Mouraviev V, Polascik TJ, Nightingale KR. Acoustic radiation force impulse imaging of human prostates ex vivo. Ultrasound in medicine & biology. 2010;36(4):576-88. Epub 2010/03/31. doi: 10.1016/j.ultrasmedbio.2009.12.006. PubMed PMID: 20350685; PMCID: PMC2857920.

125. Zhai L, Polascik TJ, Foo WC, Rosenzweig S, Palmeri ML, Madden J, Nightingale KR. Acoustic radiation force impulse imaging of human prostates: initial in vivo demonstration. Ultrasound in medicine & biology. 2012;38(1):50-61. Epub 2011/11/23. doi: 10.1016/j.ultrasmedbio.2011.10.002. PubMed PMID: 22104533; PMCID: PMC3403291.

126. Rosskopf AB, Ehrmann C, Buck FM, Gerber C, Fluck M, Pfirrmann CW. Quantitative Shear-Wave US Elastography of the Supraspinatus Muscle: Reliability of the Method and Relation to Tendon Integrity and Muscle Quality. Radiology. 2016;278(2):465-74. Epub 2015/11/06. doi: 10.1148/radiol.2015150908. PubMed PMID: 26540450.

127. Slane LC, Martin J, DeWall R, Thelen D, Lee K. Quantitative ultrasound mapping of regional variations in shear wave speeds of the aging Achilles tendon. European radiology. 2017;27(2):474-82. Epub 2016/05/30. doi: 10.1007/s00330-016-4409-0. PubMed PMID: 27236815; PMCID: PMC5125901.

128. Taljanovic MS, Gimber LH, Becker GW, Latt LD, Klauser AS, Melville DM, Gao L, Witte RS. Shear-Wave Elastography: Basic Physics and Musculoskeletal Applications. Radiographics. 2017;37(3):855-70. doi: 10.1148/rg.2017160116. PubMed PMID: 28493799.

129. Nadeau M-J, Desrochers A, Lamontagne M, Larivière C, Gagnon DH. Quantitative ultrasound imaging of Achilles tendon integrity in symptomatic and asymptomatic individuals: reliability and minimal detectable change. J Foot Ankle Res. 2016;9:30-. doi: 10.1186/s13047-016-0164-3. PubMed PMID: 27540416.

130. Nightingale K, Bentley R, Trahey G. Observations of tissue response to acoustic radiation force: opportunities for imaging. Ultrasonic imaging. 2002;24(3):129-38. doi: 10.1177/016173460202400301. PubMed PMID: 12503770.

131. Shen ZL, Vince DG, Li ZM. In vivo study of transverse carpal ligament stiffness using acoustic radiation force impulse (ARFI) imaging. PloS one. 2013;8(7):e68569. Epub 2013/07/19. doi: 10.1371/journal.pone.0068569. PubMed PMID: 23861919; PMCID: PMC3702590.

132. Mhanna C, Marquardt TL, Li ZM. Adaptation of the Transverse Carpal Ligament Associated with Repetitive Hand Use in Pianists. PloS one. 2016;11(3):e0150174. Epub 2016/03/10. doi: 10.1371/journal.pone.0150174. PubMed PMID: 26953892; PMCID: PMC4783057.

133. Sarvazyan AP, Rudenko OV, Swanson SD, Fowlkes JB, Emelianov SY. Shear wave elasticity imaging: a new ultrasonic technology of medical diagnostics. Ultrasound in medicine & biology. 1998;24(9):1419-35. doi: 10.1016/s0301-5629(98)00110-0. PubMed PMID: 10385964.

134. Wang M, Byram B, Palmeri M, Rouze N, Nightingale K. Imaging transverse isotropic properties of muscle by monitoring acoustic radiation force induced shear waves using a 2-D matrix ultrasound array. IEEE Trans Med Imaging. 2013;32(9):1671-84. Epub 2013/05/14. doi: 10.1109/TMI.2013.2262948. PubMed PMID: 23686942.

135. DeWall RJ, Slane LC, Lee KS, Thelen DG. Spatial variations in Achilles tendon shear wave speed. Journal of biomechanics. 2014;47(11):2685-92. Epub 2014/05/16. doi: 10.1016/j.jbiomech.2014.05.008. PubMed PMID: 24933528.

136. Chen X-M, Cui L-G, He P, Shen W-W, Qian Y-J, Wang J-R. Shear wave elastographic characterization of normal and torn achilles tendons: a pilot study. J Ultrasound Med. 2013;32(3):449-55. doi: 10.7863/jum.2013.32.3.449. PubMed PMID: 23443185.

137. Cortes DH, Suydam SM, Silbernagel KG, Buchanan TS, Elliott DM. Continuous Shear Wave Elastography: A New Method to Measure Viscoelastic Properties of Tendons in Vivo. Ultrasound in medicine & biology. 2015;41(6):1518-29. Epub 2015/03/19. doi: 10.1016/j.ultrasmedbio.2015.02.001. PubMed PMID: 25796414.

138. Baumer TG, Dischler J, Davis L, Labyed Y, Siegal DS, van Holsbeeck M, Moutzouros V, Bey MJ. Effects of age and pathology on shear wave speed of the human rotator cuff. Journal of orthopaedic research : official publication of the Orthopaedic Research Society. 2017. Epub 2017/06/29. doi: 10.1002/jor.23641. PubMed PMID: 28657192.

139. Hatta T, Giambini H, Uehara K, Okamoto S, Chen S, Sperling JW, Itoi E, An KN. Quantitative assessment of rotator cuff muscle elasticity: Reliability and feasibility of shear wave elastography. Journal of biomechanics. 2015;48(14):3853-8. Epub 2015/10/17. doi: 10.1016/j.jbiomech.2015.09.038. PubMed PMID: 26472309; PMCID: PMC4655159.

140. Martin JA, Biedrzycki AH, Lee KS, DeWall RJ, Brounts SH, Murphy WL, Markel MD, Thelen DG. In Vivo Measures of Shear Wave Speed as a Predictor of Tendon Elasticity and Strength. Ultrasound in medicine & biology. 2015;41(10):2722-30. Epub 2015/07/26. doi: 10.1016/j.ultrasmedbio.2015.06.008. PubMed PMID: 26215492.

141. Weiss JA, Gardiner JC, Bonifasi-Lista C. Ligament material behavior is nonlinear, viscoelastic and rate-independent under shear loading. Journal of biomechanics. 2002;35(7):943-50. Epub 2002/06/08. PubMed PMID: 12052396.

142. Voycheck CA, Rainis EJ, McMahon PJ, Weiss JA, Debski RE. Effects of region and sex on the mechanical properties of the glenohumeral capsule during uniaxial extension. Journal of applied physiology (Bethesda, Md : 1985). 2010;108(6):1711-8. Epub 2010/04/17. doi: 10.1152/japplphysiol.01175.2009. PubMed PMID: 20395545; PMCID: PMC2886678.

143. Miller RM, Thunes J, Musahl V, Maiti S, Debski RE. Effects of tear size and location on predictions of supraspinatus tear propagation. Journal of biomechanics. 2018;68:51-7. Epub 2018/01/08. doi: 10.1016/j.jbiomech.2017.12.017. PubMed PMID: 29306551.

144. Sano H, Wakabayashi I, Itoi E. Stress distribution in the supraspinatus tendon with partial-thickness tears: an analysis using two-dimensional finite element model. Journal of shoulder and elbow surgery. 2006;15(1):100-5. Epub 2006/01/18. doi: 10.1016/j.jse.2005.04.003. PubMed PMID: 16414477.

145. Quental C, Folgado J, Monteiro J, Sarmento M. Full-thickness tears of the supraspinatus tendon: A three-dimensional finite element analysis. Journal of biomechanics. 2016;49(16):3962-70. Epub 2016/11/29. doi: 10.1016/j.jbiomech.2016.11.049. PubMed PMID: 27890533.

146. Inoue A, Chosa E, Goto K, Tajima N. Nonlinear stress analysis of the supraspinatus tendon using three-dimensional finite element analysis. Knee surgery, sports traumatology, arthroscopy : official journal of the ESSKA. 2013;21(5):1151-7. Epub 2012/05/24. doi: 10.1007/s00167-012-2008-4. PubMed PMID: 22618155.

147. Seki N, Itoi E, Shibuya Y, Wakabayashi I, Sano H, Sashi R, Minagawa H, Yamamoto N, Abe H, Kikuchi K, Okada K, Shimada Y. Mechanical environment of the supraspinatus tendon: three-dimensional finite element model analysis. Journal of orthopaedic science : official journal of the Japanese Orthopaedic Association. 2008;13(4):348-53. Epub 2008/08/13. doi: 10.1007/s00776-008-1240-8. PubMed PMID: 18696194.

148. Engelhardt C, Farron A, Becce F, Pioletti D, Terrier A. Impact of partial-thickness tears on supraspinatus tendon strain based on a finite element analysis. Computer methods in biomechanics and biomedical engineering. 2014;17 Suppl 1:118-9. Epub 2014/07/31. doi: 10.1080/10255842.2014.931514. PubMed PMID: 25074193.

149. Engelhardt C, Ingram D, Müllhaupt P, Farron A, Becce F, Pioletti D, Terrier A. Effect of partial-thickness tear on loading capacities of the supraspinatus tendon: a finite element analysis. Computer methods in biomechanics and biomedical engineering. 2016;19(8):875-82.

150. Celemín A, Vargas-Ariza R, Briceño JC, González-Gómez JC, Suárez DR. Influence of tear size on the load bearing capacity of the supraspinatus tendon. Ingeniería y Universidad. 2014;18(2):253-69.

151. Wakabayashi I, Itoi E, Sano H, Shibuya Y, Sashi R, Minagawa H, Kobayashi M. Mechanical environment of the supraspinatus tendon: a two-dimensional finite element model analysis. Journal of shoulder and elbow surgery. 2003;12(6):612-7. Epub 2003/12/13. doi: 10.1016/s1058274603002143. PubMed PMID: 14671529.

152. Palmeri ML, Sharma AC, Bouchard RR, Nightingale RW, Nightingale KR. A finite-element method model of soft tissue response to impulsive acoustic radiation force. IEEE transactions on

ultrasonics, ferroelectrics, and frequency control. 2005;52(10):1699-712. doi: 10.1109/tuffc.2005.1561624. PubMed PMID: 16382621.

153. Palmeri ML, McAleavey SA, Fong KL, Trahey GE, Nightingale KR. Dynamic mechanical response of elastic spherical inclusions to impulsive acoustic radiation force excitation. IEEE transactions on ultrasonics, ferroelectrics, and frequency control. 2006;53(11):2065-79. doi: 10.1109/tuffc.2006.146. PubMed PMID: 17091842.

154. Palmeri ML, Qiang B, Chen S, Urban MW. Guidelines for Finite-Element Modeling of Acoustic Radiation Force-Induced Shear Wave Propagation in Tissue-Mimicking Media. IEEE transactions on ultrasonics, ferroelectrics, and frequency control. 2017;64(1):78-92. Epub 2016/12/21. doi: 10.1109/TUFFC.2016.2641299. PubMed PMID: 28026760.

155. Rouze NC, Wang MH, Palmeri ML, Nightingale KR. Finite element modeling of impulsive excitation and shear wave propagation in an incompressible, transversely isotropic medium. Journal of biomechanics. 2013;46(16):2761-8. Epub 2013/09/13. doi: 10.1016/j.jbiomech.2013.09.008. PubMed PMID: 24094454.

156. Hossain MM, Moore CJ, Gallippi CM. Acoustic Radiation Force Impulse (ARFI)-Induced Peak Displacements Reflect Degree of Anisotropy in Transversely Isotropic Elastic Materials. IEEE transactions on ultrasonics, ferroelectrics, and frequency control. 2017;64(6):989-1001. Epub 2017/03/31. doi: 10.1109/TUFFC.2017.2690223. PubMed PMID: 28371775.

157. Minagawa H, Yamamoto N, Abe H, Fukuda M, Seki N, Kikuchi K, Kijima H, Itoi E. Prevalence of symptomatic and asymptomatic rotator cuff tears in the general population: From mass-screening in one village. Journal of orthopaedics. 2013;10(1):8-12. Epub 2014/01/10. doi: 10.1016/j.jor.2013.01.008. PubMed PMID: 24403741; PMCID: Pmc3768248.

158. Itoi E, Tabata S. Conservative treatment of rotator cuff tears. Clinical orthopaedics and related research. 1992(275):165-73. Epub 1992/02/01. PubMed PMID: 1735208.

159. Kuhn JE. Exercise in the treatment of rotator cuff impingement: a systematic review and a synthesized evidence-based rehabilitation protocol. Journal of shoulder and elbow surgery. 2009;18(1):138-60. Epub 2008/10/07. doi: 10.1016/j.jse.2008.06.004. PubMed PMID: 18835532.

160. Moosmayer S, Lund G, Seljom US, Haldorsen B, Svege IC, Hennig T, Pripp AH, Smith HJ. Tendon repair compared with physiotherapy in the treatment of rotator cuff tears: a randomized controlled study in 103 cases with a five-year follow-up. The Journal of bone and joint surgery American volume. 2014;96(18):1504-14. Epub 2014/09/19. doi: 10.2106/jbjs.m.01393. PubMed PMID: 25232074.

161. Kukkonen J, Joukainen A, Lehtinen J, Mattila KT, Tuominen EK, Kauko T, Aarimaa V. Treatment of non-traumatic rotator cuff tears: A randomised controlled trial with one-year clinical

results. The bone & joint journal. 2014;96-b(1):75-81. Epub 2014/01/08. doi: 10.1302/0301-620x.96b1.32168. PubMed PMID: 24395315.

162. Kuhn JE, Dunn WR, Sanders R, An Q, Baumgarten KM, Bishop JY, Brophy RH, Carey JL, Holloway BG, Jones GL, Ma CB, Marx RG, McCarty EC, Poddar SK, Smith MV, Spencer EE, Vidal AF, Wolf BR, Wright RW, Group MS. Effectiveness of physical therapy in treating atraumatic full-thickness rotator cuff tears: a multicenter prospective cohort study. J Shoulder Elbow Surg. 2013;22(10):1371-9. doi: 10.1016/j.jse.2013.01.026. PubMed PMID: 23540577; PMCID: 3748251.

163. Knight KL. Knee rehabilitation by the daily adjustable progressive resistive exercise technique. Am J Sports Med. 1979;7(6):336-7. Epub 1979/11/01. PubMed PMID: 507268.

164. McCann PD, Wootten ME, Kadaba MP, Bigliani LU. A kinematic and electromyographic study of shoulder rehabilitation exercises. Clin Orthop Relat Res. 1993(288):179-88. PubMed PMID: 8458132.

165. Reinold MM, Wilk KE, Fleisig GS, Zheng N, Barrentine SW, Chmielewski T, Cody RC, Jameson GG, Andrews JR. Electromyographic analysis of the rotator cuff and deltoid musculature during common shoulder external rotation exercises. J Orthop Sports Phys Ther. 2004;34(7):385-94. Epub 2004/08/07. doi: http://dx.doi.org/10.2519/jospt.2004.0665. PubMed PMID: 15296366.

166. Reinold MM, Escamilla RF, Wilk KE. Current concepts in the scientific and clinical rationale behind exercises for glenohumeral and scapulothoracic musculature. J Orthop Sports Phys Ther. 2009;39(2):105-17. Epub 2009/02/06. doi: http://dx.doi.org/10.2519/jospt.2009.2835. PubMed PMID: 19194023.

167. King GJ, Richards RR, Zuckerman JD, Blasier R, Dillman C, Friedman RJ, Gartsman GM, Iannotti JP, Murnahan JP, Mow VC, Woo SL. A standardized method for assessment of elbow function. Research Committee, American Shoulder and Elbow Surgeons. J Shoulder Elbow Surg. 1999;8(4):351-4. Epub 1999/09/03. PubMed PMID: 10472009.

168. Kirkley A, Alvarez C, Griffin S. The development and evaluation of a disease-specific quality-of-life questionnaire for disorders of the rotator cuff: the Western Ontario Rotator Cuff Index. Clin J Sport Med. 2003;13(2):84-92. Epub 2003/03/12. PubMed PMID: 12629425.

169. Hudak PL, Amadio PC, Bombardier C. Development of an upper extremity outcome measure: the DASH (disabilities of the arm, shoulder and hand) [corrected]. The Upper Extremity Collaborative Group (UECG). American journal of industrial medicine. 1996;29(6):602-8. doi: 10.1002/(SICI)1097-0274(199606)29:6<602::AID-AJIM4>3.0.CO;2-L. PubMed PMID: 8773720.

170. Michener LA, McClure PW, Sennett BJ. American Shoulder and Elbow Surgeons Standardized Shoulder Assessment Form, patient self-report section: reliability, validity, and

responsiveness. J Shoulder Elbow Surg. 2002;11(6):587-94. doi: http://dx.doi.org/10.1067/mse.2002.127096. PubMed PMID: 12469084.

171. de Witte PB, Henseler JF, Nagels J, Vliet Vlieland TP, Nelissen RG. The Western Ontario rotator cuff index in rotator cuff disease patients: a comprehensive reliability and responsiveness validation study. The American journal of sports medicine. 2012;40(7):1611-9. doi: 10.1177/0363546512446591. PubMed PMID: 22582227.

172. Beaton DE, Katz JN, Fossel AH, Wright JG, Tarasuk V, Bombardier C. Measuring the whole or the parts? Validity, reliability, and responsiveness of the Disabilities of the Arm, Shoulder and Hand outcome measure in different regions of the upper extremity. J Hand Ther. 2001;14(2):128-46. PubMed PMID: 11382253.

173. Jaeschke R, Singer J, Guyatt GH. Measurement of health status. Ascertaining the minimal clinically important difference. Control Clin Trials. 1989;10(4):407-15. Epub 1989/12/01. PubMed PMID: 2691207.

174. Kirkley A, Griffin S, Dainty K. Scoring systems for the functional assessment of the shoulder. Arthroscopy. 2003;19(10):1109-20. Epub 2003/12/16. doi: http://dx.doi.org/10.1016/j.arthro.2003.10.030. PubMed PMID: 14673454.

175. Roy JS, MacDermid JC, Woodhouse LJ. Measuring shoulder function: a systematic review of four questionnaires. Arthritis Rheum. 2009;61(5):623-32. Epub 2009/05/01. doi: http://dx.doi.org/10.1002/art.24396. PubMed PMID: 19405008.

176. Bey MJ, Zauel R, Brock SK, Tashman S. Validation of a new model-based tracking technique for measuring three-dimensional, in vivo glenohumeral joint kinematics. J Biomech Eng. 2006;128(4):604-9. Epub 2006/07/04. doi: http://dx.doi.org/10.1115/1.2206199. PubMed PMID: 16813452.

177. Wu G, van der Helm FC, Veeger HE, Makhsous M, Van Roy P, Anglin C, Nagels J, Karduna AR, McQuade K, Wang X, Werner FW, Buchholz B. ISB recommendation on definitions of joint coordinate systems of various joints for the reporting of human joint motion--Part II: shoulder, elbow, wrist and hand. Journal of biomechanics. 2005;38(5):981-92. Epub 2005/04/23. PubMed PMID: 15844264.

178. Bey MJ, Kline SK, Zauel R, Kolowich PA, Lock TR. In Vivo Measurement of Glenohumeral Joint Contact Patterns. EURASIP journal on advances in signal processing. 2010;2010. doi: 10.1155/2010/162136. PubMed PMID: 21546990; PMCID: 3086287.

179. Bey MJ, Peltz CD, Ciarelli K, Kline SK, Divine GW, van Holsbeeck M, Muh S, Kolowich PA, Lock TR, Moutzouros V. In vivo shoulder function after surgical repair of a torn rotator cuff: glenohumeral joint mechanics, shoulder strength, clinical outcomes, and their interaction. The

American journal of sports medicine. 2011;39(10):2117-29. doi: 10.1177/0363546511412164. PubMed PMID: 21737834.

180. Dal Maso F, Raison M, Lundberg A, Arndt A, Allard P, Begon M. Glenohumeral translations during range-of-motion movements, activities of daily living, and sports activities in healthy participants. Clin Biomech (Bristol, Avon). 2015;30(9):1002-7. Epub 2015/07/15. doi: 10.1016/j.clinbiomech.2015.06.016. PubMed PMID: 26162226.

181. Sano H, Ishii H, Trudel G, Uhthoff HK. Histologic evidence of degeneration at the insertion of 3 rotator cuff tendons: a comparative study with human cadaveric shoulders. J Shoulder Elbow Surg. 1999;8(6):574-9. PubMed PMID: 10633891.

182. Riley GP, Goddard MJ, Hazleman BL. Histopathological assessment and pathological significance of matrix degeneration in supraspinatus tendons. Rheumatology (Oxford). 2001;40(2):229-30. PubMed PMID: 11257166.

183. Hashimoto T, Nobuhara K, Hamada T. Pathologic evidence of degeneration as a primary cause of rotator cuff tear. Clin Orthop Relat Res. 2003(415):111-20. doi: 10.1097/01.blo.0000092974.12414.22. PubMed PMID: 14612637.

184. Maffulli N, Barrass V, Ewen SW. Light microscopic histology of achilles tendon ruptures. A comparison with unruptured tendons. Am J Sports Med. 2000;28(6):857-63. PubMed PMID: 11101109.

185. Longo UG, Franceschi F, Ruzzini L, Rabitti C, Morini S, Maffulli N, Denaro V. Histopathology of the supraspinatus tendon in rotator cuff tears. Am J Sports Med. 2008;36(3):533-8. doi: 10.1177/0363546507308549. PubMed PMID: 18006676.

186. Arnoczky SP, Lavagnino M, Egerbacher M. The mechanobiological aetiopathogenesis of tendinopathy: is it the over-stimulation or the under-stimulation of tendon cells? Int J Exp Pathol. 2007;88(4):217-26. doi: 10.1111/j.1365-2613.2007.00548.x. PubMed PMID: 17696902.

187. Galloway MT, Lalley AL, Shearn JT. The role of mechanical loading in tendon development, maintenance, injury, and repair. The Journal of bone and joint surgery American volume. 2013;95(17):1620-8. doi: 10.2106/JBJS.L.01004. PubMed PMID: 24005204.

188. Ferrer GA, Miller RM, Yoshida M, Wang JHC, Musahl V, Debski RE. Localized Rotator Cuff Tendon Degeneration for Cadaveric Shoulders with and Without Tears Isolated to the Supraspinatus Tendon. Clin Anat. 2019:10.1002/ca.23526. doi: 10.1002/ca.23526. PubMed PMID: 31750575.

189. Galatz LM, Charlton N, Das R, Kim HM, Havlioglu N, Thomopoulos S. Complete removal of load is detrimental to rotator cuff healing. Journal of shoulder and elbow surgery. 2009;18(5):669-75. doi: https://doi.org/10.1016/j.jse.2009.02.016.

190. Miller RM, Thunes JR, Musahl V, Maiti S, Debski RE. A Validated, Subject-Specific Finite Element Model for Predictions of Rotator Cuff Tear Propagation. Journal of biomechanical engineering. 2019:10.1115/1.4043872. doi: 10.1115/1.4043872. PubMed PMID: 31141596.

191. Snedeker JG, Foolen J. Tendon injury and repair - A perspective on the basic mechanisms of tendon disease and future clinical therapy. Acta Biomater. 2017;63:18-36. Epub 2017/09/01. doi: 10.1016/j.actbio.2017.08.032. PubMed PMID: 28867648.

192. Weiss JA, Maker BN, Govindjee S. Finite element implementation of incompressible, transversely isotropic hyperelasticity. Computer Methods in Applied Mechanics and Engineering. 1996;135(1):107-28. doi: http://dx.doi.org/10.1016/0045-7825(96)01035-3.

193. Pal S, Tsamis A, Pasta S, D'Amore A, Gleason TG, Vorp DA, Maiti S. A mechanistic model on the role of "radially-running" collagen fibers on dissection properties of human ascending thoracic aorta. Journal of biomechanics. 2014;47(5):981-8. Epub 2014/02/04. doi: 10.1016/j.jbiomech.2014.01.005. PubMed PMID: 24484644; PMCID: PMC4082402.

194. Vahdati A, Wagner DR. Implant size and mechanical properties influence the failure of the adhesive bond between cartilage implants and native tissue in a finite element analysis. Journal of biomechanics. 2013;46(9):1554-60. Epub 2013/04/27. doi: 10.1016/j.jbiomech.2013.03.019. PubMed PMID: 23618130.

195. Fortunato RN, Robertson AM, Sang C, Maiti S. Computational modeling reveals the relationship between intrinsic failure properties and uniaxial biomechanical behavior of arterial tissue. Biomech Model Mechanobiol. 2019;18(6):1791-807. Epub 2019/06/04. doi: 10.1007/s10237-019-01177-7. PubMed PMID: 31165377.

196. Maiti S, Geubelle PH. A cohesive model for fatigue failure of polymers. Engineering Fracture Mechanics. 2005;72(5):691-708. doi: https://doi.org/10.1016/j.engfracmech.2004.06.005.

197. Juncosa-Melvin N, Shearn JT, Boivin GP, Gooch C, Galloway MT, West JR, Nirmalanandhan VS, Bradica G, Butler DL. Effects of mechanical stimulation on the biomechanics and histology of stem cell-collagen sponge constructs for rabbit patellar tendon repair. Tissue Eng. 2006;12(8):2291-300. doi: 10.1089/ten.2006.12.2291. PubMed PMID: 16968169.

198. Wang JHC. Mechanobiology of tendon. Journal of biomechanics. 2006;39(9):1563-82. Epub 2005/07/05. doi: 10.1016/j.jbiomech.2005.05.011. PubMed PMID: 16000201.

199. Yamamoto N, Ohno K, Hayashi K, Kuriyama H, Yasuda K, Kaneda K. Effects of stress shielding on the mechanical properties of rabbit patellar tendon. Journal of biomechanical engineering. 1993;115(1):23-8. doi: 10.1115/1.2895466. PubMed PMID: 8445894.

200. Hughes RE, An KN. Force analysis of rotator cuff muscles. Clinical orthopaedics and related research. 1996(330):75-83. doi: 10.1097/00003086-199609000-00010. PubMed PMID: 8804277.

201. Gomez MA, Woo SL, Amiel D, Harwood F, Kitabayashi L, Matyas JR. The effects of increased tension on healing medical collateral ligaments. The American journal of sports medicine. 1991;19(4):347-54. doi: 10.1177/036354659101900405. PubMed PMID: 1897648.

202. Kamps BS, Linder LH, DeCamp CE, Haut RC. The influence of immobilization versus exercise on scar formation in the rabbit patellar tendon after excision of the central third. The American journal of sports medicine. 1994;22(6):803-11. doi: 10.1177/036354659402200612. PubMed PMID: 7856805.

203. Yamanaka K, Matsumoto T. The joint side tear of the rotator cuff. A followup study by arthrography. Clin Orthop Relat Res. 1994(304):68-73. Epub 1994/07/01. PubMed PMID: 8020236.

204. Naqvi GA, Jadaan M, Harrington P. Accuracy of ultrasonography and magnetic resonance imaging for detection of full thickness rotator cuff tears. International journal of shoulder surgery. 2009;3(4):94-7. Epub 2010/06/10. doi: 10.4103/0973-6042.63218. PubMed PMID: 20532011; PMCID: PMC2878704.

205. de Jesus JO, Parker L, Frangos AJ, Nazarian LN. Accuracy of MRI, MR arthrography, and ultrasound in the diagnosis of rotator cuff tears: a meta-analysis. AJR American journal of roentgenology. 2009;192(6):1701-7. Epub 2009/05/22. doi: 10.2214/ajr.08.1241. PubMed PMID: 19457838.

206. Smith TO, Back T, Toms AP, Hing CB. Diagnostic accuracy of ultrasound for rotator cuff tears in adults: a systematic review and meta-analysis. Clinical radiology. 2011;66(11):1036-48. Epub 2011/07/09. doi: 10.1016/j.crad.2011.05.007. PubMed PMID: 21737069.

207. Hung CY, Chang KV, Ozcakar L, Wang TG, Chen WS. Can Quantification of Biceps Peritendinous Effusion Predict Rotator Cuff Pathologies?: A Retrospective Analysis of 1352 Shoulder Ultrasound. American journal of physical medicine & rehabilitation. 2016;95(3):161-8. Epub 2016/02/02. doi: 10.1097/phm.0000000000000442. PubMed PMID: 26829075.

208. Drolet P, Martineau A, Lacroix R, Roy JS. Reliability of ultrasound evaluation of the long head of the biceps tendon. Journal of rehabilitation medicine. 2016;48(6):554-8. Epub 2016/05/05. doi: 10.2340/16501977-2095. PubMed PMID: 27144392.

209. Chang KV, Chen WS, Wang TG, Hung CY, Chien KL. Quantitative ultrasound facilitates the exploration of morphological association of the long head biceps tendon with supraspinatus tendon full thickness tear. PloS one. 2014;9(11):e113803. Epub 2014/11/21. doi: 10.1371/journal.pone.0113803. PubMed PMID: 25412357; PMCID: PMC4239113.

210. Gellhorn AC, Carlson MJ. Inter-rater, intra-rater, and inter-machine reliability of quantitative ultrasound measurements of the patellar tendon. Ultrasound in medicine & biology. 2013;39(5):791-6. Epub 2013/03/08. doi: 10.1016/j.ultrasmedbio.2012.12.001. PubMed PMID: 23465140.

211. Ingwersen KG, Hjarbaek J, Eshoej H, Larsen CM, Vobbe J, Juul-Kristensen B. Ultrasound assessment for grading structural tendon changes in supraspinatus tendinopathy: an inter-rater reliability study. BMJ open. 2016;6(5):e011746. Epub 2016/05/26. doi: 10.1136/bmjopen-2016-011746. PubMed PMID: 27221128; PMCID: PMC4885468.

212. Yu TY, Tsai WC, Cheng JW, Yang YM, Liang FC, Chen CH. The effects of aging on quantitative sonographic features of rotator cuff tendons. Journal of clinical ultrasound : JCU. 2012;40(8):471-8. Epub 2012/04/18. doi: 10.1002/jcu.21919. PubMed PMID: 22508403.

213. Felix ER, Cowan RE, Clark TS, Cardenas DD, Irwin RW. Increased Reliability of Quantitative Ultrasound Measures of the Supraspinatus Tendon Using Multiple Image Analysts and Analysis Runs. Am J Phys Med Rehabil. 2018;97(1):62-7. Epub 2017/09/06. doi: 10.1097/phm.0000000000000820. PubMed PMID: 28872465.

214. Hogaboom NS, Huang BL, Worobey LA, Koontz AM, Boninger ML. Cross-Sectional Investigation of Acute Changes in Ultrasonographic Markers for Biceps and Supraspinatus Tendon Degeneration After Repeated Wheelchair Transfers in People With Spinal Cord Injury. Am J Phys Med Rehabil. 2016;95(11):818-30. Epub 2016/10/22. doi: 10.1097/phm.0000000000000509. PubMed PMID: 27088477.

215. Crass JR, Craig EV, Feinberg SB. The hyperextended internal rotation view in rotator cuff ultrasonography. Journal of clinical ultrasound : JCU. 1987;15(6):416-20. Epub 1987/07/01. PubMed PMID: 3134443.

216. Ferri M, Finlay K, Popowich T, Stamp G, Schuringa P, Friedman L. Sonography of full-thickness supraspinatus tears: comparison of patient positioning technique with surgical correlation. AJR American journal of roentgenology. 2005;184(1):180-4. Epub 2004/12/24. doi: 10.2214/ajr.184.1.01840180. PubMed PMID: 15615971.

217. Jacobson JA. Shoulder US: anatomy, technique, and scanning pitfalls. Radiology. 2011;260(1):6-16. Epub 2011/06/24. doi: 10.1148/radiol.11101082. PubMed PMID: 21697306.

218. Shindle MK, Chen CC, Robertson C, DiTullio AE, Paulus MC, Clinton CM, Cordasco FA, Rodeo SA, Warren RF. Full-thickness supraspinatus tears are associated with more synovial inflammation and tissue degeneration than partial-thickness tears. Journal of shoulder and elbow surgery. 2011;20(6):917-27. Epub 2011/05/27. doi: 10.1016/j.jse.2011.02.015. PubMed PMID: 21612944; PMCID: PMC3156316.

219. Palmeri ML, Frinkley KD, Zhai L, Gottfried M, Bentley RC, Ludwig K, Nightingale KR. Acoustic radiation force impulse (ARFI) imaging of the gastrointestinal tract. Ultrasonic imaging. 2005;27(2):75-88. doi: 10.1177/016173460502700202. PubMed PMID: 16231837.

220. Zhan J, Jin J-M, Diao X-H, Chen Y. Acoustic radiation force impulse imaging (ARFI) for differentiation of benign and malignant thyroid nodules--A meta-analysis. European journal of radiology. 2015;84(11):2181-6. Epub 2015/07/17. doi: 10.1016/j.ejrad.2015.07.015. PubMed PMID: 26259701.

221. McGough RL, Debski RE, Taskiran E, Fu FH, Woo SL. Mechanical properties of the long head of the biceps tendon. Knee surgery, sports traumatology, arthroscopy : official journal of the ESSKA. 1996;3(4):226-9. doi: 10.1007/bf01466622. PubMed PMID: 8739718.

222. Moore SM, McMahon PJ, Azemi E, Debski RE. Bi-directional mechanical properties of the posterior region of the glenohumeral capsule. Journal of biomechanics. 2005;38(6):1365-9. doi: 10.1016/j.jbiomech.2004.06.005. PubMed PMID: 15863121.

223. Morrow DA, Haut Donahue TL, Odegard GM, Kaufman KR. Transversely isotropic tensile material properties of skeletal muscle tissue. J Mech Behav Biomed Mater. 2010;3(1):124-9. Epub 2009/04/05. doi: 10.1016/j.jmbbm.2009.03.004. PubMed PMID: 19878911.

224. Kuthe CD, Uddanwadiker RV. Investigation of effect of fiber orientation on mechanical behavior of skeletal muscle. J Appl Biomater Funct Mater. 2016;14(2):e154-e62. doi: 10.5301/jabfm.5000275. PubMed PMID: 27149942.

225. Samani A, Zubovits J, Plewes D. Elastic moduli of normal and pathological human breast tissues: an inversion-technique-based investigation of 169 samples. Physics in medicine and biology. 2007;52(6):1565-76. Epub 2007/02/16. doi: 10.1088/0031-9155/52/6/002. PubMed PMID: 17327649.

226. Umemoto T, Ueno E, Matsumura T, Yamakawa M, Bando H, Mitake T, Shiina T. Ex vivo and in vivo assessment of the non-linearity of elasticity properties of breast tissues for quantitative strain elastography. Ultrasound in medicine & biology. 2014;40(8):1755-68. Epub 2014/05/05. doi: 10.1016/j.ultrasmedbio.2014.02.005. PubMed PMID: 24802305.

227. Nguyen MM, Ding X, Leers SA, Kim K. Multi-Focus Beamforming for Thermal Strain Imaging Using a Single Ultrasound Linear Array Transducer. Ultrasound in medicine & biology. 2017;43(6):1263-74. Epub 2017/03/18. doi: 10.1016/j.ultrasmedbio.2017.01.015. PubMed PMID: 28318887.

228. Nguyen MM, Ding X, Yu F, Kim K, editors. Adaptive beamforming for thermal strain imaging using a single ultrasound linear array. 2014 IEEE International Ultrasonics Symposium; 2014 3-6 Sept. 2014.

229. Nguyen MM, Ding X, Leers SA, Kim K. Multi-Focus Beamforming for Thermal Strain Imaging Using a Single Ultrasound Linear Array Transducer. Ultrasound in Medicine and Biology. 2017;43(6):1263-74.

230. Pinton GF, Dahl JJ, Trahey GE. Rapid tracking of small displacements with ultrasound. IEEE transactions on ultrasonics, ferroelectrics, and frequency control. 2006;53(6):1103-17.

231. Fahey BJ, Nelson RC, Bradway DP, Hsu SJ, Dumont DM, Trahey GE. In vivo visualization of abdominal malignancies with acoustic radiation force elastography. Physics in medicine and biology. 2008;53(1):279-93. Epub 2008/01/10. doi: 10.1088/0031-9155/53/1/020. PubMed PMID: 18182703; PMCID: PMC2238175.

232. Uchida H, Tohyama H, Nagashima K, Ohba Y, Matsumoto H, Toyama Y, Yasuda K. Stress deprivation simultaneously induces over-expression of interleukin-1beta, tumor necrosis factor-alpha, and transforming growth factor-beta in fibroblasts and mechanical deterioration of the tissue in the patellar tendon. Journal of biomechanics. 2005;38(4):791-8. doi: 10.1016/j.jbiomech.2004.05.009. PubMed PMID: 15713300.

233. Miller DL. Overview of experimental studies of biological effects of medical ultrasound caused by gas body activation and inertial cavitation. Prog Biophys Mol Biol. 2007;93(1-3):314-30. Epub 2006/08/22. doi: 10.1016/j.pbiomolbio.2006.07.027. PubMed PMID: 16989895.

234. Good CR, Shindle MK, Kelly BT, Wanich T, Warren RF. Glenohumeral chondrolysis after shoulder arthroscopy with thermal capsulorrhaphy. Arthroscopy : the journal of arthroscopic & related surgery : official publication of the Arthroscopy Association of North America and the International Arthroscopy Association. 2007;23(7):797.e1-.e7975. doi: 10.1016/j.arthro.2007.03.092. PubMed PMID: 17637423.

235. Martin JA, Schmitz DG, Ehlers AC, Allen MS, Thelen DG. Calibration of the shear wave speed-stress relationship in ex vivo tendons. Journal of biomechanics. 2019;90:9-15. Epub 2019/04/17. doi: 10.1016/j.jbiomech.2019.04.015. PubMed PMID: 31088754.

236. Martin JA, Brandon SCE, Keuler EM, Hermus JR, Ehlers AC, Segalman DJ, Allen MS, Thelen DG. Gauging force by tapping tendons. Nat Commun. 2018;9(1):1592-. doi: 10.1038/s41467-018-03797-6. PubMed PMID: 29686281.

237. Yavuz A, Bora A, Bulut MD, Batur A, Milanlioglu A, Göya C, Andic C. Acoustic Radiation Force Impulse (ARFI) elastography quantification of muscle stiffness over a course of gradual isometric contractions: a preliminary study. Med Ultrason. 2015;17(1):49-57. doi: 10.11152/mu.2013.2066.171.yvz. PubMed PMID: 25745658.

238. Ikeda J, Zhao C, Chen Q, Thoreson AR, An K-N, Amadio PC. Compressive properties of cd-HA-gelatin modified intrasynovial tendon allograft in canine model in vivo. Journal of

biomechanics. 2011;44(9):1793-6. Epub 2011/05/06. doi: 10.1016/j.jbiomech.2010.12.030. PubMed PMID: 21549380.

239. Woo SL, Gomez MA, Akeson WH. The time and history-dependent viscoelastic properties of the canine medical collateral ligament. Journal of biomechanical engineering. 1981;103(4):293-8. doi: 10.1115/1.3138295. PubMed PMID: 7311496.

240. Lake SP, Miller KS, Elliott DM, Soslowsky LJ. Tensile properties and fiber alignment of human supraspinatus tendon in the transverse direction demonstrate inhomogeneity, nonlinearity, and regional isotropy. Journal of biomechanics. 2010;43(4):727-32. Epub 2009/11/11. doi: 10.1016/j.jbiomech.2009.10.017. PubMed PMID: 19900677; PMCID: PMC2823853.

241. Amin VR. Ultrasonic attenuation estimation for tissue characterization1989.

242. Fung Y-c. Biomechanics: mechanical properties of living tissues: Springer Science & Business Media; 2013.

243. Davidson J, Burkhart SS. The geometric classification of rotator cuff tears: a system linking tear pattern to treatment and prognosis. Arthroscopy : the journal of arthroscopic & related surgery : official publication of the Arthroscopy Association of North America and the International Arthroscopy Association. 2010;26(3):417-24. Epub 2010/03/09. doi: 10.1016/j.arthro.2009.07.009. PubMed PMID: 20206053.

244. Davidson JFJ, Burkhart SS, Richards DP, Campbell SE. Use of preoperative magnetic resonance imaging to predict rotator cuff tear pattern and method of repair. Arthroscopy : the journal of arthroscopic & related surgery : official publication of the Arthroscopy Association of North America and the International Arthroscopy Association. 2005;21(12):1428-. doi: 10.1016/j.arthro.2005.09.015. PubMed PMID: 16376230.

245. Dal Maso F, Raison M, Lundberg A, Arndt A, Allard P, Begon M. Glenohumeral translations during range-of-motion movements, activities of daily living, and sports activities in healthy participants. Clinical biomechanics (Bristol, Avon). 2015. Epub 2015/07/15. doi: 10.1016/j.clinbiomech.2015.06.016. PubMed PMID: 26162226.